Functional characterization of the mitochondrial microprotein SMIM26

DISSERTATION ZUR ERLANGUNG DES
DOKTORGRADES DER NATURWISSENSCHAFTEN (DR. RER. NAT.)
DER FAKULTÄT FÜR BIOLOGIE UND VORKLINISCHE MEDIZIN
DER UNIVERSITÄT REGENSBURG

vorgelegt von

Kevin Michael Heizler

aus Furth im Wald

im Jahr 2025

Das Promotionsgesuch wurde eingereicht am:

03.12.2025

Die Arbeit wurde angeleitet von:

Prof. Dr. Gunter Meister

_____

(Kevin Michael Heizler)

„Kreativität ist Intelligenz, die Spaß hat“

-Albert Einstein-

Contents

1 Abstract

Microproteins represent a class of short polypeptides with very diverse cellular functions. These small proteins frequently escape proteomic-based identifications, making their extent and theeir potential functions largely elusive. Many microproteins originate from transcripts that are annotated as non-coding such as long non-coding RNAs (lncRNAs), circular RNAs (circRNAs) and micro RNAs (miRNAs). However, also messenger RNAs (mRNAs) can contain additional short open reading frames (sORFs) that encode microproteins.

In this work, we functionally characterize SMIM26, a microprotein localized to mitochondria. In biochemical and single molecule tracking studies, we find that SMIM26 interacts with VDAC1/2 in the outer mitochondrial membrane and SLC25A6 in the inner mitochondrial membrane. We show that it spans the intermembrane space where it interacts with PGAM5 and is phosphorylated at distinct residues. Knockout cancer cell lines are viable but have strongly reduced respiratory chain activity and are sensible to glucose starvation. Interestingly, knockout mice are not viable and die already at early developmental stages. Zebrafish homozygous *smim26* mutants are viable, but show reduced fitness and survival compared to their wild-type or heterozygous siblings. Surprisingly, loss of *smim26* induces female-to-male sex reversal in mutant fish. Consistent with the mitochondrial phenotype in cell lines, respiration is reduced in homozygous zebrafish embryos and components of the N- and Q-module in respiratory chain complex I are downregulated. In cancer, loss of SMIM26 leads to dysregulated signaling pathways and high expression levels of SMIM26 alone or in combination with its binding partners is associated with worse survival in liver cancer. Based on the functional characterization and patient data, in a pilot anti-cancer drug screen we identify two compounds that display a stronger effect SMIM26 on knockout cell lines compared to wild-type.

Our work suggests that SMIM26 coordinates metabolite transport through the inner and outer mitochondrial membranes and is essential for respiratory function *in vivo*. Therefore, SMIM26 could be an interesting target for anti-cancer therapies in the future.

2 Introduction

2.1 The Dark Proteome – short open reading frame encoded microproteins

2.1.1 Identification of short ORFs and microproteins

In the late twentieth century, a global collaborative effort known as the Human Genome Project (HGP) was launched to provide comprehensive insights into the human genome. With its completion in 2003, the HGP helped to elucidate the molecular basis of human biology and disease and enabled an in-depth look into previously uncharacterized genomic regions, and by extension also the transcriptome and proteome (Lander et al., 2001). Based on its initial findings, the HGP estimated approximately 20,000 – 25,000 human protein-coding genes (International Human Genome Sequencing Consortium, 2004). However, this annotation relied on stringent parameters to filter out putative open reading frames (ORFs) that could arise randomly due to in-frame arrangements of start and stop codons. These included a minimum protein length of 100 amino acids (aa), an AUG start codon, monocistronic transcripts and no overlapping ORFs (Okazaki et al., 2002; International Human Genome Sequencing Consortium, 2004). However, these restrictions were detrimental to the detection of short ORF (sORF)-encoded microproteins and other non-canonical genes.

These assumptions defining the properties of functional ORFs were challenged by a series of key discoveries demonstrating that sORFs and microproteins, which are protein products of up to 100 aa and translated from an independent ORF, are ubiquitously expressed and biologically relevant (Duffy et al., 2024). In 1987, Marilyn Kozak reported the existence of upstream ORFs (uORFs) within human messenger RNAs (mRNAs) that could lead to translation outside of known protein-coding regions. At that time, these uORFs were thought to function solely as *cis*-regulatory elements controlling the translation of downstream protein-coding sequences (CDS) (Kozak, 1987). However, it later became evident that some uORFs produce functional small proteins (Rathore et al., 2018; Cloutier et al., 2020; Rocha et al., 2024). While

many studies on sORFs suggested ribosome engagement based on early computational approaches (Kozak, 1987), ribosome binding models (Hemm et al., 2008), and genetic approaches (Kastenmayer et al., 2006), Oyama et al. (2004) provided proteomic evidence for the translation of uORFs in human cell lines. These findings offered early support for sORF translation beyond annotated CDS, including non-canonical start codon usage (Oyama et al., 2007). A combination of these methods led to the discovery of individual, functional sORF-encoded microproteins across different species, including human (Hashimoto et al., 2001a; Ikonen et al., 2003), insects (Tupy et al., 2005), plants (Sousa et al., 2001) and prokaryotes (Handler et al., 2008). In 2011, Ingolia et al. developed a method called ribosome profiling (Ribo-seq) that enabled transcriptome-wide mapping of actively translated regions at nucleotide resolution (Ingolia et al., 2009; Ingolia et al., 2011). Although the exact number of sORF-encoded functional microproteins in pro- and eukaryotic genomes remains debated, these studies provided substantial evidence for their presence and relevance in various biological processes.

As the early discoveries of expressed sORFs occurred before their widespread existence was recognized, various terminologies for sORFs and their protein products exist. sORFs (Olexiouk et al., 2016) are also known as small ORFs (smORFs) (Basrai et al., 1997), while microproteins (Staudt and Wenkel, 2011) are still referred to as micropeptides (Anderson et al., 2015), sORF-encoded polypeptides (SEPs) (Slavoff et al., 2013), alternative proteins (altProts) (Vanderperre et al., 2013) or small proteins (Storz et al., 2014). Exact definitions vary, with upper limits ranging from 100 aa to 150 aa in some studies. In prokaryotes, small proteins are frequently defined as unannotated proteins shorter than 50 aa. These different nomenclatures are often used interchangeably to describe small, previously unannotated proteins that are hidden in the “dark proteome” of cells.

2.1.2 Discovery of sORFs and microproteins

The discovery and functional characterization of sORFs faces several challenges and technical limitations. Many commonly used approaches to identify novel proteins struggle with their small size, sometimes low abundance, short half-life and low evolutionary conservation. Over the last decade, extensive efforts have focused on

developing methods and tools to identify sORF-encoded microproteins and overcome these limitations.

Ribosome profiling has emerged as a powerful method to study genome-wide active translation of canonical and short ORFs, even outside of annotated CDSs (**Figure 2-1**) (Ingolia et al., 2009; van Heesch et al., 2019; Chen et al., 2020; Martinez et al., 2020). Ribo-seq relies on a nucleotide-precise resolution of ribosome footprints, typically ~28 – 30 nucleotide (nt) long fragments of ribosome-bound RNA protected from nuclease digestion. To obtain these footprints, elongating ribosomes are arrested using a translation elongation inhibitor such as cycloheximide, and unprotected RNA is subsequently digested by nucleases. Ribosome-protected fragments from purified monosomes can be isolated, sequenced and mapped to the genome to identify regions of active translation (Ingolia et al., 2009).

However, ribosome occupancy does not necessarily indicate translation of an ORF, as ribosomes can associate with mRNAs without actively producing proteins (Guttman et al., 2013). Accordingly, Ribo-seq data requires careful computational analysis, especially for sORFs, as their short length and lower abundance can lead to a lower signal-to-noise ratio in sORF-mapped reads (Martinez et al., 2020). Computational tools like ORFscore (Bazzini et al., 2014), PRICE (Erhard et al., 2018), RibORF (Cao et al., 2023) and many others have been developed to accurately predict sORFs from Ribo-seq data, relying on parameters that define active translation such as three-nucleotide periodicity.

Although Ribosome profiling is an effective tool to identify unannotated coding regions, commonly used translation elongation inhibitors like cycloheximide are not ideal for deconvoluting some translation initiation sites, especially for polycistronic transcripts or overlapping ORFs (Lee et al., 2012). To identify such sORFs with higher confidence, Ribo-seq can be combined with translation initiation sequencing (TI-seq). TI-seq investigates the footprints of initiating eukaryotic ribosomes using specific inhibitors like harringtonine, lactimidomycin or puromycin to stall ribosomes and resolve nested or out-of-frame sORFs (Fritsch et al., 2012; Ingolia et al., 2012; Gao et al., 2015). In a global effort to curate translated sORFs from multiple Ribo-seq datasets, Mudge et al. (2022) generated the first publicly available, high-confidence

Ribo-seq translatome catalog, displaying the strength of this method for the discovery of novel sORF-encoded microproteins.

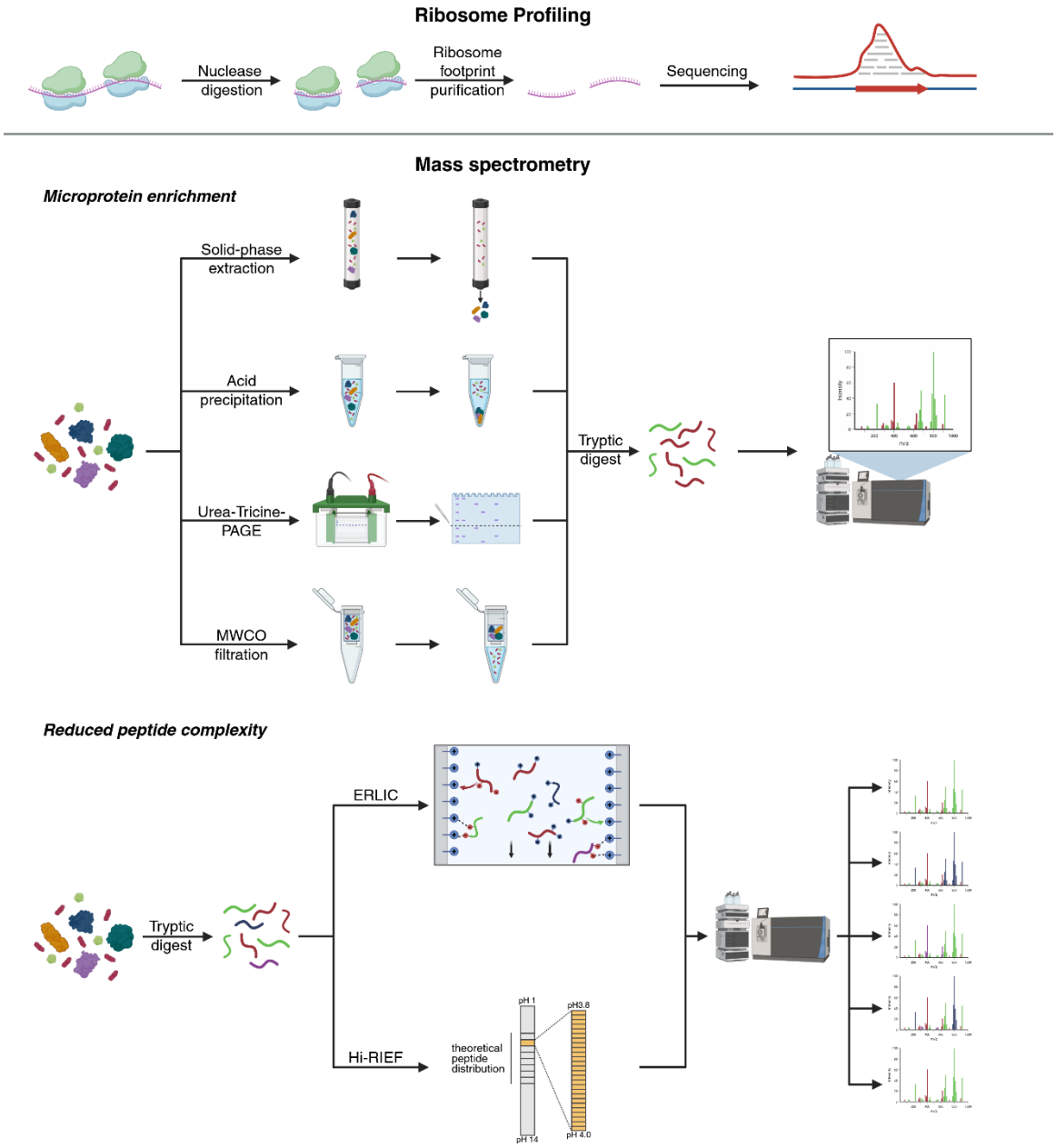

Figure 2-1: Advanced methods to identify sORFs and microproteins.
Ribosome profiling and mass spectrometry (MS)-based methods have been optimized for the detection of microprotein-encoding sORFs. Top: Stalled and crosslinked translating ribosomes are treated with nucleases, ribosome protected RNA fragments (Ribosome protected footprints) are purified and subsequently sequenced. Reads can then be matched to the transcriptome to identify novel sORFs. Bottom: Mass spectrometry workflows need to be optimized for the detection of small proteins. To enrich for microproteins before tryptic digest and mass spectrometric analysis, bigger proteins are removed via solid-phase extraction, acid precipitation, Urea-Tricine-polyacrylamide gel electrophoresis (PAGE) or molecular weight cutoff (MWCO) filtration. Better coverage in MS experiments can also be achieved by reducing the complexity of tryptic peptides via fractionation using electrostatic repulsion-hydrophilic interaction chromatography (ERLIC) or high-resolution isoelectric focusing (Hi-RIEF).

Mass spectrometry (MS) has been established as the gold standard for protein identification. The standard protocol for MS analysis requires the generation of cell or tissue extracts followed by several processing steps generating tryptic peptides that are subsequently analyzed by liquid chromatography coupled with tandem mass spectrometry (LC-MS/MS) (McCormack et al., 1997). However, several challenges hinder the detection of microproteins by standard mass spectrometry protocols. First, due to their small size and often low abundance, microproteins are frequently lost during common sample preparation methods (He et al., 2018). Second, microproteins often yield only one or a few tryptic peptides, making them difficult to detect in presence of the significantly higher number of peptides generated from larger proteins (Khitun and Slavoff, 2019). Third, many protein databases used for data analysis of MS experiments do not contain unannotated microproteins, resulting in unique microprotein peptide fragments being unmapped (Slavoff et al., 2013).

To overcome these difficulties, protocols have been optimized to increase the detection rate of microproteins in mass spectrometry experiments (**Figure 2-1**). One successful approach was the enrichment of microproteins prior to digestion to enhance their detection sensitivity. Common enrichment methods include solid-phase extraction, acid extraction, urea-tricine polyacrylamide gel electrophoresis (PAGE), and molecular weight cutoff (MWCO) filtration (Ma et al., 2016; He et al., 2018). Additionally, the complexity of tryptic peptide samples can be reduced. For example, varying charges of individual peptides in a complex mixture due to phosphorylation or other post-translational modifications can be utilized to fractionate by anion exchange chromatography (electrostatic repulsion-hydrophilic interaction chromatography, ERLIC) (Khitun and Slavoff, 2019) or high-resolution isoelectric focusing (Hi-RIEF) (Branca et al., 2014) prior to mass spectrometry analysis.

Nonetheless, even with improved enrichment strategies, some challenges remain. To increase the number of detectable peptides in MS-experiments, trypsin can be replaced or combined with other proteases cleaving at alternative amino acid residues (Low et al., 2013; Tsiatsiani and Heck, 2015). Additionally, optimized sample preparation should be paired with specialized protein databases, as many microproteins are absent from common proteome reference sets. These databases

may include curated sORF repositories such as sORFs.org (Olexiouk et al., 2018), SmProt (Hao et al., 2018), and nORFs.org (Neville et al., 2021), or custom-constructed databases of translated sORFs combining Ribo-seq and mass spectrometry (Ouspenskaia et al., 2022).

In addition to omics-based strategies to detect microproteins, extensive efforts have been made to develop computational approaches to predict unannotated sORFs *in silico*. Coding regions in the genome generally exhibit higher conservation than non-coding sequences. Many prediction tools exploit this feature by assessing nonsynonymous versus synonymous substitution ratios (dN/dS) across homologous sequences (Lin et al., 2011). However, the limited length of microprotein-coding regions can preclude robust alignments and substitution rate estimation (Lin et al., 2011; Ruiz-Orera and Albà, 2019). PhyloCSF addresses this limitation by incorporating phylogenetic models to improve prediction accuracy (Lin et al., 2011).

Other tools take additional features of CDS into account, including Kozak consensus sequence upstream of eukaryotic start codons (Camargo et al., 2020) or ribosome binding sites in prokaryotes (Hemm et al., 2008). Yet, some functional sORFs have evolved *de novo* from non-coding regions and lack conservation across species (McLysaght and Hurst, 2016). In such cases, population genetic metrics like single nucleotide variants can be utilized to identify selection pressure (Ruiz-Orera et al., 2018). Other machine learning approaches such as RNAsamba (Camargo et al., 2020) or DeepCPP (Zhang et al., 2021) completely abolish the need for alignment information and predict the coding potential of transcripts directly from sequence features.

Although predicting and detecting sORF-encoded microproteins remains challenging, the integration of advanced omics approaches such as ribosome profiling and mass spectrometry with improved computational frameworks has markedly enhanced their confidence and output. These developments lay the foundation for the identification and functional characterization of a growing number of microproteins across different species.

2.1.3 Classes of sORFs

2.1.3.1 Genome-derived sORFs

Advances in various methods (**2.1.2**) identified novel sORFs within a broad spectrum of transcrupts such as non-coding RNAs (ncRNAs), annotated mRNAs and even in the mitochondrial genome.

Perhaps the biggest and best studied group of sORFs arises from annotated non-coding transcripts such as long non-coding RNAs (lncRNAs), transcribed pseudogenes, antisense RNAs, circular RNAs (circRNAs) and primary microRNAs (pri-miRNAs) (**Figure 2-2**). Interestingly, some studies suggest that approximately 40% of all lncRNAs may be translated (Ji et al., 2015). In fact, many of these lncRNAs might have been misannotated due to the strict parameters applied to predict coding potential, as many cytoplasmic lncRNAs are spliced, polyadenylated and 7-methyl-guanosine (m^7G)-capped, therefore resembling canonical mRNAs (Losko et al., 2016). Surprisingly, even non-polyadenylated lncRNAs have been identified to associate with translating ribosomes. For instance, MALAT1 (Metastasis associated lung adenocarcinoma transcript 1), one of the most studied lncRNAs, can be translated in differentiating neurons under specific conditions (Xiao et al., 2024).

Other studies suggest that a subset of microprotein-encoding lncRNAs may even exert dual coding and non-coding functions. In *Escherichia coli*, the bifunctional RNA SgrT/SgrS blocks sugar phosphate accumulation by reducing the expression level and activity of a glucose permease *ptsG*. The lncRNA SgrS binds to the 5' end of the ptsG mRNA to block its translation while the microprotein SgrT binds to PtsG and inhibits glucose transport (Vanderpool and Gottesman, 2004; Wadler and Vanderpool, 2007; Lloyd et al., 2017). Antisense RNAs have also been described to contain sORFs. The primate-specific LINE-1 (Long interspersed nuclear element-1) retrotransposon promotor contains an antisense sORF encoding the microprotein *orf0*, which enhances LINE-1 mobility and therefore leads to more frequent transposition events within the genome (Denli et al., 2015). Other sORFs embedded in antisense transcripts, like PIGBOS (PIGB opposite strand), have been shown to play important roles in various cellular mechanisms (Chu et al., 2019).

Moreover, sORFs have been identified in other classes of ncRNAs such as pri-miRNA (**Figure 2-2**). These microRNA-encoded peptides (miPEPs) have first been reported in plants (Lauressergues et al., 2015; Couzigou et al., 2016; Lauressergues et al., 2022). Many miPEPs, such as miPEP858, have been shown to regulate the expression of their miRNA and its associated target genes (Sharma et al., 2020). Recently, miPEPs have been discovered in *Drosophila melanogaster* (Immarigeon et al., 2021; Montigny et al., 2021) and human (Kang et al., 2020; Niu et al., 2020). However, apart from one study (Kang et al., 2020), a positive autoregulatory loop, as observed in plants, does not appear to be a general feature of human miPEPs (Prel et al., 2021). For instance, miPEP155 suppresses autoimmune inflammation by modulating the antigen presentation in T cells independently of its host miRNA (Niu et al., 2020).

Another class of ncRNAs harboring sORFs are covalently closed circRNAs, which are generated by back-splicing of exons on precursor mRNAs. Current studies have linked circRNAs to a wide range of non-coding functions (Li et al., 2018). However, several circRNAs have been proposed to be translated (**Figure 2-2**) (Zhang et al., 2018; Yang et al., 2021). For example, the microprotein p113 is encoded by circCUX1 (Circular RNA CUT-like homeobox 1) and promotes lipid metabolic reprogramming, mitochondrial activity, proliferation and metastasis in neuroblastoma cells (Yang et al., 2021).

In addition to non-coding transcripts, sORFs have also been discovered in intergenic regions of the genome (**Figure 2-2**). Early studies found a large number of intergenic, non-annotated sORFs in *Arabidopsis thaliana* and other plants (Hanada et al., 2007), while more advanced approaches expand the number of newly identified sORFs in intergenic regions in other organisms like human or mouse (Yang et al., 2025).

Translated sORFs are not restricted to non-coding transcripts alone. They also frequently occur within mRNAs (Yang et al., 2024), where they can regulate the translation of the long, canonical CDS in *cis* or encode functional microproteins . The polycistronic nature of these transcripts expands the historic view of protein-coding RNAs and gives rise to complex regulations and mechanisms (Brunet et al., 2018; Brunet et al., 2020).

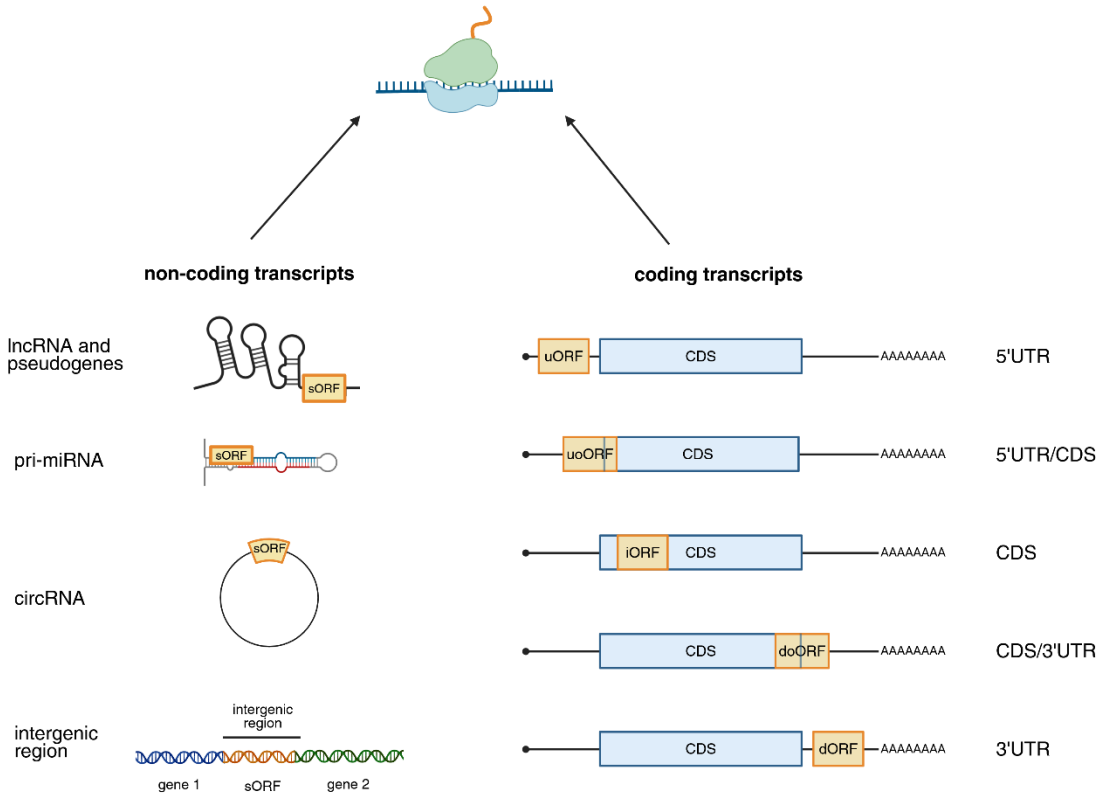

Figure 2-2: Nuclear-encoded sORFs.
sORFs have been identified on non-coding and coding transcripts. Non-coding transcripts include long non-coding RNAs (lncRNA), pseudogenes, circular RNAs (circRNA), primary micro RNAs (pri-miRNA) and intergenic regions. mRNAs can harbor sORFs in the 5' untranslated region (5'UTR; upstream ORF; uORF), overlapping the 5'UTR and the coding sequence (CDS; upstream overlapping ORF; uoORF), out-of-frame within a CDS (nested or internal ORF; iORF), overlapping the CDS and the 3'UTR (downstream overlapping ORF; doORF) or in the 3'UTR (downstream ORF; dORF).

sORFs within mRNAs are categorized based on their location relative to the annotated CDS (**Figure 2-2**). Hence, sORFs that initiate within the 5' untranslated region (UTR) are called upstream ORFs. While most uORFs terminate before the start codon of the downstream CDS, some initiate at an out-of-frame start codon in the 5'UTR and extend into the annotated CDS. These are referred to as upstream overlapping ORFs (uoORFs). uORFs and uoORFs generally act as translational repressors of the downstream ORF (Johnstone et al., 2016) through different mechanisms, including competitive translation (Johnstone et al., 2016; Dever et al., 2023), induction of nonsense-mediated decay (NMD) (Hurt et al., 2013) or modulation of internal ribosome entry sites (IRES) usage (Fernandez et al., 2005; Bastide et al., 2008). One well-studied example of uORF translational control is the mammalian transcription

factor ATF4 (activating transcription factor 4) (Vattem and Wek, 2004), or *GCN4* (general control transcription factor) in yeast (Hinnebusch, 2005), where the main ORF is repressed by its uORFs under normal conditions and is only translated in response to stress (Vattem and Wek, 2004; Dever et al., 2023). Although uORF-mediated translational repression is mostly independent of the produced peptides, a small subset of uORF- and uoORF- encoded microproteins are evolutionarily conserved at amino acid level, giving evidence for potential coding function. For example, a uORF on the MIEF1 (Mitochondrial elongation factor 1) transcript produces a microprotein (MIEF1-MP) that controls mitochondrial translation (Rathore et al., 2018). Another uORF, found on the SLC35A4 (Solute carrier family 35 member A4) mRNA, encodes the microprotein SLC35A4-MP, regulating cellular metabolism (Rocha et al., 2024).

Recently, frameshifted sORFs fully contained within an annotated CDS have been of emerging interest. These sORFs are called nested, internal (iORFs) or alternative ORFs (alt-ORF) (**Figure 2-2**). While some studies found up to 30% of all newly identified non-canonical proteins to originate from iORFs (Slavoff et al., 2013; Yang et al., 2024), these are challenging to discover and study by mass spectrometry, ribosome profiling or genetic tools due to their overlap with the annotated CDS. Hence, only a handful of iORF-encoded microproteins have been characterized, including the pre-60S assembly checkpoint inhibitor MINAS-60 (Microprotein that negatively regulates assembly of the pre-60S ribosomal subunit) (Cao et al., 2022), the autophagy inhibitor altFUS (Brunet et al., 2021), and an anti-apoptotic microprotein produced from an iORF on DEDD2 (Death effector domain containing 2) (Su et al., 2025). Interestingly, these examples show that iORF encoded microproteins can act agonistic (altFUS), antagonistic (DEDD2 iORF) or be functionally unrelated (MINAS-60) in respect to their canonical ORF.

Analogous to uORFs, downstream ORFs (dORFs) and downstream overlapping ORFs (doORFs) are fully embedded within the 3'UTR, but appear to be less prevalent (**Figure 2-2**) (Slavoff et al., 2013; Yang et al., 2024). Interestingly, dORFs translation has been reported to enhance translation of the CDS, suggesting a cis-regulatory effect independent of the dORF sequence or length (Wu et al., 2020a). To date, dORFs have

not yet been described to produce functional microproteins, so whether the role of this sORF class goes beyond translational control remains unknown.

2.1.3.2 Mitochondrial genome-derived sORFs

Mitochondria are the only organelle that possesses their own genome, a highly compact, circular DNA which is believed to mainly be transcribed as one long polycistronic RNA (Temperley et al., 2010). The mitochondrial genome (mtDNA) encodes for 13 proteins of the respiratory chain, 22 mitochondrial transfer RNAs (mt-tRNAs), and two mitochondrial ribosomal RNAs (mt-rRNAs) (**Figure 2-3**).

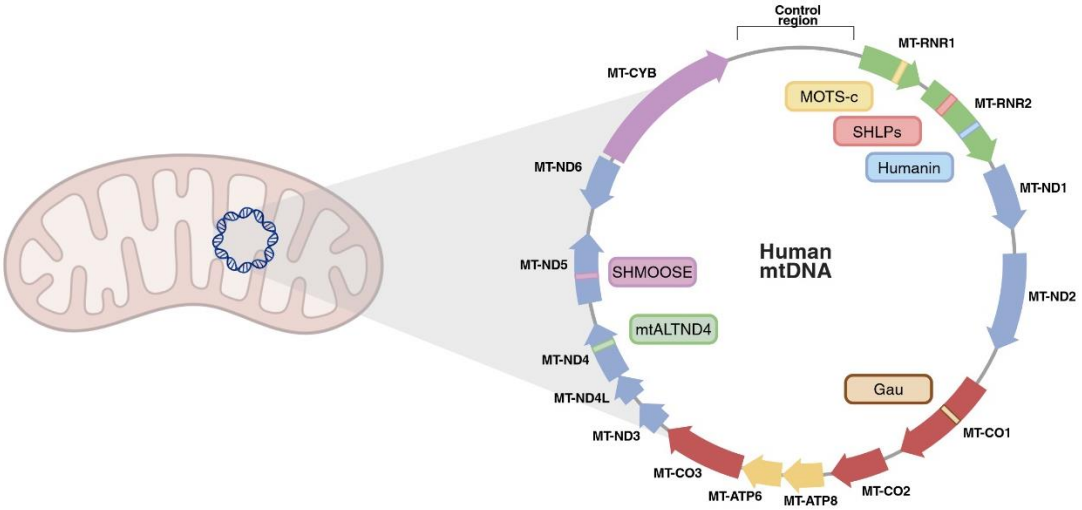

Figure 2-3: Mitochondrial DNA embedded sORFs
Annotated mitochondrial genes are indicated on the circular DNA. Recently discovered sORFs within the mtDNA including MOTS-c, SHLPs, Humanin, Gau, mtALTND4 and SHMOOSE are highlighted.

However, this view appears outdated in light of recent discoveries. In 2001, the first mitochondrial sORF was identified, encoding the cytoprotective microprotein HN (Humanin) (Hashimoto et al., 2001a; Hashimoto et al., 2001c; Hashimoto et al., 2001b). The discovery of numerous previously uncharacterized small RNAs transcribed from mtDNA (Mercer et al., 2011) subsequently led to the identification of additional mitochondrial sORFs producing microproteins such as Gau (Gene antisense ubiquitous in mtDNAs) (Faure et al., 2011), MOTS-c (Mitochondrial ORF of the 12S rRNA type-c) (Lee et al., 2015), SHMOOSE (Small human mitochondrial ORF over serine tRNA) (Miller et al., 2023), MTALTND4 (Mitochondrial alternative ND4 protein) (Kienzle et al., 2023), and six SHLPs (Small humanin-like peptides)

(**Figure 2-3**) (Cobb et al., 2016). These sORFs are embedded within mt-rRNA or protein-coding genes. Interestingly, two of the previously annotated mitochondria-encoded proteins, MT-ATP8 (Mitochondrially encoded ATP synthase membrane subunit 8) and MT-ND4L (Mitochondrially encoded NADH:ubiquinone oxidoreductase core subunit 4L), also meet the definition of microproteins. Strikingly, both represent the only mitochondrial ORFs that also overlap with other genes, resembling the features of novel mitochondrial sORFs.

2.2 Biological functions of microproteins

2.2.1 Cellular functions of microproteins

2.2.1.1 Functions of soluble microproteins

Microproteins are known to perform a wide range of functions, covering many of the same mechanisms as larger proteins. For example, they often serve as allosteric regulators of larger proteins. ASRPS (A small regulatory peptide of STAT3) represses the transcription factor STAT3 (Signal transducer and activator of transcription 3) by masking a phosphorylation site, thereby inhibiting STAT3 activity (Wang et al., 2020). Similarly, microproteins can regulate cellular processes by competitive binding to substrates of larger proteins via molecular mimicry. Due to their small size, they can share sequence identity while lacking the enzymatic activity of their competitor proteins (Min et al., 2017). They can also act as assembly factors of larger protein complexes such as the respiratory chain complexes in the mitochondria (Mick et al., 2012; van Vranken et al., 2014; Floyd et al., 2016; Liang et al., 2022). Other microproteins have been reported to act in signaling cascades. For example, LITTLE NINJA modulates jasmonic acid signaling in plants by binding and attenuating repressors of this pathway (Hong et al., 2020).

Microproteins have also been shown to act across different cellular compartments, including the cytoplasm and nucleus. For instance, the nuclear microprotein SEHB (Short ORF-encoded histone binding protein) is associated with chromatin by binding to histone H2B and acts as a uORF-encoded transcriptional regulator (Koh et al., 2021). Another example is CYREN (Cell cycle regulator of non-homologous end joining), which recruits non-homologous end joining (NEHJ) factors to stimulate DNA

double-strand break repair (Slavoff et al., 2014; Arnoult et al., 2017). Several nucleolar microproteins have been described to regulate ribosome biogenesis. The iORF-encoded microprotein MINAS-60 acts as a checkpoint inhibitor of pre-60S assembly and suppresses large ribosomal subunit export (Cao et al., 2022) while alt-LAMA3 (Alternative lamin subunit alpha-3) promotes ribosomal RNA transcription in the nucleolus (Na et al., 2022). Other microproteins regulate gene expression in the cytoplasm. For instance, NoBody (Non-annotated P-body dissociating polypeptide) is a 7-kDa protein that localizes to processing bodies (P-bodies) and interacts with the mRNA decapping complex to regulate mRNA turnover (D'Lima et al., 2017; Na et al., 2020; Na et al., 2021). In *D. melanogaster*, the microprotein pri (polished rice) regulates proteasome-mediated processing of the transcription repressor Svb (Shavenbaby) through its association with the E2-E3 ubiquitin-conjugating complex (Zanet et al., 2015).

2.2.1.2 Functions of transmembrane microproteins

Interestingly, many microproteins are predicted to contain transmembrane α-helices, suggesting a role in various membrane systems such as the endoplasmatic reticulum (ER), lysosomes, endosomes, plasma membrane or mitochondria (Aspden et al., 2014). For example, NEMEP (Nodal enhanced mesendoderm peptide), a murine microprotein enhanced by Nodal signaling, promotes glucose uptake across the plasma membrane (Fu et al., 2022) while members of the FXYD family regulate ion exchange in cardiomyocytes (Crambert and Geering, 2003; Ahlers et al., 2005; Cheung et al., 2013). Similarly, microproteins are involved in the calcium ion transport into the sarco-/endoplasmatic reticulum through SERCA (Sarcoplasmic/endoplasmic reticulum calcium ATPase). SERCA is negatively regulated by several tissue-specific microproteins referred to as regulins, including PLN (Phospholamban) (MacLennan and Kranias, 2003; Kranias and Hajjar, 2012), SLN (Sarcolipin) (Odermatt et al., 1998), MLN (Myoregulin) (Anderson et al., 2015), ELN (Endoregulin), and ALN (Another-regulin) (Anderson et al., 2016), whereas DWORF (Dwarf open reading frame) acts as an antagonistic activator of SERCA activity (Nelson et al., 2016). Microproteins can also regulate the transport of other molecules such as lipids. For example, alt-RPL36 which is expressed from an iORF within the ribosomal protein L36 (RPL36), regulates the transport of phosphatidylinositol across ER-plasma

membrane contact points by TMEM24 (Transmembrane protein 24) and modulates Akt signaling as well as insulin secretion (Lees et al., 2017; Cao et al., 2021).

Transmembrane microproteins have also been found to act in other cytoplasmic organelles. The endosomal microprotein CASIMO1 (Cancer-associated small integral membrane open reading frame 1) regulates endocytosis and is associated with cell migration and proliferation (Polycarpou-Schwarz et al., 2018). Another microprotein, the lysosomal/endosomal protein SPAR (Small regulatory polypeptide of amino acid response), interacts with the membrane-associated v-ATPase hydrogen pump, acting as an inhibitor of mTORC1 (Mechanistic target of rapamycin complex 1) and thereby modulating cell proliferation and muscle regeneration (Matsumoto et al., 2017).

Microproteins do not only act intracellularly but can also be secreted. For example, *Mustn1* (Musculoskeletal embryonic nuclear protein 1) is secreted from smooth muscle cells upon exercise or injury in mice and modulates the extracellular matrix (Ducommun et al., 2024) and ELABELA functions as a growth factor in human embryogenesis (Ho et al., 2015).

Taken together, the variety of different cellular functions underlines the importance of microproteins. Given the number of identified, yet uncharacterized sORFs, it can be assumed that they play a role in even more mechanisms than currently recognized.

2.2.2 Mitochondrial microproteins

2.2.2.1 Mitochondria - central hub for cellular functions

Mitochondria are highly dynamic organelles that fulfill essential functions in eukaryotic cells (**Figure 2-4**). They contain an outer mitochondrial membrane (OMM) and inner mitochondrial membrane (IMM), dividing the mitochondria into the intermembrane space (IMS) between the two membranes and the matrix, containing the mtDNA and the mitochondrial translation machinery. Most eukaryotic cells typically contain up to 8000 mitochondria, although their numbers vary between species and cell type and undergo dynamic changes due to continuous cycles of mitochondrial fusion and fission (Moura et al., 2025). Mitochondria are central hubs for many cellular functions, including energy production, biosynthesis, ion

homeostasis, signaling and apoptosis (Suomalainen and Nunnari, 2024; Moura et al., 2025).

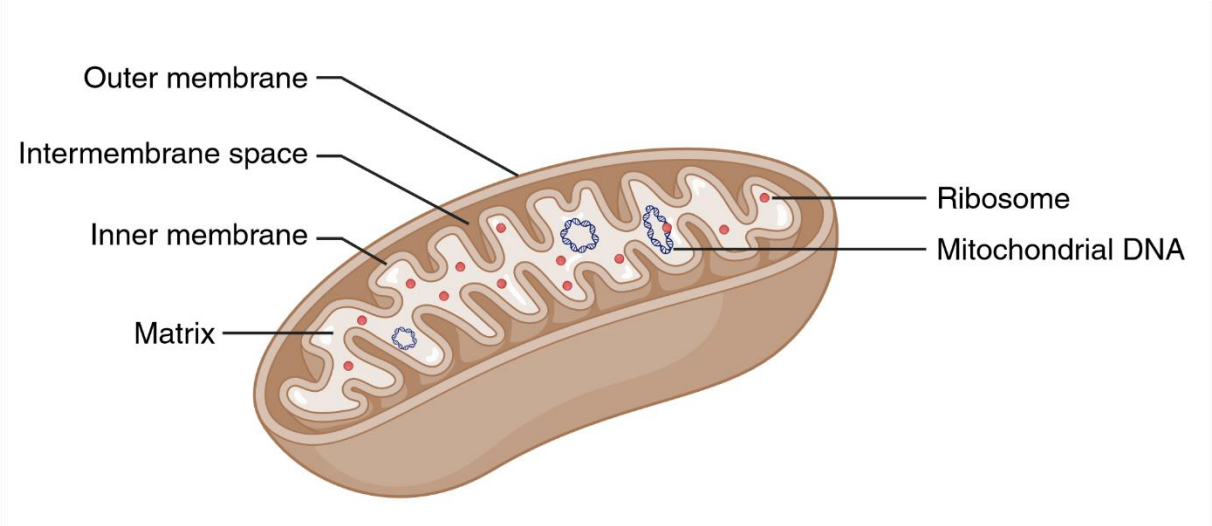

Figure 2-4 Schematic of the architecture of a mitochondrion
Mitochondrial membranes are indicated in brown, the matrix in ocher and mitochondrial ribosomes in red.

In healthy cells, mitochondria produce more than 90% of all adenosine triphosphate (ATP) required for cellular processes. The synthesis of ATP represents the final step of oxidative phosphorylation (OXPHOS), which depends on the four multisubunit complexes of the respiratory chain (also referred to as electron transport chain; ETC) and the ATP synthase embedded in the inner membrane (**Figure 2-5**). In short, reduced nicotinamide adenine dinucleotide (NADH) dehydrogenase, or complex I, oxidizes NADH and transfers two electrons through a series of iron-sulfur clusters to the lipid soluble redox carrier Coenzyme Q (CoQ) while pumping protons into the intermembrane space. The reduction of CoQ is promoted by complex II, also referred to as succinate dehydrogenase, transporting electrons through flavin adenine dinucleotide (FAD) as a prosthetic group alongside iron-sulfur clusters without translocating protons. Reduced Coenzyme Q donates electrons to complex III, or cytochrome c (Cyt c) reductase, which passes them to Cyt c and releases additional protons. Ultimately, four cytochrome c molecules donate each one electron to an iron-copper active site in complex IV, also referred to as cytochrome c oxidase, to convert one oxygen (O_2) into two H_2O molecules (Osellame et al., 2012). The electron transfer through complex I-IV produces a proton concentration gradient across the inner mitochondrial membrane, resulting in a membrane potential ($\Delta\Psi m$) of approximately

-150 to -180 mV (Zorova et al., 2018), which facilitates the production of ATP in the mitochondrial matrix by the ATP synthase, also referred to as complex V. This propeller-shaped enzyme utilizes the flow of protons through a transmembrane proton channel domain F_0 to induce rotation of a soluble hexamer domain F_1 catalyzing ATP synthesis (Osellame et al., 2012).

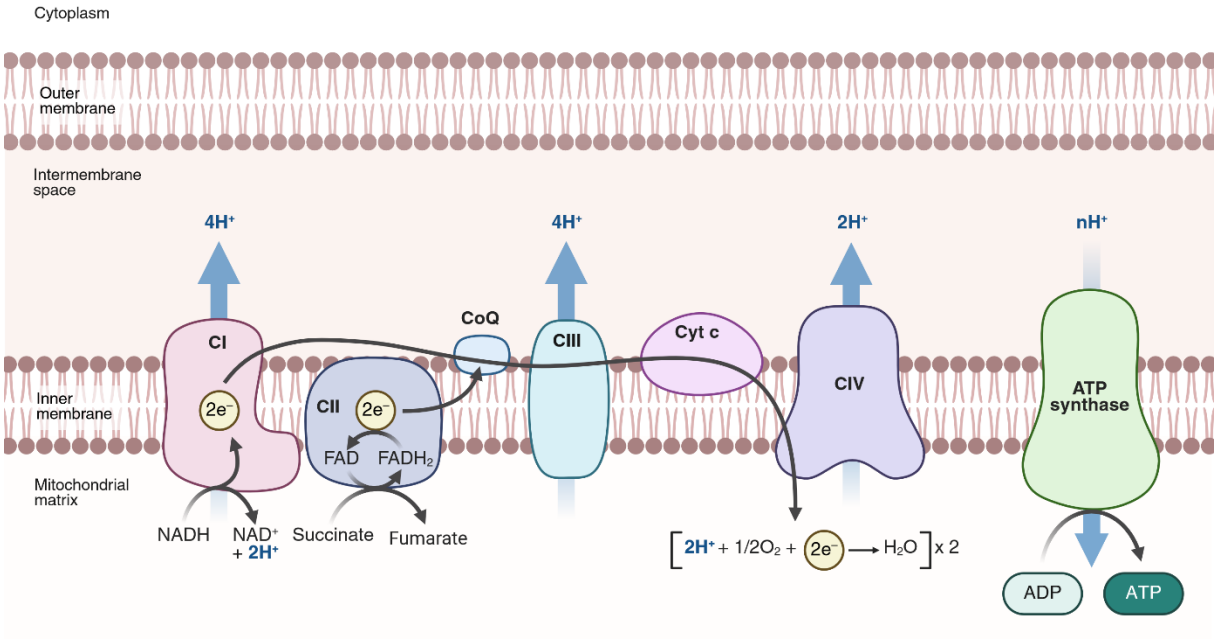

Figure 2-5 Schematic of the Electron transport chain in the inner mitochondrial membrane
The transport of electrons through the respiratory chain complexes is indicated by black arrows, pumped protons by blue arrows. CI-IV: Complex I-IV, CoQ: Coenzyme Q, Cyt c: Cytochrome c.

The bioenergetic function of the ETC is closely linked to metabolic pathways in the mitochondria. Catabolic pathways such as glycolysis or ß-oxidation use sugars, fatty acids and proteins to supply acetyl-Coenzyme A (CoA) to the tricarboxylic acid cycle (also known as Krebs cycle or citric acid cycle), which produces NADH and $FADH_2$ to fuel the respiratory chain (Osellame et al., 2012). At the same time, mitochondria serve as biosynthetic hubs for different macromolecules including nucleotides, fatty acids, cholesterol, amino acids and heme (Spinelli and Haigis, 2018).

To coordinate cellular energy demand and mitochondrial ATP production, mitochondria are in constant communication with the cytosol, primarily through calcium signaling. Most processes with increased demand for energy are associated with a rise in cytosolic calcium level. The subsequent transport of calcium across the

mitochondrial membranes along its gradient then leads to the activation of ATP producing pathways (Osellame et al., 2012).

Mitochondria play a pivotal role in coordinating cell death. Upon apoptotic signaling, pro-apoptotic proteins BAK (Bcl-2 homologous antagonist killer) and BAX (Bcl-2 associated X protein) oligomerize in the outer membrane, facilitating the release of cytochrome c, SMAC (Second mitochondria-derived activator of caspase) and AIF (Apoptosis inducing factor) into the cytoplasm through these BAK/BAX-formed pores. Cytochrome c interaction with APAF1 (Apoptotic peptidase activating factor 1) then promotes apoptosome complex formation, activating caspase 9 to initiate the apoptotic cascade (Flores-Romero et al., 2023; Zong et al., 2024).

All in all, mitochondria play a pivotal role in metabolism, energy homeostasis and cellular stress to maintain cellular functions.

2.2.2.2 Functions of mitochondrial microproteins

As shown above, mitochondria coordinate processes such as protein import, translation and oxidative phosphorylation in large protein complexes. Interestingly, while the term microproteins is relatively new, many well-studied mitochondrial proteins fulfill their definition, highlighting the importance of small proteins in regulating mitochondrial functions. Nevertheless, this chapter focuses only on recently discovered mitochondrial microproteins and their influence on different mitochondrial processes.

As energy production represents the major function of mitochondria, it is not surprising that various microproteins tightly regulate this critical process. Generally, small proteins associated with OXPHOS can be divided into two groups, assembly factors of respiratory chain complexes and regulators of energy production that interact with the mature complexes. The importance of numerous microproteins for the assembly of complex III has already been studied in detail. For instance, BR (Brawnin), SMIM4 (Small integral membrane protein 4) and UQCC4 (Ubiquinol-cytochrome c reductase complex assembly factor 4) coordinate the initial steps of complex III formation, which leads to the membrane insertion of the complex and together with UQCC3 (Ubiquinol-cytochrome c reductase complex assembly factor 3)

subsequent cytochrome b hemylation (Zhang et al., 2020; Dennerlein et al., 2021; Liang et al., 2022). Additionally, UQCC3 has been shown to regulate supercomplex assembly between complex III and IV (Desmurs et al., 2015). Similarly, MTLBN (Mitolamban) is involved in complex III assembly and has been linked to immunity and cardiomyopathy (Bhatta et al., 2020; Makarewich et al., 2022). Interestingly, MTLBN has also been described to enhance mitochondrial fission (Xie et al., 2022).

In contrast to these small protein assembly factors, other microproteins have been described to alter mitochondrial respiration by interacting with the mature ETC complexes. For example, SLC35A4-MP enhances respiratory activity (Rocha et al., 2024) by a yet unknown mechanism and ASAP interaction increases ATP synthase activity (Ge et al., 2021). Notably, two mitochondria-derived peptides modulate mitochondrial respiration. MTALTND4 increases H_2O_2 release and reduces respiratory activity (Kienzle et al., 2023), whereas SHMOOSE boosts respiratory activity by interacting with Mitofilin (Kumagai et al., 2023; Miller et al., 2023), a protein essential for christae integrity and mitochondrial function (John et al., 2005). A striking example of a microprotein indirectly regulating respiratory chain activity is Mitoregulin (MTLN; MOXI; MPM). MTLN interacts with the trifunctional protein to enhances fatty acid ß-oxidation (Makarewich et al., 2018a; Friesen et al., 2020; Zhang et al., 2023). However, other studies demonstrated a role in complex I and supercomplex formation (Stein et al., 2018; Chugunova et al., 2019; Xiao et al., 2022). Mechanistically, Chugunova et al. linked the effects on respiratory complex I to changes in the lipid composition of the membrane, providing a possible model that combines all findings.

Mitochondrial microproteins have also been shown to regulate metabolism outside of the respiratory chain. The uORF-encoded MP31 (Microprotein-31) inhibits lactate-to-pyruvate conversion by competing for NAD^+ through binding to mLDH (Mitochondrial lactate dehydrogenase) (Huang et al., 2021), whereas MOTS-c enhances glucose uptake, insulin sensitivity and fatty acid oxidation by interacting with protein kinase CK2 (Casein kinase 2) and activating the AMPK (AMP-activated protein kinase) pathway (Lee et al., 2015; Lu et al., 2019; Kumagai et al., 2024). Similarly, Humanin was found to regulate AMPK and STAT3 signaling to improve insulin sensitivity and

glucose consumption (Hashimoto et al., 2001a; Hashimoto et al., 2009; Muzumdar et al., 2009; Kim et al., 2016; Wang et al., 2021).

Microproteins are further involved in mitochondrial dynamics processes. A such, the uORF-encoded microprotein MIEF1-MP (also annotated as MIDUO) was initially thought to be involved in DRP1 (Dynamin-related protein 1)-dependent mitochondrial fission, similar to the annotated canonical CDS product MIEF1 (also referred to as MID51) (Samandi et al., 2017). However, Rathore et al. (2018) later found that it interacts with the mitoribosome to regulate mitochondrial translation. Microproteins are also associated with cellular stress response. For instance, the outer mitochondrial membrane-localized microprotein PIGBOS interacts with the ER protein CLCC1 (Chloride channel CLIC like 1) at ER-mitochondria contact sites to regulate unfolded protein response (UPR), thereby preventing cell death (Chu et al., 2019). Last, mitochondrial microproteins can play influence diverse physiological processes. The murine microproteins Kastor and Polluks interact with VDAC3 (Voltage-dependent anion channel 3) and are essential for mitochondrial sheath formation during spermatogenesis, thereby ensuring male fertility (Mise et al., 2022).

Overall, both nuclear- and mitochondria-encoded microproteins exert wide-ranging functions in metabolism and beyond. Given recent predictions of dozens of yet uncharacterized mitochondrial microproteins, it seems likely that additional small proteins with key regulatory roles will soon be uncovered (van Heesch et al., 2019; Zhang et al., 2020).

2.2.3 Microproteins in disease and immunity

As microproteins often act as regulators of channels, enzymes or multi-protein complexes in critical cellular processes, their dysregulation can lead to diseases. In recent years, several microproteins have been linked to obesity (Lee et al., 2015; Lu et al., 2019), cardiovascular (Makarewich et al., 2018b; van Heesch et al., 2019; Morales et al., 2023) and neurodegenerative diseases (Hashimoto et al., 2001b; Hashimoto et al., 2001c; Miller et al., 2023).

Lately, a major focus has been placed on understanding the role of microproteins in cancer. Generally, both oncogenic and tumor-suppressive microproteins contribute

to the regulation of multiple hallmarks of cancer (Hanahan and Weinberg, 2011). For example, the LINC00266-1 encoded microprotein RBRP (RNA-binding regulatory peptide) interacts with m^{6}A reader IGF2BP1 (Insulin-like growth factor 2 mRNA-binding protein 1), thereby increasing c-MYC mRNA stability and expression to promote tumorigenesis in colorectal cancer (CRC) (Zhu et al., 2020a). Similarly, APPLE (A peptide located in ER) expression has been linked to poor prognosis in acute myeloid leukemia (AML) by enhancing translation of oncoproteins (Sun et al., 2021). Another well-studied oncogene is the ER-anchored microprotein SMIM30 (Small integral membrane protein 30), which is upregulated in several cancers. SMIM30 enhances SERCA activity, reducing cytosolic calcium levels to promote G1/S transition and cell proliferation (Yang et al., 2023). It has further been reported to promote hepatocellular carcinoma (HCC) development by inducing the membrane anchoring of tyrosine-kinases and subsequent activation of MAPK (Mitogen-activated kinase) signaling (Pang et al., 2020).

Other microproteins have been identified to stimulate metabolism in cancer cells. For example, the antisense lncRNA-encoded microprotein TRPC5OS (Transient receptor potential channel 5 opposite strand) promotes tumorigenesis in breast cancer (BRCA) by ENO1 (Enhancing enolase 1)-mediated glucose uptake to reprogram metabolism (Cui et al., 2022), whereas ASAP increases ATP synthase activity to drive proliferation in CRC (Ge et al., 2021). Several additional oncogenic microproteins have been reported, such as PACMP (PAR-amplifying and CtIP-maintaining micropeptide) (Zhang et al., 2022), ASDURF (ASNSD1 upstream open reading frame protein) (Hofman et al., 2024), CRNDEP (Colorectal neoplasia differentially expressed protein) (Szafron et al., 2015) or ZFAS1 (Guo et al., 2019), underscoring the potential of microproteins as promising target for cancer diagnostics and therapy.

In contrast to these oncogenes, several studies have identified tumor-suppressive microproteins. For example, miPEP133 induces apoptosis in nasopharyngeal carcinoma (NPC) cells via p53 transcriptional activation (Kang et al., 2020). MIAC (Micropeptide inhibiting actin cytoskeleton) suppresses cell growth, migration, and enhances apoptosis in head and neck squamous cell carcinoma (HNSCC) and renal cell carcinoma (RCC) by inhibiting actin cytoskeleton organization through EREG (Epiregulin)/EGFR (Epidermal growth factor) signaling (Li et al., 2020; Li et al., 2022).

Other tumor suppressor microproteins act on the regulation of gene expression and RNA processing. The circRNA-encoded PINT-87aa associates with the PAF1 (Polymerase associated factor 1) complex, causing RNA II polymerase pausing at oncogene promotors to limit proliferation and self-renewal in glioblastoma (GBM) (Zhang et al., 2018). Another nuclear microprotein suppresses cancer growth by influencing metabolic reprogramming in CRC and oral squamous cell carcinoma (OSCC). The lncRNA-encoded protein HOXB-AS3-53aa competitively binds to hnRNP A1, antagonizing PKM (Pyruvate kinase M) splicing towards the oncogenic PKM2 isoform (Huang et al., 2017; Leng et al., 2021). Other microproteins can suppress tumor growth by preventing cancer cells to switch into a proliferative state. For example, the p53-activated microprotein pTINCR (Peptide encoded by terminal differentiation-induced lncRNA) promotes epithelial differentiation in cutaneous squamous cell carcinoma (CSCC) through SUMOylation of CDC42 (Boix et al., 2022).

Additional tumor suppressor microproteins such as YYB1M (Yin Yang 1-binding micropeptide) (Wu et al., 2020b), N1DARP (Notch1 degradation-associated regulatory polypeptide) (Zhai et al., 2023), CIP2A-BP (CIP2A binding peptide) (Guo et al., 2020), MP31 (Huang et al., 2021) or KRASIM (KRAS-interacting microprotein) (Xu et al., 2020) have been reported, highlighting small proteins as central players in many antitumorigenic processes.

Other promising anti-cancer therapy targets are MHC-I (Major histocompatibility complex class I)-presented novel or unannotated ORFs (nuORFs). In a comprehensive approach combining Ribo-seq with LC-MS/MS to profile MHC-I-bound antigens, Ouspenskaia et al. showed that approximately 16% of all detected antigens in healthy and cancer samples derive from non-canonical or unannotated ORFs. Considering somatic mutations in nuORF, these non-canonical proteins and microproteins may represent a rich source of neoantigens for personalized immunotherapy (Ouspenskaia et al., 2022; Cai et al., 2024; Camarena et al., 2024).

Antigen presentation itself can be regulated by microproteins as well. For instance, miPEP155 modulates MHC-II antigen presentation and subsequent T cell priming in dendritic cells to suppress autoimmune inflammation (Niu et al., 2020). Moreover, multiple microproteins have been linked to inflammation and immune regulation.

The murine lncRNA *Aw112010* produces a secreted small protein in M1 macrophages that is essential for IL-12 (Interleukin-12) production and antibacterial immune response (Jackson et al., 2018; Martinez et al., 2023), whereas Mm47 (Mitochondrial micropeptide-47) activates the NLRP3 (NLR family pyrin domain containing 3) inflammasome in human and murine myeloid cells (Bhatta et al., 2020). Moreover, the ER-localized MAVI1 (Microprotein in antiviral immunity 1) inhibits MAVS (Mitochondrial antiviral-signaling protein) aggregation and type I interferon signaling in viral infections (Shi et al., 2023).

An intriguing mechanism of immune response regulation is the microprotein MOCCI (Modulator of cytochrome C oxidase during inflammation, also referred to as C15ORF48), a paralog of the mitochondrial complex IV subunit NDUFA4. Its transcript also generates miR-147b, which targets the *NDUFA4* mRNA. Through a coordinated downregulation of NDUFA4 and upregulation of MOCCI, it replaces NDUFA4 in complex IV to reduce reactive oxygen species (ROS) production, lower mitochondrial membrane potential and enhance viral immunity during infection, leading to cyto-protection of the host cell (Lee et al., 2021).

Taken together, microproteins emerge as important regulators in cancer, infection and immunity and represent promising therapeutic targets for future research.

2.3 Aim of this thesis

Microproteins play important roles in cellular homeostasis and are increasingly implicated in disease, including cancer. In a previous study from our lab (Ho-Xuan et al., 2020), several lncRNAs which are predicted to harbor a translated sORF, were identified in an *in vivo* xenograft colorectal cancer mouse model. One of the candidates was LINC00493 (Long intergenic non-protein coding RNA 493), which encodes the microprotein SMIM26 (Small integral membrane protein 26). In this work, we aim to elucidate the function of SMIM26 on a molecular and organismal level.

Therefore, we will first determine the subcellular localization using orthogonal approaches. To obtain a better understanding of the cellular processes, in which SMIM26 might be involved, the SMIM26-interactome will be studied by mass spectrometry, followed by the validation of candidate interactors via co-immuno-precipitation. To study the cellular functions of SMIM26, knockout and rescue cell lines will be generated and phenotypically characterized. Additionally, knockout models in mouse and zebrafish will provide valuable insights into organismal effects. Lastly, SMIM26 expression in gastrointestinal cancer will be analyzed and an anti-cancer drug screening approach will assess whether SMIM26 might be a potential therapeutic target in cancer.

3 Results

3.1 LINC00493-encoded SMIM26 is differentially expressed in an *in vivo* CRC xenograft mouse model

In a study to identify differentially expressed miRNAs, circRNAs and lncRNAs during cancer progression, metastasis and upon chemotherapy treatment, Ho-Xuan et al. (2020) generated *in vivo* xenograft mouse models injecting colorectal human HT29 cancer cell lines into the spleen of CB17.SCID mice (**Figure 3-1A**). After 9 – 11 weeks, tumor, metastasis and healthy tissue samples were collected and differentially expressed ncRNAs were analyzed by next-generation sequencing (NGS). One candidate lncRNA identified by this experiment was LINC00493. To further validate the NGS results, we performed quantitative polymerase chain reaction (qPCR) (**Figure 3-1B**), which confirmed a differential expression of LINC00493 in primary tumor and metastasis compared to HT29 cells under optimal conditions.

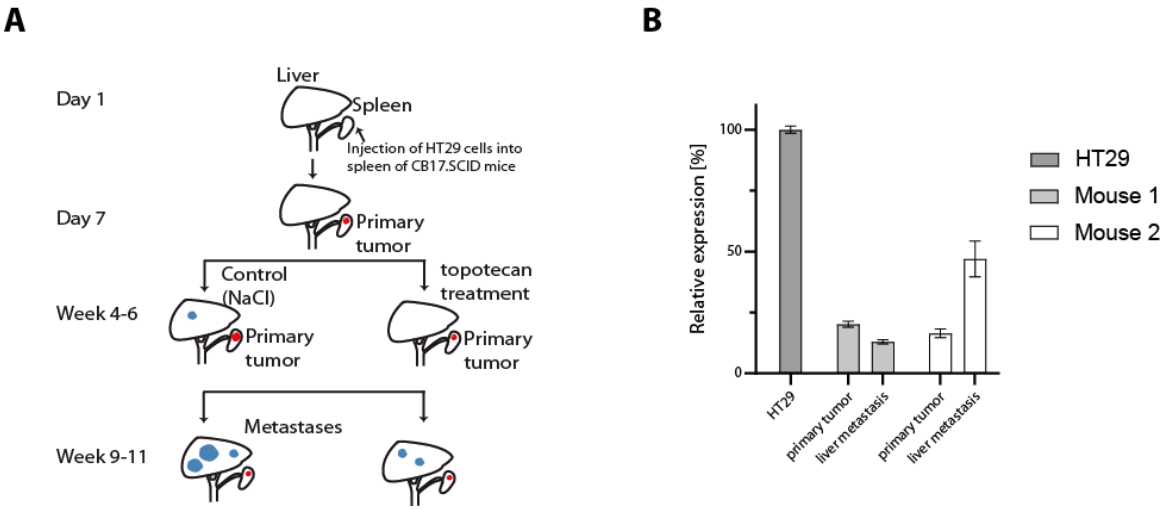

Figure 3-1: In vivo CRC xenograft mouse model identifies differentially expressed LINC00493
(A) Schematic of the in vivo CRC xenograft mouse model. Human HT29 cells stably expressing luciferase were injected into the spleen of CB17-SCID mice to form a primary tumor. After 7 days, mice were either treated with sodium chloride (NaCl) as control or chemotherapy using topotecan to identify therapy-related transcripts. After 9-11 weeks, mice were sacrificed and gene expression of ncRNAs was analyzed. (B) qPCR of LINC00493 levels in HT29 cells or primary tumor and liver metastasis samples from two different mice. GAPDH was used as normalization control (means ± SD). Topotecan treatment showed no effect on LINC00493 expression (data not shown)

Detailed analysis of this lncRNA revealed a sORF encoding for the microprotein SMIM26 (**Figure 3-2**) and three isoforms producing a 95 aa, 94 aa or 73 aa protein, respectively. In this work, we focus on elucidating the function of the long SMIM26 isoform encoded by LINC00493.

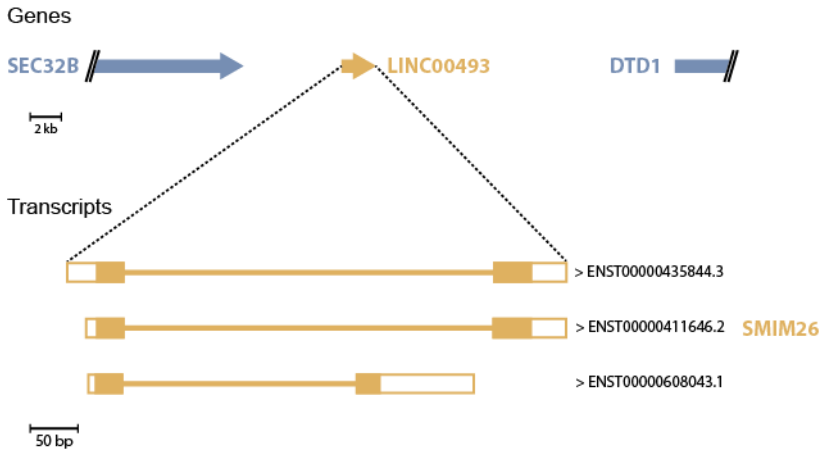

Figure 3-2: LINC00493 encodes the microprotein SMIM26
Schematic of the LINC00493 locus (top) and the transcripts encoding for SMIM26 (bottom).

3.2 SMIM26 is a mitochondrial transmembrane protein

In 2021, 2023 and 2025 it was reported that SMIM26 localizes to the mitochondria (Yeasmin et al., 2021; Meng et al., 2023; Nah et al., 2025). To confirm these findings, we performed co-immunofluorescence experiments (**Figure 3-3A**). C-terminally FLAG-HA-tagged (F/H) SMIM26 was transiently expressed in HCT116 cells. After48 h, cells were co-stained with antibodies against the FLAG-tag and either the outer mitochondrial membrane protein TOMM20 (**Figure 3-3A**, upper panel) or the inner mitochondrial membrane protein TIMM44 (**Figure 3-3A**, lower panel). In both conditions, SMIM26 localization overlaps with the mitochondrial proteins, confirming that SMIM26 is a mitochondrial microprotein.

To further empathize these findings, SMIM26 sublocalization was validated by biochemical fractionations (**Figure 3-3B**). Therefore, mitochondria were isolated from HEK293T cells transiently expressing SMIM26-F/H and fractions (debris including nuclear, cytoplasm and mitochondria) were analyzed by western blotting. While GAPDH was exclusively detected in the cytoplasmic fractions and the nuclear protein NONO in nuclear-containing debris fractions, TIMM44 was found in

mitochondrial fractions, confirming successful fractionation. SMIM26 was exclusively identified in the mitochondrial fractions, which corroborates the co-immunofluorescence findings. A proteinase K treatment of mitochondria prior to lysis had no effect on SMIM26 enrichment in the mitochondrial fraction, excluding unspecific binding of SMIM26 to the mitochondrial surface and therefore indicating that the SMIM26 C-terminus resides within the mitochondria.

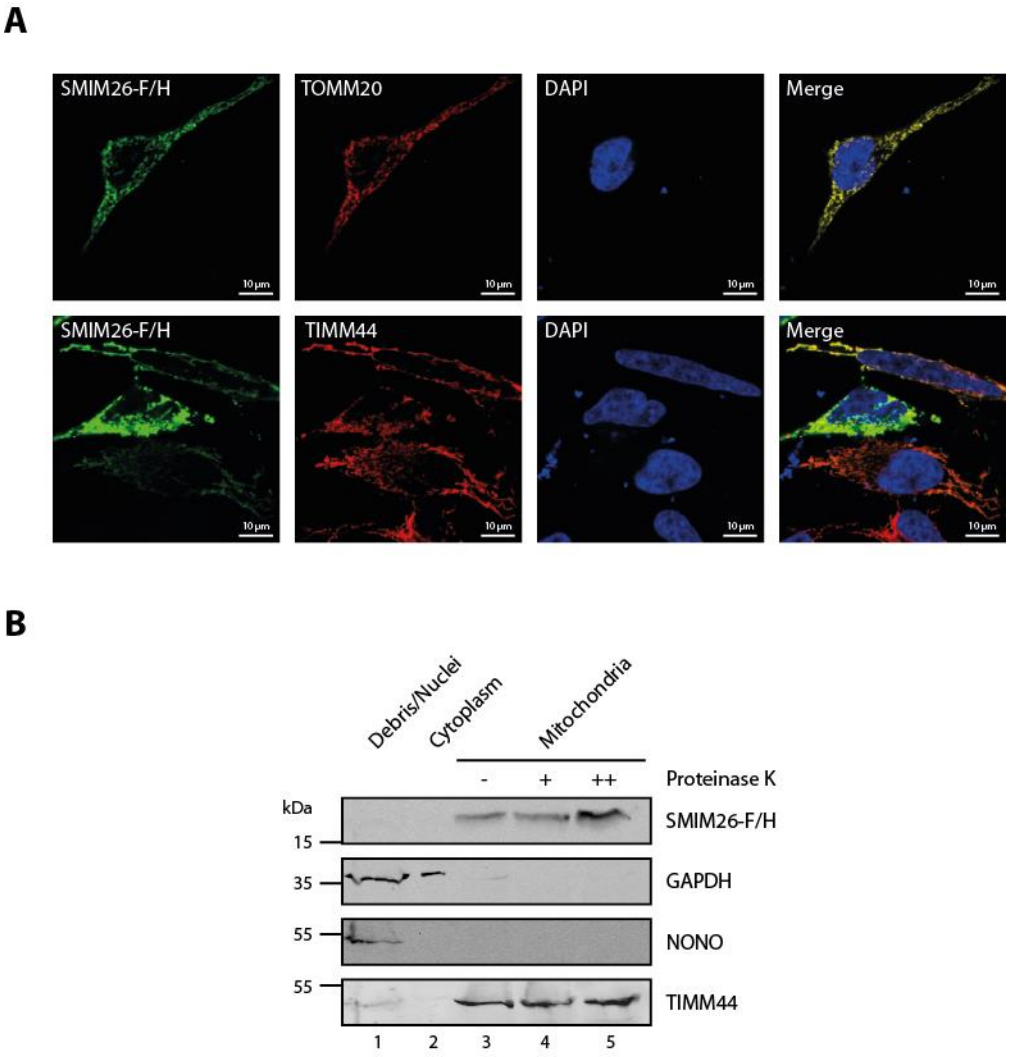

Figure 3-3: SMIM26 is a mitochondrial microprotein
(A) Immunofluorescence analysis of HCT116 cells transiently expressing SMIM26-F/H. Anti-FLAG (green) detects SMIM26 localization. Co-staining with TOMM20 (red, upper panel; outer mitochondrial membrane, OMM) and TIMM44 (red, lower panel; inner mitochondrial membrane, IMM). Nuclei were counterstained with DAPI (blue). Scale bars: 10 µm. (B) Subcellular fractionation of HEK293T cells transiently expressing SMIM26-F/H into debris/nuclei (NONO), cytosol (GAPDH), and mitochondria (TIMM44). Isolated mitochondria were left untreated (–), or treated with proteinase K in sucrose-free buffer (+) or stabilizing SEM buffer (++).

AlphaFold3 (Abramson et al., 2024) predicted SMIM26 to contain a hydrophobic α-helix, which might resemble a single-pass transmembrane domain (**Figure 3-4A**). To assess SMIM26 membrane association, mitochondria were isolated from HEK293T cells transiently expressing SMIM26-F/H and treated with sodium carbonate or the detergent Triton X-100 to extract membrane-associated and transmembrane proteins, respectively (**Figure 3-4B**). While SMIM26 remained in the pellet fractions under control and salt-treated conditions, it was partially solubilized upon detergent-treatment albeit to a lesser extent compared to the membrane proteins TOMM20 and TIMM44. Therefore, our experiments suggest that SMIM26 is tightly anchored into mitochondrial membranes through a N-terminal transmembrane domain.

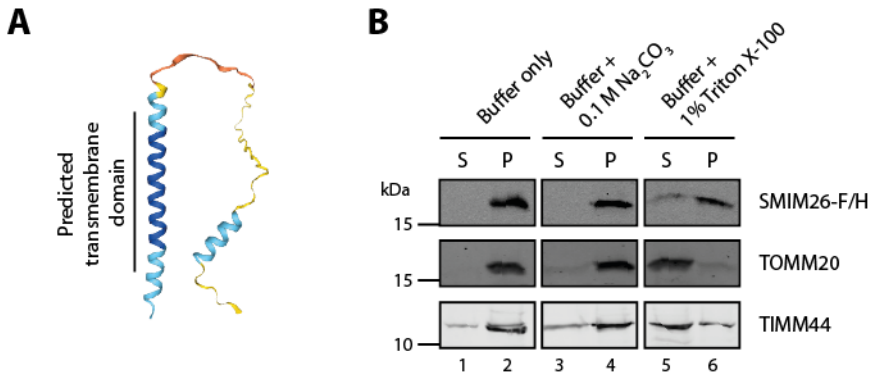

Figure 3-4: SMIM26 is an integral single-pass transmembrane protein
(A) AlphaFold3-based predicted structure of SMIM26 (Abramson et al., 2024). SMIM26 is predicted to contain a transmembrane domain. Structure is colored by predicted Local Distance Difference Test (pLDDT) scores indicating model confidence: deep blue (very high, pLDDT > 90), light blue (confident, 90 > pLDDT > 70), yellow (low, 70 > pLDDT > 50), orange (very low, pLDDT < 50). (B) Membrane fractionation of HEK293T cells transiently expressing SMIM26-F/H. Isolated mitochondria were extracted with buffer only (soluble proteins), 0.1 M Na_2CO_3 (peripherally associated proteins), or 1% TritonX-100 (integral membrane proteins). S: supernatant; P: pellet.

3.3 SMIM26 interacts with proteins in the inner and outer mitochondrial membrane

Understanding the interactome of a protein can help elucidating its molecular functions. To identify potential protein interaction partners of SMIM26, we transiently expressed SMIM26-F/H in HEK293T cells, isolated mitochondria and performed immunoprecipitations using anti-FLAG antibodies (**Figure 3-5A**) followed by mass spectrometry analysis of co-precipitated proteins. We identified 458 protein candidates that were at least 5-fold enriched compared to the empty vector control in

at least two of the three replicates and 187 proteins that were either less enriched or unspecifically bound to the beads during immunoprecipitation (**Figure 3-5B, Table 8-1**). Gene ontology (GO) analysis for the group of putative interactors showed enrichment for biological processes including mitochondrial organization, transmembrane transport and cellular respiration (**Figure 3-5C**).

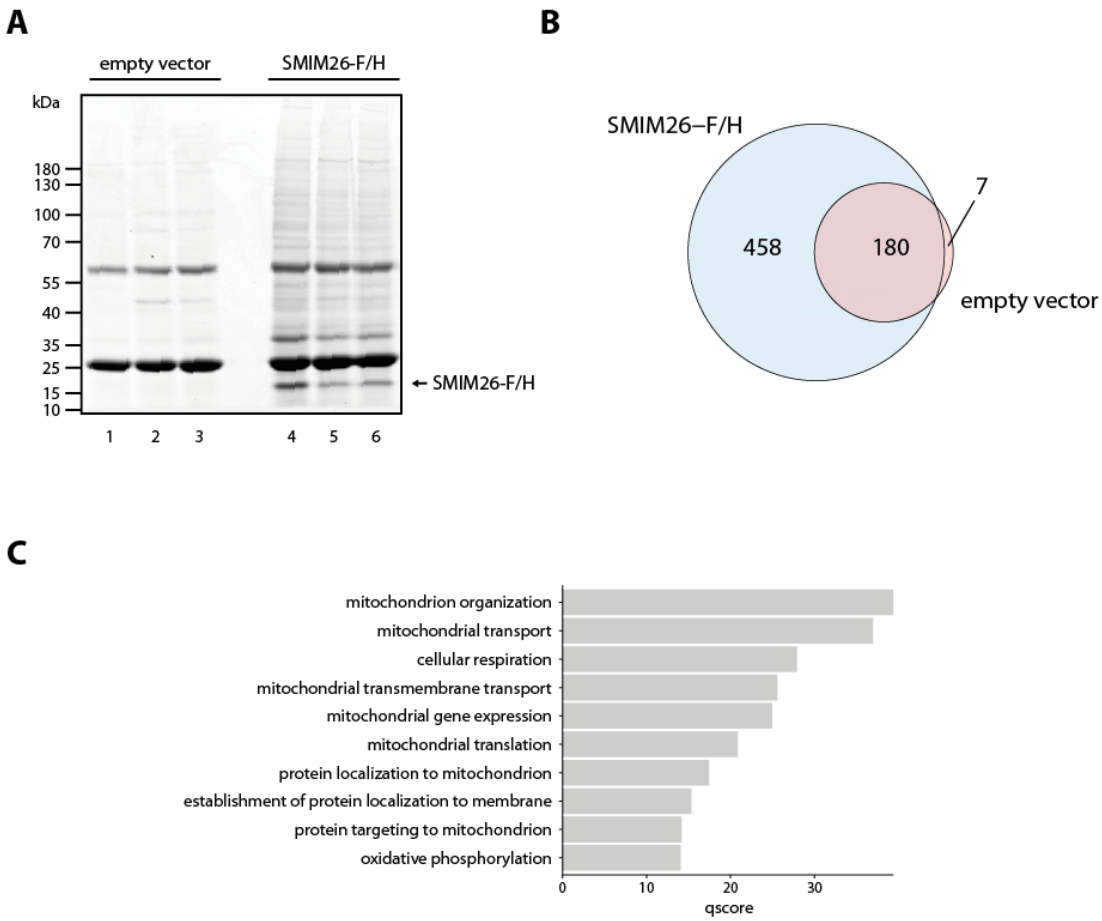

Figure 3-5: SMIM26 interacts with proteins involved in various mitochondrial functions
(A) Anti-FLAG immunoprecipitation of SMIM26-F/H from mitochondria isolated from transfected HEK293T cells. An empty vector expressing FLAG-HA was used as a negative control. The SDS-PAGE gel was stained with Coomassie Blue. (B) Venn diagram of proteins co-immunoprecipitated with SMIM26-F/H versus empty vector control, identified in at least 2 of 3 replicates by mass spectrometry. (C) Gene Ontology (GO) enrichment analysis (Biological Process) of proteins co-precipitated with SMIM26-F/H. q-scores reflect Benjamini-Hochberg–corrected p-values with a cutoff of 0.05.

To assess the specificity of the immunoprecipitation, we selected candidates associated with mitochondrial membranes and performed co-immunoprecipitation experiments using anti-FLAG antibodies (**Figure 3-6**). Therefore, mitochondria were isolated from HEK293T cells transiently expressing HA-tagged SMIM26 with either MFN2-F/H, VDAC1-F/H, PGAM5-FLAG, SLC25A6-F/H, SLC25A5-F/H, HIGD1A-F/H, RHOT2-F/H or an empty vector as control followed by immunoprecipitation and

western blotting. VDAC1-F/H, PGAM5-FLAG and SLC25A6-F/H efficiently co-precipitated SMIM26-HA, while MFN2-F/H, SLC25A5-F/H, HIGD1A-F/H and RHOT2-F/H did not interact with SMIM26-HA (**Figure 3-6**).

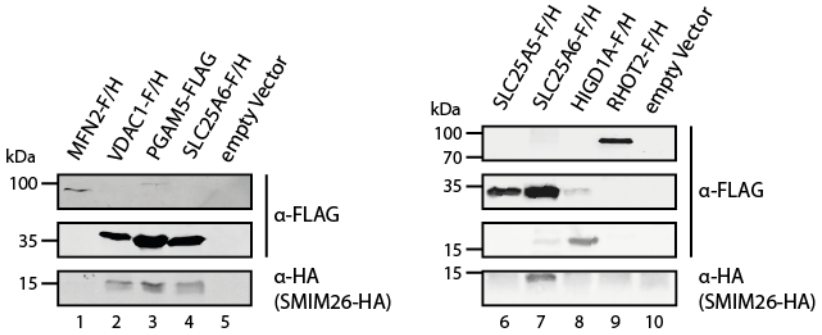

Figure 3-6: Validation of putative SMIM26 binding partners
Western blot validation of SMIM26 interactors. FLAG- or FLAG/HA-tagged putative interactors (MFN2, VDAC1, PGAM5, SLC25A5, SLC25A6, HIGD1A, RHOT2) were immunoprecipitated from transfected HEK293T cells using anti-FLAG, and co-elution of SMIM26-HA was assessed.

Taken together, our results suggest that SMIM26 interacts with at least three mitochondrial proteins localizing to the outer membrane (VDAC1), inner membrane (SLC25A6) or the intermembrane space (PGAM5) indicating a potential function in both membrane systems.

3.4 SMIM26 forms oligomers

To obtain a better understanding of the SMIM26 interactome, we performed protein-protein crosslinking followed by mass spectrometry. Isolated mitochondria from wild-type (WT) or transiently expressing SMIM26-F/H HEK293T cells were treated with the chemical crosslinker Bis(sulfosuccinimidyl) suberate (BS3) and crosslinked peptides originating from SMIM26 were investigated in the mass spectra. Surprisingly, we identified peptides that indicate crosslinking of two SMIM26 molecules at K43 and S46, suggesting di-or multimerization (**Figure 3-7A**). The observed dimerization would also be consistent with an AlphaFold3 prediction, with the crosslink located at the end of the transmembrane helix in the intermembrane space (**Figure 3-7B**).

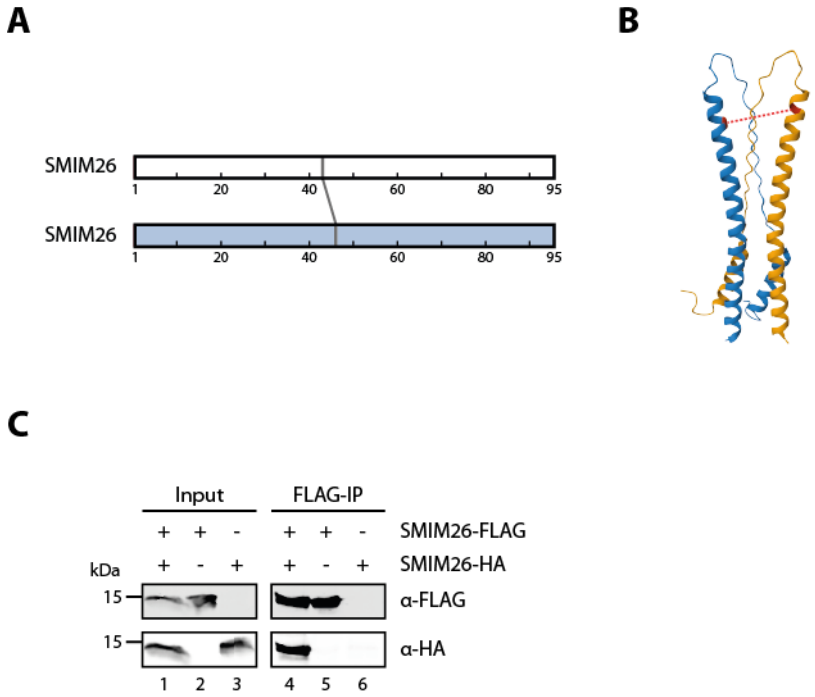

Figure 3-7: Crosslinking MS identifies SMIM26 oligomerization
(A) 2D-cross-linking map of BS3-crosslinked SMIM26-dimers. Cross-links were identified using MeroX (Götze et al., 2015) and visualized with xiVIEW (Combe et al., 2024). (B) AlphaFold3-predicted structure of a SMIM26 dimer (Abramson et al., 2024). Crosslinked residues K43 and S46 are highlighted in red. (C) Western blot analysis of SMIM26-dimers. SMIM26-HA was co-immunoprecipitated with SMIM26-FLAG using α-FLAG.

To validate the crosslinking results, we performed co-immunoprecipitation of differentially tagged SMIM26 using anti-FLAG antibodies (**Figure 3-7C**). Therefore, FLAG- and HA-tagged variants of SMIM26 were transiently expressed in HEK293T cells and mitochondria were isolated prior to co-immunoprecipitation and western blotting. SMIM26-HA was detected only when co-transfected with SMIM26-FLAG but not alone, confirming the crosslinking results. All in all, these findings suggest a di- or multimerization of SMIM26. However, the exact molecular mechanisms requires further investigation.

3.5 SMIM26 is phosphorylated and PGAM5 serves as endogenous phosphatase

Mass spectrometry analysis from SMIM26 binding partners identified the mitochondrial serine/threonine phosphatase PGAM5 as putative interactor (**Figure 3-5**, **Figure 3-6**). PGAM5 is a well-studied phosphatase involved in various

mitochondrial functions including mitochondrial dynamics, biogenesis, programmed cell death, autophagy and mitophagy (He et al., 2025).

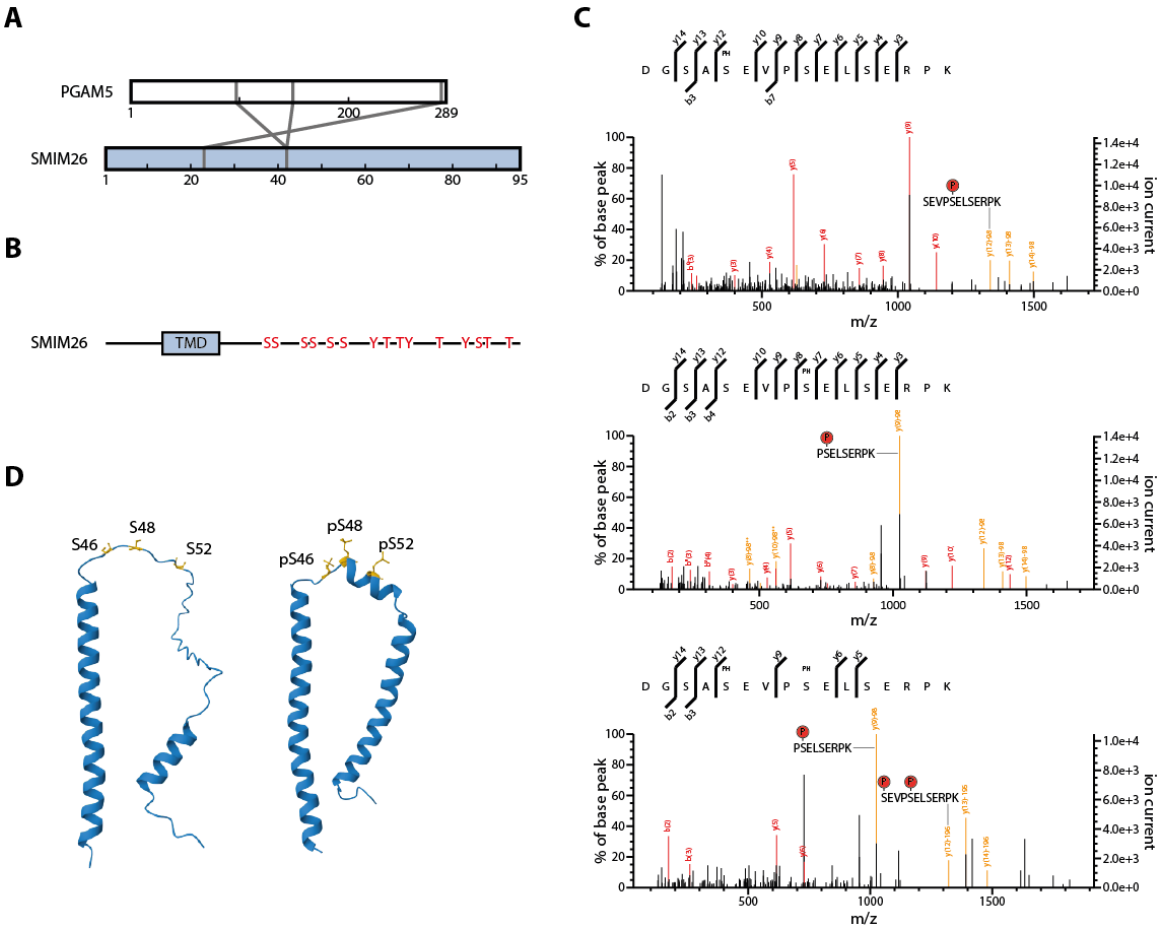

Figure 3-8: SMIM26 is phosphorylated and PGAM5 serves as endogenous phosphatase
(A) Cross-linking mass spectrometry (XL-MS) of SMIM26 and PGAM5. Cross-links were identified by MeroX (Götze et al., 2015) and visualized with xiVIEW (Combe et al., 2024). (B) Schematic of serine (S), tyrosine (Y) and threonine (T) residues in the C-terminal part of SMIM26 that could act as phosphosites. The transmembrane domain (TMD) is indicated in blue. (C) Representative collision-induced dissociation (CID) fragment spectra of phosphorylated SMIM26 peptides (S48, S52) identified by LC-MS/MS. Top: Monophosphorylated SMIM26 peptide DGSApSEVPSELSERPK (Monoisotopic mass: 589.932380 (3+); Mascot ion score: 75; expectation value: 9.8e-8). Middle: Monophosphorylated SMIM26 peptide DGSASEVPpSELSERPK (Monoisotopic mass: 589.932950 (3+); Mascot ion score: 49; expectation value: 3.3e-5). Lower panel: Diphosphorylated SMIM26 peptide DGSApSEVPpSELSERPK (Monoisotopic mass: 616.586670 (3+); Mascot ion score: 34; expectation value: 6.9e-4). Exemplary fragment ions containing phosphorylated serine residues are annotated. (D) AlphaFold3-predicted structure (Abramson et al., 2024) of phosphorylated and unphosphorylated SMIM26. Phosphosites (orange) are highlighted.

To further experimentally validate the interaction between SMIM26 and PGAM5, we performed protein-protein crosslinking followed by MS as previously described (**3.4**) and focused specifically on peptides crosslinking SMIM26 and PGAM5 in the analysis. Interestingly, we found two crosslinking sites in the central region of SMIM26 (**Figure 3-8A**). These efficient crosslinks between SMIM26 and a phosphatase

motivated us to analyze potential phosphorylation sites on SMIM26, as it contains several serine, tyrosine or threonine residues in the intermembrane space-residing part of the microprotein (**Figure 3-8B**).

Therefore, mitochondrial lysates from HEK293T cells transiently expressing SMIM26-F/H were treated with phosphatase inhibitors. SMIM26-F/H was isolated and phosphorylated peptides were identified by mass spectrometry. Analysis of the spectra revealed three specific phosphorylation sites S46, S48 and S52 (**Figure 3-8C**) as well as peptides simultaneously phosphorylated at S48 and S52 (**Figure 3-8C**, lower panel). Strikingly, this phosphorylation cluster is located in an unstructured region downstream of the transmembrane domain (**Figure 3-8D**, left panel) in close proximity to the identified SMIM26-PGAM5 crosslinks (**Figure 3-8A**). These findings indicate a potential role in cellular transmembrane signaling. Interestingly, AlphaFold3 predicts structural changes of this region upon phosphorylation (**Figure 3-8D**, right panel) (Abramson et al., 2024). However, whether this could serve as a regulatory mechanism needs to be further tested and experimentally validated.

Next, we examined the effect of PGAM5 on SMIM26 phosphorylation, performing selected reaction monitoring (SRM) mass spectrometry to quantify the phosphorylated SMIM26 pool. Therefore, we generated a HCT116 cell line stably expressing SMIM26-F/H via lentiviral transduction. From these cells, mitochondrial lysates with endogenous levels or upon knockdown of PGAM5 (**Figure 3-9A**) were treated with phosphatase inhibitors. To quantify the level of phosphorylation, phosphorylated or unphosphorylated isotope-labeled peptides were spiked in prior to mass spectrometry. For all identified serine residues, we found approximately 0.02% of detected peptides to be phosphorylated. Upon PGAM5 knockdown, the phosphorylated pool moderately increased suggesting that PGAM5 could act as phosphatase for SMIM26 (**Figure 3-9B**).

Hence, our findings show that SMIM26 can be phosphorylated at its central part in close proximity to the transmembrane domain and suggest that PGAM5 could be involved in the de-phosphorylation of SMIM26. However, the exact mechanisms and physiological roles of this putative signaling requires further investigation.

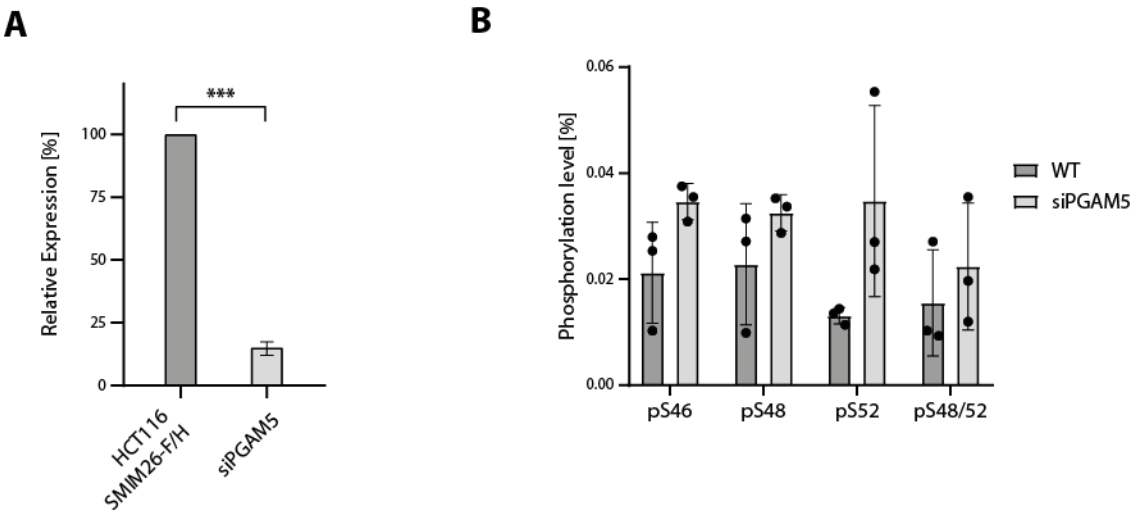

Figure 3-9: Quantification of SMIM26 phosphosites indicates dephosphorylation by PGAM5
(A) qPCR of PGAM5 levels in stable SMIM26-F/H expressing HCT116 cells in the presence versus absence of PGAM5 (siPGAM5, PGAM5 knockdown). GAPDH was used as normalization control (means ± SD). (B) Quantification of SMIM26 phosphorylation in HCT116 cells overexpressing SMIM26-F/H in the presence versus absence of PGAM5 (siPGAM5, PGAM5 knockdown). SMIM26-F/H was purified by α-FLAG immunoprecipitation. Phosphorylation at S46, S48, S52, and dual phosphorylation at S48/52 was quantified by selected reaction monitoring (SRM) following spike-in of isotope-labeled phosphopeptides. Bars indicate the ratio of phosphorylated to non-phosphorylated peptide (p./n.p.).

3.6 SMIM26 resides in the outer membrane and interacts with the inner membrane protein SLC25A6

The interactome of SMIM26 contains proteins residing in the inner and outer mitochondrial membrane (**Figure 3-5**). As proteins in both membrane systems collaborate for efficient metabolite, lipid and protein transport between the cytosol and the mitochondria (Cunningham and Rutter, 2020; Busch et al., 2023; Mavuduru et al., 2024), we hypothesized that SMIM26 could be involved in these processes.

We identified two ion and metabolite channels, VDAC1 and SLC25A6, as binding partners for SMIM26 (**Figure 3-6**). VDAC1 forms a voltage-dependent transport channel through the outer mitochondrial membrane to exchange metabolites and ions with the cytoplasm and plays a central role in apoptosis, mitophagy and a numerous signaling pathways (Shoshan-Barmatz et al., 2020). The adenine nucleotide translocase SLC25A6 is a member of the solute carrier family 25 (SLC25) and exchanges adenosine diphosphate (ADP) and ATP across the inner mitochondrial membrane (Kunji et al., 2020). The nucleotides then transit between the intermembrane space and the cytoplasm through VDAC channels in the outer

mitochondrial membrane (Noskov et al., 2013). The interaction with SMIM26 could facilitate this process and was investigated in detail.

3.6.1 SMIM26 interacts with mitochondrial transporters

To further experimentally validate the interaction of SMIM26 with mitochondrial transporters, we performed protein-protein crosslinking followed by MS as previously described (**3.4**) and crosslinked peptides originating from SMIM26, VDAC1 and the structurally related VDAC2 were specifically investigated in the analysis. Our results confirmed that SMIM26 contacts VDAC1 and VDAC2 through its N-terminal and central parts in close proximity to the transmembrane helix (**Figure 3-10A**). Of note, crosslinking interactions within membranes might be technically inefficient and therefore underrepresented in our experiment.

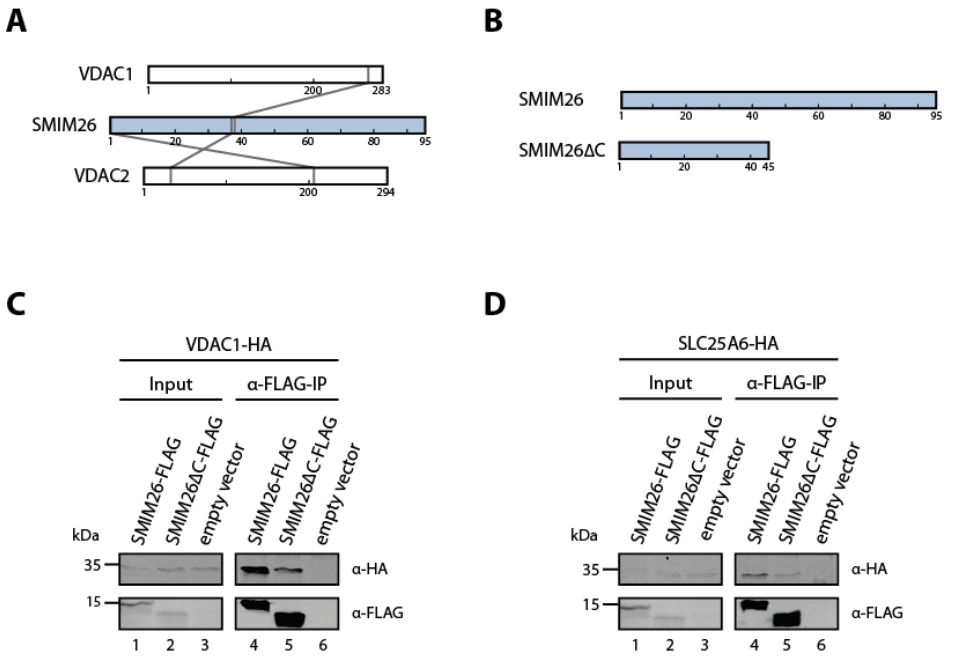

Figure 3-10: SMIM26 interacts with VDAC1 and SLC25A6
(A) 2D map of BS3-crosslinks between SMIM26 with VDAC1 or VDAC2. Cross-linked peptides were analyzed using MeroX (Götze et al., 2015) and visualized in xiVIEW (Combe et al., 2024). (B) Schematic representation of the SMIM26ΔC mutant lacking its C-terminal region. This truncated construct was used in interaction and functional assays. (C) Western Blot analysis validating the interaction between SMIM26 and VDAC1. VDAC1-FLAG was immunoprecipitated using α-FLAG, and co-precipitation of SMIM26-HA or SMIM26ΔC-HA was assessed. An empty FLAG vector served as negative control. (D) Western Blot analysis validating the interaction between SMIM26 and SLC25A6. SLC25A6-FLAG was immunoprecipitated using α-FLAG,and co-precipitation of SMIM26-HA or SMIM26ΔC-HA was assessed. An empty FLAG vector served as negative control.

The crosslinking data was further validated in co-immunoprecipitation experiments with a C-terminally truncated SMIM26 variant (SMIM26ΔC, **Figure 3-10B**) using anti-

FLAG antibodies. Therefore, mitochondria were isolated from HEK293T cells transiently expressing VDAC1-F/H with either full length or truncated SMIM26-HA or an empty vector as control followed by immunoprecipitation and western blotting (**Figure 3-10C**). Consistently, SMIM26 lacking the C-terminal part continues to interact with VDAC1, albeit at reduced level. Hence, interactions with VDAC1 are likely close to the transmembrane helix of SMIM26.

We could not detect crosslinks between SMIM26 and SLC25A6. However, this may be due to technical limitations of the experiment. Nevertheless, we performed co-immunoprecipitations with the C-terminally truncated SMIM26 variant using anti-FLAG antibodies to validate the interaction between SMIM26 and SLC25A6 (**Figure 3-10D**). Mitochondria were isolated from HEK293T cells transiently expressing SLC25A6-F/H with either full length or truncated SMIM26-HA or an empty vector as control followed by immunoprecipitation and western blotting. The truncated variant shows a clear reduction in SLC25A6-F/H binding, suggesting that SLC25A6 mainly interacts with the C-terminal part of SMIM26.

Overall, our findings indicate that SMIM26 interacts with VDAC1 in the outer mitochondrial membrane at its transmembrane domain and with SLC25A6 at the inner mitochondrial membrane through the C-terminal part.

3.6.2 SMIM26 movement in the outer membrane is defined by its interactions in both membranes

Our interaction studies suggested that SMIM26 may reside in the outer mitochondrial membrane with its N-terminal transmembrane helix where it interacts with VDAC1 while the C-terminal part reaches into the intermembrane space to contact SLC25A6, connecting the two transporters for efficient exchange. To test this hypothesis, we collaborated with Mara Hofmann and Christof M. Gebhardt (Institute of Experimental Physics, Ulm University, Ulm, Germany) to perform live-cell single-molecule tracking experiments using fluorescently labeled proteins (**Figure 3-11**, **Figure 3-12, Figure 3-13**).

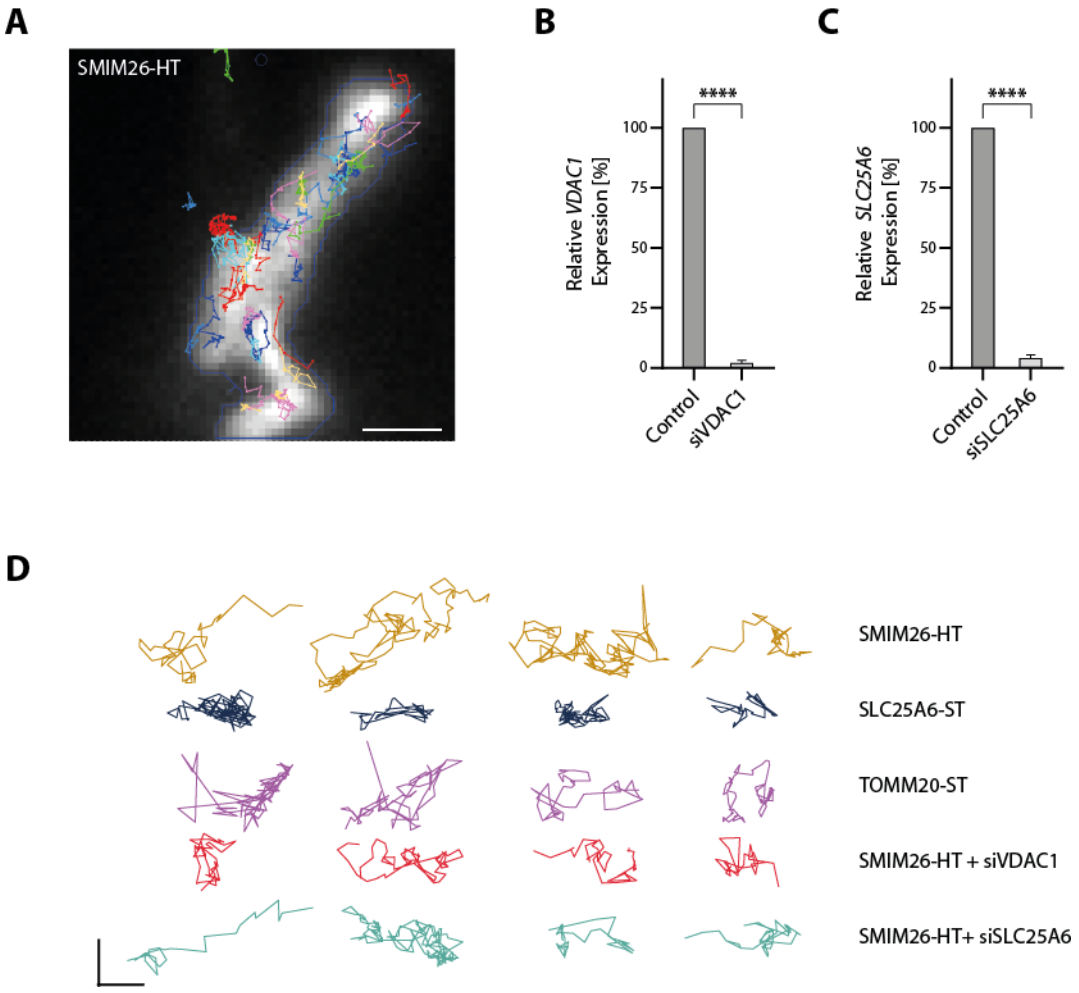

Figure 3-11: Live-cell single-molecule tracking displays SMIM26 movement in the mitochondrial membranes

(A) Representative single-molecule tracks (colored) of PA-JF646-labeled SMIM26-HT (HaloTag), shown overlaid with BioTracker 488-labeled mitochondria (blue outline). Scale bar: 2 µm. (B) qPCR of VDAC1 levels in stable SMIM26-HT expressing HeLa cells in the presence (Control) versus absence of VDAC1 (siVDAC1). GAPDH was used as normalization control (means ± SD). (C) qPCR of SLC25A6 levels in stable SMIM26-HT expressing HeLa cells in the presence (Control) versus absence of SLC25A6 (siSLC25A6). GAPDH was used as normalization control (means± SD). (D) Representative individual single-molecule tracks of SMIM26-HT (ocher), SLC25A6-ST (Snap-Tag, dark blue), TOMM20-ST (magenta), and SMIM26-HT upon knockdown of VDAC1 (red) or SLC25A6 (teal). Scale bars: 500 nm.

To observe the mobility of SMIM26 in mitochondria, we stably expressed SMIM26 carrying a C-terminal Halo-tag (SMIM26-HT) (Los et al., 2008) in HeLa cells. In these cells, we concurrently imaged SMIM26-HT single molecules and BioTracker-488 stained mitochondria at 100 Hz temporal resolution using a custom-built single-molecule-sensitive microscope (Reisser et al., 2018). We then identified and tracked individual molecules using the software TrackIt (Kuhn et al., 2021). Consistent with our previous findings, SMIM26-HT tracks spatially overlapped with mitochondria

(**Figure 3-11A**). Upon closer visual examination of mitochondrial SMIM26-HT molecules, a heterogenous movement behavior of SMIM26-HT with both locally-confined and more wide-spread motion was observed (**Figure 3-11D**, ocher). To validate the interactions identified in our biochemical assays in this cellular system, SLC25A6 was fused to a SnapTag (SLC25A6-ST). Since ectopically-expressed VDAC1 induces cell death (Zaid et al., 2005), we did not manage to generate a VDAC1-ST cell line. Nevertheless, to analyze the mobility and precise localization of SMIM26, we compared its movement with the outer mitochondrial membrane protein TOMM20. Interestingly, SLC25A6-ST showed a uniform short-distance motion (**Figure 3-11D**, dark blue), while TOMM20-ST tracks displayed a more wide-spread motion (**Figure 3-11D**, magenta). These differences can likely be explained by the topological differences of the two mitochondrial membrane systems.

As the mobility of SLC25A6-ST and TOMM20-ST resembled the two different movement behaviors of SMIM26-HT, we knocked down VDAC1 (**Figure 3-11B**) or SLC25A6 (**Figure 3-11C**) in HeLa cells stably expressing SMIM26-HT. While loss of VDAC1 induced increased short-distance motion of SMIM26-HT (**Figure 3-11D**, red), knockdown of SLC25A6 led to a shift towards more long-distance jumps (**Figure 3-11D**, teal).

To quantify these observations, we analyzed the mean squared displacement (MSD) of individual tracks using a model of confined diffusion (**Figure 3-12A**, **B**) (Kuhn et al., 2021). Plotting the histogram of confinement radii confirmed a bimodal behavior for SMIM26-HT consistent with the two different motions observed for single tracks (**Figure 3-12A**, **B**, ocher graph). SLC25A6-ST showed one clear peak at shorter radii of approximately 0.1 µm (**Figure 3-12A**, dark blue), while a broader peak at medium radii around 0.2 – 0.3 µm was observed for TOMM20-ST (**Figure 3-12B**, magenta). Thus, the two SMIM26-HT peaks overlap with the mobility of the outer mitochondrial membrane protein TOMM20-ST and the inner mitochondrial membrane protein SLC25A6-ST, respectively. Upon VDAC1 knockdown (**Figure 3-11B**), SMIM26-HT motion closely resembled WT conditions (**Figure 3-12A**, red). In contrast, when SLC25A6 was knocked down (**Figure 3-11C**) the MSD of SMIM26-HT was similar to the distribution of TOMM20-ST (**Figure 3-12A**, teal). This observation suggests that upon loss of its interaction with SLC25A6 at the inner mitochondrial membrane,

SMIM26-HT mobility is defined by motion parameters of the outer mitochondrial membrane. Hence, SMIM26 localizes to the outer mitochondrial membrane and transiently interacts with SLC25A6 in the inner membrane.

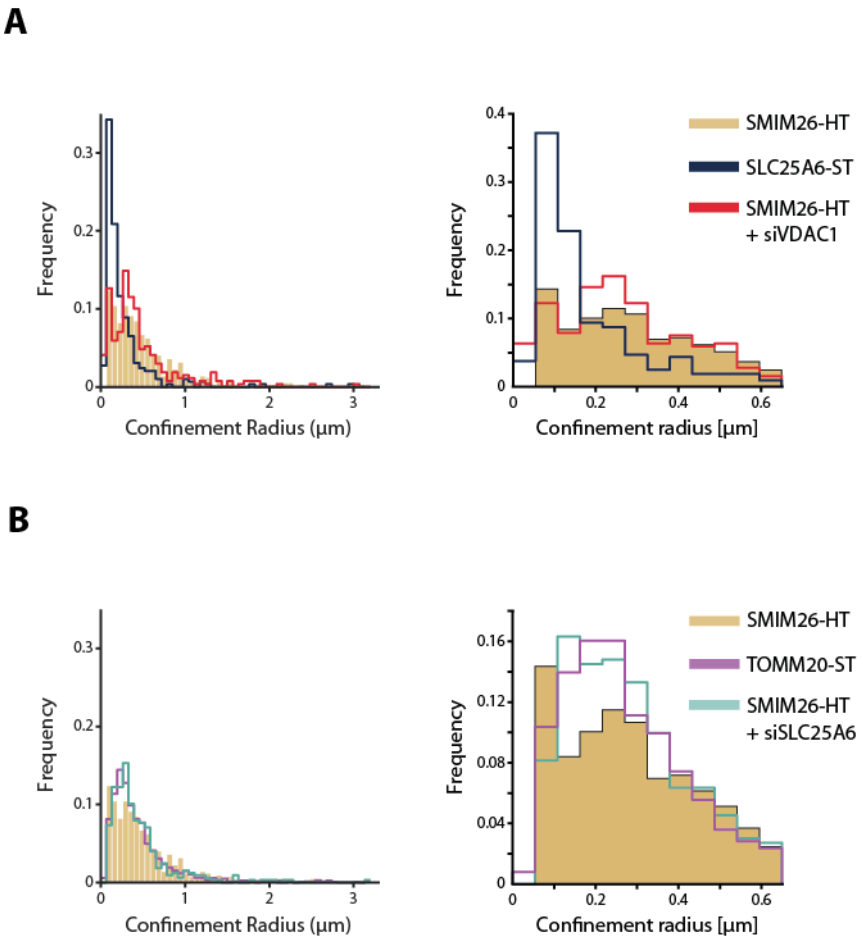

Figure 3-12: Mobility of SMIM26 and other mitochondrial membrane proteins
(A) Distributions of confinement radii of SMIM26-HT (ocher), SLC25A6-ST (dark blue), or SMIM26-HT upon knockdown of VDAC1 (siVDAC1, red), obtained from mean squared displacement (MSD) analysis of individual tracks. Left panel: full distribution. Right panel: Zoom into distribution of shorter confinement radii. (B) Zoom into distributions of confinement radii of SMIM26-HT (ocher), TOMM20-ST (magenta), or SMIM26-HT upon knockdown of SLC25A6 (siSLC25A6, teal), obtained from mean squared displacement (MSD) analysis of individual tracks. Left panel: full distribution. Right panel: Zoom into distribution of shorter confinement radii.

To support our motion model further, we used a second computational method to analyze individual tracks called ExTrack (Simon et al., 2023). ExTrack enables the identification of different motion states within noisy and short single-molecule tracks as observed in our data. Since we identified a bimodal distribution of confinement radii for SMIM26 (**Figure 3-12A**, **B**, ocher), we performed the analysis using a two-state model. Based on all tracks, ExTrack defined shorter (D0) and longer (D1) distance states (**Figure 3-13A**). When analyzing longer distances D1, we identified a

similarly fast diffusion coefficient for SMIM26-HT and TOMM20-ST of ~0.27 – 0.28 µm²/s while SLC25A6-ST showed a reduced diffusion coefficient of ~0.15 µm²/s (**Figure 3-13B**, **D**, **Table 3-1**), which can be explained by the diffusion constraints of the three-dimensional organization in the inner mitochondrial membrane.

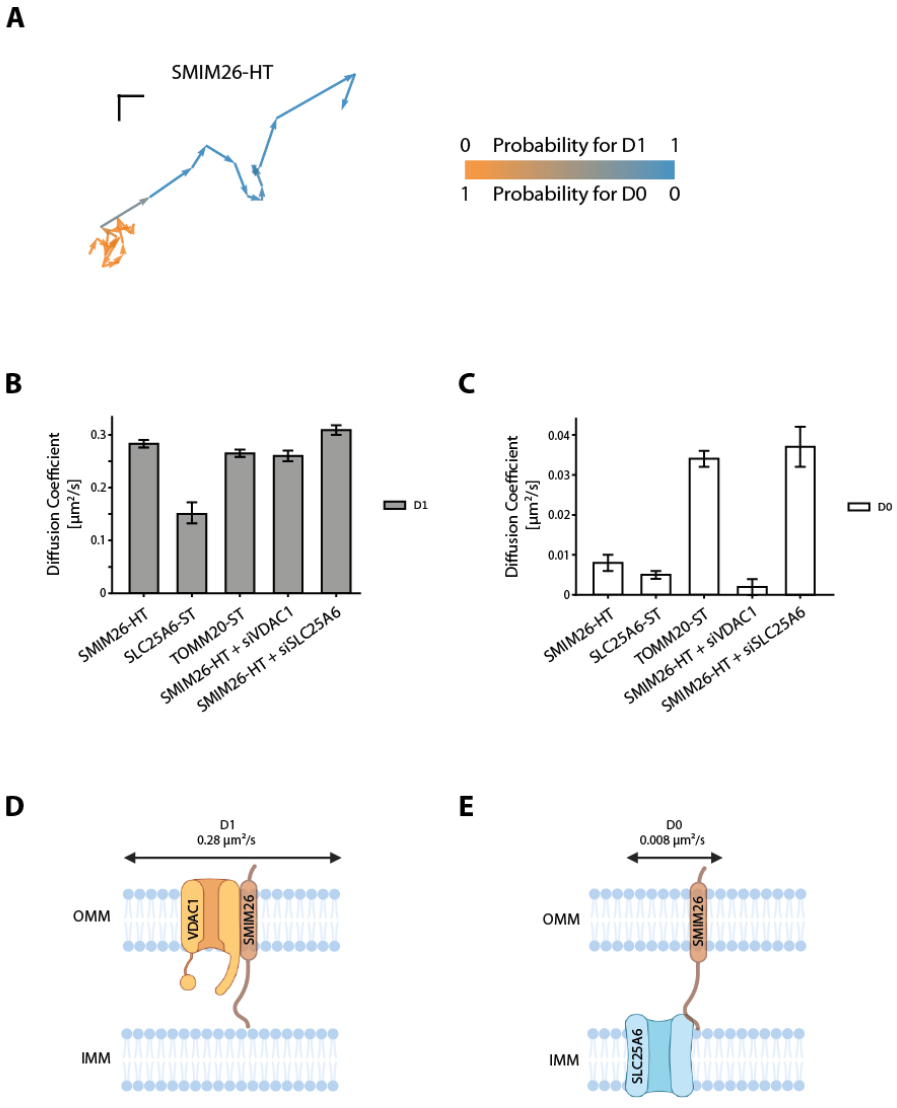

Figure 3-13: Diffusion coefficient of SMIM26 and other mitochondrial membrane proteins
(A) Example track of SMIM26-HT colored by the ExTrack-derived (Simon et al., 2023) probability to be categorized as state 0 (orange) or state 1 (blue). Scale bars: 100 nm. (B) Diffusion coefficients D1 obtained from ExTrack (Simon et al., 2023) two-state modeling analysis across all tracks. (C) Diffusion coefficients D0 obtained from ExTrack (Simon et al., 2023) two-state modeling analysis across all tracks. (D-E) Schematic representation of SMIM26 diffusion state D0 and D1. OMM: Outer mitochondrial membrane. IMM: Inner mitochondrial membrane.

Knockdown of VDAC1 had no influence on the diffusion coefficient of SMIM26-HT, whereas loss of SLC25A6 slightly increase the coefficient to ~0.31 µm²/s. In contrast, the slow diffusion coefficient D0 was similar for SMIM26-HT and SLC25A6-ST with

~0.005-0.008 μm²/s, while it was higher for TOMM20-ST at ~0.034 μm²/s (**Figure 3-13C**, **E**, **Table 3-1**), consistent with recently published values (Bhagawati et al., 2021). Strikingly, the slow diffusion coefficient reduced to ~0.002 μm²/s upon VDAC1 knockdown and increased to ~0.037 μm²/s upon knockdown of SLC25A6. Thus, knockdown of SLC25A6 aligned the motion pattern of SMIM26-HT with that of the outer membrane protein TOMM20, consistent with the analysis of confinement radii.

Taken together, live-cell single-molecule tracking suggests a model where SMIM26 interacts with VDAC1 in the outer membrane and transiently binds SLC25A6 at the inner membrane to arrest at specific spots in the mitochondrial membrane systems.

Table 3-1: Diffusion coefficients D0 and D1 (Values are given in μm²/s) and corresponding fractions F0 and F1 (Values are given in %) determined in ExTrack using two states

	SMIM26-HT	SLC25A6-ST	TOMM20-ST	SMIM26-HT + siVDAC1	SMIM26-HT + siSLC25A6
D0	0.008±0.002	0.005±0.001	0.034±0.002	0.002±0.002	0.037±0.005
D1	0.28±0.01	0.15±0.02	0.27±0.01	0.26±0.01	0.31±0.01
F0	0.25±0.02	0.54±0.04	0.58±0.01	0.26±0.03	0.31±0.03
F1	0.75±0.02	0.46±0.04	0.42±0.01	0.74±0.03	0.69±0.03

3.7 Loss of SMIM26 leads to impaired mitochondrial function

The mitochondrial localization and interaction with PGAM5, VDAC1 and SLC25A6 suggests that SMIM26 might be involved in cellular metabolism potentially by regulating mitochondrial functions. To elucidate the molecular role of SMIM26, we generated *SMIM26* knockout (KO) cell lines. Therefore, we first screened suitable colorectal cancer cell lines for high *SMIM26* expression levels by qPCR (**Figure 3-14A**). We observed high expression in HEK293T, HT29 and HCT116 cells, while other colorectal cancer cell lines (CaCo2, SW620) displayed low *SMIM26* levels. For technical reasons including transfection efficiency and proliferation rate, we selected HCT116 to study the cellular functions of SMIM26 and generated two Clustered Regularly Interspaced Short Palindromic Repeats (CRISPR) knockout clones (**Figure 3-14B**, KO1, KO2) disrupting the production of the microprotein. The knockout was validated by sequencing (**Figure 3-14B**, mutation indicated for each

clone). These cell lines were used to assess mitochondrial activity and cellular proliferation.

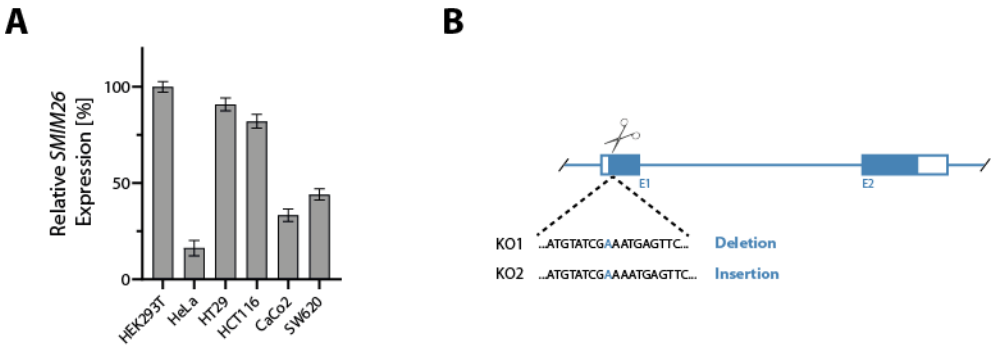

Figure 3-14: Generation of SMIM26 knockout HCT116 cells
(A) qPCR of SMIM26 levels in HEK293T, HeLa and various colorectal cancer cell lines (HT29, HCT116, CaCo2, SW620). GAPDH was used as normalization control and expression was compared to HEK293T level (means ± SD). (B) Schematic of CRISPR-generated SMIM26 knockout in HCT116 cells. Knockout was verified by sequencing.

3.7.1 Loss of SMIM26 affects respiratory chain activity

To investigate the effect of *SMIM26* knockout on respiratory chain activity, we performed respirometry with wild-type and *SMIM26* knockout HCT116 cells using the Agilent Seahorse XF system (Agilent Technologies, Santa Clara, USA). Using the Seahorse XF Cell Mito Stress Test protocol (Agilent Technologies, Santa Clara, USA), we measured oxygen consumption rate of cells treated with oligomycin, carbonyl cyanide-p-trifluoromethoxyphenylhydrazone (FCCP) and rotenone/antimycin A at different timepoints (**Figure 3-15**). Both knockout cell lines exhibited a drastic decrease of consumed oxygen compared to wild-type HCT116 cells (**Figure 3-15A**). These measurements allowed us to analyze different parameters of respiratory activity, specifically basal respiration, maximal respiration and ATP-related oxygen consumption. All described parameters were significantly reduced in both *SMIM26* knockout clones (**Figure 3-15B**, KO1, KO2).

To exclude off-target effects caused by the knockout generation, we performed rescue experiments with *SMIM26* knockout cells stably expressing SMIM26-F/H (**Figure 3-16A**, **B**). Therefore, the Seahorse XF Cell Mito Stress Test protocol was used as mentioned above. Oxygen consumption under standard conditions and upon treatment with oligomycin, FCCP and rotenone/antimycin A was completely restored when reintroducing SMIM26 in the knockout cell lines (**Figure 3-16A**), resulting in

similar levels of basal respiration, maximal respiration and ATP-related oxygen consumption when compared with wild-type cells (**Figure 3-16B**).

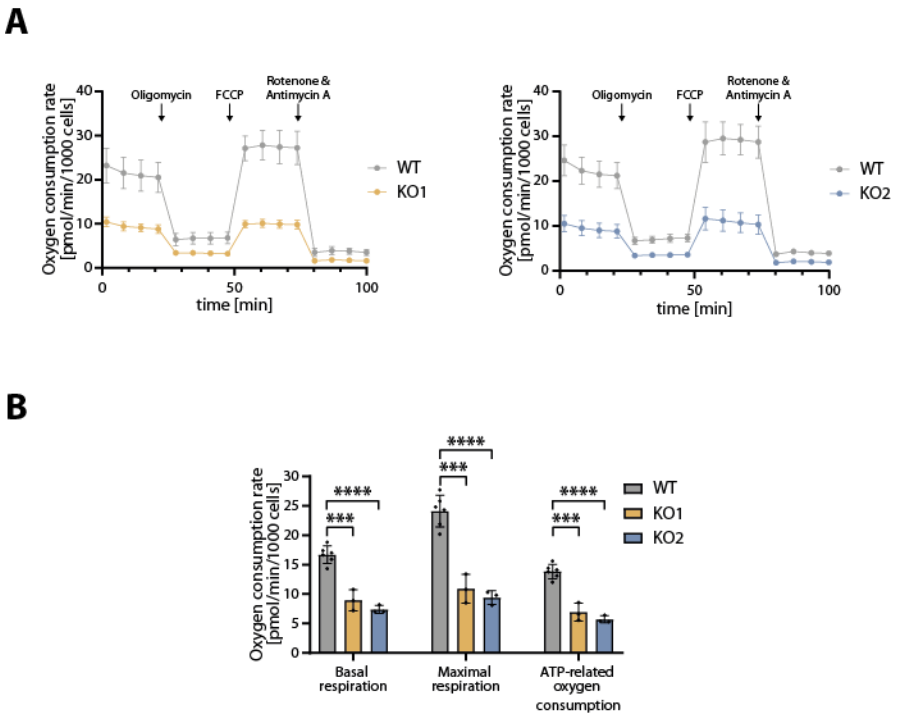

Figure 3-15: Loss off SMIM26 impairs respiratory activity
(A) Representative Seahorse XFp (Agilent Technology) analysis of non-permeabilized HCT116 wild-type (WT, gray) and SMIM26 knockout (KO) cell lines (KO1: ocher, KO2: blue). Oxygen consumption rate (OCR) was measured and normalized to total cell count. Injections followed protocol of the Seahorse XF Cell Mito Stress Test Kit are indicated. (B) Quantification of basal respiration, maximal respiration and ATP-related oxygen consumption in WT (gray) and SMIM26 KO cells (ocher, blue), based on three independent biological replicates (mean ± SD).

Previously, we confirmed that SMIM26 resides in the outer mitochondrial membrane where it interacts with VDAC1 and spans the intermembrane space to bind to SLC25A6. To assess whether these interactions are relevant for respiratory chain activity, we generated a C-terminally truncated variant (**Figure 3-10**, **Figure 3-16C**) and performed rescue respirometry experiments (**Figure 3-16D**, **E**). Indeed, the truncated SMIM26 variant could only partially rescue OXPHOS activity, suggesting that SMIM26 interactions at the inner mitochondrial membrane are important for its function.

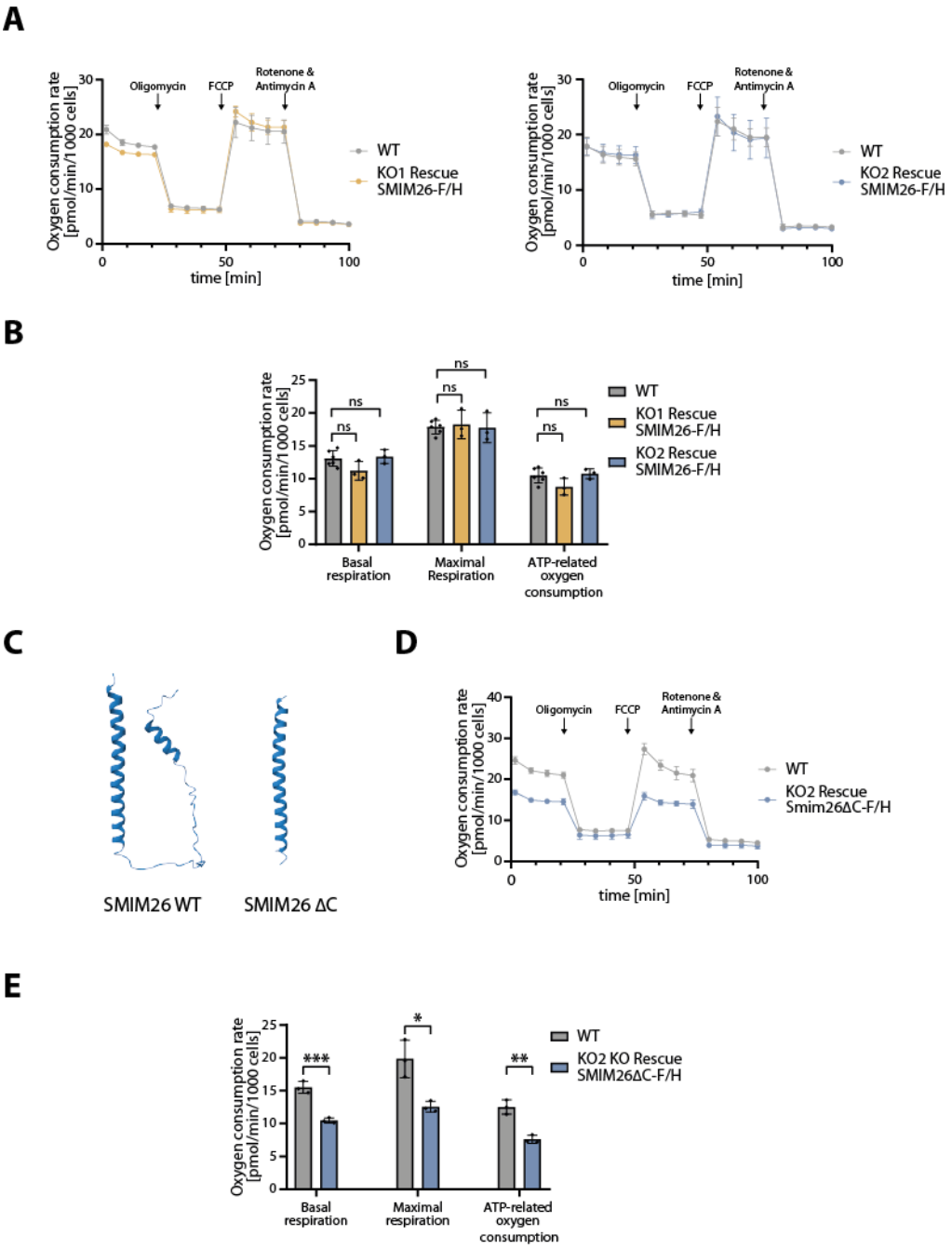

Figure 3-16: Respiratory phenotype can be rescued by reintroduction of SMIM26
(A) Representative Seahorse XFp (Agilent Technology) analysis of non-permeabilized HCT116 WT (gray) and rescued SMIM26 KO cell lines expressing SMIM26-F/H (ocher, blue). OCR was measured and normalized to total cell count and compound injections following the Seahorse XF Cell Mito Stress Test Kit are indicated. (B) Quantification of basal respiration, maximal respiration and ATP-related oxygen consumption in WT (gray) and SMIM26 KO cells rescued with SMIM26-F/H (ocher, blue), based on three independent biological replicates (mean ± SD). (C) AlphaFold3-predicted structure of SMIM26 and SMIM26ΔC. (D) Representative Seahorse XFp (Agilent Technology) analysis of non-permeabilized HCT116 WT (gray) and SMIM26 KO cells rescued with SMIM26ΔC-F/H (blue). OCR was measured and normalized to total cell count. Injections followed protocol of the Seahorse XF Cell Mito Stress Test Kit. (E) Quantification of basal respiration, maximal respiration and ATP-related oxygen consumption in WT (gray) and SMIM26 KO cells rescued with SMIM26ΔC-F/H (blue), based on three independent biological replicates (mean ± SD).

We hypothesized that impaired OXPHOS function might coincide with an accumulation of NADH, which acts as electron donor driving respiratory activity and is being oxidized at complex I (**2.2.2.1**). To test the redox state of NADH, we performed NAD/NADH-Glo-Assays (Promega, Madison, USA) to measure NAD/NADH ratios. As expected, *SMIM26* knockout cells showed a reduction in NAD/NADH ratio, suggesting increased NADH levels in mutant cells (**Figure 3-17**).

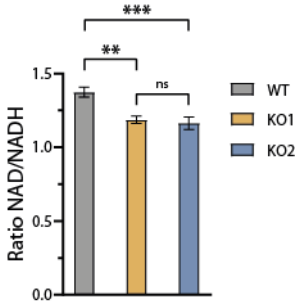

Figure 3-17: SMIM26 knockout affects redox state of NADH
Relative NAD/NADH ratios in HCT116 WT (gray) and SMIM26 KO cells (ocher, blue). NAD and NADH level were measured using the NAD/NADH-Glo® Assay (Promega) (means ± SD).

Overall, our findings indicate that SMIM26 regulates respiratory chain activity likely through an indirect mechanism. Moreover, the C-terminal part interacting with SLC25A6 seems to be important for OXPHOS activity. As a result, loss of SMIM26 leads to an accumulation of NADH.

3.7.2 Loss of SMIM26 impairs cell growth

Reduced respiratory chain activity and thus impaired ATP production as well as NADH redox level may affect cell proliferation. To test this, we performed proliferation assays comparing wild-type and SMIM26-deficient HCT116 cell lines using an Incucyte S3 system (Sartorius, Göttingen, Germany). Under optimal tissue culture conditions, cell growth of *SMIM26* knockout cells was mildly decreased, suggesting reduced dependence on OXPHOS (**Figure 3-18A**).

However, when switching to Dulbecco's modified Eagle's medium (DMEM) containing lower levels of different amino acids, vitamins and other components cell proliferation showed stronger reduction in SMIM26-deficient cells even under high glucose conditions compared to optimal tissue culture medium (**Figure 3-18B**). When challenging the cells with low glucose concentrations, cell growth of knockout cells was markedly reduced compared to wild-type cells (**Figure 3-18C**), indicating

that optimal respiratory chain activity is mandatory when glucose availability is limited.

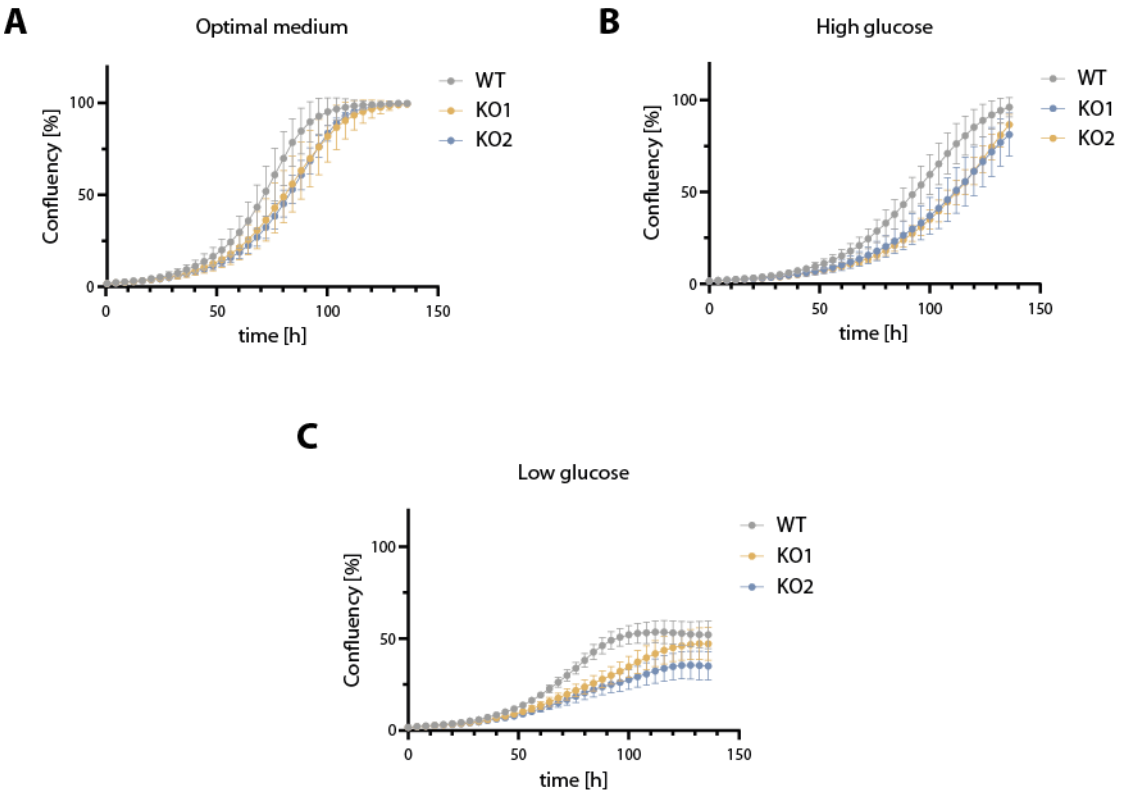

Figure 3-18: Loss of SMIM26 impairs proliferation
(A) Proliferation of HCT116 WT (gray) and KO cell lines (ocher, blue) in optimal McCoy's 5A Medium (means ± SD). (B) Proliferation of HCT116 WT (gray) and KO cell lines (ocher, blue) in high glucose (25 mM) Dulbecco's Modified Eagle Medium (DMEM) (means ± SD). (B) Proliferation of HCT116 WT (gray) and KO cell lines (ocher, blue) in low glucose (0.1 mM) DMEM (means ± SD).

To estimate whether the observed growth defects are caused by reduced cell viability, we performed an orthogonal experimental approach independent of knockout cell lines. Therefore, we efficiently knocked down SMIM26 in HCT116 cells using siPOOLs (**Figure 3-19A**) and measured cell viability 120 h post transfection using the CellTiter Glo® Cell Viability Assay (Promega, Madison, USA) (**Figure 3-19B**). Consistent with cell proliferation of the knockout cells, only a moderate effect was observed under high glucose conditions. However, when grown in low glucose conditions, cell viability was significantly lower upon SMIM26 knockdown compared to wild-type cells.

Taken together, our findings suggest that SMIM26 expression is necessary for cell growth and viability under glucose starvation conditions.

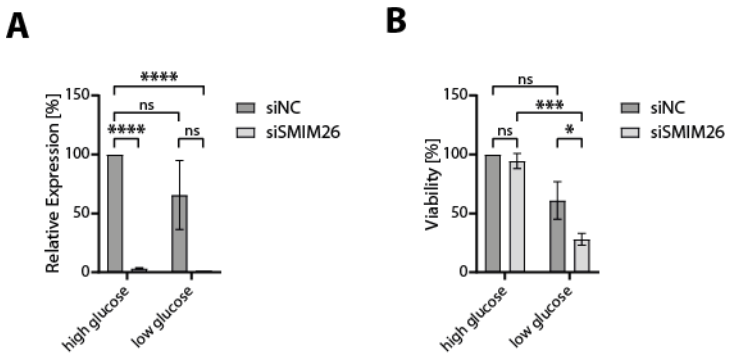

Figure 3-19: SMIM26 knockdown affects cell viability upon starvation
(A) qPCR of SMIM26 knockdown in HCT116 cells using PPIA as reference gene (means ± SD). (B) Viability of HCT116 cells after knockdown with scrambled (siNC) or SMIM26-specific (siSMIM26) siPOOLs. Cell viability was measured 120 h post transfection using the CellTiter-Glo® Cell Viability Assay (Promega).

3.7.3 Some mitochondrial functions are unaffected by SMIM26 depletion

The SMIM26 interactor VDAC1 is a central transporter in the outer mitochondrial membrane which is linked to most major functions of mitochondria (Shoshan-Barmatz et al., 2020). To assess the effect of SMIM26 knockout on some of these related functions, we microscopically examined mitochondrial membrane potential and intracellular calcium level in wild-type and SMIM26-deficient HCT116 cells. We stained cells with the mitochondrial membrane potential dye JC-1, which forms green fluorescent JC-1 monomers at lower concentrations and red fluorescent J-aggregates upon accumulation in the mitochondria (Reers et al., 1991). Therefore, a shift in the red/green fluorescence intensity ratio indicates mitochondrial depolarization. However, we could only observe a slight increase in mitochondrial membrane potential of one of the mutant cell lines (**Figure 3-20A**). Similarly, knockout of SMIM26 showed no effect on intracellular calcium levels when stained with fluorescent calcium indicator Fura-2/AM (**Figure 3-20B**).

Hence, despite the interaction with VDAC1 we could not find any evidence that SMIM26 influences the mitochondrial membrane potential or intracellular calcium level.

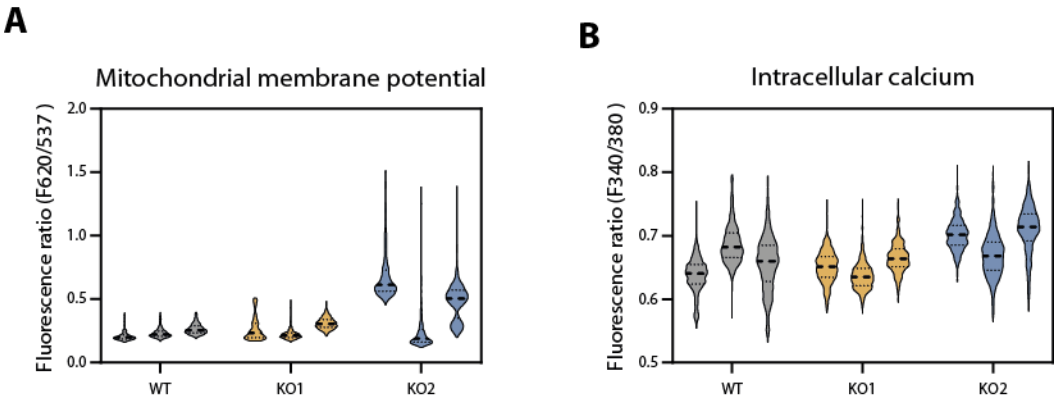

Figure 3-20: SMIM26-deficiency has no influence on mitochondrial membrane potential or intracellular calcium level
(A) Mitochondrial membrane potential of wild-type (gray) and SMIM26 knockout (KO1: ocher, KO2: blue) HCT116 cells stained with JC-1. Absorbance per cell was measured and fluorescence ratio F_{620nm}/F_{537nm} is displayed in three technical replicates are displayed. (B) Intracellular calcium level of wild-type (gray) and SMIM26 knockout (KO1: ocher, KO2: blue) HCT116 cells stained with Fura-2. Absorbance per cell was measured and the fluorescence ratio F_{340nm}/F_{380nm} is displayed in three technical replicates.

3.8 SMIM26-deficiency causes severe phenotypes in animals

Mitochondrial defects can lead to drastic phenotypes in organisms. To identify suitable model organisms, SMIM26 conservation was analyzed, and subsequently knockout animals were generated and phenotyped.

3.8.1 SMIM26 is conserved in vertebrates

To investigate the conservation of SMIM26 across vertebrates we performed a multiple sequence alignment (MSA) from SMIM26 homologues identified by protein basic local alignment search tool (protein BLAST) to generate a phylogenetic tree. SMIM26, and not LINC00493, is highly conserved in vertebrates, including most of the mayor clades of mammals, amphibians, reptiles, birds and both clades of fish (cartilaginous fish and bony fish) (**Figure 3-21A**).

Among the highly conserved organisms are mouse (*mus musculus*) and zebrafish (*danio rerio*), two commonly used model organisms. AlphaFold3 modeling (Abramson et al., 2024) suggests the transmembrane domain to be structurally conserved in these organisms and that the C-terminal part is highly similar between mouse and human while showing structural variations in zebrafish (**Figure 3-21B**). Hence, the conserved microprotein SMIM26 can be studied in mouse and fish model organisms to unravel its physiological functions.

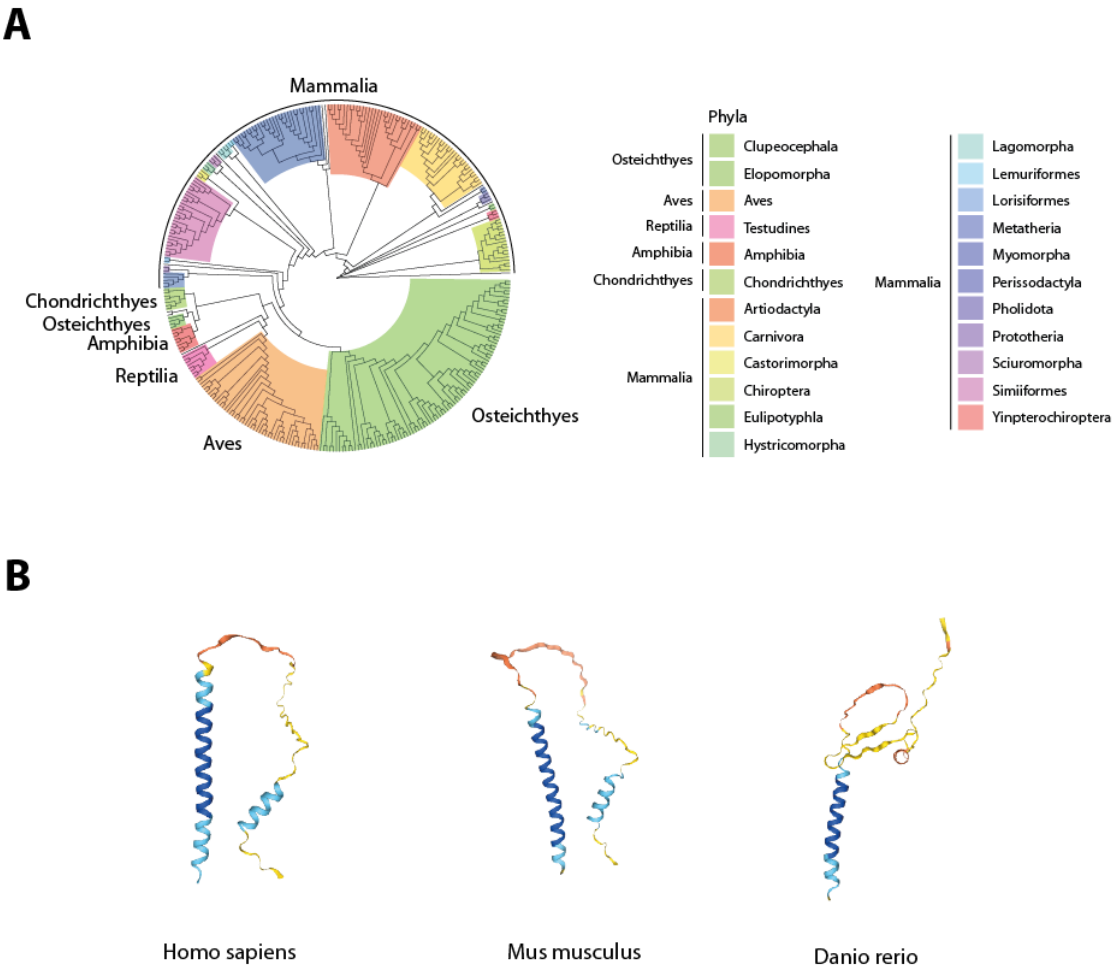

Figure 3-21: SMIM26 is highly conserved across vertebrates
(A) Unrooted maximum likelihood phylogenetic tree of SMIM26 orthologs, based on aligned protein sequences. Branch lengths are proportional to the number of substitutions per site. Phyla with full representation in specific clades are grouped together. (B) AlphaFold3-predicted structure of SMIM26 in human (Homo sapiens, top), mouse (Mus musculus, middle) and zebrafish (Danio rerio, bottom) (Abramson et al., 2024). Structures are colored by predicted Local Distance Difference Test (pLDDT) scores indicating model confidence: deep blue (very high, pLDDT > 90), light blue (confident, 90 > pLDDT > 70), yellow (low, 70 > pLDDT > 50), orange (very low, pLDDT < 50).

3.8.2 *Smim26* deficiency is embryonic lethal in mice

To assess the physiological functions of SMIM26, we generated knockout mice with our collaborators Michaela Prochazkova, Jan Procházka and Radislav Sedlacek (Czech Centre for Phenogenomics and Laboratory of Transgenic Models of Diseases, Institute of Molecular Genetics of the CAS, Prague, Czech Republic). Therefore, we deleted a short sequence including the start codon of *Smim26* in C57BL/6NCrl mice using CRISPR/Cas9-mediated gene editing to disrupt the production of the protein while leaving the RNA intact (**Figure 3-22A**).

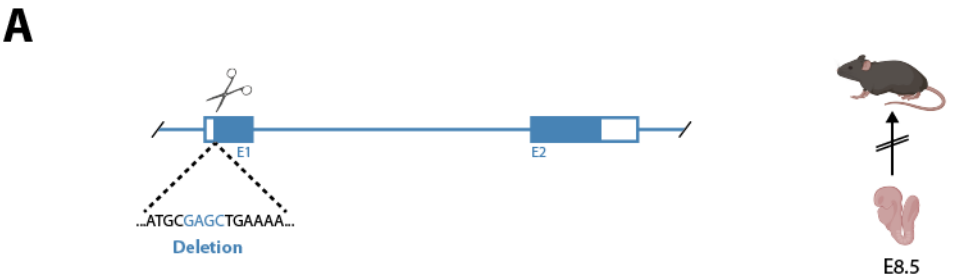

B

	WT	HET	HOM
Observed	51	98	0
Expected	37.25	79.5	37.25

χ^2 test: $p = 2.70 \times 10^{-11}$
N = 149

C

	WT	HET	HOM
E9.5	15	18	2 dead
E12.5	8	18	0

Figure 3-22: Smim26 knockout is embryonic lethal in mice
(A) Schematic of CRISPR-generated Smim26 knockout in Mus musculus. Homozygous knockout in C57Bl/6NCrl background mice is embryonically lethal at E8.5. (B) Expected and observed number of Smim26 WT, heterozygous (HET) and homozygous knockout (HOM) pups. p-values calculated using a chi-square test of Mendelian random assortment. (C) Collected Smim26 WT, HET and HOM mouse embryos at E9.5 and E12.5. HOM embryos were already dead at the time of collection.

While wild-type and heterozygous knockout pups were born at mendelian ratios, no homozygous knockout offspring was found, indicating embryonic lethality (**Figure 3-22B**). Interestingly, when collecting early-stage embryos, we could not find any homozygous knockout mice at E12.5 and collected only two dead embryos at E9.5 (**Figure 3-22C**). Hence, *Smim26* knockout mice died already prior to E9.5, demonstrating that the microprotein is essential for early embryogenesis in mice. This very severe and early phenotype prevented further functional analysis of the embryos. Off note, heterozygous mice were not distinguishable from wild-type animals and did not show any obvious phenotype (data not shown).

3.8.3 *smim26* deficiency causes severe mitochondrial phenotypes in zebrafish

To investigate the function of SMIM26 in embryogenesis and beyond further, we generated smim26 knockout zebrafish lines with our collaborators Anastasia Chugunova and Andrea Pauli (Research Institute of Molecular Pathology, Vienna BioCenter, Vienna, Austria). Therefore, we edited a short sequence within codon 1 of smim26 in TLAB fish using CRISPR/Cas9-mediated gene editing. We generated two mutant lines with one carrying a deletion (Mutant 1, d49) and one an insertion and

deletion (Mutant 2, insdel) at the cleavage site (**Figure 3-23A**). The successful knockout was validated by scheduled Parallel Reaction Monitoring (sPRM) mass spectrometry analysis (Peterson et al., 2012) (**Figure 3-23B**). In both mutant lines no smim26 could be detected while it was present in wild-type lines, confirming the loss of the microproteins. These fish lines were further used for phenotypical analysis and physiological experiments including respirometry and shotgun mass spectrometry.

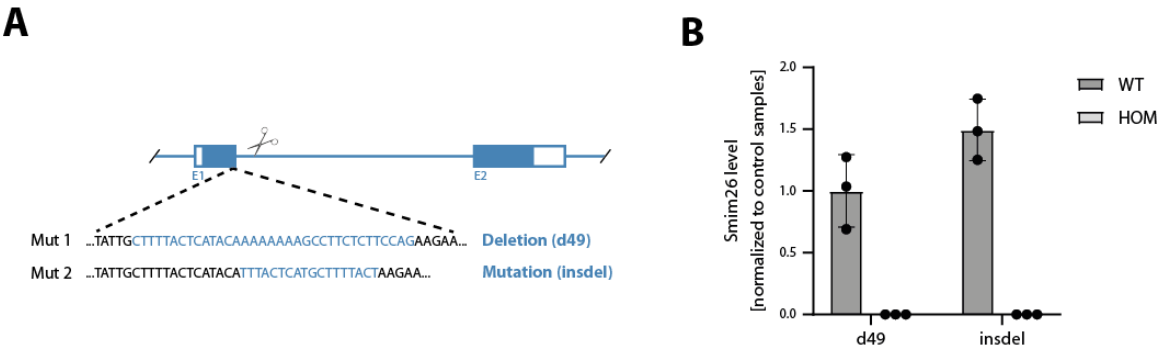

Figure 3-23: Generation of smim26 knockout zebrafish lines
(A) Schematic of CRISPR-generated Smim26 knockout in Danio rerio. Homozygous knockout has been generated in two independent lines (Mut1 and Mut2). (B) Relative Smim26 protein levels in 7 dpf wild-type and homozygous mutant zebrafish larvae, assessed by PRM-MS. Quantification was normalized to four reference proteins (apolipoprotein A-I precursor, keratin 4, creatine kinase, small ribosomal subunit protein eS25).

3.8.3.1 Loss of *smim26* affects survival and growth of zebrafish

To observe the effect of *smim26* knockout in zebrafish, we analyzed the phenotype of progeny of heterozygous mutant parents. Mutant larvae present at mendelian ratios and phenotypically indistinguishable from their heterozygous and wild-type siblings in the first 14 days (**Figure 3-24A**). During later stages of development, survival of homozygous mutant larvae was severely compromised when raised in competition with their heterozygous and wild-type siblings. Hence, if not separated early only 10% of *smim26* knockouts survived at 3 months post fertilization.

To facilitate survival of knockout larvae, we separated larvae based on their genotype at 5 days post fertilization (dpf), raised them at low density and measured their length every 14 days. Even under these conditions, mutant fish showed significantly slower growth compared to their heterozygous and wild-type siblings (**Figure 3-24B**, **C**). Off note, growth of heterozygous mutants and wild-type zebrafish was indistinguishable. However, with progressing development, smim26 knockout lines eventually caught

up in size with their wild-type siblings (**Figure 3-24C**). Interestingly, all homozygous *smim26* knockout mutants developed into males, preventing us to obtain any knockout females (**Figure 3-24D**). The reason for this male-bias is still unclear and an exciting question to answer in the future. To exclude fertility as cause of the observed phenotypes we analyzed the fertility of male homozygous mutants, showing no difference when compared to their heterozygous and wild-type siblings (**Figure 3-24E**).

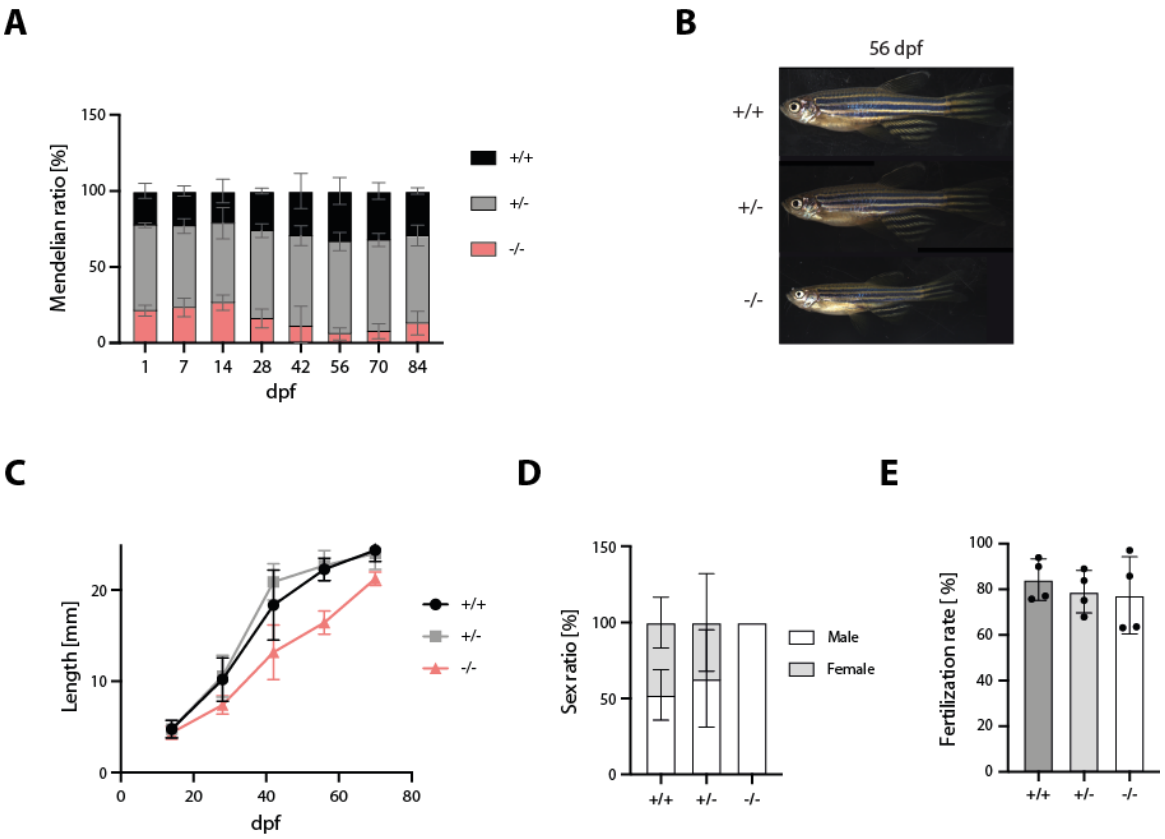

Figure 3-24: smim26 knockout causes growth defect in fish and is embryonic lethal in female
(A) Mendelian ratios of offspring from heterozygous intercrosses, genotyped at the indicated developmental stages. Data represent the mean of at least two clutches per time point and genotype, with a minimum of 30 larvae per clutch (means ± SD). (B) Representative images of clutch-mates (wild-type, heterozygous, and zygotic mutants) at 56 dpf. (C) Standard length (mm) of clutch-mates (wild-type, heterozygous, and zygotic mutants) genotyped and segregated at 5 dpf. Data are from two independent experiments across two mutant lines. (D) Female-to-male sex ratios among clutch-mates (wild-type, heterozygous, and zygotic mutants). Data represent means from at least two clutches per genotype. (E) Fertilization rates of males from clutch-mates (wild-type, heterozygous, and zygotic mutants). Data represent means from at least two clutches per genotype.

In conclusion, *smim26* knockout drastically affects the survival of larvae when not separated from their heterozygous and wild-type siblings. If separated early,

knockout zebrafish exclusively develop into fertile males that exhibit impaired growth.

3.8.3.2 Loss of *smim26* impairs respiratory chain activity in zebrafish

To investigate the mitochondrial functions of *smim26* in homozygous knockout zebrafish, we measured oxygen consumption in 7 dpf larvae as an indicator of mitochondrial activity. Consistent with our findings in human cell lines, *smim26* deficient mutants exhibited reduced basal respiration by approximately 50% (**Figure 3-25A**, **B**) compared to their wild-type siblings. These findings support our data obtained from human cell lines, suggesting that SMIM26 plays an important role in mitochondrial functions.

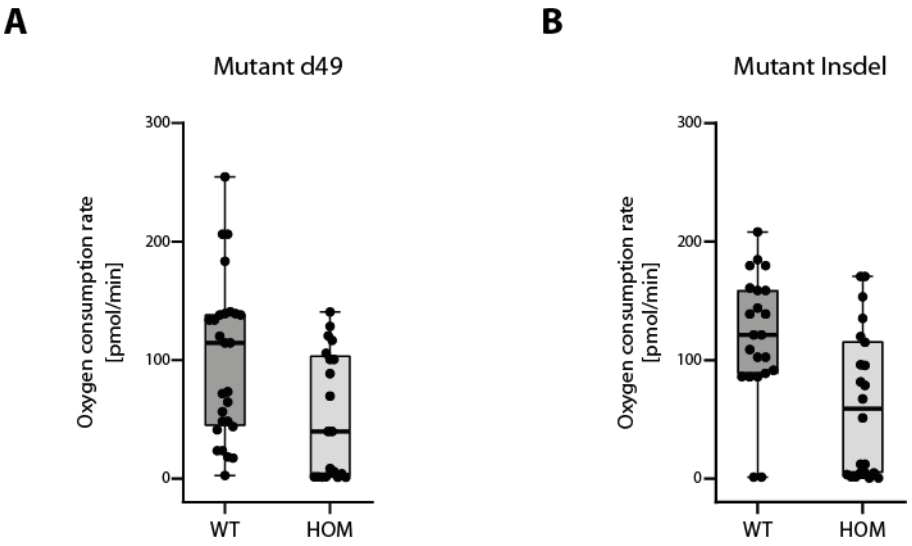

Figure 3-25: smim26 knockout impairs respiration in zebrafish larvae
(A-B) Basal respiration rates 7 dpf wild-type and homozygous mutant larvae, measured using the Agilent Seahorse XF platform. Data represent means from three independent experiments per genotype. (A) Mutant line d49. (B) Mutant line Insdel.

To evaluate the mechanism by which *smim26* impairs respiration further, we analyzed the proteome of wild-type and homozygous mutant larvae at 7 dpf by mass spectrometry. Proteomic analysis revealed a significant downregulation of most respiratory chain complex I components (**Figure 3-26A**, **B**). The effect on complex I seemed to be very specific, as none of the other respiratory chain complexes was dysregulated. Interestingly, the most downregulated proteins mainly localize to the N- and Q-module of complex I (**Figure 3-26C**). However, we were not able to identify the exact cause for this selective downregulation in our work.

These results suggest that loss of *smim26* leads to respiratory chain defects *in vivo*, likely due to a direct or indirect downregulation of complex I components.

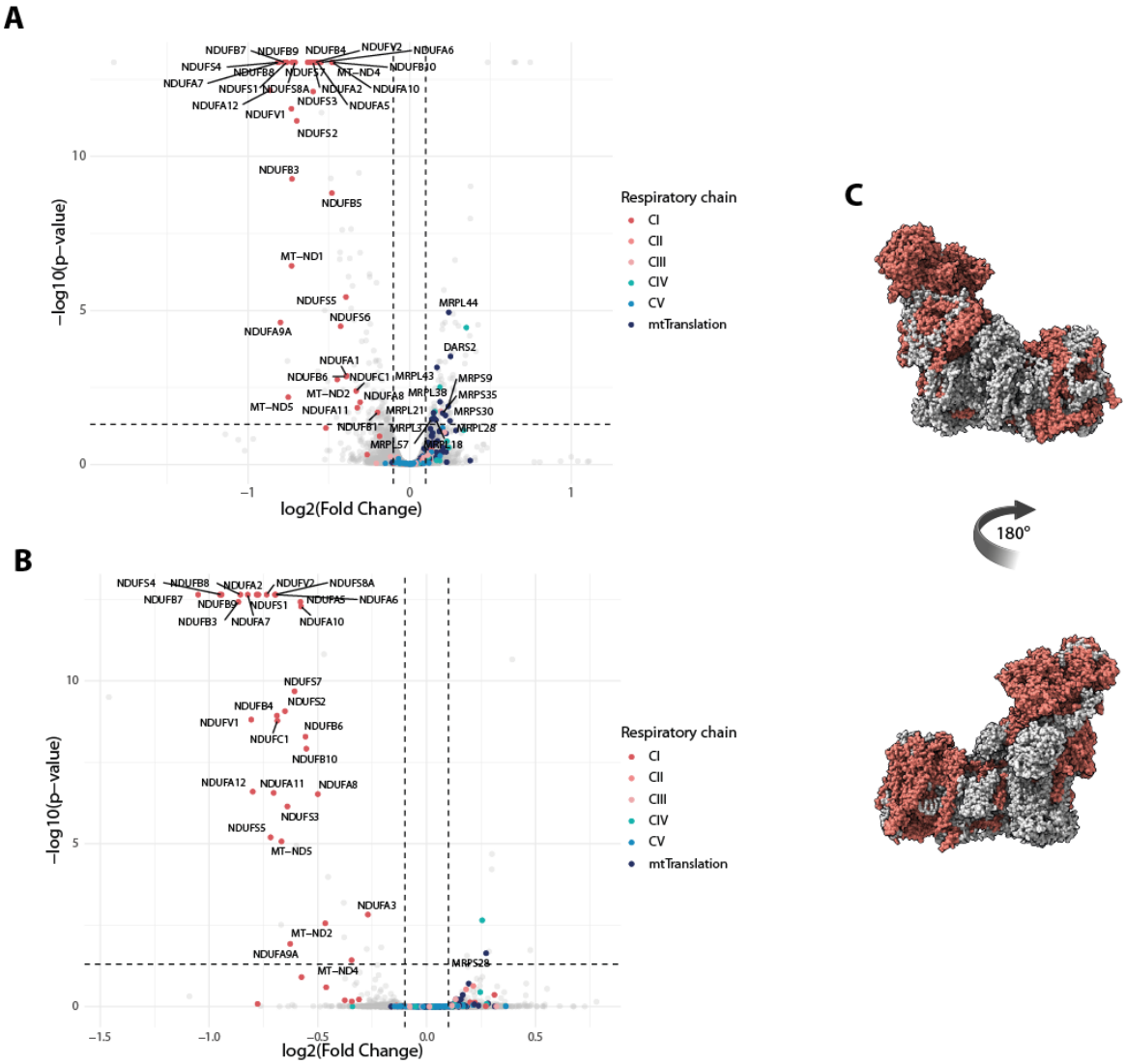

Figure 3-26: smim26 knockout impairs respiratory chain complex I
(A-B) Quantitative proteomic analysis of 7 dpf wild-type and homozygous mutant larvae. Volcano plot displays mean log_2 fold changes (mutant/wild-type) across three biological replicates. Electron transport chain complex subunits (CI–CV = Complex I–V) and mitochondrial translation-related proteins (mtTranslation) are color-coded. p-values calculated using a two-sided unpaired t-test. (A) Mutant line d49. (B) Mutant line Insdel. (C) Structure model of respiratory chain complex I (bottom) indicates most downregulated proteins (p-Value < 0.05, log2(Fold Change) < -0.5) of in red.

3.9 SMIM26 affects cancer progression

SMIM26 was initially identified in a colorectal cancer mouse model, and we showed that SMIM26-deficient HCT116 display a strong mitochondrial phenotype. Since mitochondria play a major role during carcinogenesis via metabolic reprogramming, mitochondrial stress response pathways and evasion of cell death (Giampazolias and Tait, 2016; Wang et al., 2023), they have emerged as promising targets for anticancer therapy. Therefore, we studied the role of SMIM26 in cancer progression.

3.9.1 SMIM26-deficiency leads to dysregulated signaling pathways in HCT116 cells

To investigate whether the loss of SMIM26 indirectly affects the transcriptome of cancer cells, we performed RNA sequencing (RNA-seq) experiments comparing wild-type and *SMIM26* knockout HCT116 cells. As expected, most transcript were unaffected by *SMIM26* knockout (**Figure 3-27A**, **B**). However, a small subset of genes was significantly dysregulated in mutant cell lines compared to wild-type.

WikiPathways gene set enrichment analysis (GSEA) of significantly changed transcripts identified enrichment of various cancer-related signaling pathways including PI3K/Akt, Wnt/ß-catenin, p53 and mesodermal commitment pathway (**Figure 3-27C**). Interestingly, we have shown that SMIM26 can be phosphorylated (**Figure 3-8**, **Figure 3-9**). Hence, our findings suggest that SMIM26 might be linked to signaling pathways in cancer facilitating cancer metabolism, proliferation, migration and epithelial-mesenchymal transition (EMT).

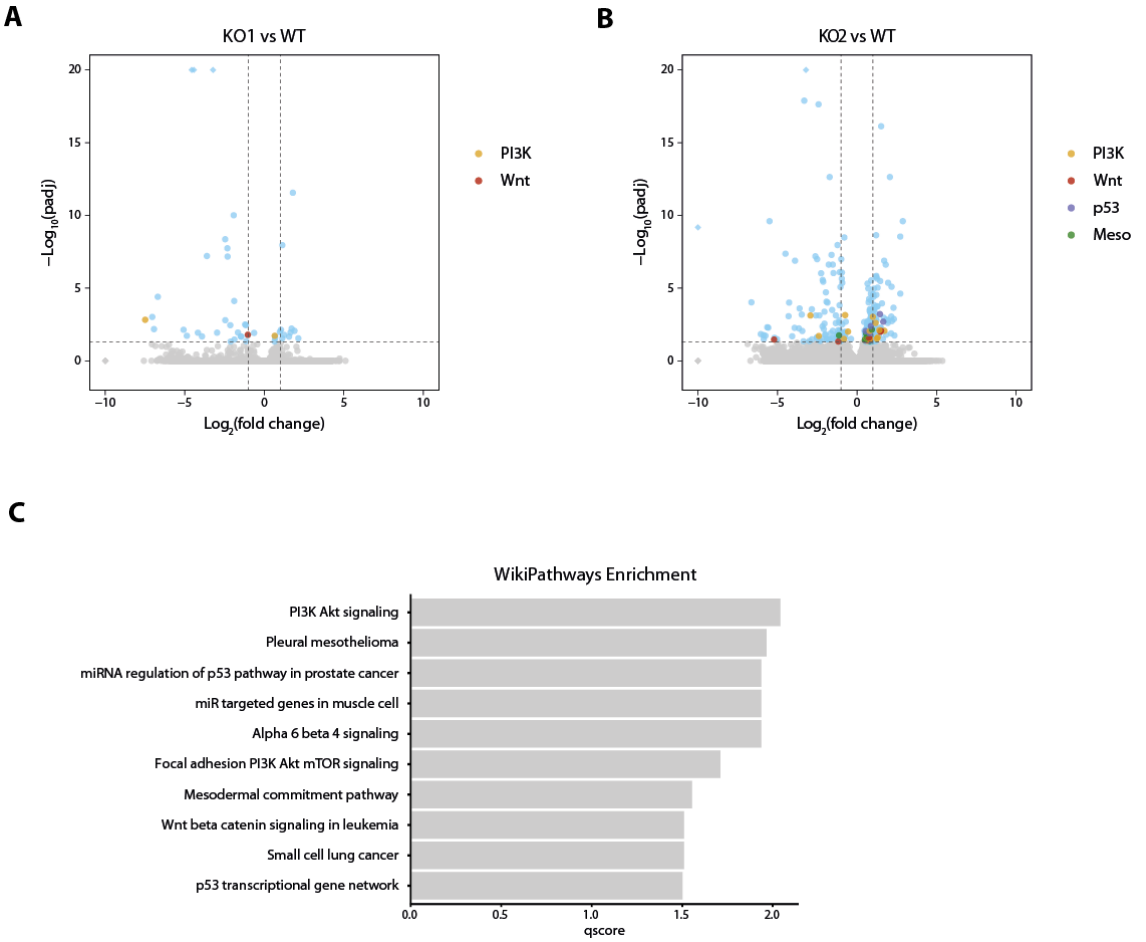

Figure 3-27: Transcriptome of SMIM26 knockout HCT116 cells
(A–B) Volcano plots of differentially expressed transcripts obtained from DESeq2 analysis of total RNA sequencing data comparing two independent SMIM26 knockout clones (KO1 and KO2) with wild-type (WT) HCT116 cells. Highlighted transcripts are associated with PI3K/Akt signaling (yellow), Wnt/ß-catenin signaling (red), p53 (brown), and mesodermal commitment (green) pathways. (C) Gene set enrichment analysis (GSEA) of differentially expressed transcripts using WikiPathways revealed significant enrichment of pathways including PI3K–Akt signaling, Wnt/β-catenin signaling, and p53-associated gene networks. Enrichment scores are shown as q-scores.

3.9.2 SMIM26 expression correlates with cancer patient survival in some cancer entities

RNA-seq experiments from the colorectal carcinoma cell line HCT116 revealed several cancer-associated signaling pathways to be differentially expressed upon knockout of SMIM26 (**Figure 3-27**). To study whether these pathways correlate with SMIM26 expression in patients as well, we performed a gene set enrichment analysis on colon adenocarcinoma (COAD) patient samples using the cancer genome atlas (TCGA) database. Therefore, we stratified patients into groups with high or low expression of SMIM26 and compared cancer-related hallmark gene sets in these groups (**Figure 3-28**). Patients with low SMIM26 level showed a significant

enrichment of metabolism, inflammatory and immune signaling pathways. Consistent with our RNA-seq data, we observed a significant enrichment of PI3K/Akt, Wnt/ß-catenin, EMT and p53 pathways, providing evidence that SMIM26 might indeed be linked to cancer biology.

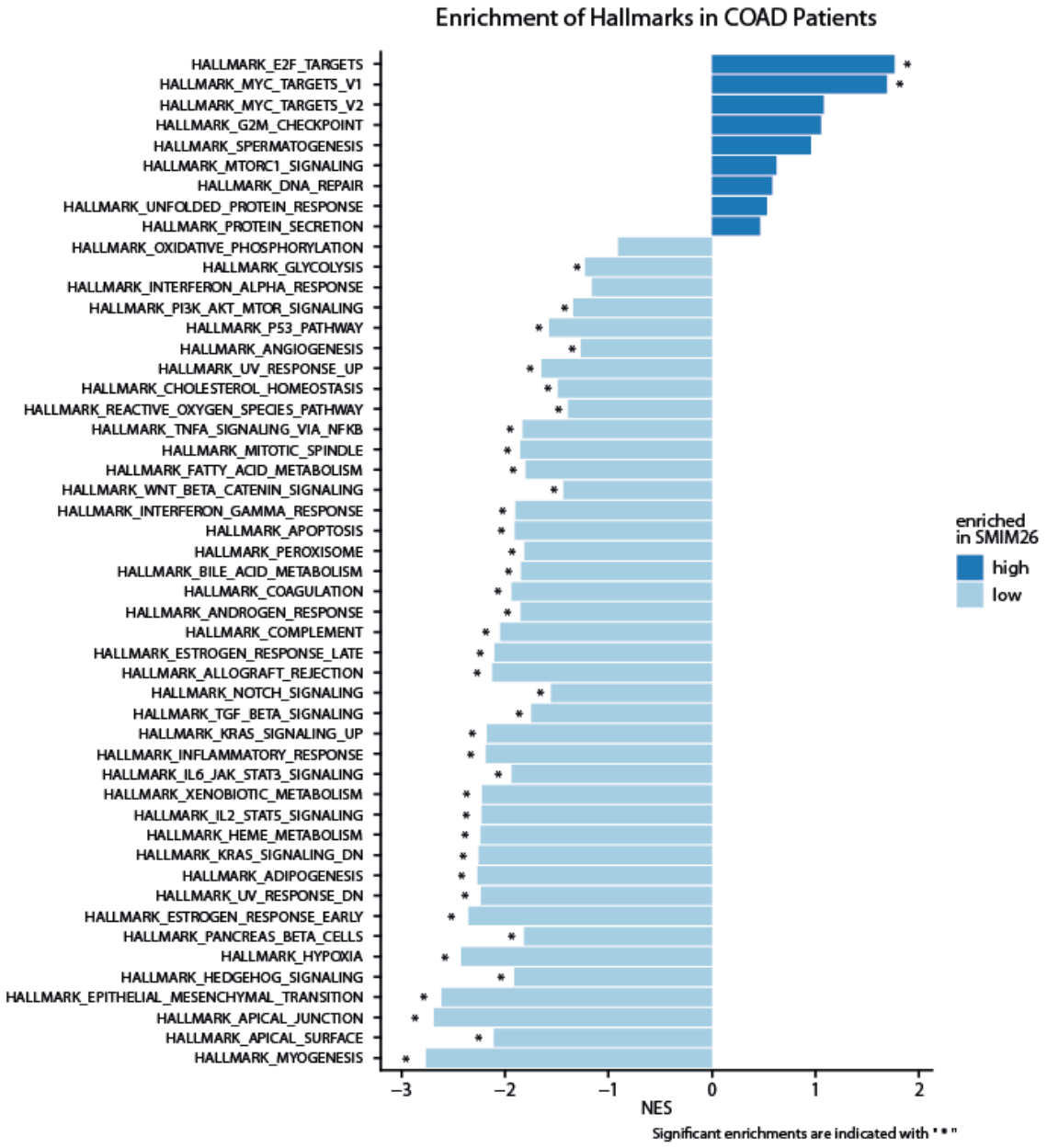

Figure 3-28: Enrichment of Hallmark gene sets in COAD patients with differential SMIM26 expression

Gene set enrichment analysis (GSEA) was performed on COAD patients stratified by low and high SMIM26 expression. Normalized enrichment scores (NES) are shown for Hallmark pathways, grouped by enrichment in patients with low (light blue) and high (dark blue) SMIM26 expression level. Significant enrichments are indicated (, $p < 0.05$).*

Next, we analyzed the expression of SMIM26 in additional tumor entities within the gastrointestinal tract. TCGA data of tumor and normal tissue was compared for esophageal carcinoma (ESCA), stomach adenocarcinoma (STAD), COAD, rectum adenocarcinoma (READ), pancreatic adenocarcinoma (PAAD), liver hepatocellular carcinoma (LIHC), and cholangiocarcinoma (CHOL) (**Figure 3-29**). COAD, READ, PAAD, LIHC and CHOL showed similar SMIM26 expression in corresponding tumor samples. However, COAD and READ displayed only mild upregulation compared to corresponding normal tissues while in PAAD, LIHC and CHOL a stronger upregulation was observed.

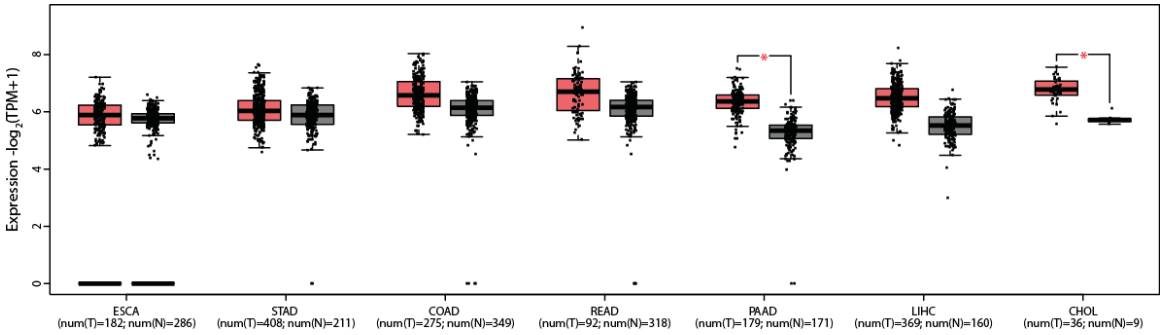

Figure 3-29: SMIM26 expression in gastrointestinal tract cancers
Boxplots represent SMIM26 expression levels (log_2(TPM+1)) in tumor (T, red) and normal (N, gray) tissue samples across seven gastrointestinal cancer types from TCGA: esophageal carcinoma (ESCA), stomach adenocarcinoma (STAD), colon adenocarcinoma (COAD), rectum adenocarcinoma (READ), pancreatic adenocarcinoma (PAAD), liver hepatocellular carcinoma (LIHC), and cholangiocarcinoma (CHOL). Sample sizes are indicated below each cancer type (num(T), num(N)).

Based on the observed SMIM26 expression profiles and our mechanistic work in HCT116 cells, we decided to assess SMIM26-correlated survival in cancer patients for colorectal and liver cancer. Surprisingly, SMIM26 showed no significant association with overall survival despite a slightly increased hazard ratio (HR) of 1.5 for the high SMIM26 expression group (**Figure 3-30A**). However, consistent with the increased upregulation of SMIM26 in LIHC, high levels of SMIM26 correlate strongly with worse overall survival and a hazard ratio of 2.1 in liver cancer (**Figure 3-30B**). These findings suggest that upregulation of SMIM26 might have a strong oncogenic effect in liver cancer.

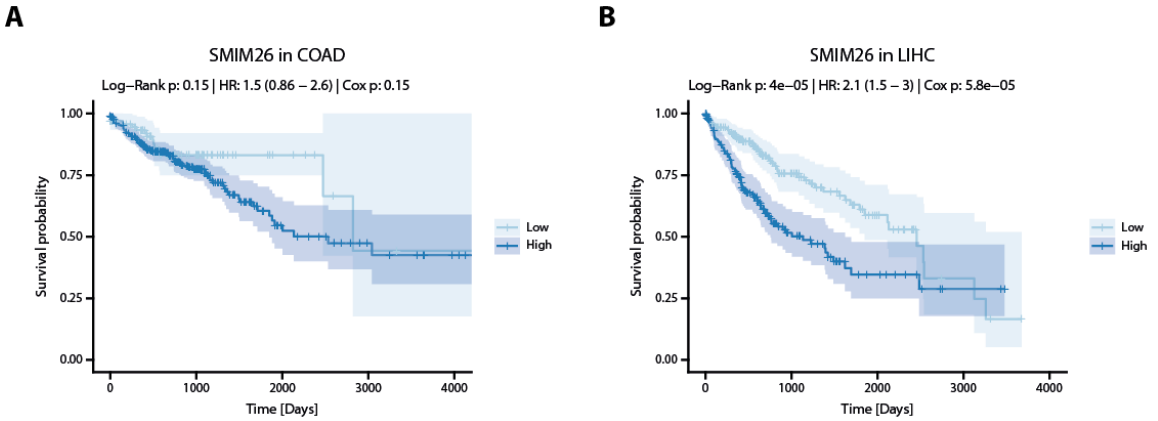

Figure 3-30: Survival analysis of SMIM26 expression in cancer patients
Kaplan-Meier survival analysis from patients stratified into low (light blue) and high (dark blue) SMIM26 expression groups. Shaded areas represent 95% confidence intervals. Log-rank p-values indicate statistical significance for overall survival. Cox proportional hazard ratios (HR) with corresponding p-values (Cox p) are shown. (A) Kaplan-Meier survival curves for SMIM26 in COAD. (B) Kaplan-Meier survival curves for SMIM26 in LIHC.

We proved that SMIM26 interacts with VDAC1, SLC25A6 and PGAM5 to regulate mitochondrial functions. Given that the role of SMIM26 is closely linked to its interaction partners, we hypothesized that co-expression of SMIM26 together with these proteins may have a stronger impact on overall survival of liver cancer patients. To test this, LIHC patients were stratified into high and low expression groups for SMIM26 and each respective interactor. Additionally, as a third group patients with concordant high (high/high) or low expression (low/low) of both genes were combined, and Kaplan-Meier survival curves were generated.

Consistent with the movement studies for SMIM26 in relation to VDAC1 and SLC25A6 (**Figure 3-11**, **Figure 3-12, Figure 3-13**), high expression of both SMIM26 and VDAC1 displayed markedly worse overall survival and an increased hazard ratio (HR: 3.2), in comparison to high expression of SMIM26 (HR: 2.04) or VDAC1 (HR: 2.24) alone (**Figure 3-31A**, **B**). In contrast, the combination of SMIM26 and SLC25A6 showed no significant effect on patient survival (**Figure 3-31C**, **D**). Notably, co-expression of SMIM26 and PGAM5 (HR: 4.6) was associated with substantially reduced survival compared to SMIM26 (HR: 2.5) or PGAM5 (HR: 3.4) alone (**Figure 3-31E**, **F**). On the other hand, patients with low expression of SMIM26 and its interactors showed no additional beneficial effect on survival (**Figure 3-31A-F**).

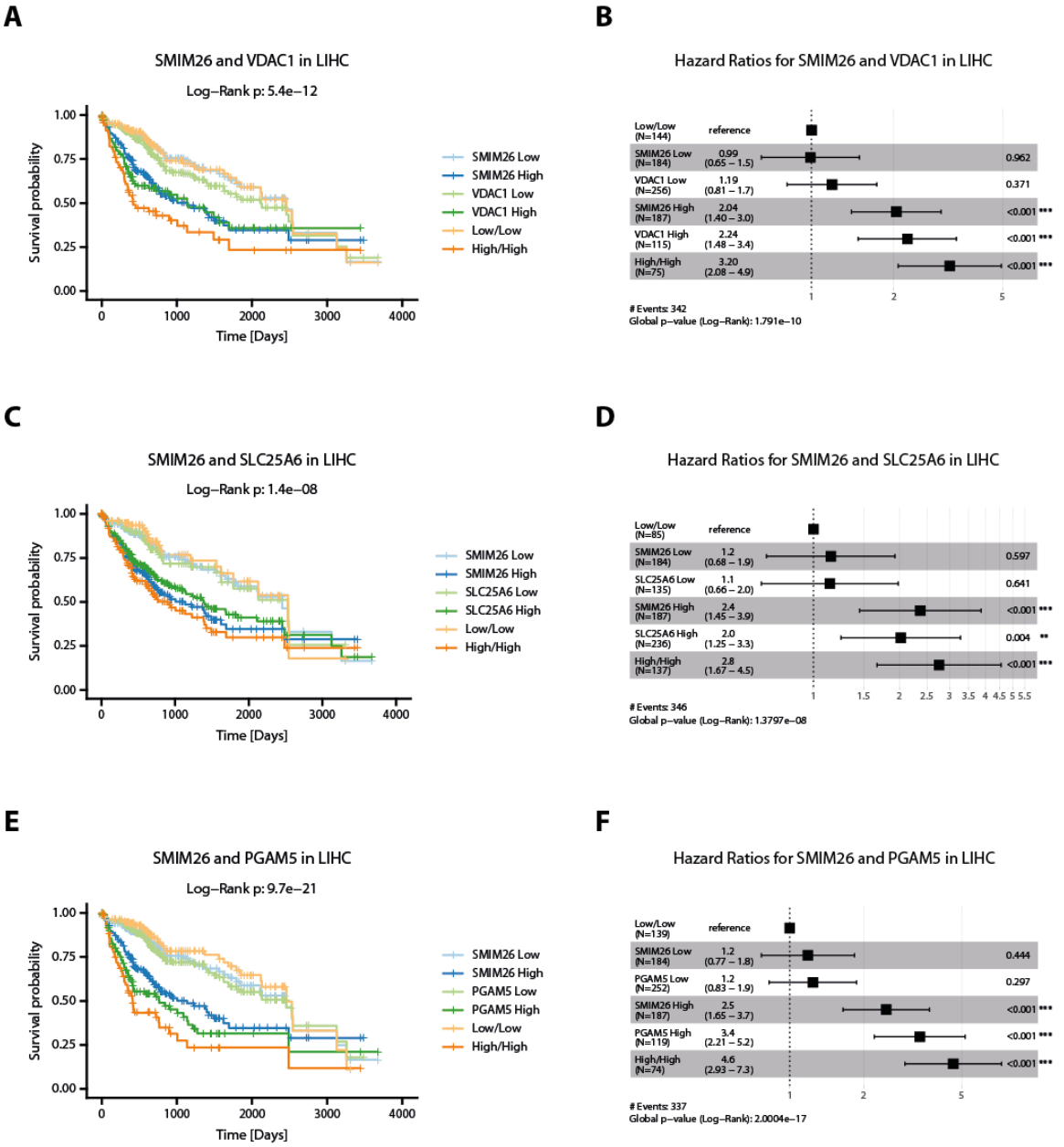

Figure 3-31: Survival analysis of SMIM26 co-expression with interactors in cancer patients. *Kaplan-Meier survival curves of patients stratified into low (light color) and high (dark color) expression groups for SMIM26 (blue), VDAC1, SLC25A6 or PGAM5 (all green). Additional groups (orange) include high (High/High) or low (Low/Low) expression for both SMIM26 and the respective interactor. Log-rank p-values indicate statistical significance for overall survival. (A) Kaplan-Meier survival curves for SMIM26 and VDAC1 co-expression in LIHC. (B) Cox proportional hazard ratios (HR) with corresponding p-values for SMIM26 and VDAC1 co-expression in LIHC. Low/Low group was used as reference. (C) Kaplan-Meier survival curves for SMIM26 and SLC25A6 co-expression in LIHC. (D) Cox proportional hazard ratios (HR) with corresponding p-values for SMIM26 and SLC25A6 co-expression in LIHC. Low/Low group was used as reference. (E) Kaplan-Meier survival curves for SMIM26 and PGAM5 co-expression in LIHC. (F) Cox proportional hazard ratios (HR) with corresponding p-values for SMIM26 and PGAM5 co-expression in LIHC. Low/Low group was used as reference.*

To sum up, our findings suggest that SMIM26 expression correlates with various hallmarks of cancer in colorectal tumors and that high expression of SMIM26 leads to poor survival prognosis in liver cancer. Additionally, co-expression with VDAC1 or PGAM5 enhances the mortality further.

3.10 Anti-cancer drug screen identifies SMIM26 as potential target

Our work showed that SMIM26 regulates mitochondrial metabolite transport and might be important for the progression and migration of cancer. As metabolic reprogramming is a common feature of cancer progression (Vasan et al., 2020; Du et al., 2025) and the SMIM26 binding partner VDAC1 and SLC25A6 have already been linked to this process in tumors (Heslop et al., 2021; Zhao et al., 2021), we hypothesized that SMIM26 could be a promising target for anti-cancer therapy.

Therefore, together with our collaborators Lukas Wöhrl and Christian Werno (Fraunhofer ITEM, Regensburg), we designed an anti-cancer drug screen using a Food and Drug Administration (FDA)-approved library of 313 bioactive compounds. To replicate high SMIM26 conditions, we generated stable SMIM26 overexpression (OE) cell lines and performed the drug screen with wild-type, SMIM26 knockout or overexpression HCT116 cells. In short, cells where incubated for 72 h with the compounds and viability was assessed using the ATPlite assay (Revvity, Waltham, USA) (**Figure 3-32A**). When comparing wild-type to SMIM26-deficient cells, we found some compounds that significantly altered viability, albeit most drugs showed no effect (**Figure 3-32B**). Interestingly, some identified candidates are known to target signaling pathways or membrane transport. When comparing wild-type to cells stably overexpressing SMIM26, only one compound significantly affected viability in the overexpression cell line (**Figure 3-32C**).

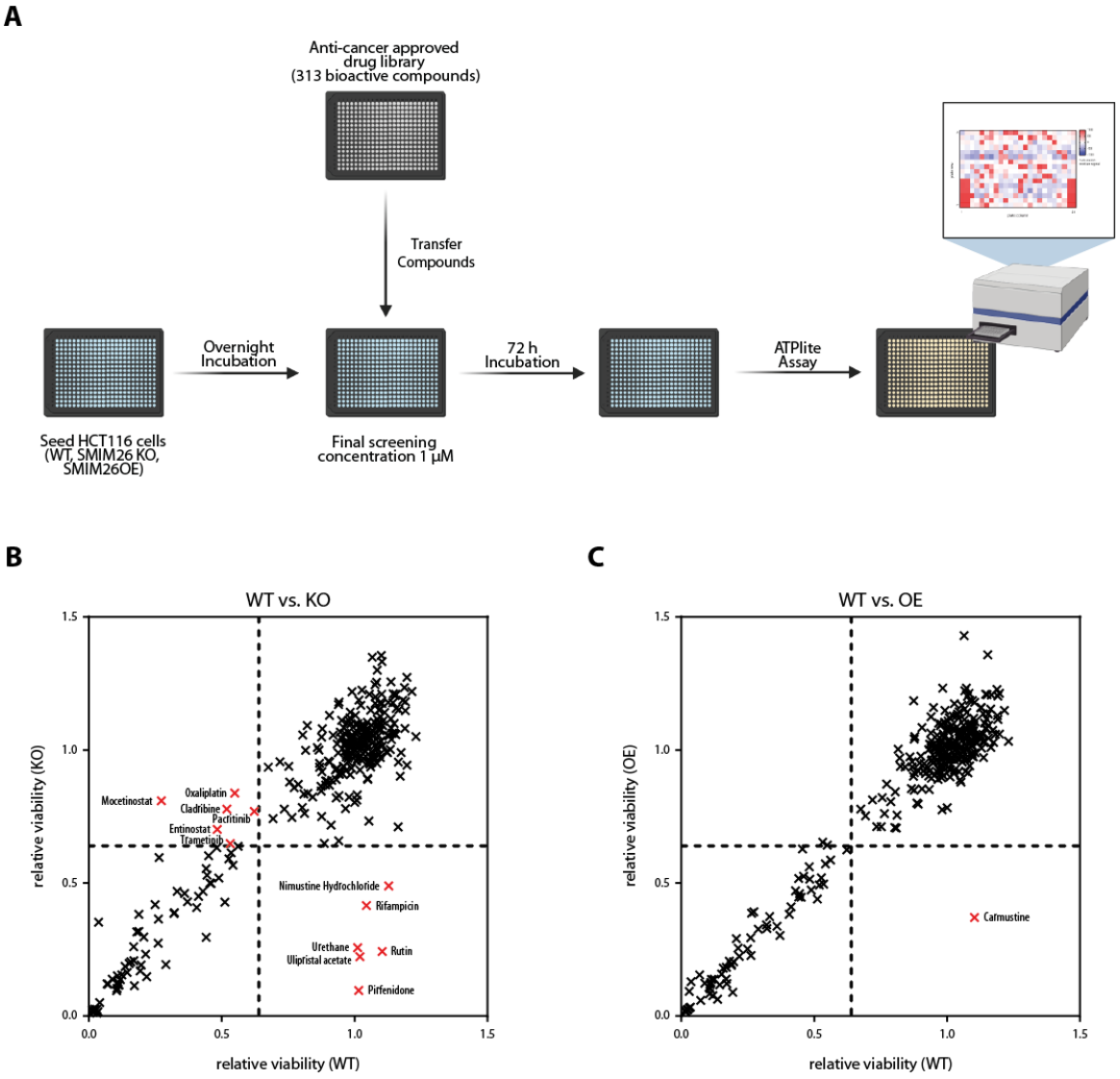

Figure 3-32: Anti-cancer drug screen in HCT116 cells
(A) Schematic of the anti-cancer drug screen workflow. HCT116 wild-type (WT), SMIM26 knockout (KO), and SMIM26 overexpression (OE) cells were seeded and treated with a library of 313 FDA-approved anticancer compounds (final concentration 1 µM). After 72 h of incubation, cell viability was assessed using an ATPlite assay. (B) Scatter plot comparing relative viability of KO versus WT cells after compound treatment. Selected compounds with differential effects are highlighted in red. (C) Scatter plot comparing relative viability of OE versus WT cells after compound treatment. Selected compounds with differential effects are highlighted in red.

To validate the effective compounds identified in the screen we performed dose response experiments comparing the effect of each drug on wild-type, SMIM26-deficient and SMIM26-overexpressing HCT116 cells in a concentration range of 1 nM to 25 µM. Most compounds including Entinostat, Mocetinostat or Oxaliplatin were confirmed as false-positive hits in the screen showing no difference between wild-type and mutant cell lines throughout the concentration gradient (**Figure 3-33A-C**). However, we were able to validate some candidates. Consistent with results in the

screen, the purine nucleoside analogue Cladribine showed weaker effects on viability of *SMIM26* knockout compared to wild-type cells (**Figure 3-33D**). Interestingly, the kinase inhibitors Pacritinib and Trametinib displayed the opposite effect. While viability of wild-type and mutant cells upon treatment with Pacritinib was almost identical at lower to medium concentrations, the maximum effect (E_{max}) was stronger for SMIM26-deficient cells when compared to wild-type (**Figure 3-33E**). On the other hand, treatment with Trametinib showed an overall stronger effect on viability in knockout cells (**Figure 3-33F**).

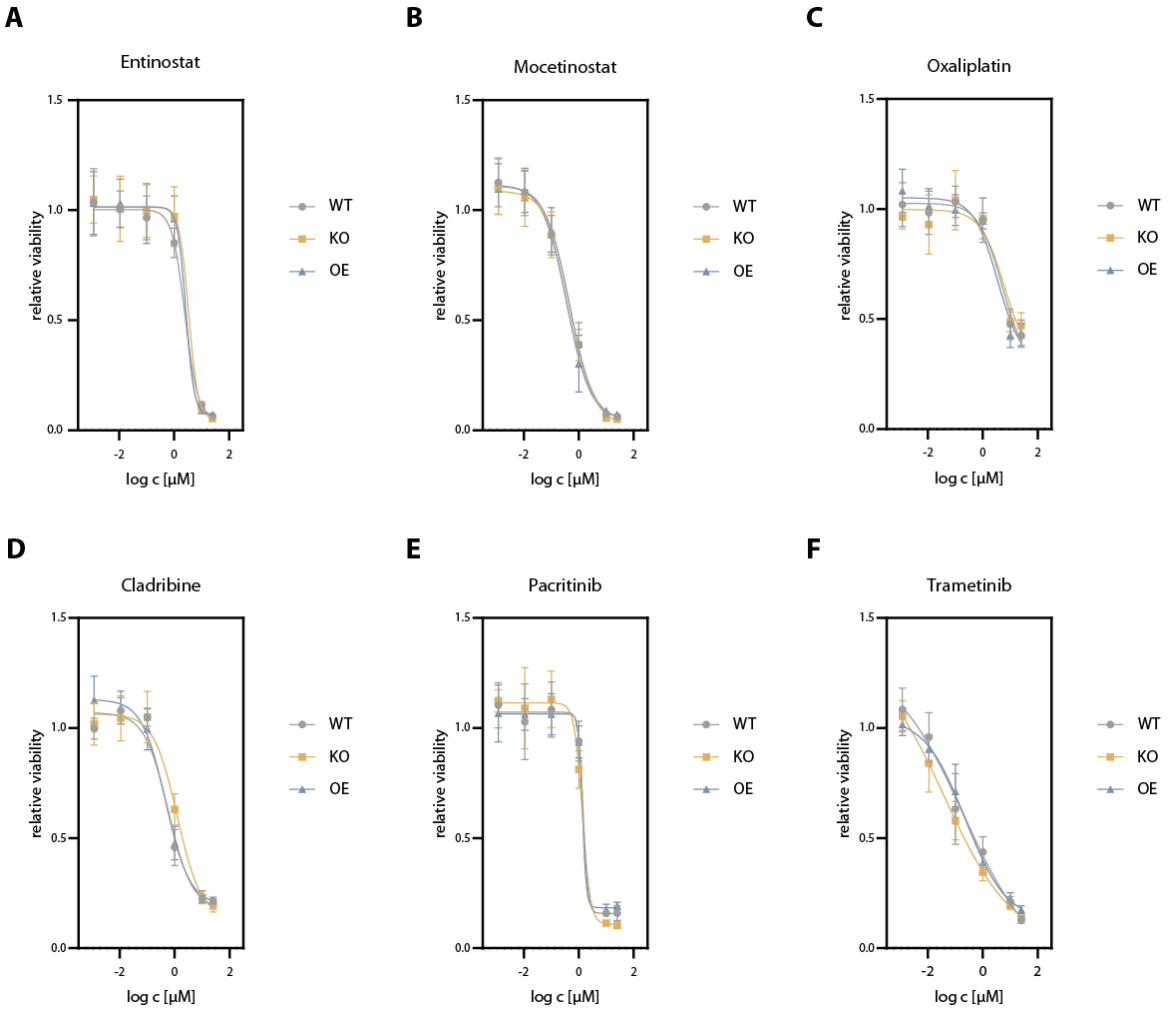

Figure 3-33: Validation of drug sensitivity in SMIM26-modified HCT116 cells
Dose–response curves of selected compounds identified in the drug screen were observed in wild-type (WT, grey), SMIM26 knockout (KO, yellow), and SMIM26 overexpression (OE, blue) HCT116 cells. Cell viability was measured after 72 h of treatment with increasing drug concentrations using the ATPlite assay. Shown are representative curves for (A) Entinostat, (B) Mocetinostat, (C) Oxaliplatin, (D) Cladribine, (E) Pacritinib, and (F) Trametinib. Data represent mean ± SD.

Overall, we could identify a small subset of bioactive compounds that affect cell survival differentially in a SMIM26-dependent manner. Expanding the screen to a larger anticancer drug library may help identify additional candidates for potential combinatorial therapies in the future.

4 Discussion

4.1 LINC00493 encodes for the mitochondrial microprotein SMIM26

LncRNAs have long been recognized to harbor sORFs and encode microproteins. Here, we identified and functionally characterized the LINC00493-encoded microprotein SMIM26 (**Figure 3-1, Figure 3-2**). Although LINC00493 was initially annotated as lncRNA, its short transcript length and common features of mRNAs, including a 5' m^7G cap and poly-(A)-tail, now support its classification as a protein-coding gene. Nevertheless, a recent study proposed non-coding functions of LINC00493 (Konina et al., 2021), albeit the underlying molecular mechanism remains unclear.

Using immunofluorescence co-staining and biochemical fractionation, we demonstrated by two orthogonal approaches that SMIM26 localizes to mitochondria (**Figure 3-3**). These findings are consistent with recent reports from other groups (Yeasmin et al., 2021; Meng et al., 2023; Nah et al., 2025). In our microscopy experiment, SMIM26 showed overlap with both the outer mitochondrial membrane marker TOMM20 and the inner mitochondrial membrane marker TIMM44. Due to technical limitations, an unambiguous assignment to a specific mitochondrial membrane was not possible. However, proteinase K treatment of mitochondrial fractions revealed that the C-terminus of SMIM26 is not exposed to the cytoplasm, suggesting that this region extends into the intermembrane space.

To validate the predicted N-terminal transmembrane α-helix, we performed membrane extraction assays, confirming that SMIM26 is an integral single-pass membrane protein (**Figure 3-4**). Interestingly, even treatment with the strong detergent Triton X-100 only partially solubilized SMIM26, indicating a strong membrane anchoring. This may reflect its short sequence and high abundance of nonpolar residues, which could promote aggregation upon extraction. Alternatively, SMIM26 could be embedded within a large transmembrane complex that prevents efficient solubilization.

Elucidating the localization of SMIM26 is an important step towards understanding its cellular functions. Proteins residing in the outer mitochondrial membrane are typically involved in processes such as mitophagy, apoptosis, cellular signaling or crosstalk with other organelles (Giacomello et al., 2020; Xian and Liou, 2021), whereas inner mitochondrial membrane proteins contribute to energy production or the transport of specific metabolites (Giacomello et al., 2020).

Although these biochemical approaches could not provide prove of its precise topology within the mitochondrial membrane systems, performed high-resolution studies indicate an outer-membrane localization (**4.2**). Additionally, protease protection assays or gradient sedimentation will be essential to define the exact sublocalization and topology of SMIM26 in the future.

4.2 SMIM26 interactions at the inner mitochondrial membrane are defined by its association with VDAC1

We employed a broad spectrum of biochemical, biophysical and genetic approaches to assess the interaction network and thereby the function of SMIM26. Using immunoprecipitation followed by mass spectrometry analysis, we identified and validated the promiscuous metabolite channel VDAC1 and the ADP/ATP antiporter SLC25A6 as binding partners (**Figure 3-5**, **Figure 3-6**). *In vitro* crosslinking mass spectrometry further confirmed the interaction of SMIM26 with VDAC1 (**Figure 3-10**), whereas no crosslinks to SLC25A6 were detected. However, this does not exclude a possible interaction as our crosslinking experiments were neither quantitative nor comprehensive. Furthermore, suitable residues for crosslinking may not be available at the interaction interface.

To improve the sensitivity of crosslinking experiments, alternative detergents or proteinases could be used during sample preparation. Moreover, the used crosslinker BS3 is a water-soluble molecule and therefore does not pass through lipid bilayers. Even though studies have shown that crosslinks at the inner mitochondrial membrane can still be observed from purified mitochondria since the outer mitochondrial membrane is partially disrupted (Linden et al., 2020), it is likely that BS3 crosslinks occur less efficiently at the inner mitochondrial membrane.

Alternatively, membrane-permeable crosslinkers like disuccinimidyl suberate (DSS) could be used instead of BS3 and immunoprecipitation of SMIM26-containing complexes prior to crosslinking may enhance recovery of low-abundance interactions and interaction sites with restrained access to suitable residues.

VDAC1 is a multifunctional channel in the outer mitochondrial membrane. It mediates metabolite, nucleotide and calcium exchange between the cytoplasm and mitochondria, thereby influencing energy production, metabolic flux and ER-mitochondria communication. During apoptosis, VDAC1 oligomerizes to form hydrophilic pores releasing apoptogenic proteins such as cytochrome c or AIF (Shoshan-Barmatz et al., 2020). SLC25A6 is a member of the SLC25 family, the largest solute transport family in humans. These solute carriers facilitate the exchange of amino acids, nucleotides, cofactors, ions, and other metabolites across the inner mitochondrial membrane. As one of four adenine nucleotide translocases, it exports synthesized ATP from the mitochondrial matrix into the intermembrane space in exchange for ADP (Ruprecht and Kunji, 2020).

To evaluate the interaction with VDAC1 and SLC25A6 in more detail and to investigate the mitochondrial sublocalization of SMIM26, we performed interaction studies with truncated variants of SMIM26. Loss of the C-terminal region markedly reduced binding to SLC25A6 while VDAC1 was unaffected (**Figure 3-10**), suggesting that SMIM26 resides in the outer mitochondrial membrane, with its C-terminus extending into the intermembrane space to interact with SLC25A6. Super-resolution microscopy single-molecule tracking supported this hypothesis. SMIM26 exhibited two distinct mobility states. Longer distance movements were consistent with diffusion in the outer mitochondrial membrane. Interestingly, short-distance jumps were significantly reduced upon knockdown of SLC25A6, indicating that short-range movements likely reflect transient interaction with proteins embedded in the inner mitochondrial membrane, (**Figure 3-11**, **Figure 3-12, Figure 3-13**). These different movement patterns align with the distinct topologies and protein densities of the mitochondrial two membrane system. While the outer membrane allows a relatively free two-dimensional diffusion, the inner mitochondrial membrane forms cristae structures stabilized by the MICOS (mitochondrial contact site and cristae organizing system) complex (Khosravi and Harner, 2020). Moreover, the inner mitochondrial

membrane contains other densely packed complexes such as the respiratory chain, significantly restricting the movement of embedded proteins. Integrating biochemical interaction data with high resolution imaging enabled us to capture these transient interactions of SMIM26 within the dual membrane architecture of mitochondria.

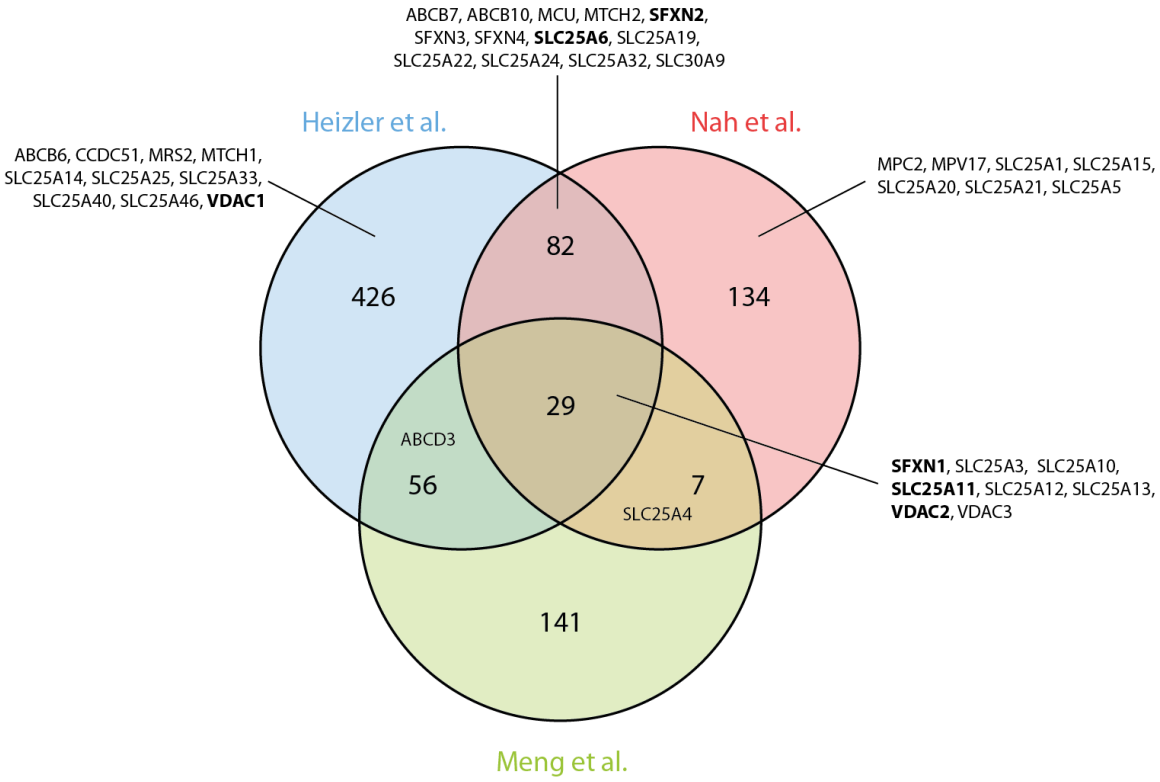

Figure 4-1: Comparison of the SMIM26 interactome from different studies
Venn diagram of >2-fold enriched proteins identified in SMIM26-FLAG IP-MS in this study (Heizler et al, blue), Nah et al. (2025) (red) and Meng et al. (2023) (green). Interactors assigned to ion or metabolite transport by MitoCarta3.0 (Rath et al., 2021) and validated in either of the three studies are highlighted.

Interestingly, other studies have reported that SMIM26 can associate to different carrier proteins in the inner mitochondrial membrane. Meng et al. (2023) described an interaction with the glutathione transporter SLC25A11 (Solute carrier family 25 member 11), while Nah et al. (2025) identified SMIM26 binding to the serine transporters SFXN1/2 (sideroflexin 1/2). Consistent with these findings, our crosslinking and co-immunoprecipitation analyses revealed interactions not only with the above-mentioned transporters but also with additional carrier proteins in the inner mitochondrial membrane (**Figure 4-1**). These observations are not necessarily contradictory, as many mitochondrial carriers are structurally similar and may provide overlapping interaction surfaces. However, the pronounced shift in

SMIM26 mobility upon SLC25A6 knockdown suggests that the interaction with this nucleotide carrier is of particular functional relevance for SMIM26.

Taken together, our findings propose a unifying model in which SMIM26 associates with VDAC1 in the outer mitochondrial membrane and transiently interacts with various metabolite transporters in the inner mitochondrial membrane, thereby bringing the two transport systems into closer proximity to facilitate more efficient metabolite exchange between the cytosol and the mitochondrial matrix (**Figure 4-2**).

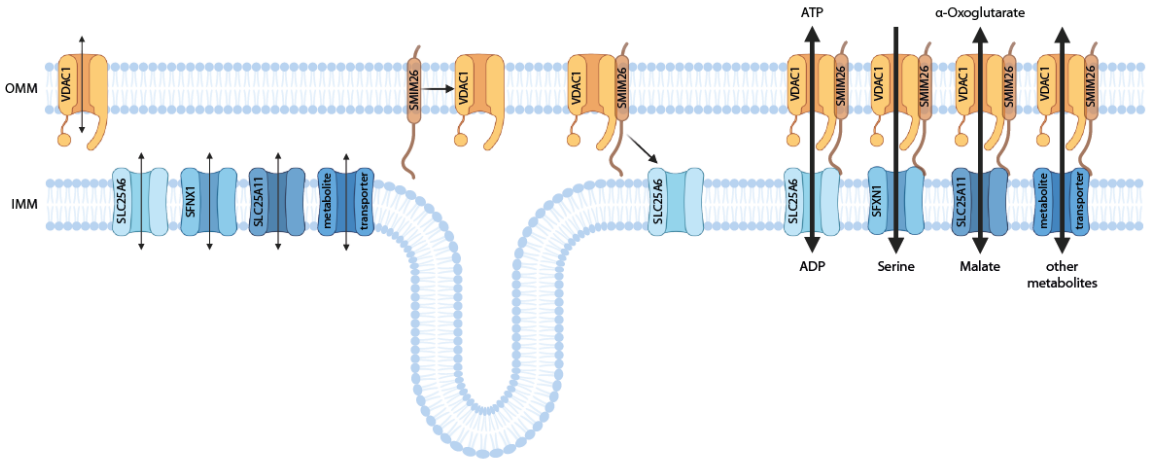

Figure 4-2: SMIM26 coordinates metabolite transport through the outer and inner mitochondrial membranes
Schematic overview of SMIM26-coordinated metabolite transport by VDAC1 through the outer and SLC25A6 as well as other solute carriers and/or transporter (e.g. SLC25A11, SFXN1, etc.) through the inner mitochondrial membrane. OMM: outer mitochondrial membrane; IMM: inner mitochondrial membrane.

However, this model needs to be further investigated to assess the influence of other inner mitochondrial membrane carrier proteins on the mobility of SMIM26 and identify the physiological stimuli and regulatory mechanisms that govern the specificity and dynamics of these interactions.

4.3 Phosphorylation of SMIM26 indicates putative role in signaling

Using complementary biochemical approaches including mass spectrometry, in vivo crosslinking and co-immunoprecipitation, we identified and validated the serine/threonine phosphatase PGAM5 as interaction partner of SMIM26 (**Figure 3-5**, **Figure 3-6**). Notably, we detected phosphorylated serine residues (S46, S48, S52) in close proximity to the identified PGAM5 crosslinks and observed a moderate increase in phosphorylation upon PGAM5 knockdown using SRM mass spectrometry analysis (**Figure 3-8**, **Figure 3-9**).

PGAM5 is a serine/threonine phosphatase with multiple targets that plays an important role in mitochondrial quality control. It regulates mitochondrial dynamics by activating DRP1 and stabilizing MFN2 (Mitofusin-2) via dephosphorylation (He et al., 2025). Additionally, PGAM5 controls both receptor-mediated mitophagy by dephosphorylation of the mitophagy receptor FUNDC1 (FUN14 domain-containing protein 1) (Chen et al., 2014) and PINK1-Parkin-mediated mitophagy through its interaction with DRP1 (Qi et al., 2025). Beyond mitochondrial dynamics and mitophagy, PGAM5 regulates several programmed cell death pathways, including apoptosis, necroptosis, pyroptosis and oxeiptosis (Qi et al., 2025). Although PGAM5 has not been directly implicated in metabolite transport across mitochondrial membranes, this phosphatase has been linked to metabolic stress in mice (Sekine et al., 2016).

Our findings suggest that SMIM26 may be regulated by cellular signaling pathways, potentially modulating its protein-protein interactions upon specific stimuli. This mechanism may be complemented by additional phosphosites within the C-terminal region of SMIM26, which contains several serine, threonine and tyrosine residues (**Figure 3-8**). Although we detected phosphorylation under optimal growth conditions only at S46, S48 and S52, these additional residues may be modified in response to metabolic stimuli or cellular stress. Similar regulatory mechanisms have been described for other microproteins. For instance, Phospholemman (PLM) acts as a regulator of the Na^+/K^+ ATPase (NKA) and Na^+/Ca^{2+} exchanger (NCX) in the plasma membrane. Dephosphorylated PLM inhibits NKA under physiological conditions. During stress, PLM is phosphorylated, dissociates from NKA and inhibits NCX instead

(Ahlers et al., 2005; Wang et al., 2006; Cheung et al., 2013). This example illustrates how phosphorylation can dynamically finetune microprotein interactions in response to stress. Alternatively, through its interaction with VDAC1, phosphorylation of SMIM26 could influence apoptosis or mitophagy However, this hypothesis requires further investigation.

Although our data provide initial evidence that SMIM26 may be regulated by phosphorylation, these findings remain preliminary and require further validation. For instance, the detected phosphorylation level of approximately 0.04% is relatively low. However, SMIM26 was overexpressed to obtain sufficient material for mass spectrometry. Repeating the experiment under endogenous SMIM26 expression levels may reflect phosphorylation dynamics better, particularly since SMIM26 and its kinase or phosphatase would be present at physiological ratios. A key future step will be the identification of the responsible kinase modifying SMIM26 and the cellular stimuli that trigger phosphorylation or dephosphorylation of SMIM26. To mechanistically validate the interaction with PGAM5, i*n vitro* dephosphorylation assays would be informative. However, such experiments may be technically challenging due to the complex mitochondrial two membrane architecture.

Ultimately, together with the interaction of SMIM26 with VDAC1 and SLC25A6 our findings support a model in which SMIM26 links mitochondrial metabolite transport with cellular signaling pathways through phosphorylation within its C-terminal region, albeit the exact mechanism of this regulation remains to be investigated.

4.4 Effects of SMIM26 knockout *in vivo*

To characterize the function of SMIM26 *in vivo*, we utilized knockout strategies in human cell lines and animal models. These knockout models were generated by CRISPR genome editing and subsequently validated. Since biochemical characterization provided evidence for a mitochondrial localization of SMIM26, we focused on mitochondrial functions in our phenotypical characterization.

4.4.1 SMIM26 knockout impairs mitochondrial functions

To study the function of SMIM26 in human cells, we generated SMIM26 knockout cell lines from HCT116 cells (**Figure 3-14**). As LINC00493 was initially identified in a colorectal cancer xenograft model (**Figure 3-1**), we focused our screening for cell lines with high SMIM26 expression primarily on colorectal cancer cell lines.

Based on the previously described localization and interaction studies (**4.1**, **4.2**, **4.3**), we examined the effect SMIM26 knockout on mitochondrial physiology. Loss of SMIM26 significantly reduced respiratory activity in HCT116 cells (**Figure 3-15**). The phenotype was rescued upon reintroduction of full-length SMIM26-FH but not by a C-terminally truncated SMIM26 variant (**Figure 3-16**). Furthermore, SMIM26 knockout decreased the NAD^+/NADH ratio (**Figure 3-17**), moderately impaired proliferation under optimal culture conditions and caused pronounced growth defects upon glucose starvation (**Figure 3-18**). An orthogonal viability assay under glucose deprivation confirmed reduced cell survival upon SMIM26 knockdown (**Figure 3-19**). In contrast, knockout of SMIM26 did not affect mitochondrial membrane potential or intracellular calcium levels.

Although the unaffected membrane potential and calcium homeostasis may seem surprising given the impaired respiratory activity in cells lacking SMIM26, these results are consistent with a defect in metabolite and nucleotide exchange rather than a global disruption of mitochondrial activity. Indeed, the mitochondrial membrane potential can be buffered even when the respiratory chain activity is impaired (Zorova et al., 2018). Likewise, calcium transport is mainly controlled by the Mitochondrial calcium uniporter (MCU) complex (Chaudhuri et al., 2013; Stefani et al., 2015), which was not found to depend on interaction with SMIM26.

All in all, the knockout phenotypes in HCT116 cells point towards a defect in mitochondrial energy metabolism. These results are consistent with previous studies reporting increased oxidative phosphorylation upon SMIM26 overexpression in renal cell adeno-carcinoma cells (Meng et al., 2023). Moreover, our data support a model where SMIM26 interacts with SLC25A6 via its C-terminal domain to facilitate an efficient ADP/ATP exchange across the mitochondrial membranes. Loss of this interaction site in SMIM26ΔC-FH prevents full restoration of respiratory activity. This

observation can be explained by an accumulation of ATP and depletion of ADP in the mitochondrial matrix due to the inefficient ADP/ATP transport. As a result, ATP synthase activity is reduced, and less protons are pumped from the intermembrane space into the mitochondrial matrix. The increased proton motive force acts as a negative feedback loop to reduce ETC activity (Hüttemann et al., 2012), which is reflected by the reduced NAD^+ regeneration in SMIM26 knockout cells. Interestingly, Luengo et al. (2021) demonstrated that when the cellular demand for NAD^+ exceeds the need for ATP in cells, aerobic glycolysis is promoted. This observation aligns with our starvation experiments and an increased lactate production in SMIM26 knockout cells (data not shown).

Although additional experiments where beyond the scope of this study, several approaches could further verify this model. First, ADP/ATP transport rates in wild-type, knockout and rescue cell lines could be measured by patch clamp, as described by Bertholet et al. (2022). Second, glycolytic activity could be quantified using a Seahorse XF Glycolysis Stress Test Kit (Agilent, Santa Clara, USA) similar to our respirometry assay. Finally, in-depth metabolomics analysis of secreted and intracellular metabolites may reveal broader effects of SMIM26 knockout on cellular metabolism.

Overall, these results suggest SMIM26 as a regulator of mitochondrial nucleotide exchange and energy production.

4.4.2 SMIM26 knockout displays drastic early development phenotype *in vivo*

Building on our findings in human cell lines and the high conservation of SMIM26 (**Figure 3-21**), we next studied the consequences of SMIM26 knockout in mouse and zebrafish. We found that homozygous SMIM26 knockout mice exhibit early embryonic lethality while heterozygous and wild-type siblings were born at Mendelian ratios. Embryos die between stage E8.5 and E9.5 in our model, preventing in depth molecular characterization (**Figure 3-22**). This observation is consistent with a recent report (Nah et al., 2025), although lethality occurred slightly later in that study, between E9.5 and E10.5. This discrepancy may be explained by subtle differences in the genetic C57BL/6 backgrounds used in these two studies. Given the high energetic and biosynthetic demands during early embryogenesis, efficient

metabolite exchange and tightly regulated mitochondrial functions are likely essential. Thus, impaired coordination and regulation of these processes in the absence of SMIM26 could induce the lethal phenotype. To nevertheless gain molecular insight into the organistic mechanisms of SMIM26 during development and in adult mice, conditional knockout models or embryonic SMIM26 knockout stem cells would be valuable tools.

To further explore the developmental and physiological roles of SMIM26 in a vertebrate system, we generated *smim26* knockout zebrafish (**Figure 3-23**). Survival of homozygous mutants was severely compromised compared to their heterozygous and wild-type siblings (**Figure 3-24**). Such a phenotype can often be explained by an inferior ability to compete for food due to reduced fitness in knockout fish. However, even when separated, homozygous knockout mutants displayed growth retardation during larval and early juvenile stages and were unable to develop a female germline in adults (**Figure 3-24**). This observation suggests a sex reversal in knockout fish, potentially driven by impaired oocyte development during juvenile stages. Apoptosis could be caused by impaired metabolite transport, energy supply and metabolic pathways upon loss of *smim26* in oocytes. Similar starvation-induced female-to-male sex reversals have already been described in zebrafish (Jiang et al., 2019). Investigating such a potential oocyte-specific phenotype further, for example by assessing apoptosis in larvae or by modulating nutrient availability during larvae development, would be an exciting avenue for future work.

Consistent with our work in human cell lines, homozygous mutant fish exhibited reduced OXPHOS activity (**Figure 3-25**), accompanied by reduced levels of respiratory chain complex I subunits, particularly those within the N and Q module (**Figure 3-26**). Generally, complex I comprises three functional units: the electron input N- (NADH-binding) module containing redox-active cofactors and iron-sulfur clusters, the electron output Q- (quinone-binding) module delivering electrons to ubiquinone and the proton translocation P-module which pumps protons across the inner membrane into the intermembrane space (Lazarou et al., 2009; Sharma et al., 2009). In contrast to recent studies (Nah et al., 2025), our data did not provide evidence for direct interactions of complex I components with SMIM26. Therefore, the downregulation of complex I likely reflects an indirect consequence of perturbed

mitochondrial metabolite homeostasis. Intriguingly, studies have shown that the N-module undergoes higher turnover rates compared to the other modules (Szczepanowska et al., 2020), providing a potential mechanism to selectively reduce electron transfer chain activity upon accumulation of ATP in the matrix. Testing this hypothesis in context with SMIM26 will be an important question for future studies.

Recent publications reported that SMIM26 interacts with the mitochondrial transporter SFXN1 (Nah et al., 2025), which is involved in one-carbon metabolism and crucial for S-adenosylmethionine (SAM) production. Strikingly, gradual decline in mitochondrial SAM has been linked to destabilization of iron-sulfur clusters and compromised complex I function (Rosenberger et al., 2021). It will be important to identify, which SMIM26-related metabolite transport pathway is ultimately responsible for the downregulation of complex I or whether they act synergistically. Therefore, approaches such as blue native PAGE or targeted metabolomics could provide mechanistic clarity.

In summary, our work identified SMIM26 as a key regulator of mitochondrial metabolite flux and respiratory chain function not only in human cell lines but also *in vivo*. Loss of SMIM26 leads to severe physiological consequences, establishing SMIM26 as an essential component of mitochondrial homeostasis.

4.5 Elucidating the role of SMIM26 for cancer development and progression

In two recent studies, SMIM26 has been linked to renal cancer (Meng et al., 2023) and AML (Nah et al., 2025). Although we did not observe such correlation in publicly available mRNA expression databases, our analyses revealed elevated SMIM26 expression levels in several cancers within the gastrointestinal tract (**Figure 3-29**). Moreover, we found that high SMIM26 expression correlated with poor prognosis in LIHC patients (**Figure 3-30**). Notably, co-expression with VDAC1 or PGAM5 further enhanced the poor survival outcome (**Figure 3-31**). These findings contradict reports describing a favorable survival correlating to SMIM26 expression in renal cancer (Meng et al., 2023), suggesting that the functional impact of SMIM26 is context-dependent. However, our data suggest that SMIM26 provides an advantage in fast

proliferative cancer cells which require an efficient metabolite flux across mitochondrial membranes to meet there high metabolic demands. The validated interactors of SMIM26 and their role in cancer biology support this hypothesis. PGAM5 stimulates NADPH synthesis and enhances proliferation in CRC and LIHC (Zhu et al., 2020b; Fu et al., 2023), while VDAC1 regulates aerobic glycolysis, mitochondrial membrane potential, ROS production and mitophagy in cancer cells to enable tumor immune escape and metabolic adaption. Nevertheless, its function can be tumor suppressive depending on the interactome of VDAC1 (Huang et al., 2025). The observed poor outcome in patients with high SMIM26 and VDAC1 implies that SMIM26 shifts VDAC1 towards oncogenic functions in LIHC.

Transcriptomic profiling of SMIM26 knockout HCT116 cells revealed a moderate gene set enrichment of important cancer-related signaling pathways, including PI3K/Akt, Wnt/ß-catenin, p53 and the mesodermal commitment (**Figure 3-27**). These results are in line with patient-derived datasets, showing an enrichment of these pathways in cohorts with low SMIM26 expression (**Figure 3-28**). Overall, these observations likely reflect a response to metabolic stress, promoting aerobic glycolysis to maintain a high proliferation rate and induce pro-survival programs (Vallée et al., 2021; Barzegar Behrooz et al., 2022). SMIM26-deficient HCT116 cells displayed a reduced OXPHOS activity and higher sensitivity to glucose starvation (**Figure 3-15**, **Figure 3-18**, **Figure 3-19**), supporting a mechanistic link between SMIM26-mediated metabolite flux and cellular adaptation.

Our transcriptomics results, albeit being consistent with patient data, show only modest expression changes. However, cancer cell lines grown under optimal conditions might not fully resemble the *in vivo* state in patients with low SMIM26 expression. Inducing hypoxia or metabolic stress by nutrient deprivation or growing tumor spheroids could better recapitulate the changes observed in tumors.

SMIM26 phosphorylation within the C-terminus suggests that cancer-associated signaling may modulate its function. A similar process has been proposed for the microprotein Alt-RPL36 that transports phosphatidylinositol from the ER to the cytosol and acts as an upstream regulator of PI3K/Akt/mTOR signaling (Cao et al., 2021). Given that many signaling cascades influence metabolite flux, OXPHOS activity

and other mitochondrial functions, we reasoned that SMIM26 could be a promising target for anti-cancer strategy. To explore this, we screened the effect of 313 FDA-approved anti-cancer drugs on HCT116 wild-type, SMIM26 knockout and overexpression cells and identified two kinase inhibitors, Pacritinib and Trametinib, that selectively impaired viability in SMIM26-deficient cells (**Figure 3-32**, **Figure 3-33**).

Pacritinib, was initially approved to treat myelofibrosis and graft-versus-host disease. It targets JAK2 (Janus kinase 2) and IRAK1 (Interleukin-1 receptor associated kinase 1) and thereby inhibits oncogenic STAT5 (Signal transducer and activator of transcription 5) signaling (Lamb, 2022). Other studies found that Pacritinib effectively reduces glycolysis and consequently enhanced sensitivity to 5-fluorouracil chemotherapy in CRC (Xin et al., 2025). Similarly, the MEK (mitogen-activated protein kinase kinase) inhibitor Trametinib is used to treat CRC patients with BRAF (B-raf proto-oncogene, serine/threonine kinase) or KRAS (Kirsten rat sarcoma viral oncogene homolog) mutations, which commonly occur in many cancers to promote proliferation and immune escape. (Ghosh et al., 2024). Both compounds target mitochondria-related pathways and showed higher efficiency when combined with additional drugs. Therefore, treatment with Pacritinib or Trametinib upon SMIM26 knockdown could be a promising therapeutic strategy as loss of SMIM26 causes a downregulation of OXPHOS and an increased dependence on glycolysis in CRC cell lines, metabolic processes which are being targeted by these two compounds.

Nevertheless, the compounds in our screen showed only moderate effects on viability when comparing SMIM26 knockout to wild-type cell lines grown under optimal oxygen and nutrient condition. These conditions, however, do not fully resemble solid tumors *in vivo*. Therefore, screening under hypoxic or metabolic stress or in tumor spheroids may reveal more severe discrepancies. Additionally, libraries containing more compounds could be used in future experiments.

In summary, our data indicate that SMIM26 contributes to cancer cell fitness by regulating metabolite flux and maintaining OXPHOS activity. Low SMIM26 expression in tumors reshapes cancer-associated signaling pathways, which makes SMIM26 an interesting therapeutic target for future studies.

5 Material and Methods

5.1 Materials

5.1.1 Enzymes, Antibodies and Kits

The following enzymes, antibodies and kits were used for the experiments in this work. For the used enzymes appropriate buffers were purchased from the same company. Experiments were performed according to the manufacturer's protocol.

Table 5-1: List of enzymes

Enzyme	Company
Alt-R™ S.p. Cas9 Nuclease V3	Integrated DNA Technologies, Coralville, USA
Dnase I	Thermo Fisher Scientific, Waltham, USA
M-MuLV reverse transcriptase	Thermo Fisher Scientific, Waltham, USA
Phusion High-Fidelity DNA Polymerase	Thermo Fisher Scientific, Waltham, USA
Proteinase K	Thermo Fisher Scientific, Waltham, USA
T4 DNA Ligase	Thermo Fisher Scientific, Waltham, USA
T4 DNA Polymerase	Thermo Fisher Scientific, Waltham, USA
T4 Polynucleotide Kinase (PNK)	Thermo Fisher Scientific, Waltham, USA
Trypsin	Sigma-Aldrich, Steinheim, Germany
Trypsin Gold	Promega, Madison, USA
Restriction enzyme	
AscI	New England Biolabs, Ipswich, USA
AgeI	Thermo Fisher Scientific, Waltham, USA
BbsI	Thermo Fisher Scientific, Waltham, USA
DpnI	Thermo Fisher Scientific, Waltham, USA
EcoRI	Thermo Fisher Scientific, Waltham, USA
FseI	New England Biolabs, Ipswich, USA
SpeI	Thermo Fisher Scientific, Waltham, USA
XbaI	Thermo Fisher Scientific, Waltham, USA

Table 5-2: List of antibodies

Antibody	Origin	Purpose	Dilution	Company
Primary antibodies				
α-FLAG	Rabbit	Western Blot	1:1000	Sigma-Aldrich, St. Louis, USA
α-FLAG M2	Mouse	Western Blot, IF	1:1000, 1:500	Sigma-Aldrich, St. Louis, USA
α-GAPDH	Mouse	Western Blot	1:1000	GeneTex, Irvine, USA
α-HA.11 (16B12)	Mouse	Western Blot	1:1000	Covance, Princeton, USA
α-p54 [nrb] (NONO)	Mouse	Western Blot	1:1000	BD Transduction Laboratories, Franklin Lakes, USA
α-TOMM20	Rabbit	Western Blot, IF	1:500, 1:50	Santa Cruz Biotechnologies, Dallas, Texas
α-TIMM44	Rabbit	Western Blot, IF	1:2000, 1:500	Proteintech, Rosemont, USA
Secondary antibodies				
α-mouse IgG (H+L) IRDye 800CW	Goat	Western Blot	1:15,000	LI-COR Bioscience, Lincoln, USA
α-rabbit IgG (H+L) IRDye 800CW	Goat	Western Blot	1:15,000	LI-COR Bioscience, Lincoln, USA
α-rabbit IgG (H+L) IRDye 680RD	Goat	Western Blot	1:15,000	LI-COR Bioscience, Lincoln, USA
α-mouse Alexa Fluor 488	Goat	IF	1:400	Invitrogen, Carlsbad, USA
α-mouse Alexa Fluor 594	Goat	IF	1:400	Invitrogen, Waltham, USA

Table 5-3: List of commercial kits

Kit	Company
AnyDeplete®	Tecan Group AG, Männedorf, Switzerland
ATPlite	Revvity, Waltham, USA
MiSeq reagent Kit V2	Illumina, San Diego, USA
NextSeq 2000 P3 Reagents	Illumina, San Diego, USA
NucleoBond Xtra Midi EF, Midi kit	Macherey-Nagel, Düren, Germany
NucleoSpin Gel and PCR Clean-up kit	Macherey-Nagel, Düren, Germany
NucleoSpin Mini Plasmid, Mini kit	Macherey-Nagel, Düren, Germany
NucleoSpin RNA, Mini kit for RNA purification	Macherey-Nagel, Düren, Germany
NuPAGE 4-12% Bis-Tris protein gels	Invitrogen, Carlsbad, USA
Ovation SoLo RNA-Seq library preparation kit	Tecan Group AG, Männedorf, Switzerland
Phusion® High-Fidelity DNA Polymerase	New England Biolabs, Ipswich, USA
Pierce™ 660nm Protein Assay Kit	Thermo Fisher Scientific, Waltham, USA
RevertAid first-strand cDNA synthesis kit	Thermo Fisher Scientific, Waltham, USA
RotiR®Quant 5x Concentrate	Carl ROTH, Karlsruhe, Germany
Takyon™ No ROX SYBR 2x MasterMix blue dTTP	Eurogentec, Seraing, Belgium
XFp Cell Mito Stress Test Kit	Agilent, Santa Clara, USA

5.1.2 Reagents and Consumables

If not stated otherwise, all chemicals and reagents were obtained from the following suppliers: AppliChem (Darmstadt, Germany), Biorad (Herkules, USA), Boerhringer Ingelheim (Ingelheim, Germany), Carl Roth GmbH & Co.KG (Karlsruhe, Germany), Cytiva (Marlborough, USA), Merck (Darmstadt, Germany), New England Biolabs (Ipswich, USA), Roche Diagnostics (Penzberg, Germany), Serva Electrophoresis (Heidelberg, Germany), Sigma-Aldrich (Steinheim, Germany) and Thermo Fisher Scientific (Waltham, USA).

Other consumables were purchased from Herkules, USA), CAWO (Schrobenhausen, Germany), Cytiva (Marlborough, USA), Eppendorf (Hamburg, Germany), Invitrogen (Carlsbad, USA), OMNI Life Science (Bremen, Germany), Sarstedt (Nümbrecht, Germany) and Sartorius (Göttingen, Germany).

Table 5-4: List of chemicals

Chemical	Company
ACL Library 10 mM Intermediate Plate	TargetMol Chemicals, Boston, USA
30% Acrylamide-Bis 37.5:1	Serva, Heidelberg, Germany
AEBSF	Sigma-Aldrich, St. Louis, USA
Alt-R™ CRISPR-Cas9 tracrRNA	Integrated DNA technologies, Coralville, USA
ANTI-FLAG M2 Affinity Gel	Sigma-Aldrich, St. Louis, USA
Aprotinin	Roche, Basel, Switzerland
APS	Carl Roth GmbH & Co.KG, Karlsruhe, Germany
ATP	Thermo Fisher Scientific, Waltham, USA
Bis-Sulfosuccinimidylsuberat	Thermo Fisher Scientific, Waltham, USA
Chloroquin	Sigma-Aldrich, St. Louis, USA
Coomassie Brilliant Blue R250	BioRad, Hercules, USA
dATP	Thermo Fisher Scientific, Waltham, USA
Digitonin	Merck, Darmstadt
dNTP mix	Thermo Fisher Scientific, Waltham, USA
DTAB	Sigma-Aldrich, St. Louis, USA
Fura-2/AM	Thermo Fisher Scientific, Waltham, USA
Glucose	Sigma-Aldrich, St. Louis, USA
GlutaMAX™ Supplement	Thermo Fisher Scientific, Waltham, USA
Hoechst 33342	Thermo Fisher Scientific, Waltham, USA
Iodaceamine	Sigma-Aldrich, St. Louis, USA
JC-1	Thermo Fisher Scientific, Waltham, USA
jetPrime®	Sartorius, Göttingen, Germany
LDS sample buffer	Thermo Fisher Scientific, Waltham, USA
Lipofectamin™ 3000	Invitrogen, Carlsbad, USA
Lipofectamin™ RNAiMAX	Invitrogen, Carlsbad, USA
MEM solution of non-essential amino acids	Thermo Fisher Scientific, Waltham, USA

NuPAGE™ 4-12% Bis-Tris, 1.0 mm, Mini-Protein-Gel	Invitrogen, Waltham, USA
PA-JF646 HaloTag ligand	HHMI Janelia Research Campus, Ashburn, USA
Penicillin/ Streptomycin	Sigma-Aldrich, St. Louis, USA
PhosSTOP™	Roche, Basel, Switzerland
Pluronic F127	Sigma-Aldrich, St. Louis, USA
Polybrene	Sigma-Aldrich, St. Louis, USA
Poly-L lysine	Sigma-Aldrich, St. Louis, USA
ProLong™ Gold Antifade Mountant	Invitrogen, Waltham, USA
Puromycin	Carl ROTH, Karlsruhe, Germany
RiboLock RNase Inhibitor	Thermo Fisher Scientific, Waltham, USA
RotiR®Quant 5x Concentrate	Carl Roth GmbH, Karlsruhe, Germany
SimplyBlue™ Safe Stain	Thermo Fisher Scientific, Waltham, USA
SiR HaloTag ligand	Kai Johnsson, Max-Planck-Institute of Medical Research
SNAP-Cell® 647-SiR	New England Biolabs, Ipswich, USA
SpikeTides-TQL 13C15N-labeled peptides	JPT Innovative Peptide solutions, Berlin, Germany
TEAD	Sigma-Aldrich, St. Louis, USA
TEMED	Sigma-Aldrich, St. Louis, USA
TMTpro16 plex reagent	Thermo Fisher Scientific, Waltham, USA
Triton X-100	Carl ROTH, Karlsruhe, Germany
Triton X-114	Sigma-Aldrich, St. Louis, USA
Urea	Sigma-Aldrich, St. Louis, USA

5.1.3 Technical Equipment

Table 5-5: List of equipments

Equipment	Company
Acclaim Pepmap100 C18 nano column	Thermo Fisher Scientific, Waltham, USA
Aurora Ultimate C18 UHPLC column	IonOpticks, Melbourne, Australia
Avanti™ J-20 Centrifuge	Beckman Coulter, Brea, USA
Axio Observer D1 microscope	ZEISS Microscopy, Oberkochen, Germany
Branson Ultrasonics™ S-450A Sonifier	Thermo Fisher Scientific, Waltham, USA
C18 Acclaim Pepmap100 preconcentration column	Thermo Fisher Scientific, Waltham, USA
CaptiveSpray nanoflow electrospray source	Bruker Daltonics, Billerica, USA
CASY Cell Counter & Analyzer	OMNI Life Science, Bremen, Germany
Centrifuge 5427R	Eppendorf, Hamburg, Germany
CFX96 real-Time System BioRad	BioRad, Hercules, USA
ChemiDoc Touch Imaging System	BioRad, Hercules, USA
Cobolt 06-MLD 405 nm laser	Hübner Photonics, Kassel, Germany
CSU10 Confocal Scanner Unit	Yokogawa Electric, Tokyo, Japan
FAIMS Pro Duo interface	Thermo Fisher Scientific, Waltham, USA
HeraCell 240i CO2 Incubator	Thermo Fisher Scientific, Waltham, USA
maXis plus UHR-QTOF System	Bruker Daltonics, Billerica, USA
Megafuge 40R Centrifuge	Thermo Fisher Scientific, Waltham, USA
Milli-Q plus	Merck Millipore, Burlington, USA
MiSeq Sequencer	Illumina, San Diego, USA
Multimode-Microplate reader Mithras LB 940	Berthold Technologies, Bad Wildbad, Germany
Nanodrop 1000 Spectrophotometer	Thermo Fisher Scientific, Waltham, USA
Nanospray Flex ion source	Thermo Fisher Scientific, Waltham, USA
NanoSprayII	Sciex, Framingham, USA
NextSeq 2000	Illumina, San Diego, USA
Observer.Z1	ZEISS Microscopy, Oberkochen, Germany
Odyssey Infrared Imaging System	LI-COR Biosciences, Lincoln, USA

Omicron Luxx 638 nm Laser	Omicron-Laserage Laserprodukte, Rodgau-Dudenhofen, Germany
Orbitrap Eclipse™ Tribrid™ Massenspektrometer	Thermo Fisher Scientific, Waltham, USA
peqSTAR Thermocycler	PeqLab, Erlangen, Germany
Potter S Homogenizer	B. Braun Biotech International, Melsungen, Germany
Prime BSI sCMOS camera	Teledyne Scientific Imaging, Thousand Oaks, USA
QTRAP4500	Sciex, Framingham, USA
Quantum ST4	PeqLab, Erlangen, Germany
Seahorse XF96e	Agilent, Santa Clara, USA
Sep-Pak Vac tC18 1cc cartridges	Waters, Milford, USA
Stemi 508 stereomicroscope	ZEISS Microscopy, Oberkochen, Germany
Thermomixer Comfort	Eppendorf, Hamburg, Germany
TSKgel SP-2SW column	TOSOH, Tokyo, Japan
UltiMate 3000 RSLCnano System	Thermo Fisher Scientific, Waltham, USA
Ultrasonic processor UP100H	Hielscher, Teltow, Germany
Ultrospec 3300 pro	Amersham Bioscience, Little Chalfont, UK
Vanquish *Neo* UHPLC-System	Thermo Fisher Scientific, Waltham, USA
XFp Seahorse Flux Analyzer	Agilent, Santa Clara, USA

5.1.4 Buffers and Solutions

Base solution buffer

100 mM	$NaHCO_3$
20 mM	Na_2CO_3
10 mM	Nicotinamide
0.05%	Triton X-100

Coomassie Staining solution

10%	Acetic Acid
30%	Ethanol (EtOH)
0.25%	Coomassie R250

Coomassie Destaining solution

10%	Acetic Acid
20%	EtOH

E3 water

5 mM	NaCl
0.17 mM	KCl
0.33 mM	$CaCl_2$
0.33 mM	$MgSO_4$
10^{-5}%	Methylene blue

Easy-Prep Buffer

51 Mm	Tris-HCl pH 8
1 mM	EDTA pH 8
15%	Sucrose
2 mg/ml	Lysozyme
0.2 mg/ml	RNaseA
0.1 mg/ml	BSA

Extraction Buffer

10 mM	Tris-HCl pH 7.4
1 mM	EDTA pH 8
320 mM	Sucrose

2x HeBS

280 mM	NaCl
10 mM	KCl
50 mM	HEPES
1.5 mM	Na_2HPO_4

2x HEPES Buffered Saline

274 mM	NaCl
1.5 mM	Na_2HPO_4
54.6 mM	HEPES pH 7.1

IF Blocking Solution

130 mM	NaCl
774 mM	Na_2HPO_4
226 mM	NaH_2PO_4
1%	BSA
0.05%	Triton X-100

IF Permeabilization Solution

130 mM	NaCl
774 mM	Na_2HPO_4
226 mM	NaH_2PO_4
1%	BSA
0.2%	Triton X-100

IP Wash Buffer

50 mM	Tris HCl pH 7.5
300 mM	KCl
1 mM	MgCl2
0.5%	NP-40

LB Medium

5 g	Yeast extract
10 g	Tryptone
10 g/l	NaCl
ad 1 l	H_2O

LB Agar

1 l	LB Medium
16.4 g	Agar

Phosphate Buffered Saline (PBS)

130 mM	NaCl
774 mM	Na_2HPO_4
226 mM	NaH_2PO_4

Proteinase K Buffer

200 mM	Tris-HCl pH 7.5
300 mM	NaCl
25 mM	EDTA pH 8
2%	SDS
0.2 mg/ml	Proteinase K

RIPA Buffer

150 mM	NaCl
1%	NP-40
0.5%	Deoxycholate
0.1%	SDS
50 mM	Tris-HCl pH 7.5

SCX Buffer A

5 mM	NaH_2PO_4 pH 2.7
15%	Acetonitrile (ACN)

SCX Buffer B

5 mM	NaH_2PO_4 pH 2.7
1 M	NaCl
15%	ACN

SCX Buffer C

5 mM	NaH_2PO_4 pH 6
15%	ACN

5x SDS Sample Buffer

300 mM	Tris-HCl pH 6.8
10%	SDS
62.5%	Glycerol
0.05%	Bromphenol blue

SDS Running Buffer

25 mM	Tris-HCl pH 7.5
200 mM	Glycine
25 mM	SDS

15% SDS-PAGE Separation Gel

15%	Acrylamide-Bis 37.5:1
400 mM	Tris-HCl pH 8.8
0.1%	SDS
0.1%	APS
0.05%	TEMED

5% SDS-PAGE Stacking Gel

5%	Acrylamide-Bis 37.5:1
75 mM	Tris-HCl pH 6.8
0.1%	SDS
0.1%	APS
0.05%	TEMED

SDT Buffer

4%	SDS
0.1 M	DTT
0.1 M	TEAB pH 7.5

SEM Buffer

10 mM	MOPS pH 7.2
250 mM	Sucrose
1 mM	EDTA pH 8
1 mM	AEBSF

Trehalose (TH) Buffer

10 mM	KCl
10 mM	HEPES-KOH pH 6.9
300 mM	Trehalose
0.1%	BSA
0.25 mg/ml	Digitonin

Tris Buffered Saline (TBS)

10 mM	Tris-HCl pH 7.5
150 mM	NaCl

TBS-T

10 mM	Tris-HCl pH 7.5
150 mM	NaCl
0.1%	Tween-20

Towbin Blotting Buffer

38.6 mM	Glycine
48 mM	Tris
0.0037%	SDS
20%	Methanol (MeOH)

Triton X-100 Lysis Buffer

25 mM	Tris-HCl pH 7.5
150 mM	KCl
2 mM	EDTA pH 8
1 mM	NaF
1%	Triton X-100
1 mM	AEBSF
1 mM	DTT

UA Solution

8 M	Urea
0.1 M	TEAB pH 8

Western Blot Blotting Buffer

5%	Milk powder
0.0025%	Sodium azide
ad	TBS-T

5.1.5 Oligonucleotides

DNA oligonucleotides used in this work were ordered from Metabion GmbH (Planegg, Germany) and are listed below (**Table 5-6**). For RNAi experiments, siPOOLs against SMIM26, PGAM5 and scrambled NC were ordered at siTOOLs Biotech GmbH (Planegg, Germany).

Table 5-6: List of oligonucleotides

Oligonucleotide name	Sequence (5' to 3')
Molecular Cloning	
SMIM26 FseI F	attataggccggccatgtatcgaaatgagttcacg
SMIM26 AscI R	tatatggcgcgcctggttctgtaccagggccaccag
MFN2 FseI F	atataggccggccATGTCCCTGCTCTTCTCTCG
MFN2 AscI R	tatatggcgcgccCTATCTGCTGGGCTGCAGG
VDAC1 FseI F	atataggccggccATGGCTGTGCCACCCACGTAT
VDAC1 AscI R	tatatggcgcgccTGCTTGAAATTCCAGTCCTAGACC
PGAM5 F FseI	tataggccggccATGGCGTTCCGGCAGGCGCTG
PGAM5 R AscI	atatggcgcgccGGATCGAGTGATCTTGTCGGGAGGC

SLC25A5 FseI F	atataggccggccATGACAGATGCCGCTGTG
SLC25A5 AscI R	tatatggcgcgccTGTGTACTTCTTGATTTCATCATACAAG
SLC25A6 FseI F	atataggccggccATGACGGAACAGGCCATC
SLC25A6 AscI R	tatatggcgcgccGATCACCTTCTTGAGCTCGT
HIGD1A FseI F	atataggccggccATGTCAACAGACACAGGTGTTT
HIGD1A AscI R	tatatggcgcgccAGGCTTAGGTTTTGCCCAG
RHOT2 SLIC F	gcggccgctattataggccggccATGAGGCGGGACGTGCGC
RHOT2 SLIC R	tcgccgctagctggcgcgccCTGGCTCTTCACCAGGACCCTGT
SMIM26-F/H SpeI F	atataactagtggccggccatgtatcgaaatg
SMIM26-F/H AgeI R	tatataccggtttaggcgtagtcgggcacg
SMIM26 EcoRI F	tatatgaattCATGTATCGAAATGAGTTCACGGC
SMIM26 XbaI R	TctagAAGCTGCACCGGAACCTGGTTCTGTACCAGGGCC
SLC25A6 EcoRI F	tatatGAATTCATGACGGAACAGGCCATCTC
SLC25A6 AscI R	tataggcgcgccGATCACCTTCTTGAGCTCGTCG
TOMM20 EcoRI F	tatatGAATTCATGGTGGGTCGGAACAGCG
TOMM20 AscI R	tataggcgcgccTTCCACATCATCTTCAGCCAAGCTC
493ΔC Trunc F	GGCGCGCCAGCTAGCGGCGA
493ΔC Trunc R	GCCATCCTTTTGGTCTACTGACGAC

qPCR primer

qPCR VDAC1 F	GCCCGGAAGGCAGAAGAT
qPCR VDAC1 R	AGCCCTTGGTGAAGACATCC
qPCR ANT3 F	CCATGACGGAACAGGCCATCT
qPCR ANT3 R	CCGCTCGATCGGAGCCAC
qPCR PGAM5 F	GCTACATCGTGTGCAGAGCA
qPCR PGAM5 R	GGTGGGTGATGCTGCCATTA
qPCR GAPDH F	ATGGGTGTGAACCATGAGAA
qPCR GAPDH R	ATGCCAGTGAGCTTCCCGTTCAGC
qPCR PPIA F	GTCAACCCCACCGTGTTCTT
qPCR PPIA R	CTGCTGTCTTTGGGACCTTGT

Illumina sequencing barcode primer

5'PCR Primer C06	AATGATACGGCGACCACCGAGATCTACAC**ATTGGC**CAC GTTCAGAGTTCTACAGTCCGA
5'PCR Primer C12	AATGATACGGCGACCACCGAGATCTACAC**TACAAG**CAC GTTCAGAGTTCTACAGTCCGA
RNA PCR Primer, Index 16	CAAGCAGAAGACGGCATACGAGAT**GGACGG**GTGACTGG AGTTCCTTGGCACCCGAGAATTCCA
RNA PCR Primer, Index 17	CAAGCAGAAGACGGCATACGAGAT**CTCTAC**GTGACTGG AGTTCCTTGGCACCCGAGAATTCCA
RNA PCR Primer, Index 18	CAAGCAGAAGACGGCATACGAGAT**GCGGAC**GTGACTGG AGTTCCTTGGCACCCGAGAATTCCA
RNA PCR Primer, Index 19	CAAGCAGAAGACGGCATACGAGAT**TTTCAC**GTGACTGG AGTTCCTTGGCACCCGAGAATTCCA
RNA PCR Primer, Index 20	CAAGCAGAAGACGGCATACGAGAT**GGCCAC**GTGACTGG AGTTCCTTGGCACCCGAGAATTCCA
RNA PCR Primer, Index 21	CAAGCAGAAGACGGCATACGAGAT**CGAAAC**GTGACTGG AGTTCCTTGGCACCCGAGAATTCCA
RNA PCR Primer, Index 22	CAAGCAGAAGACGGCATACGAGAT**CGTACG**GTGACTGG AGTTCCTTGGCACCCGAGAATTCCA
RNA PCR Primer, Index 23	CAAGCAGAAGACGGCATACGAGAT**CCACTC**GTGACTGG AGTTCCTTGGCACCCGAGAATTCCA
RNA PCR Primer, Index 24	CAAGCAGAAGACGGCATACGAGAT**GCTACC**GTGACTGG AGTTCCTTGGCACCCGAGAATTCCA
RNA PCR Primer, Index 25	CAAGCAGAAGACGGCATACGAGAT**ATCAGT**GTGACTGG AGTTCCTTGGCACCCGAGAATTCCA
RNA PCR Primer, Index 26	CAAGCAGAAGACGGCATACGAGAT**GCTCAT**GTGACTGG AGTTCCTTGGCACCCGAGAATTCCA
RNA PCR Primer, Index 27	CAAGCAGAAGACGGCATACGAGAT**AGGAAT**GTGACTGG AGTTCCTTGGCACCCGAGAATTCCA
RNA PCR Primer, Index 28	CAAGCAGAAGACGGCATACGAGAT**CTTTTG**GTGACTGG AGTTCCTTGGCACCCGAGAATTCCA
RNA PCR Primer, Index 29	CAAGCAGAAGACGGCATACGAGAT**TAGTTG**GTGACTGG AGTTCCTTGGCACCCGAGAATTCCA
RNA PCR Primer, Index 30	CAAGCAGAAGACGGCATACGAGAT**CCGGTG**GTGACTGG AGTTCCTTGGCACCCGAGAATTCCA
RNA PCR Primer, Index 31	CAAGCAGAAGACGGCATACGAGAT**ATCGTG**GTGACTGG AGTTCCTTGGCACCCGAGAATTCCA

RNA PCR Primer, Index 32	CAAGCAGAAGACGGCATACGAGAT**TGAGTG**GTGACTGG AGTTCCTTGGCACCCGAGAATTCCA
RNA PCR Primer, Index 33	CAAGCAGAAGACGGCATACGAGAT**CGCCTG**GTGACTGG AGTTCCTTGGCACCCGAGAATTCCA
RNA PCR Primer, Index 34	CAAGCAGAAGACGGCATACGAGAT**GCCATG**GTGACTGG AGTTCCTTGGCACCCGAGAATTCCA
RNA PCR Primer, Index 35	CAAGCAGAAGACGGCATACGAGATAAAATGGTGACTGG AGTTCCTTGGCACCCGAGAATTCCA
RNA PCR Primer, Index 36	CAAGCAGAAGACGGCATACGAGAT**TGTTGG**GTGACTGG AGTTCCTTGGCACCCGAGAATTCCA
RNA PCR Primer, Index 37	CAAGCAGAAGACGGCATACGAGAT**ATTCCG**GTGACTGG AGTTCCTTGGCACCCGAGAATTCCA
RNA PCR Primer, Index 38	CAAGCAGAAGACGGCATACGAGAT**AGCTAG**GTGACTGG AGTTCCTTGGCACCCGAGAATTCCA

CRISPR human SMIM26

SMIM26 sgRNA F	CACCGCGTACCCATGTATCGAAAT
SMIM26 sgRNA R	AAACATTTCGATACATGGGTACGC
PCR sgRNA SMIM26 F	GTTCAGAGTTCTACAGTCCGACGATCGCGACGCCCTCAC CGGAAGT
PCR sgRNA SMIM26 R	CCTTGGCACCCGAGAATTCCAGAGCCCAACACAGACCAG GTGC

CRISPR murine SMIM26

sgRNA *SMIM26*	AGAGGCCTTTTCAGCTCGCA
Smim26 F	TGCCGGGATTAACTATGGAC
Smim26 R	CATGCGACAGTTTCAAGGAA

CRISPR fish SMIM26

sgRNA *smim26*	TTCCAGGTGAAGTATAACCG
PCR genotyping *smim26 F*	AGGAAGTGACGACATAGAGGCA
PCR genotyping *smim26 R*	GTCTGTCACGAAAACAAACTCCT

5.1.6 Plasmids and Constructs

Generated plasmids are listed in **Table 5-7**.

Table 5-7: List of plasmids

Plasmid	Source
pIRES-VP5 ANT2-F/H	this paper
pIRES-VP5 ANT3-F/H	this paper
pIRES-VP5 FLAG	this paper
pIRES-VP5 HA	this paper
pIRES-VP5 HIG1A-F/H	this paper
pIRES-VP5 MFN2-F/H	this paper
pIRES-VP5 modified F/H	(Meister et al., 2004)
pIRES-VP5 PGAM5-FLAG	this paper
pIRES-VP5 RHOT2-F/H	this paper
pIRES-VP5 SMIM26-F/H	this paper
pIRES-VP5 SMIM26-FLAG	this paper
pIRES-VP5 SMIM26-HA	this paper
pIRES-VP5 SMIM26ΔC-FLAG	this paper
pIRES-VP5 VDAC1-F/H	this paper
pLenti-Dest	(Campeau et al., 2009)
pLenti-Dest SMIM26-F/H	this paper
pLenti-Dest SMIM26ΔC-F/H	this paper
pLV-tetO-Oct4	(Stadtfeld et al., 2008)
pLV-tetO-Oct4 ANT3-ST	this paper
pLV-tetO-Oct4 SMIM26-HT	this paper
pLV-tetO-Oct4 TOMM20-ST	this paper
pMD2.G	Addgene #12259
psPAX2	Addgene #12260
pSpCas9(BB)-2A-Puro (pX459)	(Ran et al., 2013)
pX459 sgRNA SMIM26	this paper

5.1.7 Bacterial Strains, Cell Lines and animal models

Table 5-8: List of bacteria strains, cell lines and animal models

Name	Specification
Bacteria strain	
E. coli XL1 blue	F^- recA1 enA1 gyrA96 thi-1 hsdR17 supE44 relA1 lac F'[proAB lacIqZΔM15 Tn10 (TetR)]
E. coli Stbl3	F^-mcrB mrrhsdS20(rB^-, mB^-) recA13 supE44 ara-14 galK2 lacY1 proA2 rpsL20(StrR) xyl-5 λ^-leumtl-1
Cell line	
HEK293T	Human embryonic kidney cells
LentiX-293T	Human embryonic kidney cells expressing the SV40 large T antigen
HCT116	Colorectal carcinoma cells
HCT116 SMIM26 KO clone 1	Colorectal carcinoma cells lacking SMIM26
HCT116 SMIM26 KO clone 2	Colorectal carcinoma cells lacking SMIM26
HCT116 SMIM26 KO clone 1 SMIM26-F/H	Colorectal carcinoma cells lacking SMIM26, rescued by stable SMIM26-F/H expression
HCT116 SMIM26 KO clone 2 SMIM26-F/H	Colorectal carcinoma cells lacking SMIM26, rescued by stable SMIM26-F/H expression
HCT116 SMIM26 KO clone 1 SMIM26ΔC-F/H	Colorectal carcinoma cells lacking SMIM26, rescued by stable SMIM26 ΔC -F/H expression
HCT116 SMIM26 SMIM26-F/H	Colorectal carcinoma cells stably expressing SMIM26-F/H
HeLa	Human cervical cancer cells
HeLa SMIM26-HT	Human cervical cancer cells stably expressing SMIM26-HT
HeLa SLC25A6-ST	Human cervical cancer cells stably expressing SLC25A6-ST
HeLa TOMM20-ST	Human cervical cancer cells stably expressing TOMM20-ST
Mouse strain	
M. musculus C57BL/6NCrl	Charles River Laboratories, MGI:2159965
Fish line	
D. rerio TLAB	Crossing of AB stock with Tupfel Longfin (TL) variant

5.2 Methods

5.2.1 Molecular biological methods

5.2.1.1 Working with DNA

5.2.1.1.1 DNA cloning

5.2.1.1.1.1 General DNA cloning

To amplify a gene of interest, a polymerase chain reaction (PCR) was performed using Phusion High-Fidelity DNA Polymerase (Thermo Fisher Scientific, Waltham, USA) following manufacturer's instructions. Annealing temperatures of individual primers were determined and selected accordingly. The elongation time was set based on the size of the amplicon, taking in account the amplification rate of the Phusion Polymerase of approximately 1 kb / 30 s. As DNA template for the reaction, either complementary DNA (cDNA) from different cell lines or plasmid DNA was used. For the PCR reaction, 35 cycles of denaturation (10 s, 95 °C), primer annealing (30 s) and elongation (72 °C) were performed. PCR products were analyzed and purified from agarose gels (1 – 2%) using the NucleoSpin Gel and PCR Clean-Up Kit (Macherey-Nagel, Düren, Germany) according to the manufacturer's protocol.

Purified PCR fragments and vector backbones were digested with restriction enzymes for 1 h at 37 °C. Vector backbones were purified from agarose gels (1%) using NucleoSpin Gel and PCR Clean-Up Kit, while digested PCR products were directly purified using the same kit. Digested and purified PCR fragments and vectors where then used for a ligation reaction using T4 DNA Ligase (Thermo Fisher Scientific, Waltham, USA) for 1 h at room temperature (RT) or overnight (o/n) at 16 °C.

Subsequently, ligation reactions were transformed into chemical competent *Escherichia coli* (*E. coli*) cells via heat shock for 1 min at 42 °C. The cell suspension was plated on LB_{Amp}-plates and incubated o/n at 37 °C. The next day, 5 ml LB_{Amp}-media cultures were inoculated with one colony each and incubated o/n at 37 °C. To screen for positive clones, DNA was isolated using EasyPrep buffer and a test digest was performed. Positive clones were purified again using the NucleoSpin Plasmid Kit

(Macherey-Nagel, Düren, Germany) according to the manufacturer's protocol and send for Sanger sequencing to Eurofins Genomics (Ebersberg, Germany).

5.2.1.1.1.2 Site-directed mutagenesis

Site directed mutagenesis was used to mutate specific bases in a gene of interest on a vector. PCR reactions were performed using Phusion High-Fidelity DNA Polymerase as described above and primers were used at 0.2 µM end concentration. The PCR was performed for 25 cycles as described above and subsequently purified using the NucleoSpin Gel and PCR Clean-Up Kit following manufacturer's instructions. Template DNA was digested with DpnI restriction enzyme for 3 h at 37 °C. Following another purification with the NucleoSpin Gel and PCR Clean-Up Kit, chemical competent *E. coli* cells were transformed, plated on LB_{Amp}-plates and incubated o/n at 37 °C. The next day, 5 ml LB_{Amp}-media cultures were inoculated with one colony each and incubated o/n at 37 °C. DNA was isolated using the NucleoSpin Plasmid Kit. Successful mutagenesis was analyzed by Sanger sequencing (Eurofins Genomics, Ebersberg, Germany).

5.2.1.1.1.3 Inverse PCR

Blunt-end mutagenesis was used to insert or delete sequences from a gene of interest on a vector. PCR reactions were performed using Phusion High-Fidelity DNA Polymerase as described above and primers were used at 0.2 µM end concentration. The PCR was performed for 25 cycles as described above and subsequently purified using the NucleoSpin Gel and PCR Clean-Up Kit following manufacturer's instructions. Template DNA was digested with DpnI restriction enzyme for 3 h at 37 °C. Following another purification with the NucleoSpin Gel and PCR Clean-Up Kit, the PCR products were phosphorylated using 10 U T4 PNK (Thermo Fisher Scientific, Waltham, USA) in 1x T4 DNA Ligase Buffer for 30 min at 37 °C. The reaction was stopped by inactivating the enzyme for 10 min at 70 °C and was chilled on ice to cool down afterwards. Next, phosphorylated linear PCR products were circularized using 1 µl ATP (Thermo Fisher Scientific, Waltham, USA) and 1 µl T4 DNA Ligase (Thermo Fisher Scientific, Waltham, USA). Ligation was performed for 1 h at RT and chemical competent *E. coli* cells were transformed, plated on LB_{Amp}-plates and incubated o/n at 37 °C. 5 ml LB_{Amp}-media cultures were inoculated with one colony each and incubated o/n at 37 °C. DNA was

isolated using the NucleoSpin Plasmid Kit. Successful mutagenesis was analyzed by Sanger sequencing (Eurofins Genomics, Ebersberg, Germany).

5.2.1.1.1.4 Sequence- and ligation independent cloning

Sequence- and ligation independent cloning (SLIC) was performed as previously described by Jeong et al. (2012). The gene of interest was amplified and purified by PCR as described above (**5.2.1.1.1.1**) with a 20-25 basepair (bp)-overhang on both sides complementary to the vector sequence. Next, the insert and vector were mixed and incubated for 2.5 min at RT with T4 DNA polymerase (Thermo Fisher Scientific, Waltham, USA) followed by 10 min on ice. Afterwards, competent *E. coli* cells were transformed, plated on LB_{Amp}-plates and incubated o/n at 37 °C. 5 ml LB_{Amp}-media cultures were inoculated with one colony each and incubated o/n at 37 °C. DNA was isolated using the NucleoSpin Plasmid Kit. Successful mutagenesis was analyzed by Sanger sequencing (Eurofins Genomics, Ebersberg, Germany).

5.2.1.1.1.5 Cloning of small guide RNAs

For CRIPSR/Cas9-directed genome editing, a chimeric single guide RNA (sgRNA) targeting SMIM26 close to the start codon was cloned into a BbsI-digested pX459 backbone. Therefore, DNA oligonucleotides were phosphorylated in a 10 µl PNK reaction (100 µM of each DNA oligonucleotide, 1x T4 DNA Ligation Buffer, T4 PNK) (Thermo Fisher Scientific) for 30 min at 37 °C and subsequently annealed by boiling at 95 °C and cooling down to 25 °C. Annealed oligonucleotides were then cloned into the vector using T4 DNA Ligase as described above (**5.2.1.1.1.1**). Then, competent *E. coli* cells were transformed, plated on LB_{Amp}-plates and incubated o/n at 37 °C. 5 ml LB_{Amp}-media cultures were inoculated with one colony each and incubated o/n at 37 °C. DNA was isolated using the NucleoSpin Plasmid Kit. Successful mutagenesis was analyzed by Sanger sequencing (Eurofins Genomics, Ebersberg, Germany).

5.2.1.1.1.6 Cloning strategies for plasmids in this thesis

CDS of SMIM26 (NM_001348957.2), MFN2 (NM_014874.4), VDAC1 (NM_003374.3), PGAM5 (NM_001170543.2), SLC25A5 (NM_001152.5), SLC25A6 (NM_001636.4), HIGD1A (NM_014056.4), RHOT2 (NM_138769.3) and TOMM20 (NM_014765.3) were

amplified from HEK293T cDNA (**5.2.1.2.2**) using target specific primer with suitable restriction sites (**Table 5-6, 5.2.1.1.1.1**).

SMIM26, MFN2, VDAC1, SLC25A5, SLC25A6 and HIGD1A were cloned into a modified pIRES-VP5 backbone encoding a C-terminal FLAG/HA tag using the restriction enzymes FseI/AscI (**5.2.1.1.1.1**). Analogously, PGAM5 (C-terminal FLAG) and SMIM26 (C-terminal FLAG or HA) were cloned into modified pIRES-VP5 backbone encoding only one of the two tags. RHOT2 was cloned into a modified pIRES-VP5 backbone encoding a C-terminal FLAG/HA tag using SLIC (**5.2.1.1.1.4**).

For lentiviral transduction, SMIM26-F/H or SMIM26ΔC-F/H was amplified from previously generated modified pIRES-VP5 SMIM26-F/H plasmids and cloned into a pLenti-Dest backbone using SpeI/AgeI. Additionally, SMIM26 was cloned into a pLV-tetO-Oct4 backbone encoding a C-terminal HaloTag (Los et al., 2008) using EcoRI/XbaI, SLC25A6 and TOMM20 into a pLV-tetO-Oct4 backbone encoding a C-terminal SNAP-Tag (Keppler et al., 2003) using EcoRI/AscI (**5.2.1.1.1.1**).

Deletion of the C-terminal part of SMIM26 (Residue 46-95) was introduced by inverse PCR (**5.2.1.1.1.3**). For CRIPSR/Cas9-directed genome editing, a sgRNA targeting SMIM26 was cloned into a pX459 backbone (**5.2.1.1.1.5**).

5.2.1.1.2 Genotyping of human cell lines

5.2.1.1.2.1 Genomic DNA isolation

To isolate genomic DNA (gDNA) for genotyping generated cell lines, cell pellets were resuspended in 500 µl Proteinase K buffer and incubated o/n at 50 °C. The next day, lysates were cleared by centrifugation (30 min, full speed, RT) and the supernatant was transferred into a new cup. 400 µl isopropanol were added and mixed by inverting the cup several times. Precipitated gDNA was pelleted for 15 min at full speed and RT, the supernatant was removed, and the pellet was washed with 1 ml 70 % Ethanol. After another centrifugation for 10 min at full speed and RT, the supernatant was removed, and the pellet was air-dried. Next, gDNA was resuspended in 100 µl H_2O and dissolved o/n at 37 °C shaking. Fully dissolved gDNA was used for PCR or stored at 4 °C.

5.2.1.1.2.2 Genomic Sequencing

To validate successful CRISPR knockout, genomic sequencing was performed, Therefore, gDNA was isolated from WT cells and putative knockout clones (**5.2.1.1.2.1**) and a 150 bp fragment containing the Cas9 cut site and flanking barcoding sequences for Illumina sequencing was amplified by PCR (**5.2.1.1.1.1**). The sequencing was performed on an Illumina MiSeq Sequencer (Illumina, San Diego, USA) using the MiSeq Reagent Micro Kit V2 (Illumina, San Diego, USA) with a 156 cycle single-end dual index run.

5.2.1.2 Working with RNA

5.2.1.2.1 RNA extraction

RNA extraction from cells for cDNA synthesis and subsequent quantitative real-time PCR (qPCR) was performed using NucleoSpin RNA Clean-up Kit (Macherey-Nagel, Düren, Germany) following manufacturer's instructions. RNA was eluted with H_2O.

5.2.1.2.2 cDNA synthesis

cDNA from previously extracted RNA was generated using First Strand cDNA synthesis Kit (Thermo Fisher Scientific, Waltham, USA) according to the manufacturer's protocol. 500 ng – 1 µg RNA was diluted in 11 µl nuclease-free H_2O, mixed with 1 µl random hexamer primer or oligo-$(dT)_{18}$ primer and incubated for 5 min at 65 °C. Samples were cooled down on ice and 4 µl reaction buffer (5x), 2 µl dNTP mix (1 mM), 1 µl RiboLock RNase Inhibitor (2 U/µl) and 1 µl M-MuLV reverse transcriptase (20 U/µl) were added to the reaction. For cDNA synthesis using random hexamer primer, the samples were incubated 5 min at 25 °C. This step was not necessary for oligo-$(dT)_{18}$ primer reactions. Afterwards, the reactions were incubated for 60 min at 37 °C and terminated for 5 min at 70 °C. Synthesized cDNA was diluted 1:10 with nuclease-free H_2O and stored at -20 °C until further use.

5.2.1.2.3 Quantitative real-time PCR

qPCR was performed to determine relative quantification of specific RNAs. The reaction was performed using Takyon™ No ROX SYBR (Eurogentec, Seraing, Belgium) according to the manufacturer's protocol. In short, 10 µl Takyon reagent (2x) were

mixed with 1 µM of each forward and reverse primer, 2 µl diluted cDNA to a final volume of 20 µl. qPCR primers are listed in **Table 5-6**. The qPCR was performed according to the manufacturer's instructions and an additional melting curve from 65 – 95 °C at the end. Data was analyzed using the $\Delta\Delta C_T$ method, normalizing to GAPDH, RPL32 or PPIA as housekeeping genes, respectively.

5.2.1.2.4 Library preparation and RNA sequencing

To generate libraries for RNA sequencing experiments from isolated RNA of HCT116 WT and Smim26 KO cells (**5.2.1.2.1**), the Ovation SoLo RNA-Seq library preparation kit (Tecan, Männedorf, Switzerland) was utilized following the manufacturer's protocol. 1 ng total RNA was used as starting material and ribosomal RNA was removed by the included AnyDeplete® kit (Tecan Group AG, Männedorf, Switzerland). Barcodes used for multiplexing were provided by the library preparation kit (Tecan, Männedorf, Switzerland). The libraries were sequenced on a NextSeq 2000 system (Illumina, San Diego, USA) using the NextSeq 2000 P3 reagents (Illumina, San Diego, USA) in 2x 108 Cycles paired-end runs with 16 nt index runs.

5.2.2 Protein biochemical methods

5.2.2.1 Preparation of whole cell extracts

To prepare whole cell extracts (WCE) of endogenously expressed or overexpressed proteins, cells or isolated mitochondria were lysed in an appropriate amount of either RIPA lysis buffer or Triton X-100 lysis buffer. Samples were solubilized by sonification (2x 10 pulses, output level 3, duty cycle 50%) using the Branson Ultrasonics S-450A Sonifier and incubated for 20 min on ice. Lysates were cleared by centrifugation (full speed, 20 min, 4 °C) and supernatants were transferred to a new cup. Lysates were supplemented with 5x sodium dodecyl sulfate (SDS) sample buffer or used for immunoprecipitation (IP). If needed, protein concentration of the WCE was determined using RotiR®Quant 5x Concentrate (Carl Roth GmbH, Karlsruhe, Germany) following manufacturer's instructions.

5.2.2.2 SDS-PAGE and Western Blot

For separation and analysis of proteins, SDS-polyacryl gel electrophoresis (SDS-PAGE) was performed. SDS-PAGE minigels were prepared with 12% or 15%

separation gels, respectively and stored at 4 °C until further use. Samples were supplemented with 5x SDS sample buffer and incubated for 5 min at 95 °C prior to loading the gel. The SDS-PAGE was performed in SDS running buffer at 140 V for until the running front reached the end of the gel. In case of precast NuPAGE™ 4-12% Bis-Tris gels (Invitrogen, Carlsbad, USA), 4x lithium dodecyl sulfate (LDS) buffer and MOPS running buffer were used according to the manufacturer's recommendations. Gels were either stained with Coomassie or used for Western blotting.

For staining of proteins, gels were incubated in Coomassie staining solution for 1 h at RT and destained with Coomassie destaining solution for several hours at RT or o/n at 4 °C. Coomassie stained gels were further used for mass spectrometry.

For identification of specific proteins, gels were blotted onto a Hybond-ECL membrane (GE Healthcare, Little Chalfont, UK) using Towbin blotting buffer for approximately 1 min per kDa protein weight, constant 2 mA per cm^2 gel size and a maximum current of 25 V. Blotted membranes were blocked in Western blot blocking solution for 30 min at RT shaking and incubated with primary antibodies diluted in Western blot blocking solution o/n at 4 °C shaking. Membranes were washed three times with TBS-T for 5 min and incubated with secondary antibodies diluted in Western blot blocking solution for 1 – 2 h at RT shaking. Membranes were washed another three times with TBS-T and proteins were detected using the Odyssey Infrared Imaging System (LI-COR Biosciences, Lincoln, USA). Used antibodies are listed in **Table 5-2**.

5.2.2.3 Immunoprecipitation

To study protein-protein interactions or precipitate a specific protein of interest, WCE were prepared as described (**5.2.2.1**) from stable HCT116 overexpression cell lines or transiently transfected HEK293T cells (**5.2.3.2.1**). A small aliquot of the WCE was taken and mixed with SDS sample buffer to obtain the input sample. The residual WCE was used for immunoprecipitation. 50 µl of FLAG-M2 beads (Sigma-Aldrich, Steinheim, Germany) were washed twice with 1x PBS and once with lysis buffer. Cell or mitochondrial lysates were added to the beads and incubated for 3 h at 4 °C on a turning wheel. Beads were washed three times in IP wash buffer, transferred to a new cup and washed once with 1x PBS. All centrifugation steps with beads were

performed for 2 min at 1,000 × g and 4 °C. Precipitated proteins were eluted by incubation with 30 µl 2x SDS sample buffer for 5 min at 95 °C or with 30 µl 3xFLAG-peptide (5 mg/ml) diluted in 1x PBS for 2 h at 4 °C on a turning wheel. Enriched proteins were analyzed by SDS-PAGE (**5.2.2.2**).

5.2.2.4 Isolation of mitochondria

Stable HCT116 cells or transiently transfected HEK293T cell expressing Smim26-FH were resuspended in 1 ml trehalose buffer per plate and disrupted using a Potter S Homogenizer (B. Braun Biotech International – sartorius group) by moving the PTFE plunger up and down at 700 rpm. Ruptured cell membrane and nuclei were sedimented for 7 min at 800 × g and 4 °C. To separate mitochondria from cytosolic components, the supernatant was transferred into new cups and mitochondria were pelleted for 10 min at 10,000 × g and 4 °C. If needed for further experiments, the supernatant containing the cytosolic fraction was collected and the mitochondria were washed three times with SEM buffer. For interaction studies, these crude mitochondria were lysed or stored at – 20 °C until further use. To study the subcellular localization of mitochondrial proteins, crude mitochondria were resuspended in 1 ml trehalose buffer containing 3 µU/ml Proteinase K (Thermo Fisher Scientific, Waltham, USA) and incubated for 20 min on ice. The reaction was stopped with 2 µg/ml Aprotinin (Roche, Basel, Switzerland) and 1 mM AEBSF (Sigma-Aldrich, St. Louis, USA). Pure mitochondria were pelleted for 5 min at 10,000 × g and 4 °C and stored at – 20 °C until further use.

5.2.2.5 Sodium carbonate extraction of membrane proteins

Isolated mitochondria from HEK293T cells were resuspended in extraction buffer containing 0.1 M Na_2CO_3 (pH 11) or 1% Triton X-100 and incubated for 1 h at 4 °C under gentle agitation. Supernatant and pellet fraction were separated by centrifugation for 30 min at 20,000 × g and the pellet was washed 3 times with extraction buffer. Soluble supernatant and insoluble pellet fractions were analyzed by SDS-PAGE and western blotting.

5.2.2.6 Mass spectrometry

5.2.2.6.1 Mass spectrometry from affinity purification IP (AP-IP MS)

To study the interactome of a protein of interest, mass spectrometry was performed from Coomassie stained gel lanes after IP. Gel lanes were cut into consecutive slices, transferred to cups and successively washed with 50 mM NH_4HCO_3, 50 mM NH_4HCO_3/acetonitrile (ACN) (3:1), 50 mM NH_4HCO_3/ACN (1:1), and ACN (100%) for 30 min at RT shaking. Subsequently, gel pieces were lyophilized, and cysteines were reduced with 5 mg/ml DTT for 30 min at 57 °C, followed by alkylation with 1 mg/ml iodacetamide for 35 min at RT in the dark. Following washing as described above and lyophilization, proteins were subjected to an *in gel* tryptic digest o/n at 37 °C with approximately 2 µg Trypsin Gold (Mass spectrometry grade, Promega, Madison, USA) per 100 µl gel volume. Peptides were eluted twice with 100 mM NH_4HCO_3 and once with 50 mM NH_4HCO_3/ACN (1:1). The combined eluates were lyophilized and reconstituted in 20 µl 1 % formic acid (FA) prior to LC-MS/MS analysis. Peptide separation was carried out by an UltiMate 3000 RSLCnano System (Thermo Fisher Scientific, Waltham, USA) equipped with C18 Acclaim Pepman100 preconcentration column (100 µm i.d. x 20 mm, Thermo Fisher Scientific, Waltham, USA). A linear gradient of 4% to 40% acetonitrile in 0.1% FA over 90 min at a flow rate of 300 nl/min was used. The LC-system was on-line coupled to a maXis plus UHR-QTOF system (Bruker Daltonics, Billerica, USA) via a CaptiveSpray nanoflow electrospray source (Bruker Daltonics, Billerica, USA). Data-dependent acquisition of MS/MS spectra after collision-induced dissociation (CID) fragmentation was performed at a minimum resolution of 60,000. For the precursor scan, the MS spectra rate was 2 Hz processing a mass range between m/z 175 and m/z 2000. A dynamic method with a fixed cycle time of 3 s was applied via the Compass 1.7 acquisition and processing software (Bruker Daltonics, Billerica, USA).

MaxQuant (v. 2.6.2.0) performed identification of interaction partners by searching against the modified human swissprot database mentioned above. Search parameters were set as follows: trypsin, 2 missed cleavage allowed, deamidation of asparagine and glutamine, oxidation of methionine, carbamidomethylation or propionamide modification of cysteine as variable modifications with 3 variable modifications

allowed per peptide, precursor tolerance 10 ppm, MS/MS tolerance 25 ppm. Intensity-based absolute quantification (iBAQ) values were calculated, the false discovery rate was set to 1% at peptide and protein level and minimum number of unique peptides was set to 1.

5.2.2.6.2 *In-situ* crosslinking of mitochondrial protein (X-link MS)

Isolated Mitochondria from HEK293T cells transiently expressing SMIM26-F/H were carefully resuspended with 1 ml of aqueous 5 mM BS3 solution. After 1 h of rotation, mitochondria again were centrifuged at 10,000 × g for 5 min at 4 °C and supernatant discarded. The crosslinking reaction was quenched by addition of 1 ml of 50 mM Tris/HCl, followed by incubation at RT for 30 min. After centrifugation at 10,000 × g for 10 min at 4 °C, the resulting mitochondrial pellet was used for further processing.

Crosslinked mitochondria were lysed in 1% [w/v] Digitonin / 1 mM sucrose in 20 mM Tris/HCl pH 8 for 30 min at 4 °C and centrifuged at 20,000 × g for 30 min at 4 °C. The supernatant was transferred to a new reaction tube and the pellet was frozen in liquid nitrogen and stored at -20 °C. 300 µl per sample were used for further processing. Protein precipitation was done by adding trichloroacetic acid (TCA) to a final concentration of 15% [v/v]. Following incubation on ice for 30 min and centrifugation at 10,000 × g for 15 min at 4 °C, the resulting pellet was washed twice with ice-cold acetone and centrifuged at 10,000 × g for 10 min at 4 °C. The air-dried pellet was re-dissolved in LDS sample buffer (Thermo Fisher Scientific, Waltham, USA) and incubated for 10 min at 70 °C. Samples can be stored until further analysis at -20 °C. SDS-PAGE was carried out on a 4-12% NuPAGE precast gel (Thermo Fisher Scientific, Waltham, USA) under constant voltage. After separation of proteins, staining with colloidal Coomassie (Thermo Fisher Scientific, Waltham, USA) was performed according to the manufacturer's instructions.

Raw data of crosslink-samples were converted to .mgf files by MSConvert (Version 3.0.23192-5bdc4c9) and identification of crosslinked peptides was performed by Merox (Version 2.0) with following settings: crosslinker BS3, enzyme specificity trypsin with a maximum of three missed cleavages, carbamidomethylation of cysteine and oxidation of methionine. Also, BS3 side reactions with serine, threonine or tyrosine were allowed. Precursor mass tolerance was set to 15 ppm and MS/MS

tolerance to 50 ppm. A database for each sample was generated by the use of Protein Scape 3.1.3 (Bruker Daltonics, Billerica, USA) in connection with Mascot 2.5.1 (Matrix Science) and a modified human swissprot database, where the Flag/HA-tagged SMIM26 amino acid sequence was added. With respect to Merox' computing time, only top100 search results were selected for database generation. Mascot search parameters were as following: enzyme specificity trypsin with a maximum of 2 missed cleavages, carbamidomethylation or propionamide modification of cysteine, oxidation of methionine, deamidation of asparagine and glutamine were set as variable modification as well as hydrolyzed BS3 (mass shift +156.077 Da) or Tris-quenched BS3 (mass shift +259.142 Da). Precursor mass tolerance was set to 10 ppm, MS/MS tolerance to 0.02 Da and minimum peptide-ion score to 15. Graphical representation of crosslinked proteins was visualized using xiVIEW (Combe et al., 2024).

5.2.2.6.3 Qualitative identification of phosphosites by MS

To identify phosphorylated putative phosphosites in SMIM26, mass spectrometry was performed from coomassie stained gel lanes after IP. Gel slices containing SMIM26-F/H bands were cut, processed and analyzed as described in **5.2.2.6.1**. For phosphosite identification raw data processing was performed in Data Analysis 4.2 (Bruker Daltonics, Billerica, USA) and Protein Scape 3.1.3 (Bruker Daltonics, Billerica, USA) in connection with Mascot 2.5.1 (Matrix Science). Peptide identification was accomplished by searching against a modified human swissprot database, where the Flag/HA-tagged SMIM26 amino acid sequence was added. Search parameters were as follows: enzyme specificity trypsin with 2 missed cleavage allowed, precursor tolerance 0.02 Da, MS/MS tolerance 0.04 Da, carbamidomethylation or propionamide modification of cysteine, oxidation of methionine, deamidation of asparagine and glutamine and phosphorylation of serine, threonine and tyrosine were set as variable modifications. Mascot peptide ion-score cut-off was set to 15. Phosphopeptide fragment spectra were evaluated manually.

5.2.2.6.4 Quantification of post-translational modifications by mass spectrometry

For stoichiometric determination of phosphorylation on selected residues, Selected Reaction Monitoring (SRM) was performed. Stable isotope-labeled phosphopeptides as well as its non-phosphorylated counterpart were used as internal standards for phosphorylation stoichiometry determination of selected phosphopeptides from human SMIM26. The following heavy peptides were synthesized as quantified SpikeTides-TQL (JPT Innovative Peptide solutions, Berlin, Germany) with a $^{13}C^{15}N$-labeled C-terminal lysine:

Table 5-9: Stable isotope-labeled peptides used for SRM

Peptide	Sequence
WT	DGSASEVPSELSERPK
pS46	DGpSASEVPSELSERPK
pS48	DGSApSEVPSELSERPK
pS52	DGSASEVPpSELSERPK
pS48/52	DGSApSEVPpSELSERPK

100 fmol of each heavy peptide were spiked into the overnight in-gel tryptic digests which were otherwise processed as described above. To create a SRM method, the open-source software Skyline (MacCoss Lab Software) was used. First, a spectral library was built from several LC-MS/MS discovery runs (DDA, data dependent analysis) on the hybrid triple quadrupole/linear ion trap instrument QTRAP4500 (SCIEX, Framingham, USA). According to their occurrence in the DDA runs, precursor charge states +2 and +3 with 5 transitions were included in the targeted method and the resulting transition list was imported into the instrument software (Analyst 1.6.1). In addition, the following parameters were set for the SRM-method: Q1 and Q3 set to unit resolution (0.7 m/z half-maximum peak width), dwell time 20 ms, cycle time < 3 s. Second, a scheduled SRM method was created in Skyline by annotating peptide retention times from the initial SRM run and setting the following parameters: cycle time: 2 s, retention time window: 5 min.

The LC-MS/MS system consisted of an UltiMate 3000 RSLCnano System (Thermo Fisher Scientific, Waltham, USA) coupled via a NanoSprayII source (SCIEX, Framingham, USA) to a QTRAP4500. Peptides were separated on an Acclaim Pepmap100 C18 nano column (75 µm i.d.x150 mm, Thermo Fisher Scientific, Waltham, USA) with a C18 Acclaim Pepmap100 preconcentration column (100 µm i.D.x20 mm, Thermo Fisher Scientific, Waltham, USA) in front. At a flow rate of 300 nl/min a 60 min linear gradient of 4% to 40% acetonitrile in 0.1% FA was run. The resulting .wiff files of the SRM-measurements were imported into Skyline, which facilitated the quantification of endogenous phosphorylated or non-phosphorylated peptides by calculating the heavy-to-light ratios of the peak areas of the respective transitions. Relative quantification of phosphorylated peptides was performed in Excel by first calculating the absolute amount of either peptide species followed by adding up the amounts of the nonmodified peptide species and the related phosphorylated peptide species. Assuming this sum to represent 100%, it was possible to calculate the percentage of the phosphopeptide species.

5.2.2.6.5 Filter-aided sample preparation

Zebrafish samples were processed using the filter-aided sample preparation (FASP) method with minor modifications (Wiśniewski et al., 2009). Briefly, 10 larvae were dissolved in 30 µl of SDT buffer and incubated 10 min at 95 °C. Then, samples were sonicated with an ultrasonication probe using the Ultrasonic processor UP100H (Hielscher, Teltow, Germany) with 30 cycles (0.5 s, 50% amplitude). Protein concentration was determined using the 660 nm assay from Pierce. Protein extracts were mixed with 200 µl of UA solution, transferred to Microcons (MWCO = 30 kDa) and centrifugated (20 min, 14 000 × g, RT). After a washing step with 200 µl of UA solution, proteins were alkylated by adding 100 µl of 0.1 M iodoacetamide in UA solution and incubation for 20 min at RT in the dark. This was followed by centrifugation at 14000 × g for 15 min at RT. Thereafter, the ultrafiltration unit was washed 3 times with 100 µl of UA and 3 times with 100 µl of 100mM HEPES pH 7.6. Proteins were digested directly in the ultrafiltration unit by adding 50 µl of 100mM HEPES buffer containing trypsin at a 1:20 ratio (protease:protein; w/w). After overnight digestion at 37 °C peptides were eluted into fresh collection tubes by centrifugation at 14,000 × g for 15 min at RT. The ultrafiltration unit was then washed

one time by addition of 50 µl 100 mM HEPES buffer and 10 min centrifugation at 14,000 × g.

To evaluate the digest efficiency and quantify the peptide yield an aliquot of each sample was analyzed by LC-UV.

5.2.2.6.6 LC-MS/MS analysis after isobaric labelling with tandem mass Ttag

5.2.2.6.6.1 Isobaric labelling with tandem mass tag

Shotgun proteomics on zebrafish larvae was performed using isobaric labelling with a tandem mass tag (TMT) followed by LC-MS/MS. About 50 µg (contained in 100 µl 100 mM HEPES pH 7.6) of each condition were labelled with one separate channel of the TMTpro16 plex reagent (Thermo Fisher Scientific, Waltham, USA) according to the manufacturer's description. The labelling efficiency was determined by LC-MS/MS on a small aliquot of each sample. Samples were mixed in equimolar amounts and equimolarity was again evaluated by LC-MS/MS.

The mixed sample was acidified to a pH below 2 with 10% trifluoroacetic acid (TFA) and was desalted using C18 cartridges (Sep-Pak Vac 1cc (50mg), Waters). Peptides were eluted with 3 x 150 µl 80% ACN in 0.1% FA, followed by freeze-drying.

100 µg of peptides in 100 µl 100 mM HEPES pH 7.6 were labelled with one separate channel of the TMTpro™ 16plex Label Reagent Set (Thermo Fischer Scientific, Waltham, USA), according to the manufacturer's description. The labelling efficiency was determined by LC-MS. Samples were mixed in equimolar amounts and equimolarity was again evaluated by LC-MS/MS. The mixed sample was acidified to a pH below 2 with 10% TFA and was desalted using C18 cartridges (Sep-Pak Vac 1cc [50 mg], Waters). Peptides were eluted with 3x 150 µl 80% ACN and 0.1% FA, followed by freeze-drying.

5.2.2.6.6.2 Strong cation exchange chromatography

Separation of TMT-labelled peptides was achieved by strong cation exchange chromatography (SCX). The dried sample was dissolved in 70 µl of SCX buffer A and 200 µg of peptides were loaded at a flow rate of 35 µl/min on a TSKgel SP-2SW column (1 mm ID x 300 mm, particle size 5 µm, TOSOH) on an UltiMate 3000 RSLC nano

system (Thermo Fisher Scientific, Waltham, USA). For the separation, a ternary gradient was used. Starting with 100% buffer A for 10 min, followed by a linear increase to 10% buffer B (5 mM NaH_2PO_4, pH 2.7, 1M NaCl, 15% ACN) and 50% buffer C (5 mM Na_2HPO_4, pH 6, 15% ACN) in 10 min, to 25% buffer B and 50% buffer C in 10 min, 50% buffer B and 50% buffer C in 5 min and an isocratic elution for further 15 min. The flow-through was collected as a single fraction, then 60 fractions were collected every minute along the gradient. Fractions with low peptide content were pooled. ACN was removed by vacuum centrifugation and the samples were acidified with 0.1% TFA and analyzed by LC-MS/MS.

5.2.2.6.6.3 LC-MS/MS-analysis of TMT fractions

The nano-HPLC system (Vanquish Neo UHPLC-System) was coupled to an Orbitrap Eclipse mass spectrometer, equipped with a FAIMS Pro Duo interface and a Nanospray Flex ion source (all parts Thermo Fisher Scientific, Waltham, USA). Peptides were loaded onto a trap column (PepMap C18, 5 mm × 300 µm ID, 5 µm particles, 100 Å pore size, Thermo Fisher Scientific, Waltham, USA) using 0.1% TFA as mobile phase. The trap column was switched in line with the analytical column (Aurora Ultimate C18, 75 µm ID × 25cm, 1.7 µm, IonOpticks, Melbourne, Australia). Electrospray voltage was set to 2.3 kV.

Peptides were eluted using a flow rate of 300 nl/min, starting with the mobile phases 98% A (0.1% FA in water) and 2% B (80% ACN, 0.1% FA) and linearly increasing to 35% B over the next 120 min. This was followed by a steep gradient to 95% B in 5 min, stayed there for 5 min and ramped down in 2 min to the starting conditions of 98% A and 2% B for equilibration at 50 °C.

The Orbitrap Eclipse was operated with a SPS real-time search method with a full scan performed in the Orbitrap (m/z range 375-1,500, resolution 120,000, automatic gain control (AGC) target 4e5) at 3 different compensation voltages (CV -40, -55, -70) followed by MS/MS scans of the most abundant ions performed in the ion trap at a cycle time of 1.2 s per CV. MS/MS spectra were acquired using an isolation width of 1.2 m/z, CID with CE 30, AGC target 1e4, q-value 0.25, maximum injection time 50 ms using the rapid scan mode. For the real time search the uniprot-reference-database for zebrafish was used (2024-01-24; 47,112 sequences; 34,768,177 residues).

Precursor ions selected for fragmentation (including charge states 2-6) were excluded for 45 s. The monoisotopic precursor selection (MIPS) mode was set to Peptide and the Exclude Isotopes feature was enabled.

For MS3 fragmentation the number of SPS ions was set to 10 using an isolation width of 1.2 m/z, fragmentation was performed by HCD at CE 50 and MS3 spectra were analyzed in the Orbitrap (resolution 50,000, AGC target 1.5e5, maximum injection time 150 ms). For the detection of the TMT reporter ions, a fixed first mass of 110 m/z was set.

For peptide identification, the RAW-files were loaded into Proteome Discoverer (version 3.1.0.638, Thermo Fisher Scientific). All MS/MS spectra were searched using MSAmanda v3.0 (Dorfer et al., 2014).

The peptide mass tolerance was set to ±10 ppm and fragment mass tolerance to ±400 mmu, the maximum number of missed cleavages was set to 2, using tryptic enzymatic specificity without proline restriction. The RAW-files were searched against the ENSEMBL-database called *Danio_rerio.GRCz11_ENSEMBL_111.pep.all.canonical.fasta* (28,268 sequences; 16,001,659 residues), supplemented with common contaminants.

Iodoacetamide derivative on cysteine was set as fixed modification and variable modifications used were oxidation on methionine, deamidation on asparagine and glutamine, carbamylation and TMTpro 16plex tandem mass tag on lysine, phosphorylation on serine, threonine and tyrosine, carbamylation and TMTpro 16plex tandem mass tag on peptide N-terminus, glutamine to pyro-glutamate conversion at peptide N-terminal glutamine and acetylation on protein N-terminus. The result was filtered to 1% FDR on protein level using the Percolator algorithm (Käll et al., 2007) integrated in Proteome Discoverer. The localization of the post-translational modification sites within the peptides was performed with the tool ptmRS, based on the tool phosphoRS (Taus et al., 2011). Identifications were filtered again to 1% FDR on protein and PSM level, additionally an Amanda score cut-off of at least 70 was applied. Proteins were filtered to be identified by a minimum of 2 PSMs in at least 1 sample. Peptides were quantified based on Reporter Ion intensities

extracted by the "Reporter Ions Quantifier"-node implemented in Proteome Discoverer and Proteins were quantified by summing unique and razor peptides.

5.2.2.6.7 Targeted MS analysis by scheduled Parallel Reaction Monitoring

sPRM was used to quantify *smim26* level in zebrafish. The nano HPLC system used was a Vanquish Neo nano system coupled with the Orbitrap Exploris 480 mass spectrometer, equipped with a NanoFlex nanospray source (Thermo Fisher Scientific, Waltham, USA). Peptides were loaded onto a trap column (PepMap C18, 5 mm × 300 µm ID, 5 µm particles, 100 Å pore size, Thermo Fisher Scientific, Waltham, USA) at a flow rate of 25 µl/min using 0.1% TFA as mobile phase. After 5 min, the trap column was switched in line with the analytical column (PepMap C18, 500 mm × 75 µm ID, 2 µm, 100 Å, Thermo Fisher Scientific, Waltham, USA). The analytical column was connected to PepSep sprayer 1 (Bruker Daltonics, Billerica, USA) equipped with a 10 µm ID fused silica electrospray emitter with an integrated liquid junction (Bruker Daltonics, Billerica, USA). Electrospray voltage was set to 1.9 kV. Peptides were eluted using a flow rate of 230 nl/min, and a binary 90 min gradient, respectively 115 min.

The gradient started with the mobile phases: 98% A (water/FA, 99.9/0.1, v/v) and 2% B (water/ACN/FA, 19.92/80/0.08, v/v/v), increased to 35% B over the next 90 min, followed by a gradient in 5 min to 90% B, stayed there for 5 min and decreased in 2 min back to the gradient 98% A and 2% B for an equilibration at 30°C.

The Orbitrap Exploris 480 mass spectrometer was operated by a mixed MS method, which consisted of one full scan (m/z range 380-1,200; 15,000 resolution; AGC target value 1e6) followed by the PRM of targeted peptides from an inclusion list (isolation window 0.8 m/z; normalized collision energy (NCE) 34; 30,000 resolution; AGC target value 2e5). The maximum injection time was set to 100 ms.

A scheduled PRM method (sPRM) development, data processing and manual evaluation of results were performed in Skyline-daily (64-bit, v24.1.1.398) (MacLean et al., 2010). Four internal reference proteins were chosen with the following criteria: protein size greater than 30 kDa and detected with at least 4 unique peptides. Reference proteins were Apolipoprotein A-Ib (Apoa1b, A0A0R4IKF0), Keratin 4 (Krt4, F1QK60), Creatine kinase (Ckmb, Q7T306) and Rps25 (Q6PBI5). For *smim26*,

the average area was calculated, normalized to the average area of all reference proteins and expressed relative to the value in the control condition sample. Mass spectrometry relevant details about all proteins and their specific peptides included in the sPRM method are listed in **Table 8-2**.

5.2.3 Cell Biological Methods

5.2.3.1 Cultivation of mammalian cells

Mammalian cell lines were cultivated under standard conditions at 37 °C in 5% CO_2 atmosphere. HEK293T cells were grown in DMEM (Thermo Fisher Scientific, Waltham, USA) supplemented with 10% Fetal bovine serum (FBS, Sigma-Aldrich, St. Louis, USA) and 1 % Penicillin/Streptavidin (Sigma-Aldrich, St. Louis, USA). HCT116 cells were grown in McCoy's 5A Medium (Thermo Fisher Scientific, Waltham, USA) supplemented with 10% FBS and 1% Penicillin/Streptavidin. Low and high glucose media were generated by supplementing DMEM without glucose and pyruvate (Thermo Fisher Scientific, Waltham, USA) with 10% FBS, 1% Penicillin/ Streptavidin and 0.1 mM or 25 mM glucose (Sigma-Aldrich, St. Louis, USA), respectively. HeLa cells were grown in DMEM (Thermo Fisher Scientific, Waltham, USA) supplemented with 10% FBS (Sigma-Aldrich, St. Louis, USA), 1% Sodium Pyruvate (Thermo Fisher Scientific, Waltham, USA), 1% GlutaMAX™ Supplement and 1% MEM solution of non-essential amino acids (Thermo Fisher Scientific, Waltham, USA).

Every two or three days, cells were passaged and splitted. Cells were washed once with 1x PBS and 0.5 – 1 ml trypsin (Sigma-Aldrich, St. Louis, USA) were added to detach the cells for 5 min at 37 °C. trypsination was stopped by adding fresh media and the cell suspension was partially transferred into a new sterile plate.

5.2.3.2 Cell transfection of mammalian cell lines

5.2.3.2.1 Cell transfection using Calcium phosphate

For transient overexpression of proteins in HEK239T cells on 15 cm plates, 10 µg plasmid DNA were mixed with 123 µl Ca_2Cl (2 M) and H2O in a final volume of 1 ml. Then, 1 ml HEPES (2x) was added dropwise while vortexing. The mix was incubated

for 15 min at RT and added dropwise to the plate. Cells were incubated for 2 days at 37 °C and 5% CO_2 and then used for further experiments.

5.2.3.2.2 Cell transfection using Lipofectamine3000

For transient overexpression of proteins in cancer cells, the Lipofectamine3000 reagent (Thermo Fisher Scientific, Waltham, USA) was used according to the manufacturer's protocol. Cells were seeded 24 h prior transfection to reach 60-80 % confluence on the day of transfection. For the transfection of a 24-well, 1 µg plasmid DNA and 1 µl P3000 were mixed in 50 µl Opti-MEM™ (Thermo Fisher Scientific, Waltham, USA) (Mix 1). Additionally, 1.5 µl Lipofecamine3000 reagent was diluted in 50 µl Opti-MEM™ (Mix 2). Both mixes were incubated for 5 min at RT and combined at a ratio of 1:1 afterwards. The reaction was mixed by vortexing and incubated for 15 – 20 min at RT. 100 µl transfection mix was added to the cells and incubated for 2 – 3 days at 37 °C and 5% CO_2.

5.2.3.2.3 siRNA knockdown using Lipofectamine RNAiMAX

For transfection of siPOOLs™ (siTOOLs Biotech, Martinsried, Germany), Lipofectamine RNAiMAX reagent (Thermo Fisher Scientific, Waltham, USA) was used following siTOOLs Biotech provided protocol. For a 24-well, two mixes were prepared with Mix 1 containing 40 µl Opti-MEM™ and 10 µl of siPOOLs (50, 150 or 250 nM for final concentration of 1, 3 or 5 nM) and Mix 2 containing 49 µl Opti-MEM™ and 1 µl Lipofectamine RNAiMAX reagent. Mix 1 and 2 were incubated for 5 min at RT, combined, mixed by vortexing and incubated for another 10 min at RT. 100 µl of the transfection mix were transferred to a 24-well and 400 µl of cell suspension was added. Cells were incubated for 2-3 days at 37 °C and 5% CO_2. Knockdown efficiency was determined with qPCR (**5.2.1.2.3**).

5.2.3.3 Generation of cell lines

5.2.3.3.1 Generation of Knockout cell lines using CRISPR/Cas

Smim26 knockout in HCT116 cells was generated by CRISPR/Cas9-directed genome editing. Complementary sgRNAs expressed from a pX459 vector were utilized to induce site-directed frameshifts in the SMIM26 gene. Cells were transfected twice with Lipofectamin3000 (**5.2.3.2.2**) with the second transfection being performed

48 h subsequent to the initial one. Cells carrying the plasmid were selected with 1µg/ml puromycin for 3 days at 37 °C and 5% CO_2. Afterwards, positive cells were separated into single clones.

HCT116 Smim26 KO clones were validated by sequencing. Genomic DNA of all clones was extracted (**5.2.1.1.2.1**) and a 150 bp region flanking the sgRNA protospacer adjacent motif (PAM) site was amplified using Phusion High-Fidelity DNA Polymerase (Thermo Fisher Scientific, Waltham, USA) following the manufacturer's recommendation as described above (**5.2.1.1.1**). PCR products were analyzed and purified from 2% agarose gels using the NucleoSpin Gel and PCR Clean-Up Kit (Macherey-Nagel, Düren, Germany) according to the manufacturer's protocol. In a second PCR, Illumina TrueSeq-System Barcodes were added to the amplicons and subsequently sequenced by a MiSeq-sequencing platform.

5.2.3.3.2 Generation of stable HCT116 cell lines using lentiviral transduction

To generate stable HCT116 cell lines, a lentiviral transduction was performed. Prior to the transduction, virus particles were produced in HEK293T cells. 6 x 10^6 cells were seeded in 10 cm plates 24 h prior transfection to reach 60 – 75% confluence the next day. The medium was replaced with 4.5 ml DMEM (Thermo Fisher Scientific, Waltham, USA) supplemented with 10% FBS, 1% Penicillin/Streptavidin, 10 mM HEPS and 25 µM Chloroquin. The cells were incubated for 1 h at 37 °C and 5% CO_2. During that time, the transfection was prepared by mixing 5 µg pMD2G (envelope plasmid), 15 µg psPAX2 (packaging plasmid), 20 µg of a lentiviral plasmid containing the gene of interest and 250 µl $CaCl_2$ (0.5 M) in a final volume of 500 µl. The mix was incubated for 2 min at RT. Then, 500 µl HeBS (2x) were added dropwise while vortexing. The final transfection mix was incubated for 25 min at RT and 1ml was added dropwise to the cells. After 6 – 8 h, the medium was replaced with fresh DMEM supplemented with 10% FBS and 1% Penicillin/Streptavidin and incubated further at 37 °C and 5% CO_2.

To harvest the generated virus, the medium was collected 48 h and 72 h post-transfection, centrifuged for 10 min at 500 × g and RT to remove cell debris and the samples collected from both time points were combined. The virus was filtered through a 0.45 µm syringe filter to prevent mammalian cell contamination and then

concentrated using Amicon Ultra-15 Centrifugal Filter columns (Sigma-Aldrich, St. Louis, USA) following the manufacturer's instructions by repeated centrifugation for 10 min at 4000 rpm and RT each until the desired virus titer was achieved. The Lentivirus was either stored at – 80 °C or used immediately for transduction of cancer cells.

For lentiviral transduction, 2 x 10^5 HCT116 cells were seeded in T-25 flasks the day prior viral treatment. Virus containing the gene of interest was diluted in McCoy's 5A Medium (Thermo Fisher Scientific, Waltham, USA) supplemented with 10% FBS, 1% Penicillin/Streptavidin and 8 µg/ml Polybrene to a final concentration of 0.1 – 10 µl virus/ml. Cancer cells were incubated with lentivirus for 3 days at 37 °C and 5% CO_2. For selection of positive clones, transduced cells were washed with 1x PBS, splitted and treated with 1 µg/ml puromycin in McCoy's 5A Medium supplemented with 10% FBS, 1% Penicillin/Streptavidin for 2 days at 37 °C and 5% CO_2. Expression of the gene of interest was determined with qPCR (**5.2.1.2.3**).

5.2.3.3.3 Generation of stable HeLa cell lines using lentiviral transduction

To generate stable HeLa cell lines for live-cell single molecule microscopy experiments, LentiX-293T cells (Takara Bio, Kusatsu, Japan) were transfected with 2.5 µg pMD2.G, 7.5 µg psPAX2 and 10 µg of the respective lentiviral pLV-tetO-Oct4 plasmid using the JetPrime kit (Sartorius, Göttingen, Germany). Two days post-transfection, the supernatant was collected, filtered through a 0.45 µm WhatmanTM membrane filter (Cytiva, Marlborough, USA), and 1 ml of the filtrate was added to HeLa cells in a 6-well dish. Following three days of incubation, the cells were washed with PBS (Thermo Fisher Scientific, Waltham, USA) and seeded into a fresh dish.

To confirm successful transduction of HeLa cells, they were seeded into a microscopy dish and labeled for 30 min with either 31.25 nM of SiR HaloTag ligand (HTL) (provided by Kai Johnsson, Max-Planck-Institute of Medical Research) or 300 nM SNAP-Cell® 647-SiR (New England Biolabs, Ipswich, USA), depending on the tag expressed. Excess dye was rinsed with PBS and medium was replaced with OptiMEM (Thermo Fisher Scientific, Waltham, USA). Protein expression was assessed using an Axio Observer D1 microscope (ZEISS Microscopy, Oberkochen, Germany) equipped with a CSU10 Confocal Scanner Unit (Yokogawa Electric, Tokyo, Japan) at an

excitation wavelength of 638 nm. Since only few cells showed expression of SMIM26-HT after transduction, the cells were sorted at the Core Facility Cytometry of Ulm University to obtain uniform expression levels.

5.2.3.4 Cell proliferation and viability

5.2.3.4.1 Cell proliferation assay

Proliferation rates of HCT116 WT, Smim26 KO and rescue cell lines were analyzed using an Incucyte S3 system (Sartorius, Göttingen, Germany). $1.5x10^3$ HCT116 cells were seeded in 96-well plates in McCoy's 5A medium (Thermo Fisher Scientific, Waltham, USA) or DMEM without glucose and pyruvate (Thermo Fisher Scientific, Waltham, USA) supplemented with 25 mM (High glucose) or 0.1 mM (Low glucose) glucose (Sigma-Aldrich, St. Louis, USA). Confluency in each well was monitored for 5 days every 4 h.

5.2.3.4.2 Cell viability assay

Cell viability upon starvation was assessed by SMIM26 knockdown using siPOOLs (siTOOLs Biotech, Martinsried, Germany). HCT116 WT cells were seeded in high glucose DMEM (25 mM) or low glucose DMEM (0.1 mM) glucose and transfected with siPOOLs against SMIM26 (**5.2.3.2.3**). After 72 h, cell viability was analyzed using the CellTiter Glo® Cell Viability Assay (Promega, Madison, USA) and knockdown efficiency was confirmed by qPCR (**5.2.1.2.3**).

5.2.3.4.3 Drug screening

Drug response to a Library containing 313 FDA-approved bioactive compounds (TargetMol Chemicals, Boston, USA) was analyzed in HCT116 WT, SMIM26 knockout and overexpression cell lines. Per cell line, two 384-well plates were seeded with 500 cells per well. After incubation overnight at 37 °C and 5% CO_2, bioactive compounds or DMSO as control were transferred from a pre-spotted plate to the cells to achieve a final concentration of 1 µM. Cells were incubated for 72 h and viability was assessed using the ATPlite Assay 1step Luminescence Assay (Revvity, Waltham, USA).

5.2.3.5 Microscopy

5.2.3.5.1 Immunofluorescence

HCT116 cells were grown on coverslips and transiently transfected with Smim26-F/H using Lipofectamin 3000 (Invitrogen, Carlsbad, USA) reagent. After 48 h, HCT116 cells were fixed with 3.7% formaldehyde solution and permeabilized with 0.2% Triton X-100. Glass slides were incubated in immunofluorescence (IF) blocking solution at RT for 1h, followed by overnight incubation at 4° with primary antibody (1x PBS, 1% [w/v] BSA, 0.05% [v/v] Triton X-100). Next, glass slides were incubated with secondary antibody (1x PBS, 1% [w/v] BSA, 0.05% [v/v] Triton X-100) for 1 h at RT. Between fixation and antibody treatments three washing steps with 1x PBS for 2 min and after permeabilization 3 washing steps with IF blocking solution (1x PBS, 1% [w/v] BSA, 0.05% [v/v] Triton X-100) were performed. Stained cells were rinsed with 1x PBS and cover slips were mounted using ProLongTM Gold Antifade Mountant with DAPI (Thermo Fisher Scientific, Waltham, USA). Images were recorded on an Observer.Z1 microscope (ZEISS Microscopy, Oberkochen, Germany) and analyzed using Fiji (Schindelin et al., 2012). Used antibodies are listed in **Table 5-2**.

5.2.3.5.2 High-resolution live-cell single-molecule microscopy

5.2.3.5.2.1 Live-cell single-molecule measurements

HeLa cells expressing SMIM26-HT, TOMM20-ST or SLC25A6-ST were grown in microscopy dishes (ibidi®) for one to two days at 37 °C, humidified air and 5% CO2. Prior to the measurement, cells were labeled with 5 nM photo-activatable (PA) JF646 HTL (HHMI Janelia Research Campus) for SMIM26-HT, 1.5 nM SNAP-Cell® 647-SiR for TOM20-ST, and 15 nM SNAP-Cell® 647-SiR for SLC25A6-ST, alongside 20 nM BioTracker 488 Green Mitochondria Dye (Sigma-Aldrich, ST. Louis, USA) for 30 min. Labeled cells were washed with 1x PBS, and incubated for 30 min in standard medium and subsequently in OptiMEM for measurements.

Measurements were performed on a custom-built inverted microscope with flat-top HILO illumination, equipped with two cameras for simultaneous dual-color measurements. A beam splitter (F48-644, AHF analysentechnik, Tübingen, Germany) allowed acquisition of single-molecule and mitochondria signal concurrently. Light

above 634 nm was captured using a Prime BSI sCMOS camera (Teledyne Scientific Imaging, Thousand Oaks, USA), while light below 634 nm was detected with a Kinetix 22 sCMOS camera (Teledyne Technologies, Thousand Oaks, USA). Each camera was equipped with a combination of an emission filter and a notch filter (F67-532 and F40-074, AHF analysentechnik, Tübingen, Germany). A pixel size of 130 nm for both cameras was achieved by 2x2 binning.

Before SMT measurements, images of TetraSpeck™ microspheres (T7279, Thermo Fisher Scientific, Waltham, USA) excited with 488 nm and 638 nm laser wavelength were captured to verify the alignment of the single-molecule and the mitochondria channels on both cameras.

For samples labeled with PA-JF646, the dye was activated with 1 ms pulses of a 405 nm laser (Cobolt 06-MLD 405 nm, Hübner Photonics, Kassel, Germany) while continuously exciting with a 638 nm laser (Omicron Luxx Laser, Omicron-Laserage Laserprodukte, Rodgau, Germany) for 10 ms exposure time per camera frame. Samples labeled with SiR were excited with the 638 nm laser. In both cases, the mitochondria dye was simultaneously excited with a 488 nm laser (Cobolt 06-MLD 488 nm, Hübner Photonics, Kassel, Germany). 2,000 frames were recorded per movie.

5.2.3.5.2.2 Data analysis with TrackIt

10 frames each of the recorded single-molecule movies were averaged and bleach corrected (Miura, 2020) with the “Histogram Matching” method using Fiji (Schindelin et al., 2012) to enhance signal-to noise. The TrackIt (Kuhn et al., 2021) software was used for spot detection and track generation of processed movies. Mitochondria movies were used as reference channel restricting the single-molecule analysis to regions of interest within the mitochondria utilizing intensity thresholds. For tracks crossing the mitochondrial border, the jumps located outside the analysis region were discarded. A spot detection threshold factor of 1.2, tracking radius of 5 pixels (=650 nm) and minimum track length of 10 frames were applied for the analysis.

The jump distance was determined for each jump within the tracks and the jump angle was defined as the angle between the jump direction of a jump and the direction of the subsequent jump (Kuhn et al., 2021). Accordingly, the corresponding mean

jump distance is described as the mean of the jump distances of both jumps making up the angle.

The mean squared displacement for each track was calculated using

$$MSD = \frac{1}{N-n}\sum_{i=1}^{N-n}(x_i - x_{i+n})^2 + (y_i - y_{i+n})^2\,,\ \ n = 1, \dots, N-1 \tag{1}$$

where x_i and y_i describe the position of the i-th spot within one track, N is the number of spots of the track and n is the time difference between two spots. The first 60% of the curve were fitted with a confined diffusion model using

$$MSD = R^2 \cdot \left(1 - e^{-4 \cdot D^* \cdot \frac{t}{R^2}}\right) + offset \tag{2}$$

with the confinement radius R and the local diffusion coefficient D*. The offset accounts for the localization precision.

5.2.3.5.2.3 Data analysis with ExTrack

To investigate transitions between two states with different diffusion coefficients, tracks derived from TrackIt where further analyzed using ExTrack (Simon et al., 2023), a maximum-likelihood estimation-based method that detects distinct diffusion states in single-molecule trajectories by fitting a multi-state Markovian diffusion model. The starting parameters where selected to ensure the inclusion of all available tracks. For parameter fitting, two spatial dimensions, a maximum diffusion coefficient of 10 $\mu m^2/s$, fraction boundaries ranging from 0.01 to 0.99, two substeps, cell dimensions of [1,2] and a four-frame sliding window were defined. The steady-state option was disabled. Additionally, the localization error for each spot was estimated using Eq. 5 from (Mortensen et al., 2010). To calculate state probabilities, cell dimensions of [1,2], two diffusion states, an eight-frame sliding window, and the estimated localization error were specified. Bootstrapping was performed with 100 iterations and a resampling fraction of 0.8 to ensure robust parameter estimation.

5.2.3.5.3 Imaging of intracellular calcium

To compare the intracellular calcium content of HCT116 WT and Smim26 KO cell lines, free Ca^{2+} was stained using the fluorescent dye Fura-2. Cells were seeded on sterile glass coverslips (25 mm) in 6-well plates and incubated at 37 °C and 5% CO_2 to reach 80 – 90% confluency. The day of the measurement, cell medium was replaced with 2 µM Fura-2/AM (Thermo Fisher Scientific, Waltham, USA) and Pluronic F127 in Opti-MEM™ (Thermo Fisher Scientific, Waltham, USA) and incubated for 30 min at 37 °C and 5% CO_2. Afterwards, the coverslips were placed in fresh Ringer's solution and imaged using a ZEISS live cell imaging setup based on a ZEISS Observer Z.1 (ZEISS Microscopy, Oberkochen, Germany) equipped with an AxioCam MRm CCD camera (ZEISS Microscopy, Oberkochen, Germany) with a 40x oil immersion objective. Illumination control and image recording were performed using a Lambda DG4 high-speed wavelength switcher (Sutter Instruments, Novato, USA) and the ZEN imaging software (ZEISS Microscopy, Oberkochen, Germany). Fura-2/AM fluorescence was measured at 510 nm after excitation at 340 nm or 380 nm, respectively. Intracellular Calcium levels were analyzed by manually drawing regions of interest around cells using ImageJ. Macros were used for background subtraction and calculation of fluorescence intensity ratios.

5.2.3.5.4 Imaging of mitochondrial membrane potential

To determine the mitochondrial membrane potential of HCT116 WT and Smim26 KO cell lines, cells were stained using the fluorescent dye JC-1. Cells were seeded on sterile glass coverslips (25 mm) in 6-well plates and incubated at 37 °C and 5% CO_2 to reach 80 – 90% confluency. The day of the measurement, cell medium was replaced with 1 µM JC-1 (Thermo Fisher Scientific, Waltham, USA) and Pluronic F127 in Opti-MEM™ (Thermo Fisher Scientific, Waltham, USA) and incubated for 30 min at 37 °C and 5% CO_2. Afterwards, the coverslips were placed in fresh Ringer's solution and imaged using the setup as described above (**5.2.3.5.3**). JC-1 fluorescence was measured at 537/42 nm (green) and 620/60 nm (red) after excitation at 480/36 nm. MMP was analyzed by manually drawing regions of interest around cells using ImageJ. Macros were used for background subtraction and calculation of fluorescence intensity ratios.

5.2.3.6 Mitochondrial respirometry using Seahorse XF Analyzer

To determine the respiratory activity of HCT116 WT, Smim26 knockout or various rescue cells, 4.5 x 10^4 HCT116 cells were seeded in XFp 8-well miniplates (Agilent Technologies, Santa Clara, USA) coated with Poly-L-lysine (Sigma-Aldrich, St. Louis, USA) and incubated for 2 days at 37 °C, humidified air and 5% CO_2. Cartridges were prepared according to the manufacturer's protocol. Mitochondrial respirometry was performed using the XFp Cell Mito Stress Test Kit (Agilent Technologies, Santa Clara, USA) according to the manufacturer's recommendations. Oxygen consumption rate (OCR) and extracellular acidification rate (ECAR) upon treatment with oligomyxin (1 µM), FCCP (0.35 µM), and rotenone/antimycin A (1 µM) were measured by a XFp Seahorse Flux Analyzer (Agilent Technologies, Santa Clara, USA).

For normalization, cells were washed with 1x PBS and fixed with 3.7% paraformaldehyde (PFA) in PBS for 10 min at RT. After washing another three times with 1x PBS, nuclei were stained with Hoe33342 (AppliChem, Darmstadt, Germany) at a final concentration of 0.1 µg/ml in 1x PBS for 10 min at RT and washed three times with 1x PBS. Labeled cells were imaged and cell numbers were determined using ImageJ. OCR and ECAR were normalized based on the cell number in each well.

5.2.3.7 Quantification of NAD^+/NADH levels

NAD^+/NADH ratio was determined using the NAD/NADH-GloTM assay (Promega, Madison, USA) according to the manufacturer's protocol with minor changes. Briefly, 4x10^3 HCT116 WT or SMIM26 KO cells were seeded in 50 µl 1x PBS in 96 well plates and lysed by adding 50 µl base solution buffer with 1% DTAB. Of this lysate, 50 µl were transferred to a new well for acid treatment, 25 µl 0.4 M HCl were added and incubated for 15 min at 60 °C followed by equilibration for 10 min at RT. 25 µl 0.5 M Trizma® base were added to the acid treated cells to neutralize the lysates. Next, 50 µl of a 1:1 mix of HCl and Trizma® base were pipetted into the base treated samples. 50 µl of the NAD/NADH-GloTM Detection Reagent were added to all samples and incubated for 1h at RT. Luminescence was measured on a Microplate reader Mithras LB940 (Berthold Technologies, Bad Wildbad, Germany).

5.2.4 Animal models

5.2.4.1 Mouse model

5.2.4.1.1 Mouse husbandry

The Smim26 KO mouse model was generated on a C57BL/6N background (Charles River Laboratories) by targeting exon 1 (ENSMUSE00000828483). A frame-shift deletion was generated using CRISPR/Cas9 technology. The guide RNAs (gRNAs) with the highest score and specificity was designed using http://crispor.tefor.net/. The gRNA (100 ng/µl) was assembled into a ribonucleoprotein (RNP) complex with Cas9 protein (500 ng/µl, Integrated DNA technologies), electroporated into 1-cell zygotes, and transferred into pseudopregnant foster mice. Putative founders were analyzed by PCR and sequencing. A founder harboring a 4 bp deletion, affecting part of exon 1, was chosen for subsequent breeding. Genotyping was performed by PCR. The Forward and Reverse products are 560 bp in the wild-type and 556 bp in the mutant animal. Selected founder was bred with C57Bl/6NCrl wild-type to confirm germ-line transmission of the target deletion.

5.2.4.1.2 Mouse embryo harvest

Heterozygous mice were bred to obtain the homozygous embryos. The day at which a vaginal plug was present was considered as day 0.5 of pregnancy (gestational/ embryonic day E0.5). Female mice were sacrificed and embryos harvested at days E12.5 and E9.5. Yolk sacks were collected for genotyping and embryos were fixed in 4% PFA until at least 28 embryos per stage were collected to assess the viability.

5.2.4.2 Zebrafish model

5.2.4.2.1 Zebrafish husbandry

Zebrafish were raised at 28 °C with a 14/10 h of light/dark cycle. Wild-type TLAB fish correspond to fish obtained by crossing AB with the natural variant TL (TupfelLongfin). All fish experiments were conducted according to Austrian and European guidelines for animal research and approved by local Austrian authorities (protocols for work GZ342445/2016/12 and MA 58-221180-2021-16). Zebrafish *smim26* mutants were generated in this study and are described below.

5.2.4.2.2 Zebrafish knockout lines

smim26 knockout zebrafish were generated using CRISPR/Cas9-mediated mutagenesis. Guide RNAs (gRNAs) targeting the first exon of si:ch211-85n16.3 were injected into one-cell stage zebrafish embryos along with recombinant Cas9 protein (provided by the Molecular Biology Service, IMP).

To identify germline mutant carriers (founders), injected adult fish were crossed with wild-type fish, and their embryos were genotyped by PCR. Embryos displaying a size difference in PCR amplicons were raised to adulthood, where heterozygous fish were confirmed via PCR-based genotyping of fin clips followed by Sanger sequence to identify the nature of the mutation.

To obtain homozygous knockout fish and their wild-type siblings, heterozygous fish were intercrossed.

5.2.4.2.3 Mendelian ratio and zebrafish growth tracking

Heterozygous crosses were performed starting at the F2 generation to produce wild-type, heterozygous, and homozygous (zygotic loss of gene product) knockout larvae. These larvae were raised at a density of 50 per tank. Every two weeks, one tank per genotype was randomly selected for genotyping to track Mendelian representation over time under unsegregated growth conditions.

To genotype larval stages, we followed a published protocol (Lambert et al., 2018). In brief, scales were lysed in 50 mM NaOH at 95 °C for 20 min to extract the DNA, followed by neutralization with 1/10 volume Tris/HCl (pH 8.0). A portion of the lysate was then used for PCR. To enable segregated growth, larvae were genotyped at 3 dpf.

Knockout fish received an additional daily feeding to promote growth. Larval length was measured every two weeks under a stereoscope following minimal anesthesia with 0.01% tricaine. Images of anesthetized fish were captured using a ZEISS Stemi 508 stereomicroscope (0.8× magnification) with FlyCapture2 software.

5.2.4.2.4 Fertility assessment of adult zebrafish

All surviving *smim26* knockout fish developed as males. Sex was determined at 4–5 months post-fertilization based on characteristic zebrafish sexual dimorphism.

To assess fertilization capability, in vivo fertilization rates were measured by mating *smim26* knockout males with wild-type females. Fertilization rates were evaluated approximately 3 hours post-fertilization. At this stage, fertilized embryos had developed to the ~1,000-cell stage, while unfertilized eggs remained at the one-cell stage.

5.2.4.2.5 Zebrafish respiratory analysis

5 dpf larvae from an incross of heterozygous *smim26* mutant parents were genotyped as previously described (Lambert et al., 2018). At 7 dpf, wild-type and homozygous mutant larvae (one per well) were placed into each well of an Agilent XF96e Spheroid microplate containing 180 µl of E3. The basal respiration rate was then recorded using a Seahorse XF96e at 29 °C.

5.2.5 Computational methods

5.2.5.1 Generation of a phylogenetic tree

To generate a phylogenetic tree of SMIM26 in R, homologous sequences were identified using BLASTp and a MSA was generated with the method ClustalOmega using standard parameters (Palme et al., 2015). The phylogenetic tree was constructed using the phangorn package (Schliep, 2011). In short, a distance matrix was computed from the MSA, and a Neighbor-Joining (NJ) tree was constructed as an initial topology. Next, a Maximum Likelihood model was created using the NJ tree as starting topology and optimized with the LG amino acid substitution model, with model parameters and branch lengths being estimated during the optimization.

5.2.5.2 TCGA analysis

5.2.5.2.1 Access and preprocessing of TCGA data

To analyze SMIM26 in patient samples, RNA sequencing data and clinical information were obtained from TCGA (Weinstein et al., 2013). Gene-level read counts and TPM

values were derived from this data, and only primary tumor samples were included in the analysis.

To stratify patients into high- and low-expression groups, optimal cutpoints were calculated separately for different cancer entity cohorts using the R package cutpointr (Thiele and Hirschfeld, 2021). For each gene of interest, repeated cases were averaged per patient, and cutpoints were determined by maximizing the Youden index.

5.2.5.2.2 GSEA of SMIM26-associated pathways

Differential expression between high and low SMIM26 expression groups was performed using DESeq2 (Love et al., 2014). Genes were annotated with org.Hs.eg.db (Marc Carlson, 2017), and enrichment analysis was performed using clusterProfiler (Wu et al., 2021). Hallmark gene sets were obtained from the MSigDB database utilizing the msigdbr package (Igor Dolgalev, 2025). Gene set enrichment scores were calculated using ranked gene lists and plots visualizing the GSEA were generated in R.

5.2.5.2.3 Patient survival analysis

Overall survival analysis was derived from the TCGA clinical follow-up files. Kaplan-Meier survival curves were generated for high and low expression groups as defined by optimal cutpoints (**5.2.5.2.1**) and differences in survival were assessed by log-rank tests and Cox proportional hazard models. The analysis was performed using the survival package (Therneau, 2001; Terry M Therneau, 2024) and visualized with survminer (Kassambara et al., 2016).

5.2.5.2.4 Analysis of SMIM26 expression across cancer entities

Expression of SMIM26 in different cancer entities and their corresponding healthy tissue was analyzed using GEPIA2 (Tang et al., 2019). Therefore, TCGA cancer data of ESCA, STAD, COAD, READ, PAAD, LIHC and CHOL was compared to TCGA normal tissue matched with GTEx data. p-value cutoff was set to 0.01 and $\log_2$-fold change cutoff to 1.

6 Contributions

Live-cell single molecule tracking experiments were performed together with Mara Hofmann in the group of Prof. Dr. J. Christof M. Gebhardt at the Ulm University (Germany)

Viability assays were performed together with Marisa Riester in the group of Prof. Dr. Sven Diederichs at the University Medical Center Freiburg (Germany).

Mouse work was performed by Michaela Prochazkova and Jan Procházka in the group of Prof. Dr. Radislav Sedlacek at the Institute of Molecular Genetics of the CAS (Prague, Czech Republic).

Zebrafish work was performed by Anastasia Chugunova in the group of Prof. Dr. Andrea Pauli at the Research Institute of Molecular Pathology (Vienna, Austria).

The anti-cancer drug screen was performed together with Lukas Wöhrl in the group of Prof. Dr. Christian Werno at the Fraunhofer ITEM (Regensburg, Germany).

Mass spectrometry analysis was performed by Patricia Luckner, Dogukan Yasar, Dr. Erman Kocak and Dr. Astrid Bruckmann at the University of Regensburg or Joerg Fallmann, Dr. Karel Stejskal, Gabriela Krssakova and Dr. Elisabeth Roitinger at the Research Institute of Molecular Pathology (Vienna, Austria).

TCGA analysis was performed together with Dr. Simon Holzinger at the University Hospital Regensburg (Germany).

Norbert Eichner contributed to the sequencing of CRISPR clones and RNAseq by performing the sequencing runs and Gerhard Lehmann performed the data analysis.

We could perform respirometry experiments, mitochondrial membrane potential and cellular calcium measurements in the group of Prof. Dr. Christof Wetzel at the University Hospital Regensburg (Germany)

7 Publications

Parts of this thesis are under revision in the following article:

Heizler K, Chugunova A, Hofmann M, Prochazkova M, Procházka5 J, Ho-Xuan H, Fallmann J, Stejskal K, Krssakova G, Bader S, Kocak E, Yasar D, Luckner P, Lehmann G, König J, Riester M, Roitinger E, Wetzel C, Sedlacek R, Diederichs S, Bruckmann A,. Gebhardt JCM, Pauli A, Meister G. The microprotein SMIM26 coordinates metabolite transport through the outer and inner mitochondrial membranes and is essential for respiratory chain function. Genes Dev.

Furthermore, I contributed to the following articles:

Ho-Xuan H, Glažar P, Latini C, **Heizler K**, Haase J, Hett R, Anders M, Weichmann F, Bruckmann A, Van den Berg D, Hüttelmaier S, Rajewsky N, Hackl C, Meister G. Comprehensive analysis of translation from overexpressed circular RNAs reveals pervasive translation from linear transcripts. Nucleic Acids Res. 2020 Oct 9;48(18):10368-10382. doi: 10.1093/nar/gkaa704. PMID: 32955563; PMCID: PMC7544230.

Ho-Xuan H, Lehmann G, Glazar P, Gypas F, Eichner N, **Heizler K**, Schlitt HJ, Zavolan M, Rajewsky N, Meister G, Hackl C. Gene Expression Signatures of a Preclinical Mouse Model during Colorectal Cancer Progression under Low-Dose Metronomic Chemotherapy. Cancers (Basel). 2020 Dec 26;13(1):49. doi: 10.3390/ cancers13010049. PMID: 33375322; PMCID: PMC7795790.

8 Appendix

8.1 Supplementary Tables

Table 8-1: FLAG-IP-MS details

Protein IDs	Pep.	SC [%]	Score	iBAQ NC I	iBAQ NC II	iBAQ NC III	iBAQ SIM I	iBAQ SIM II	iBAQ SIM III
A2NJV5, KV229	3	19,2	110,69	1,28E+06	4,05E+06	1,88E+06	4,41E+06	2,57E+06	4,81E+06
A0A096LP01+FLAG, SIM26+FLAG	10	83,7	323,31	0,00E+00	0,00E+00	0,00E+00	5,40E+06	9,56E+05	2,52E+06
A0FGR8, ESYT2	7	9	46,944	0,00E+00	0,00E+00	0,00E+00	3,96E+04	9,52E+03	1,60E+04
A2RRP1, NBAS	21	11,2	146,32	0,00E+00	0,00E+00	0,00E+00	2,13E+04	6,46E+03	1,37E+04
A3KMH1, VWA8	25	17,7	190,86	0,00E+00	2,03E+02	1,13E+03	2,66E+04	1,86E+04	2,28E+04
A4D1E9, GTPBA	4	14	47,385	0,00E+00	0,00E+00	0,00E+00	3,25E+04	5,82E+03	8,59E+03
A4D1U4, DEN11	2	6,4	11,763	0,00E+00	0,00E+00	0,00E+00	9,73E+03	3,57E+03	1,07E+03
A5YKK6, CNOT1	14	7,3	84,292	0,00E+00	0,00E+00	1,95E+02	7,49E+03	1,21E+03	7,76E+03
A6NCN2, KR87P	11	32,9	18,569	7,13E+03	0,00E+00	0,00E+00	0,00E+00	0,00E+00	1,65E+04
A6NEC2, PSAL	1	2,7	6,8691	0,00E+00	0,00E+00	0,00E+00	8,27E+03	4,05E+03	3,50E+03
A6NHR9, SMHD1	2	1,1	11,437	0,00E+00	0,00E+00	0,00E+00	8,80E+02	0,00E+00	2,41E+02
A6NJ78, MET15	9	29,5	114,46	0,00E+00	0,00E+00	0,00E+00	1,18E+05	3,20E+04	5,92E+04
A8MXV4, NUD19	1	3,7	6,9714	0,00E+00	0,00E+00	0,00E+00	5,37E+03	0,00E+00	0,00E+00
Q99613, EIF3C	1	1,1	6,4235	0,00E+00	0,00E+00	0,00E+00	0,00E+00	0,00E+00	2,41E+03
P0CG08, GPHRB	2	5,3	11,847	0,00E+00	0,00E+00	0,00E+00	1,67E+04	0,00E+00	7,19E+03
L0R6Q1, S35U4	3	36,9	18,137	0,00E+00	0,00E+00	0,00E+00	1,74E+04	0,00E+00	2,28E+04
M0R2J8, DCDC1	1	0,8	6,3343	0,00E+00	0,00E+00	0,00E+00	0,00E+00	0,00E+00	1,05E+03
O00116, ADAS	5	12,3	35,663	0,00E+00	0,00E+00	0,00E+00	2,20E+04	9,98E+03	0,00E+00
O00124, UBXN8	1	6,3	9,6347	0,00E+00	0,00E+00	0,00E+00	6,22E+03	0,00E+00	0,00E+00
O00148, DX39A	3	8,4	20,078	0,00E+00	0,00E+00	0,00E+00	9,64E+03	7,71E+03	1,28E+04
O00159, MYO1C	18	23,1	148,64	0,00E+00	5,49E+04	2,69E+04	1,36E+04	2,92E+04	1,43E+04
O00165, HAX1	14	64,2	323,31	0,00E+00	6,82E+03	1,22E+04	6,02E+05	2,50E+05	3,19E+05
O00192, ARVC	4	6,3	24,306	0,00E+00	0,00E+00	0,00E+00	7,16E+03	0,00E+00	1,20E+03
O00217, NDUS8	2	9,5	12,096	0,00E+00	0,00E+00	0,00E+00	9,28E+03	0,00E+00	4,53E+04
O00268, TAF4	1	1,3	7,2182	0,00E+00	2,56E+03	3,87E+03	0,00E+00	1,74E+03	0,00E+00
O00303, EIF3F	3	14,3	24,548	0,00E+00	0,00E+00	1,47E+03	3,66E+03	2,37E+04	2,82E+04
O00400, ACATN	2	4,9	13,266	0,00E+00	0,00E+00	0,00E+00	2,17E+04	7,16E+03	1,83E+04
O00410, IPO5	11	14,7	144,12	0,00E+00	9,70E+02	8,59E+02	6,45E+04	3,29E+04	4,84E+04
O00411, RPOM	8	9,5	51,568	0,00E+00	0,00E+00	1,49E+03	1,38E+04	6,66E+03	5,60E+03
O00425, IF2B3	5	12,1	19,41	0,00E+00	0,00E+00	7,00E+03	0,00E+00	3,56E+03	1,01E+04
O00461, GOLI4	1	1,9	7,7436	0,00E+00	0,00E+00	0,00E+00	0,00E+00	3,21E+03	0,00E+00
O00469, PLOD2	3	6	23,301	0,00E+00	0,00E+00	0,00E+00	1,01E+04	7,77E+03	5,77E+03
O00483, NDUA4	2	27,2	19,099	0,00E+00	0,00E+00	0,00E+00	1,80E+05	0,00E+00	2,51E+05
O00571, DDX3X	8	16,8	53,322	0,00E+00	0,00E+00	1,62E+03	1,80E+04	5,14E+03	1,33E+04
O00767, ACOD	4	19,8	68,427	0,00E+00	0,00E+00	0,00E+00	1,12E+05	9,38E+04	8,66E+04
O14654, IRS4	17	22,4	114,08	0,00E+00	0,00E+00	0,00E+00	5,74E+04	8,25E+03	1,65E+04

O14656, TOR1A	3	10,8	17,541	0,00E+00	0,00E+00	0,00E+00	6,62E+03	1,10E+04	4,08E+03
Q99666, RGPD5	3	2,2	6,6082	0,00E+00	0,00E+00	0,00E+00	1,07E+03	0,00E+00	0,00E+00
O14734, ACOT8	3	16	84,839	0,00E+00	0,00E+00	0,00E+00	8,33E+04	4,80E+04	4,88E+04
O14735, CDIPT	3	19,2	29,841	0,00E+00	0,00E+00	0,00E+00	7,93E+04	6,35E+04	1,26E+05
O14744, ANM5	21	38,5	263,58	7,75E+04	8,37E+05	3,80E+05	9,15E+03	1,75E+05	6,66E+04
O14773, TPP1	3	9,8	17,81	0,00E+00	0,00E+00	0,00E+00	4,79E+03	7,45E+03	1,26E+04
O14828, SCAM3	5	22,8	74,733	0,00E+00	0,00E+00	0,00E+00	3,34E+05	1,55E+05	1,64E+05
O14880, MGST3	3	18,4	31,06	0,00E+00	0,00E+00	6,54E+03	3,08E+05	4,37E+04	1,81E+05
O14925, TIM23	2	12,9	39,248	0,00E+00	0,00E+00	0,00E+00	1,03E+05	0,00E+00	7,09E+04
O14949, QCR8	3	32,9	28,588	0,00E+00	0,00E+00	0,00E+00	9,11E+04	3,39E+04	1,49E+05
P19105, ML12A	1	6,4	6,3474	0,00E+00	0,00E+00	0,00E+00	8,87E+03	0,00E+00	0,00E+00
O14967, CLGN	3	8,9	34,096	0,00E+00	0,00E+00	0,00E+00	7,47E+03	1,89E+04	1,70E+04
O14979, HNRDL	1	3,8	6,5119	0,00E+00	0,00E+00	3,36E+03	0,00E+00	0,00E+00	0,00E+00
O14980, XPO1	5	6,3	30,092	0,00E+00	0,00E+00	0,00E+00	0,00E+00	1,46E+03	7,12E+03
O15020, SPTN2	9	4,9	41,744	0,00E+00	0,00E+00	1,95E+02	7,97E+02	3,81E+02	2,91E+03
O15027, SC16A	2	2,2	11,201	0,00E+00	0,00E+00	0,00E+00	1,19E+03	0,00E+00	4,26E+02
O15091, MRPP3	5	13,9	38,821	0,00E+00	0,00E+00	0,00E+00	0,00E+00	1,20E+04	2,93E+04
O15118, NPC1	1	0,9	6,5184	0,00E+00	0,00E+00	0,00E+00	1,44E+03	0,00E+00	1,25E+03
O15127, SCAM2	1	6,1	7,238	0,00E+00	0,00E+00	0,00E+00	1,53E+04	0,00E+00	0,00E+00
O15173, PGRC2	2	14,8	13,382	0,00E+00	0,00E+00	0,00E+00	2,41E+04	0,00E+00	1,22E+04
O15228, GNPAT	3	7,6	23	0,00E+00	0,00E+00	0,00E+00	1,87E+03	3,90E+03	2,00E+03
O15260, SURF4	2	10,8	27,479	0,00E+00	0,00E+00	0,00E+00	4,28E+04	3,15E+04	5,05E+04
O15269, SPTC1	8	27,5	323,31	4,12E+03	1,00E+04	9,42E+03	2,17E+05	1,24E+05	2,13E+05
O15270, SPTC2	5	13	32,532	0,00E+00	0,00E+00	0,00E+00	0,00E+00	8,34E+03	2,77E+04
O15321, TM9S1	2	3,8	12,551	0,00E+00	0,00E+00	0,00E+00	2,31E+04	0,00E+00	0,00E+00
O15439, MRP4	11	10,5	87,285	0,00E+00	0,00E+00	0,00E+00	2,09E+04	1,29E+04	9,22E+03
O15460, P4HA2	5	14,4	36,412	0,00E+00	0,00E+00	0,00E+00	0,00E+00	4,35E+03	1,22E+04
O43149, ZZEF1	1	0,4	6,338	0,00E+00	0,00E+00	0,00E+00	2,77E+02	0,00E+00	0,00E+00
O43150, ASAP2	1	0,8	7,1478	0,00E+00	4,15E+04	0,00E+00	0,00E+00	0,00E+00	0,00E+00
O43264, ZW10	5	10,4	47,126	0,00E+00	0,00E+00	0,00E+00	3,08E+04	8,28E+03	3,00E+04
O43390, HNRPR	4	8,7	17,579	0,00E+00	0,00E+00	5,31E+03	0,00E+00	0,00E+00	0,00E+00
O43464, HTRA2	7	19,9	44,938	0,00E+00	0,00E+00	0,00E+00	5,54E+04	3,67E+03	5,05E+03
O43488, ARK72	1	5,3	6,8244	0,00E+00	3,71E+03	0,00E+00	0,00E+00	0,00E+00	0,00E+00
O43505, B4GA1	6	15,9	38,182	0,00E+00	0,00E+00	0,00E+00	5,58E+04	2,88E+03	2,32E+04
O43615, TIM44	8	18,8	66,563	0,00E+00	0,00E+00	1,19E+03	9,72E+04	2,71E+04	2,35E+04
O43678, NDUA2	2	31,3	11,684	0,00E+00	0,00E+00	0,00E+00	2,99E+04	0,00E+00	5,13E+04
O43772, MCAT	2	5,3	11,645	0,00E+00	0,00E+00	0,00E+00	1,42E+04	0,00E+00	0,00E+00
O43795, MYO1B	17	21,6	136,93	0,00E+00	2,54E+04	1,69E+04	3,31E+03	9,59E+03	9,57E+03
O43808, PM34	3	13,4	18,255	0,00E+00	0,00E+00	0,00E+00	2,06E+04	7,03E+03	1,23E+04
O43819, SCO2	2	10,5	13,97	0,00E+00	0,00E+00	0,00E+00	6,94E+03	0,00E+00	1,12E+04
O43837, IDH3B	4	15,6	29,749	0,00E+00	0,00E+00	0,00E+00	1,17E+04	1,70E+04	1,81E+04
O43852, CALU	8	35,2	106,24	0,00E+00	0,00E+00	0,00E+00	1,47E+05	4,90E+03	8,28E+04
O43920, NDUS5	1	11,3	7,498	0,00E+00	0,00E+00	0,00E+00	3,39E+04	0,00E+00	2,77E+04
O43933, PEX1	1	0,9	6,3551	0,00E+00	0,00E+00	0,00E+00	9,19E+02	0,00E+00	1,24E+03
O60220, TIM8A	1	11,3	11,32	0,00E+00	0,00E+00	0,00E+00	9,34E+04	4,23E+04	0,00E+00
O60245, PCDH7	2	3,1	11,394	0,00E+00	0,00E+00	0,00E+00	4,46E+03	1,13E+03	0,00E+00

O60264, SMCA5	1	1	6,8006	0,00E+00	0,00E+00	0,00E+00	2,17E+03	0,00E+00	0,00E+00
O60313, OPA1	19	24,2	175,54	0,00E+00	0,00E+00	1,34E+03	8,78E+04	3,27E+04	4,57E+04
O60427, FADS1	3	8,8	17,853	0,00E+00	0,00E+00	0,00E+00	4,73E+03	4,59E+03	1,17E+04
O60488, ACSL4	4	9,1	11,185	0,00E+00	0,00E+00	0,00E+00	0,00E+00	3,16E+03	0,00E+00
O60493, SNX3	1	8,6	6,4442	0,00E+00	0,00E+00	0,00E+00	2,02E+04	0,00E+00	1,08E+04
O60506, HNRPQ	4	8,8	25,826	0,00E+00	4,55E+03	8,35E+03	0,00E+00	0,00E+00	9,70E+02
O60518, RNBP6	6	8,1	55,861	0,00E+00	0,00E+00	0,00E+00	9,25E+03	7,07E+02	2,85E+03
O60568, PLOD3	3	5,4	19,843	0,00E+00	0,00E+00	0,00E+00	9,45E+02	4,16E+03	1,23E+03
O60716, CTND1	12	14,8	78,694	0,00E+00	0,00E+00	0,00E+00	3,45E+04	1,89E+04	2,54E+04
O60762, DPM1	12	50,4	153,71	0,00E+00	0,00E+00	0,00E+00	2,78E+05	1,13E+05	1,92E+05
O60763, USO1	4	5,2	24,128	0,00E+00	0,00E+00	0,00E+00	2,81E+03	1,34E+03	3,18E+03
O60783, RT14	2	21,9	30,02	1,34E+04	3,56E+04	2,35E+04	1,20E+05	5,21E+04	8,54E+04
Q99880, H2B1L	2	19	29,412	0,00E+00	2,02E+05	5,59E+04	5,55E+04	9,12E+04	2,65E+05
O60830, TI17B	4	34,9	59,605	0,00E+00	0,00E+00	0,00E+00	9,77E+04	3,58E+04	8,62E+04
O60831, PRAF2	1	6,2	6,5648	0,00E+00	0,00E+00	0,00E+00	0,00E+00	0,00E+00	1,04E+04
O75027, ABCB7	9	16,4	58,646	0,00E+00	2,88E+03	0,00E+00	1,10E+04	5,72E+04	2,67E+04
O75063, XYLK	3	10,5	21,313	0,00E+00	0,00E+00	0,00E+00	1,11E+04	5,15E+03	3,44E+03
O75127, PTCD1	8	19	49,662	0,00E+00	0,00E+00	0,00E+00	2,98E+04	1,12E+04	2,24E+04
O75131, CPNE3	2	4,7	12,613	0,00E+00	0,00E+00	0,00E+00	0,00E+00	7,45E+03	0,00E+00
O75165, DJC13	14	9,1	88,642	0,00E+00	0,00E+00	0,00E+00	9,91E+03	2,52E+03	3,50E+03
O75190, DNJB6	4	15,6	28,699	0,00E+00	0,00E+00	0,00E+00	3,08E+04	1,13E+04	5,43E+04
O75251, NDUS7	2	10,8	12,214	0,00E+00	0,00E+00	0,00E+00	2,93E+04	0,00E+00	3,58E+04
O75306, NDUS2	15	43,2	229,53	0,00E+00	3,91E+03	3,15E+03	4,48E+05	6,09E+04	1,68E+05
O75323, NIPS2	6	25,5	48,753	0,00E+00	0,00E+00	0,00E+00	2,35E+05	6,31E+04	1,29E+05
O75352, MPU1	2	9,7	15,275	0,00E+00	0,00E+00	0,00E+00	0,00E+00	0,00E+00	1,53E+05
O75369, FLNB	5	2,7	24,902	0,00E+00	0,00E+00	0,00E+00	2,21E+03	1,74E+03	1,54E+03
O75380, NDUS6	2	29	11,474	0,00E+00	0,00E+00	0,00E+00	1,11E+04	0,00E+00	1,02E+04
O75390, CISY	5	13,1	34,403	0,00E+00	0,00E+00	0,00E+00	6,94E+04	2,48E+04	2,94E+04
O75431, MTX2	6	31,6	123,16	0,00E+00	0,00E+00	0,00E+00	4,83E+04	1,04E+05	3,37E+04
O75439, MPPB	7	18,6	68,55	0,00E+00	0,00E+00	0,00E+00	9,29E+04	3,27E+04	5,66E+04
O75477, ERLN1	6	22,7	35,13	0,00E+00	0,00E+00	0,00E+00	1,13E+05	7,16E+04	6,17E+04
O75489, NDUS3	12	48,5	156,36	1,20E+03	6,79E+03	1,41E+04	3,81E+05	1,45E+05	2,54E+05
O75533, SF3B1	3	3,9	17,006	0,00E+00	0,00E+00	0,00E+00	0,00E+00	0,00E+00	3,01E+03
O75600, KBL	5	19,3	42,903	0,00E+00	0,00E+00	0,00E+00	1,78E+05	5,06E+04	9,51E+04
O75616, ERAL1	7	22,4	60,281	0,00E+00	0,00E+00	7,28E+03	1,75E+05	9,01E+04	5,23E+04
O75643, U520	4	2,8	27,875	0,00E+00	0,00E+00	0,00E+00	3,60E+03	6,82E+02	2,48E+03
O75648, MTU1	4	11,2	25,613	0,00E+00	0,00E+00	0,00E+00	1,87E+04	0,00E+00	9,14E+02
O75688, PPM1B	2	5,6	14,59	4,77E+03	1,89E+04	2,22E+04	0,00E+00	0,00E+00	6,70E+03
O75694, NU155	7	6,9	56,682	0,00E+00	0,00E+00	0,00E+00	1,49E+04	3,44E+03	1,85E+04
O75746, CMC1	24	43,8	264,71	1,23E+03	6,27E+03	9,30E+03	3,26E+05	1,80E+05	2,57E+05
P16152, CBR1	1	4,7	6,5729	0,00E+00	2,37E+03	0,00E+00	0,00E+00	0,00E+00	0,00E+00
O75844, FACE1	5	13,5	78,643	0,00E+00	0,00E+00	0,00E+00	1,50E+05	7,59E+04	1,54E+05
O75880, SCO1	4	12	27,838	0,00E+00	0,00E+00	0,00E+00	1,62E+04	2,45E+04	5,60E+04
O75891, AL1L1	3	4,4	24,86	0,00E+00	6,66E+02	0,00E+00	1,02E+04	6,35E+03	7,59E+03
O75907, DGAT1	1	4,3	8,0009	0,00E+00	0,00E+00	0,00E+00	0,00E+00	5,50E+03	5,92E+03
O75955, FLOT1	9	30	74,999	0,00E+00	0,00E+00	0,00E+00	4,76E+04	3,59E+04	3,62E+04

O75964, ATP5L	7	54,4	94,388	0,00E+00	2,33E+04	2,02E+04	1,25E+06	7,72E+05	2,28E+06
O75976, CBPD	18	15,7	123,31	5,96E+02	0,00E+00	0,00E+00	7,44E+04	3,29E+04	2,78E+04
O76031, CLPX	15	29,9	123,32	1,92E+03	0,00E+00	0,00E+00	0,00E+00	1,50E+05	1,37E+05
O76062, ERG24	2	9,3	13,909	0,00E+00	0,00E+00	0,00E+00	0,00E+00	1,37E+04	2,04E+04
O76094, SRP72	2	5,2	11,231	0,00E+00	0,00E+00	0,00E+00	0,00E+00	2,27E+03	9,67E+02
O94813, SLIT2	5	5,5	34,676	0,00E+00	0,00E+00	0,00E+00	6,47E+03	4,92E+03	2,59E+03
O94826, TOM70	3	10,2	49,874	0,00E+00	0,00E+00	0,00E+00	1,54E+04	3,00E+04	9,82E+03
O94832, MYO1D	13	15,4	93,537	0,00E+00	3,22E+04	7,12E+03	0,00E+00	1,54E+03	1,35E+03
O94874, UFL1	13	21,9	95,827	0,00E+00	0,00E+00	0,00E+00	6,17E+04	9,57E+03	4,08E+04
O94898, LRIG2	2	2,5	12,654	0,00E+00	0,00E+00	0,00E+00	2,32E+03	1,09E+03	0,00E+00
O94905, ERLN2	9	32,7	126,07	0,00E+00	0,00E+00	0,00E+00	6,17E+05	3,02E+05	4,56E+05
O94925, GLSK	7	17	48,753	0,00E+00	0,00E+00	0,00E+00	0,00E+00	2,40E+04	3,35E+04
O94966, UBP19	1	0,8	6,9864	0,00E+00	0,00E+00	0,00E+00	0,00E+00	0,00E+00	0,00E+00
O95140, MFN2	11	17,7	89,236	0,00E+00	0,00E+00	0,00E+00	7,63E+04	7,38E+03	1,26E+04
O95168, NDUB4	4	31	26,135	0,00E+00	0,00E+00	0,00E+00	1,93E+05	1,19E+05	1,17E+05
O95182, NDUA7	2	24,8	12,78	0,00E+00	0,00E+00	0,00E+00	0,00E+00	0,00E+00	4,69E+04
O95202, LETM1	9	16,9	61,313	0,00E+00	0,00E+00	0,00E+00	5,25E+04	3,30E+04	1,23E+04
O95258, UCP5	4	16,6	29,169	0,00E+00	0,00E+00	0,00E+00	5,32E+04	2,91E+04	4,58E+04
O95292, VAPB	1	6,6	6,3589	0,00E+00	0,00E+00	0,00E+00	5,42E+03	0,00E+00	0,00E+00
O95298, NDUC2	3	22,7	19,16	0,00E+00	0,00E+00	0,00E+00	0,00E+00	3,38E+04	2,38E+04
O95299, NDUAA	11	41,7	323,31	2,70E+03	6,22E+03	1,42E+04	3,42E+05	1,28E+05	2,42E+05
O95347, SMC2	3	3,1	18,357	0,00E+00	0,00E+00	0,00E+00	4,99E+03	0,00E+00	0,00E+00
O95363, SYFM	2	5,1	12,06	0,00E+00	0,00E+00	0,00E+00	9,61E+03	0,00E+00	2,05E+03
O95373, IPO7	1	0,9	6,7146	0,00E+00	0,00E+00	0,00E+00	4,06E+03	0,00E+00	0,00E+00
O95399, UTS2	1	6,5	7,2676	0,00E+00	4,82E+04	3,93E+04	5,93E+05	2,34E+05	2,56E+05
O95490, AGRL2	5	4,5	31,131	0,00E+00	0,00E+00	0,00E+00	1,30E+04	1,00E+04	0,00E+00
O95563, MPC2	1	9,4	7,2443	0,00E+00	0,00E+00	0,00E+00	0,00E+00	1,06E+04	2,52E+04
O95573, ACSL3	13	23,9	111,49	0,00E+00	1,59E+03	0,00E+00	9,17E+04	8,33E+04	1,14E+05
O95674, CDS2	3	10,8	21,733	0,00E+00	0,00E+00	0,00E+00	8,61E+04	5,08E+04	3,53E+04
O95714, HERC2	2	0,5	11,665	0,00E+00	0,00E+00	0,00E+00	0,00E+00	2,93E+02	0,00E+00
O95831, AIFM1	21	43,7	323,31	9,44E+03	4,05E+04	5,00E+04	2,31E+04	5,71E+05	3,37E+05
O95864, FADS2	2	5	13,844	0,00E+00	0,00E+00	0,00E+00	0,00E+00	4,49E+03	6,97E+03
O95881, TXD12	6	43,6	128,34	1,65E+05	1,96E+05	3,01E+05	2,43E+05	2,47E+05	4,72E+05
O95996, APCL	1	0,5	6,4062	0,00E+00	0,00E+00	0,00E+00	0,00E+00	0,00E+00	6,46E+02
O96000, NDUBA	2	14,5	11,32	0,00E+00	0,00E+00	0,00E+00	0,00E+00	5,58E+03	1,64E+04
O96005, CLPT1	7	15,5	66,502	0,00E+00	0,00E+00	0,00E+00	2,33E+04	1,92E+04	7,78E+03
O96008, TOM40	6	19,7	96,299	0,00E+00	0,00E+00	0,00E+00	5,47E+05	1,91E+05	3,46E+05
P00403, COX2	4	18,9	30,878	0,00E+00	0,00E+00	0,00E+00	1,40E+05	3,69E+04	3,12E+05
P00505, AATM	4	10,5	36,051	0,00E+00	0,00E+00	3,47E+03	3,90E+04	1,33E+04	2,21E+04
P00533, EGFR	2	1,6	11,2	0,00E+00	0,00E+00	0,00E+00	1,45E+03	1,59E+03	0,00E+00
P00846, ATP6	1	4,4	6,834	0,00E+00	1,09E+05	7,50E+04	5,69E+05	7,76E+05	1,73E+06
P01130, LDLR	1	1,9	8,2858	0,00E+00	0,00E+00	0,00E+00	2,02E+03	9,28E+02	1,41E+03
P01859, IGHG2	1	2,8	7,0476	0,00E+00	0,00E+00	0,00E+00	0,00E+00	0,00E+00	0,00E+00
P01876, IGHA1	3	9,6	17,708	0,00E+00	0,00E+00	0,00E+00	0,00E+00	1,48E+04	0,00E+00
P01889, HLAB	6	20,7	20,364	0,00E+00	0,00E+00	0,00E+00	4,63E+04	1,49E+04	3,07E+04
P02786, TFR1	20	33,3	266,64	0,00E+00	0,00E+00	0,00E+00	3,60E+05	4,29E+04	3,94E+04

P02810, PRPC	1	10,2	7,7805	0,00E+00	0,00E+00	0,00E+00	0,00E+00	2,07E+04	0,00E+00
P04035, HMDH	2	3	12,691	0,00E+00	0,00E+00	0,00E+00	4,45E+03	0,00E+00	0,00E+00
P04062, GLCM	1	3	6,7017	0,00E+00	0,00E+00	0,00E+00	0,00E+00	0,00E+00	3,24E+03
P04080, CYTB	1	12,2	7,1494	0,00E+00	3,73E+04	0,00E+00	0,00E+00	0,00E+00	0,00E+00
P04083, ANXA1	1	4,6	6,4922	0,00E+00	0,00E+00	0,00E+00	0,00E+00	3,29E+03	0,00E+00
P04114, APOB	3	0,8	11,636	0,00E+00	0,00E+00	0,00E+00	2,15E+03	2,11E+02	0,00E+00
P04181, OAT	11	34,6	113,56	6,80E+04	1,12E+05	1,98E+05	2,88E+05	2,47E+05	1,81E+05
P04279, SEMG1	3	9,5	20,796	0,00E+00	1,65E+04	0,00E+00	0,00E+00	0,00E+00	0,00E+00
P04406, G3P	4	19,7	30,649	0,00E+00	2,66E+04	0,00E+00	1,31E+04	6,45E+03	0,00E+00
P04439, HLAA	4	14	7,5197	2,25E+03	0,00E+00	0,00E+00	5,46E+04	2,85E+04	2,75E+04
P04626, ERBB2	1	1,7	9,9345	0,00E+00	0,00E+00	0,00E+00	0,00E+00	2,24E+03	2,51E+03
P04637, P53	3	10,4	45,021	8,24E+03	6,96E+03	6,08E+03	3,77E+04	1,21E+04	4,44E+03
P04792, HSPB1	3	21	21,598	2,06E+03	0,00E+00	0,00E+00	4,20E+04	2,04E+04	8,56E+03
P04843, RPN1	24	55	319,47	2,19E+03	2,54E+04	2,69E+04	5,51E+05	4,67E+05	6,12E+05
P04844, RPN2	23	62,6	323,31	2,51E+03	1,17E+03	2,44E+03	7,41E+04	3,87E+05	4,66E+05
P04899, GNAI2	6	23,4	25,034	0,00E+00	0,00E+00	0,00E+00	5,18E+04	5,90E+04	3,93E+04
Q99878, H2A1J	3	27,3	54,466	1,85E+05	5,63E+05	6,18E+05	3,54E+05	1,36E+05	8,17E+05
P04920, B3A2	3	2,9	18,593	0,00E+00	0,00E+00	0,00E+00	1,07E+04	3,13E+03	0,00E+00
P05023, AT1A1	33	37,3	323,31	7,14E+03	3,49E+04	3,64E+04	2,14E+06	1,23E+06	1,16E+06
P05026, AT1B1	1	3,6	9,041	0,00E+00	0,00E+00	0,00E+00	1,68E+04	1,42E+04	2,13E+04
P05067, A4	2	2,9	13,711	0,00E+00	0,00E+00	0,00E+00	1,22E+04	5,11E+03	5,11E+03
P05141, ADT2	15	44,3	250,73	4,48E+05	1,09E+06	1,22E+06	2,46E+06	5,26E+05	2,13E+06
P05165, PCCA	1	2,1	6,8641	0,00E+00	0,00E+00	0,00E+00	2,26E+03	2,28E+03	0,00E+00
P05386, RLA1	1	14	8,9572	3,03E+04	6,35E+04	3,93E+04	1,01E+05	0,00E+00	5,58E+04
P05387, RLA2	4	69,6	28,324	0,00E+00	0,00E+00	0,00E+00	0,00E+00	0,00E+00	5,27E+04
P05388, RLA0	7	31,2	220,7	3,11E+04	1,19E+05	1,09E+05	5,16E+05	4,19E+05	6,80E+05
P06280, AGAL	1	2,8	7,5839	0,00E+00	0,00E+00	0,00E+00	1,31E+04	6,50E+03	9,16E+03
P06493, CDK1	2	10,8	12,725	0,00E+00	0,00E+00	0,00E+00	5,41E+03	0,00E+00	0,00E+00
P06576, ATPB	14	40,3	323,31	0,00E+00	7,60E+03	1,45E+03	1,52E+05	1,18E+05	2,28E+05
P06702, S10A9	2	24,6	14,682	4,25E+04	2,01E+04	0,00E+00	0,00E+00	2,06E+04	0,00E+00
P06730, IF4E	1	6,5	6,8062	0,00E+00	0,00E+00	0,00E+00	0,00E+00	0,00E+00	1,47E+04
P06733, ENOA	6	23	42,359	0,00E+00	4,42E+04	0,00E+00	0,00E+00	0,00E+00	1,74E+03
P06748, NPM	1	4,4	7,3592	0,00E+00	2,87E+03	0,00E+00	1,16E+04	0,00E+00	1,40E+04
P07237, PDIA1	3	12	35,82	0,00E+00	2,61E+03	0,00E+00	2,38E+03	5,30E+03	5,45E+03
P07355, ANXA2	4	13	24,439	0,00E+00	0,00E+00	0,00E+00	0,00E+00	1,52E+04	0,00E+00
P07384, CAN1	7	13,3	45,331	0,00E+00	0,00E+00	0,00E+00	1,89E+03	9,41E+03	8,81E+03
P07437, TBB5	14	47,1	166,08	0,00E+00	5,68E+03	0,00E+00	1,72E+05	1,73E+05	3,02E+05
P07814, SYEP	14	11,8	90,918	0,00E+00	0,00E+00	0,00E+00	3,59E+04	2,88E+03	1,75E+04
P07900, HS90A	10	16,1	27,196	0,00E+00	0,00E+00	0,00E+00	8,89E+03	1,30E+04	3,25E+03
P07910, HNRPC	5	19	49,778	0,00E+00	7,43E+04	8,73E+04	1,12E+05	8,71E+04	2,02E+05
P08133, ANXA6	5	10,7	39,57	0,00E+00	0,00E+00	0,00E+00	0,00E+00	1,11E+04	0,00E+00
P08134, RHOC	1	8,8	15,773	0,00E+00	0,00E+00	0,00E+00	9,83E+03	2,90E+04	3,82E+04
P08183, MDR1	2	2,7	11,427	0,00E+00	0,00E+00	0,00E+00	9,90E+02	0,00E+00	8,55E+02
P08195, 4F2	16	32,1	124,56	0,00E+00	2,40E+03	0,00E+00	2,34E+05	1,44E+05	1,09E+05
P08238, HS90B	14	24,2	108,39	0,00E+00	5,82E+03	7,51E+03	1,36E+05	1,09E+05	9,52E+04
P08240, SRPRA	3	8,9	22,479	0,00E+00	0,00E+00	0,00E+00	4,43E+03	3,74E+03	4,09E+03

P08559, ODPA	4	17,2	30,471	0,00E+00	8,30E+03	7,44E+03	8,62E+04	6,84E+04	3,73E+04
P08574, CY1	3	12,6	28,211	0,00E+00	0,00E+00	0,00E+00	2,89E+04	1,54E+04	3,13E+04
P08670, VIME	6	14,6	43,073	0,00E+00	1,16E+04	1,21E+04	4,30E+03	4,19E+03	1,51E+04
P08754, GNAI3	7	26,6	83,069	0,00E+00	0,00E+00	0,00E+00	1,70E+05	2,39E+05	1,20E+05
P08758, ANXA5	9	32,5	98,736	0,00E+00	0,00E+00	0,00E+00	0,00E+00	1,85E+05	2,77E+03
P08865, RSSA	3	15,3	21,954	0,00E+00	1,65E+04	0,00E+00	5,04E+03	4,89E+04	4,13E+04
P09001, RM03	2	6	13,873	0,00E+00	5,91E+03	0,00E+00	1,44E+04	0,00E+00	1,35E+04
P09110, THIK	2	7,5	12,581	0,00E+00	0,00E+00	0,00E+00	7,02E+03	1,77E+03	0,00E+00
P09211, GSTP1	3	22,4	22,191	0,00E+00	7,30E+04	0,00E+00	0,00E+00	0,00E+00	0,00E+00
P09543, CN37	4	13,1	34,767	0,00E+00	3,18E+03	0,00E+00	5,76E+04	2,62E+04	1,32E+04
Q32P51, RA1L2	1	5	7,2524	0,00E+00	6,51E+03	0,00E+00	0,00E+00	0,00E+00	6,02E+03
P09874, PARP1	4	5	25,79	0,00E+00	0,00E+00	0,00E+00	1,80E+04	1,13E+04	5,79E+03
P62987, RL40	3	26,6	161,05	2,36E+04	1,33E+04	4,96E+04	2,58E+06	1,40E+06	2,04E+06
P0DMV9, HS71B	16	40,9	162,83	1,03E+03	1,57E+03	5,89E+03	1,65E+05	1,43E+05	1,50E+05
P10321, HLAC	8	29,2	85,646	0,00E+00	3,83E+03	4,66E+03	2,43E+05	8,99E+04	1,68E+05
P16403, H12	2	10,8	12,401	0,00E+00	0,00E+00	0,00E+00	0,00E+00	2,90E+04	6,86E+04
P10515, ODP2	5	9,3	34,251	0,00E+00	1,90E+04	8,24E+03	6,21E+04	3,36E+04	3,64E+04
P10586, PTPRF	5	3,3	31,282	0,00E+00	0,00E+00	0,00E+00	3,89E+03	1,78E+03	0,00E+00
P10599, THIO	1	12,4	7,0002	0,00E+00	3,41E+04	0,00E+00	0,00E+00	0,00E+00	2,34E+04
P10809, CH60	23	52,4	323,31	1,04E+04	7,76E+04	7,72E+04	5,90E+04	1,07E+06	5,02E+05
P11021, BIP	26	45	323,31	3,61E+04	5,10E+04	6,85E+04	1,18E+06	9,02E+05	6,71E+05
P11142, HSP7C	16	37,5	171,85	0,00E+00	1,40E+04	8,98E+03	2,63E+05	2,95E+05	2,09E+05
P11166, GTR1	6	14,8	39,074	0,00E+00	0,00E+00	0,00E+00	2,91E+05	4,37E+04	8,18E+04
P11177, ODPB	7	26,2	72,064	0,00E+00	1,30E+04	7,58E+03	1,59E+05	2,03E+05	7,63E+04
P11279, LAMP1	2	6	13,576	0,00E+00	0,00E+00	0,00E+00	1,04E+04	1,77E+04	4,84E+03
P11310, ACADM	15	40,4	323,31	3,17E+03	0,00E+00	2,22E+03	1,66E+06	4,51E+05	3,36E+05
P11388, TOP2A	2	1,5	11,585	0,00E+00	0,00E+00	0,00E+00	2,00E+03	0,00E+00	0,00E+00
P11498, PYC	17	21	164,33	0,00E+00	0,00E+00	0,00E+00	8,22E+04	8,37E+03	1,88E+03
P11586, C1TC	6	8,3	36,219	0,00E+00	0,00E+00	0,00E+00	0,00E+00	1,10E+04	0,00E+00
P11717, MPRI	10	4,7	64,618	0,00E+00	0,00E+00	0,00E+00	7,96E+03	1,52E+03	1,81E+03
P11940, PABP1	6	10,4	40,071	0,00E+00	5,41E+03	7,97E+03	3,61E+03	2,42E+03	1,27E+04
P12074, CX6A1	2	25,7	14,361	0,00E+00	0,00E+00	0,00E+00	2,21E+04	2,61E+04	0,00E+00
P12235, ADT1	11	37,6	12,637	0,00E+00	3,77E+03	3,61E+03	3,20E+03	0,00E+00	3,15E+04
P12236, ADT3	14	43,3	55,371	4,93E+04	1,05E+05	1,16E+05	3,67E+05	7,54E+04	2,66E+05
P12273, PIP	1	8,2	7,5344	0,00E+00	1,49E+04	1,62E+04	0,00E+00	0,00E+00	0,00E+00
P12532, KCRU	4	12,2	32,058	0,00E+00	0,00E+00	0,00E+00	3,82E+04	4,69E+03	0,00E+00
P13073, COX41	1	6,5	7,8703	0,00E+00	0,00E+00	0,00E+00	0,00E+00	0,00E+00	1,62E+04
P13196, HEM1	1	2,3	7,7447	0,00E+00	0,00E+00	0,00E+00	0,00E+00	0,00E+00	1,25E+03
P13473, LAMP2	2	4,9	12,298	0,00E+00	0,00E+00	0,00E+00	2,89E+04	1,48E+04	5,95E+03
P13637, AT1A3	16	22,5	27,091	0,00E+00	0,00E+00	0,00E+00	1,61E+04	2,03E+03	0,00E+00
P13639, EF2	3	6,2	19,599	0,00E+00	0,00E+00	0,00E+00	9,70E+03	0,00E+00	0,00E+00
P13674, P4HA1	12	33,7	193,7	0,00E+00	0,00E+00	0,00E+00	1,34E+03	9,39E+04	1,07E+05
P13804, ETFA	8	35,1	122,4	0,00E+00	0,00E+00	0,00E+00	1,59E+05	8,06E+04	8,47E+04
P13995, MTDC	6	29,7	49,977	2,73E+03	6,72E+03	1,15E+04	7,40E+04	4,41E+04	3,19E+04
P14406, CX7A2	2	27,7	14,889	0,00E+00	0,00E+00	0,00E+00	5,93E+04	5,37E+04	2,76E+05
P14625, ENPL	27	35,5	260,5	0,00E+00	1,84E+04	8,79E+03	3,00E+05	4,13E+05	3,04E+05

P14866, HNRPL	4	10,2	35,248	4,29E+03	2,19E+04	2,11E+04	0,00E+00	5,56E+03	5,26E+03
P14923, PLAK	6	12,9	46,293	0,00E+00	1,48E+03	0,00E+00	4,12E+03	8,47E+02	2,17E+03
P15880, RS2	1	4,4	7,1348	0,00E+00	0,00E+00	3,72E+03	4,43E+03	4,46E+03	1,00E+04
P15924, DESP	2	1,1	11,41	0,00E+00	2,08E+02	0,00E+00	0,00E+00	0,00E+00	3,20E+02
P16219, ACADS	1	3,2	6,8724	0,00E+00	0,00E+00	0,00E+00	6,33E+03	0,00E+00	0,00E+00
P16260, GDC	1	3,6	6,6294	0,00E+00	0,00E+00	0,00E+00	5,56E+03	0,00E+00	0,00E+00
P16435, NCPR	3	7,2	18,04	0,00E+00	0,00E+00	0,00E+00	6,23E+03	4,52E+03	0,00E+00
P16615, AT2A2	33	38,4	323,31	0,00E+00	2,01E+03	3,02E+03	4,58E+05	2,41E+05	3,42E+05
P17066, HSP76	6	11,7	91,784	9,37E+03	1,12E+04	1,53E+04	1,98E+05	1,09E+05	9,17E+04
P17152, TMM11	2	12,5	14,5	0,00E+00	0,00E+00	0,00E+00	9,70E+04	4,51E+04	9,32E+04
P17655, CAN2	1	2,1	6,3811	0,00E+00	0,00E+00	0,00E+00	0,00E+00	2,86E+03	0,00E+00
P17693, HLAG	2	6,8	6,3552	0,00E+00	0,00E+00	0,00E+00	1,46E+04	7,10E+03	9,60E+03
P17844, DDX5	3	5,4	19,146	0,00E+00	0,00E+00	0,00E+00	6,13E+03	3,58E+03	1,98E+04
P17987, TCPA	3	6,8	19,641	0,00E+00	1,87E+03	0,00E+00	0,00E+00	6,69E+03	1,05E+04
P18031, PTN1	2	5,7	12,151	0,00E+00	0,00E+00	0,00E+00	6,59E+03	3,44E+03	0,00E+00
P18085, ARF4	6	43,3	36,491	0,00E+00	0,00E+00	0,00E+00	6,23E+04	1,90E+04	7,70E+04
P18124, RL7	5	25,8	36,606	1,26E+04	7,48E+04	4,81E+04	2,48E+03	0,00E+00	1,53E+04
P19086, GNAZ	2	9	12,643	0,00E+00	0,00E+00	0,00E+00	0,00E+00	0,00E+00	1,74E+04
P19367, HXK1	11	12,2	64,256	0,00E+00	0,00E+00	0,00E+00	9,33E+04	1,69E+04	1,44E+04
P20020, AT2B1	19	22	199,06	0,00E+00	0,00E+00	0,00E+00	1,93E+05	1,14E+05	8,19E+04
P20336, RAB3A	3	19,1	17,92	0,00E+00	0,00E+00	0,00E+00	1,86E+04	0,00E+00	7,79E+03
Q9NRW1, RAB6B	1	5,3	6,9033	0,00E+00	0,00E+00	0,00E+00	4,34E+04	1,72E+04	3,68E+04
P20674, COX5A	2	14	11,351	0,00E+00	0,00E+00	0,00E+00	8,25E+03	7,77E+04	0,00E+00
P20700, LMNB1	7	16	62,327	0,00E+00	0,00E+00	0,00E+00	5,83E+04	1,10E+04	1,41E+04
P21333, FLNA	11	6,8	82,429	0,00E+00	2,87E+02	4,47E+02	1,29E+04	3,00E+03	4,69E+03
P21796, VDAC1	15	66,4	323,31	0,00E+00	0,00E+00	5,18E+03	1,28E+06	4,93E+05	1,11E+06
P21953, ODBB	1	4,6	29,003	0,00E+00	0,00E+00	0,00E+00	1,58E+04	0,00E+00	0,00E+00
P21964, COMT	1	5,9	19,319	0,00E+00	0,00E+00	0,00E+00	0,00E+00	0,00E+00	0,00E+00
P22413, ENPP1	2	2,5	15,308	0,00E+00	0,00E+00	0,00E+00	4,13E+03	6,07E+02	0,00E+00
P22570, ADRO	7	17,7	45,526	0,00E+00	0,00E+00	0,00E+00	2,55E+03	1,73E+04	0,00E+00
P22626, ROA2	2	7,4	15,836	0,00E+00	7,00E+03	7,28E+03	5,97E+03	0,00E+00	1,35E+04
P22695, QCR2	16	62	323,31	0,00E+00	0,00E+00	4,11E+03	8,35E+05	5,63E+05	6,22E+05
P23258, TBG1	2	7,8	13,757	0,00E+00	0,00E+00	0,00E+00	3,69E+04	0,00E+00	1,07E+04
P23396, RS3	6	32,9	38,798	0,00E+00	2,80E+04	2,12E+04	1,25E+04	5,73E+03	3,46E+04
P23458, JAK1	13	16,4	112,28	1,10E+04	0,00E+00	1,01E+04	1,58E+04	4,59E+04	1,07E+04
P23588, IF4B	3	5,7	18,111	0,00E+00	4,84E+03	1,12E+04	0,00E+00	3,45E+03	7,97E+03
P23634, AT2B4	12	12,3	28,857	0,00E+00	0,00E+00	0,00E+00	5,18E+03	2,93E+03	2,45E+03
P24390, ERD21	2	13,7	14,309	0,00E+00	0,00E+00	0,00E+00	9,28E+03	1,35E+04	6,96E+04
P24534, EF1B	1	6,7	27,511	0,00E+00	0,00E+00	0,00E+00	0,00E+00	0,00E+00	2,82E+03
P24752, THIL	3	11,2	26,405	0,00E+00	0,00E+00	0,00E+00	4,36E+04	5,70E+03	3,25E+03
P25325, THTM	1	4,4	7,5318	0,00E+00	0,00E+00	0,00E+00	1,46E+04	0,00E+00	0,00E+00
P25398, RS12	1	16,7	55,971	0,00E+00	1,01E+04	0,00E+00	3,27E+04	1,86E+04	6,96E+04
P25705, ATPA	10	25,7	62,305	0,00E+00	6,81E+03	8,85E+03	1,97E+04	1,79E+04	7,83E+03
P25789, PSA4	2	9,2	12,578	0,00E+00	7,02E+03	0,00E+00	0,00E+00	0,00E+00	0,00E+00
P35221, CTNA1	2	2,9	12,516	0,00E+00	0,00E+00	0,00E+00	5,29E+03	0,00E+00	0,00E+00
P26373, RL13	5	23,2	37,413	1,08E+04	0,00E+00	0,00E+00	9,83E+04	2,33E+04	9,63E+04

P26640, SYVC	3	3	16,84	0,00E+00	0,00E+00	0,00E+00	6,11E+03	0,00E+00	6,20E+02
P26641, EF1G	12	28,4	135,96	0,00E+00	3,75E+03	1,58E+04	4,24E+05	8,33E+04	1,81E+05
P27105, STOM	1	6,6	7,1724	0,00E+00	0,00E+00	0,00E+00	1,34E+04	0,00E+00	6,69E+03
P27348, 1433T	2	9,8	6,5556	0,00E+00	0,00E+00	0,00E+00	2,51E+03	0,00E+00	0,00E+00
P27482, CALL3	3	26,8	23,03	1,21E+04	5,92E+04	7,81E+03	0,00E+00	0,00E+00	0,00E+00
P27708, PYR1	9	4,9	57,802	0,00E+00	0,00E+00	0,00E+00	1,25E+04	3,10E+03	4,70E+03
P27797, CALR	3	12,5	21,43	0,00E+00	0,00E+00	0,00E+00	0,00E+00	0,00E+00	2,69E+04
P27824, CALX	16	34,8	323,31	5,03E+03	1,29E+04	2,41E+04	5,71E+05	8,47E+05	7,26E+05
P28288, ABCD3	20	37,8	180,9	0,00E+00	0,00E+00	0,00E+00	3,74E+03	1,93E+05	1,78E+05
P28331, NDUS1	19	41,4	253,08	0,00E+00	0,00E+00	0,00E+00	2,03E+05	8,16E+04	1,30E+05
P29692, EF1D	2	7,5	12,934	0,00E+00	0,00E+00	2,51E+03	3,06E+04	0,00E+00	9,04E+03
P29992, GNA11	5	21,2	33,815	0,00E+00	1,92E+03	0,00E+00	3,48E+04	6,21E+04	4,52E+04
P30038, AL4A1	4	11,2	25,508	0,00E+00	0,00E+00	0,00E+00	0,00E+00	1,42E+04	3,54E+03
P30044, PRDX5	1	7,9	7,4726	0,00E+00	4,36E+03	2,87E+03	0,00E+00	0,00E+00	0,00E+00
P30048, PRDX3	1	5,5	7,7153	2,11E+03	1,22E+04	3,37E+03	5,33E+03	0,00E+00	7,89E+03
P30049, ATPD	1	8,3	7,5345	0,00E+00	1,27E+04	0,00E+00	1,06E+04	0,00E+00	0,00E+00
P30050, RL12	4	33,9	36,499	0,00E+00	1,07E+04	9,20E+03	1,44E+04	1,26E+04	1,41E+05
P30084, ECHM	5	25,9	47,658	0,00E+00	0,00E+00	0,00E+00	1,08E+05	0,00E+00	8,59E+03
P30825, SL7A1	3	5,7	18,394	0,00E+00	0,00E+00	0,00E+00	1,29E+04	1,70E+04	8,33E+03
P31040, SDHA	4	7,5	27,901	0,00E+00	0,00E+00	0,00E+00	1,60E+04	6,80E+03	4,20E+03
P31327, CPSM	9	7	47,644	0,00E+00	0,00E+00	0,00E+00	1,41E+04	2,46E+03	2,53E+03
P31689, DNJA1	2	9,6	15,324	0,00E+00	0,00E+00	0,00E+00	1,87E+04	1,95E+04	9,08E+03
P31930, QCR1	8	23,8	201,87	0,00E+00	0,00E+00	0,00E+00	3,00E+04	1,46E+05	4,83E+04
P31943, HNRH1	5	17,8	69,196	0,00E+00	5,39E+03	1,22E+04	5,76E+04	4,35E+04	7,71E+04
P31947, 1433S	4	26,6	19,85	0,00E+00	6,66E+03	0,00E+00	0,00E+00	0,00E+00	0,00E+00
P31949, S10AB	1	15,2	7,3013	0,00E+00	2,22E+04	0,00E+00	0,00E+00	0,00E+00	0,00E+00
P32322, P5CR1	6	28,8	39,606	0,00E+00	0,00E+00	0,00E+00	9,95E+04	1,19E+04	5,66E+03
P33121, ACSL1	5	10,2	37,353	0,00E+00	0,00E+00	0,00E+00	3,87E+04	2,65E+03	3,08E+03
P33527, MRP1	14	13	100,01	0,00E+00	0,00E+00	0,00E+00	2,14E+04	2,17E+04	1,34E+04
P33764, S10A3	1	18,8	8,2105	0,00E+00	0,00E+00	0,00E+00	0,00E+00	0,00E+00	0,00E+00
P33908, MA1A1	4	8,3	23,705	0,00E+00	0,00E+00	0,00E+00	1,59E+04	5,39E+03	0,00E+00
P33947, ERD22	5	35,4	38,029	0,00E+00	0,00E+00	0,00E+00	6,79E+04	7,57E+03	1,08E+04
P34897, GLYM	2	5	14,451	0,00E+00	0,00E+00	0,00E+00	3,03E+04	3,41E+03	1,70E+04
P35232, PHB	13	58,5	323,31	1,23E+04	3,36E+04	3,45E+04	5,40E+04	4,94E+03	1,21E+05
P35250, RFC2	3	11,6	19,317	0,00E+00	0,00E+00	0,00E+00	8,05E+03	0,00E+00	2,63E+03
P35556, FBN2	2	1	11,509	0,00E+00	0,00E+00	0,00E+00	0,00E+00	6,12E+02	0,00E+00
P35579, MYH9	25	17,1	175,87	0,00E+00	2,01E+04	1,21E+04	1,05E+03	2,47E+03	2,35E+03
P35580, MYH10	26	19,2	241,26	0,00E+00	2,90E+04	1,38E+04	5,29E+03	1,30E+04	5,46E+03
P35606, COPB2	2	3,1	11,499	0,00E+00	0,00E+00	0,00E+00	0,00E+00	1,95E+03	2,58E+03
P35610, SOAT1	7	15,8	47,099	0,00E+00	0,00E+00	0,00E+00	2,70E+04	9,93E+03	3,13E+04
P35613, BASI	5	13,2	35,816	0,00E+00	0,00E+00	0,00E+00	1,17E+05	1,16E+05	1,08E+05
P35658, NU214	4	2,7	27,541	0,00E+00	0,00E+00	0,00E+00	5,69E+03	0,00E+00	4,31E+03
P35670, ATP7B	1	0,9	6,3833	0,00E+00	0,00E+00	0,00E+00	3,17E+03	1,20E+03	1,96E+03
P36404, ARL2	3	20,1	18,217	0,00E+00	0,00E+00	0,00E+00	5,31E+04	0,00E+00	0,00E+00
P36542, ATPG	8	35,2	76,944	1,97E+04	5,38E+04	1,10E+05	3,56E+05	1,48E+05	2,93E+05
P36551, HEM6	4	10,8	26,647	0,00E+00	5,09E+03	3,37E+03	3,21E+04	4,40E+03	3,15E+03

P36578, RL4	7	23,7	48,183	0,00E+00	4,60E+03	1,29E+04	1,80E+05	7,28E+04	7,89E+04
P36776, LONM	14	21,7	146,63	0,00E+00	0,00E+00	0,00E+00	5,15E+04	7,65E+04	2,89E+04
P36873, PP1G	4	17	38,202	0,00E+00	0,00E+00	0,00E+00	6,43E+04	6,61E+03	3,83E+03
P36957, ODO2	3	7,3	30,566	0,00E+00	0,00E+00	1,79E+03	8,25E+04	1,27E+04	2,94E+04
P37268, FDFT	5	17	36,568	0,00E+00	0,00E+00	0,00E+00	5,84E+04	1,42E+04	3,23E+04
P38117, ETFB	4	17,6	28,553	0,00E+00	0,00E+00	0,00E+00	6,09E+04	1,21E+04	0,00E+00
P38159, RBMX	3	10,2	19,974	2,65E+03	0,00E+00	9,76E+03	0,00E+00	0,00E+00	5,81E+03
P38435, VKGC	4	8	25,615	0,00E+00	0,00E+00	0,00E+00	2,17E+04	5,47E+03	6,34E+03
P38646, GRP75	21	49,8	323,31	7,16E+04	1,51E+05	1,40E+05	1,02E+06	6,08E+05	6,27E+05
P39019, RS19	2	15,2	11,53	0,00E+00	1,79E+04	3,38E+03	0,00E+00	0,00E+00	0,00E+00
P39023, RL3	4	10,9	23,594	3,43E+03	0,00E+00	0,00E+00	1,46E+04	0,00E+00	2,25E+04
P39656, OST48	13	45,6	323,31	3,22E+03	8,19E+03	1,40E+04	6,77E+05	4,93E+05	5,34E+05
P40926, MDHM	4	16,6	27,603	0,00E+00	0,00E+00	1,88E+03	5,24E+04	1,54E+04	2,31E+04
P40939, ECHA	17	29,9	207,29	0,00E+00	1,15E+03	0,00E+00	2,77E+05	8,09E+04	1,10E+05
P41250, GARS	8	18	73,108	0,00E+00	0,00E+00	0,00E+00	3,87E+04	0,00E+00	0,00E+00
P41252, SYIC	21	21,2	136,77	0,00E+00	0,00E+00	5,33E+02	7,78E+04	1,66E+04	2,82E+04
P42126, ECI1	1	4,3	6,6434	0,00E+00	0,00E+00	0,00E+00	0,00E+00	0,00E+00	6,87E+03
P42345, MTOR	8	4,2	48,888	0,00E+00	0,00E+00	0,00E+00	4,91E+02	1,19E+03	5,96E+03
P42356, PI4KA	20	13,3	181,57	0,00E+00	3,74E+02	5,07E+02	2,75E+04	6,44E+03	1,23E+04
P42677, RS27	3	29,8	20,332	0,00E+00	0,00E+00	0,00E+00	2,50E+04	1,28E+05	0,00E+00
P42704, LPPRC	61	51,9	323,31	6,64E+04	1,29E+05	1,25E+05	4,04E+05	4,32E+05	3,77E+05
P42766, RL35	1	8,1	6,7547	0,00E+00	0,00E+00	0,00E+00	0,00E+00	0,00E+00	8,66E+04
P42771, CDN2A	2	18,6	11,15	0,00E+00	0,00E+00	0,00E+00	2,92E+03	0,00E+00	0,00E+00
P43003, EAA1	2	5,9	21,969	0,00E+00	0,00E+00	0,00E+00	4,93E+03	3,68E+04	4,61E+04
P43007, SATT	2	4,5	13,437	0,00E+00	0,00E+00	0,00E+00	1,86E+04	1,01E+04	2,31E+04
P43243, MATR3	5	10,6	129,25	0,00E+00	8,52E+02	9,06E+03	2,10E+04	2,82E+03	2,00E+04
P43246, MSH2	3	4,3	17,594	0,00E+00	0,00E+00	0,00E+00	3,94E+03	1,14E+03	2,38E+03
P43304, GPDM	9	16,8	73,909	0,00E+00	0,00E+00	0,00E+00	3,23E+04	2,72E+03	7,87E+03
P43307, SSRA	4	19,9	323,31	0,00E+00	0,00E+00	1,05E+04	7,01E+05	1,95E+05	4,13E+05
P43897, EFTS	1	5,2	8,7494	0,00E+00	0,00E+00	0,00E+00	0,00E+00	2,25E+04	0,00E+00
P45880, VDAC2	11	46,3	323,31	3,44E+03	0,00E+00	1,38E+04	9,45E+05	3,58E+05	6,39E+05
P45954, ACDSB	7	24,1	141,58	0,00E+00	0,00E+00	0,00E+00	1,16E+05	3,13E+04	2,99E+04
P46199, IF2M	5	9,5	35,247	0,00E+00	0,00E+00	0,00E+00	4,21E+04	1,62E+04	1,19E+04
P46379, BAG6	2	2	12,209	0,00E+00	0,00E+00	0,00E+00	6,73E+03	0,00E+00	1,93E+03
P46459, NSF	20	27,6	149,3	0,00E+00	0,00E+00	0,00E+00	1,64E+05	5,34E+04	3,80E+04
P46776, RL27A	2	14,2	13,417	0,00E+00	0,00E+00	9,93E+03	8,55E+04	5,37E+04	9,78E+04
P46783, RS10	2	13,9	13,284	0,00E+00	0,00E+00	0,00E+00	1,92E+04	0,00E+00	5,45E+04
P46939, UTRO	3	1,1	18,283	0,00E+00	0,00E+00	0,00E+00	1,68E+03	0,00E+00	0,00E+00
P46977, STT3A	13	20,3	78,605	0,00E+00	0,00E+00	0,00E+00	6,06E+03	2,90E+04	1,07E+05
P47755, CAZA2	3	15	12,633	0,00E+00	7,86E+03	0,00E+00	0,00E+00	0,00E+00	0,00E+00
P47756, CAPZB	4	13,4	26,077	0,00E+00	2,17E+04	0,00E+00	0,00E+00	0,00E+00	0,00E+00
P47897, SYQ	3	5,8	45,708	0,00E+00	0,00E+00	0,00E+00	8,63E+03	2,31E+03	3,15E+03
P47929, LEG7	4	36,8	25,683	2,89E+04	0,00E+00	0,00E+00	0,00E+00	0,00E+00	0,00E+00
P48643, TCPE	2	6,1	14,787	0,00E+00	4,00E+03	1,78E+03	0,00E+00	6,18E+03	0,00E+00
P48651, PTSS1	4	11,2	27,165	1,58E+03	3,28E+03	3,84E+03	2,89E+04	4,55E+04	4,95E+04
P48735, IDHP	13	32,5	142,74	0,00E+00	0,00E+00	0,00E+00	1,32E+05	9,03E+04	7,05E+04

P49327, FAS	15	8,6	95,434	0,00E+00	0,00E+00	4,64E+02	4,02E+03	3,24E+03	2,58E+03
P49368, TCPG	3	6,1	19,882	1,24E+03	6,97E+03	4,00E+03	0,00E+00	8,19E+03	1,37E+04
P49406, RM19	4	14,7	30,445	0,00E+00	1,76E+04	6,24E+03	0,00E+00	0,00E+00	2,96E+03
P49411, EFTU	25	63,7	323,31	4,22E+04	1,88E+05	2,35E+05	3,45E+06	1,86E+06	2,11E+06
P49590, SYHM	8	21,7	52,585	0,00E+00	0,00E+00	0,00E+00	4,63E+04	0,00E+00	1,31E+04
P49755, TMEDA	3	20,1	60,156	0,00E+00	0,00E+00	0,00E+00	1,10E+05	6,95E+03	1,55E+05
P49768, PSN1	2	7,3	15,653	0,00E+00	0,00E+00	0,00E+00	4,94E+03	0,00E+00	1,24E+04
P49792, RBP2	15	6,8	105,85	0,00E+00	0,00E+00	0,00E+00	1,72E+04	1,71E+03	9,64E+03
P49821, NDUV1	8	22	74,347	0,00E+00	0,00E+00	0,00E+00	7,89E+04	7,24E+03	4,77E+04
P50213, IDH3A	4	14,5	29,427	0,00E+00	0,00E+00	0,00E+00	8,86E+04	4,56E+04	5,08E+04
P50336, PPOX	3	8,8	17,567	0,00E+00	0,00E+00	0,00E+00	1,11E+04	2,53E+03	0,00E+00
P50402, EMD	7	37,8	120,6	0,00E+00	4,82E+03	1,55E+04	2,23E+05	2,38E+04	1,21E+05
P50416, CPT1A	7	10,7	64,119	0,00E+00	0,00E+00	0,00E+00	3,26E+04	1,87E+04	2,06E+04
P50454, SERPH	12	44,5	96,856	0,00E+00	0,00E+00	0,00E+00	1,91E+05	1,02E+05	6,84E+04
P50851, LRBA	3	1,1	16,884	0,00E+00	5,79E+02	0,00E+00	0,00E+00	9,75E+02	1,85E+02
P50897, PPT1	3	15	36,382	0,00E+00	0,00E+00	0,00E+00	1,25E+05	2,97E+04	2,72E+04
P50914, RL14	2	10,7	19,813	3,60E+04	4,60E+04	6,42E+04	1,82E+05	8,39E+04	1,57E+05
P50991, TCPD	2	5,4	13,249	1,17E+03	6,63E+03	2,80E+03	0,00E+00	4,03E+03	6,41E+03
P51153, RAB13	2	9,4	6,4441	0,00E+00	0,00E+00	0,00E+00	1,30E+04	0,00E+00	1,62E+04
P51398, RT29	10	36,4	114	1,32E+04	4,96E+04	4,38E+04	2,05E+05	9,77E+04	1,06E+05
P51553, IDH3G	3	9,9	17,592	0,00E+00	0,00E+00	0,00E+00	1,62E+04	0,00E+00	1,31E+04
P51571, SSRD	4	30,6	57,971	1,76E+04	2,95E+04	1,78E+04	1,53E+05	6,09E+04	1,43E+05
P51648, AL3A2	2	4,3	12,427	0,00E+00	0,00E+00	0,00E+00	0,00E+00	0,00E+00	2,00E+04
P51659, DHB4	10	19,7	67,523	0,00E+00	0,00E+00	2,18E+03	2,95E+04	2,86E+04	9,24E+03
P51790, CLCN3	1	1,2	6,4029	0,00E+00	0,00E+00	0,00E+00	5,42E+03	1,94E+03	0,00E+00
P51798, CLCN7	2	4,1	12,14	0,00E+00	0,00E+00	0,00E+00	2,70E+03	0,00E+00	0,00E+00
P52272, HNRPM	7	14,1	69,618	0,00E+00	2,48E+03	0,00E+00	8,07E+04	3,68E+04	4,53E+04
P52292, IMA1	1	2,8	7,6749	0,00E+00	0,00E+00	0,00E+00	0,00E+00	0,00E+00	1,59E+04
P52429, DGKE	1	2,3	7,0004	0,00E+00	0,00E+00	0,00E+00	0,00E+00	4,30E+03	6,55E+03
P52597, HNRPF	4	14,5	23,011	0,00E+00	0,00E+00	0,00E+00	2,31E+04	1,05E+04	1,79E+04
P52701, MSH6	2	2,3	11,324	0,00E+00	0,00E+00	0,00E+00	2,33E+03	0,00E+00	0,00E+00
P52732, KIF11	30	37,8	323,31	8,30E+04	1,74E+05	3,57E+05	1,06E+04	1,40E+04	1,09E+04
P52789, HXK2	12	16,4	84,696	0,00E+00	0,00E+00	0,00E+00	5,58E+04	1,17E+04	1,72E+04
P52907, CAZA1	6	32,9	58,739	0,00E+00	1,32E+05	6,50E+04	1,03E+04	2,93E+04	0,00E+00
P52948, NUP98	6	4,2	40,038	0,00E+00	0,00E+00	0,00E+00	1,49E+04	3,34E+02	7,06E+03
P53007, TXTP	5	16,7	30,272	0,00E+00	1,34E+04	1,38E+04	2,04E+04	0,00E+00	2,98E+04
P53597, SUCA	3	13,3	41,662	0,00E+00	0,00E+00	0,00E+00	2,38E+04	6,86E+03	5,72E+03
P53618, COPB	3	4,1	19,474	0,00E+00	0,00E+00	9,09E+02	5,41E+03	1,87E+03	0,00E+00
P53621, COPA	8	7,9	53,981	0,00E+00	0,00E+00	0,00E+00	8,35E+03	3,71E+03	1,30E+04
P53985, MOT1	8	18,4	323,31	1,00E+04	6,32E+03	1,39E+04	6,93E+05	3,45E+05	3,50E+05
P53992, SC24C	2	2,1	13,73	0,00E+00	0,00E+00	0,00E+00	8,80E+03	0,00E+00	0,00E+00
P54098, DPOG1	2	2,4	12,851	0,00E+00	0,00E+00	0,00E+00	1,96E+03	0,00E+00	8,47E+02
P54105, ICLN	1	5,5	6,3169	0,00E+00	3,35E+04	1,07E+04	0,00E+00	0,00E+00	0,00E+00
P54136, SYRC	2	5,2	13,339	0,00E+00	0,00E+00	0,00E+00	1,12E+03	1,83E+03	3,29E+03
P54707, AT12A	5	5,3	25,238	0,00E+00	0,00E+00	0,00E+00	0,00E+00	0,00E+00	0,00E+00
P54709, AT1B3	3	12,9	25,752	0,00E+00	0,00E+00	0,00E+00	1,74E+05	2,52E+05	8,36E+04

P54802, ANAG	4	8,3	28,479	0,00E+00	0,00E+00	0,00E+00	9,49E+03	1,10E+03	1,29E+04
P54819, KAD2	4	27,2	26,584	0,00E+00	0,00E+00	0,00E+00	2,56E+04	0,00E+00	0,00E+00
P54886, P5CS	26	39	308,06	0,00E+00	6,50E+03	3,50E+03	5,82E+05	2,11E+05	6,57E+04
P55011, S12A2	4	5,2	26,102	0,00E+00	0,00E+00	0,00E+00	9,06E+03	7,51E+02	3,96E+03
P55060, XPO2	2	3,2	13,883	0,00E+00	0,00E+00	0,00E+00	0,00E+00	0,00E+00	3,05E+03
P55084, ECHB	10	21,5	83,373	0,00E+00	0,00E+00	1,17E+03	2,03E+05	7,43E+04	9,51E+04
P55196, AFAD	2	1,6	12,971	0,00E+00	0,00E+00	0,00E+00	1,38E+03	0,00E+00	8,23E+02
P55884, EIF3B	2	4,3	12,48	0,00E+00	0,00E+00	0,00E+00	3,24E+03	9,50E+02	4,94E+03
P56134, ATPK	3	39,4	34,067	0,00E+00	1,56E+04	1,00E+04	7,23E+05	2,36E+05	3,94E+05
P56181, NDUV3	1	14,8	6,5096	0,00E+00	0,00E+00	0,00E+00	0,00E+00	0,00E+00	1,76E+04
P56192, SYMC	5	6,2	39,903	0,00E+00	0,00E+00	0,00E+00	2,42E+04	3,48E+03	5,04E+03
P56385, ATP5I	3	50,7	20,842	0,00E+00	0,00E+00	0,00E+00	7,71E+05	1,84E+05	1,07E+06
P56556, NDUA6	3	21,1	19,206	0,00E+00	0,00E+00	0,00E+00	2,07E+04	1,19E+04	4,96E+04
P56589, PEX3	4	15,5	27,631	0,00E+00	0,00E+00	0,00E+00	3,05E+04	1,57E+04	3,01E+04
P56937, DHB7	2	6,5	13,349	0,00E+00	0,00E+00	0,00E+00	1,50E+04	8,38E+03	1,18E+04
P56962, STX17	2	7,9	16,36	0,00E+00	0,00E+00	0,00E+00	3,41E+04	0,00E+00	0,00E+00
P57088, TMM33	1	4,9	6,4129	0,00E+00	0,00E+00	0,00E+00	0,00E+00	0,00E+00	1,22E+04
P57105, SYJ2B	2	17,9	13,144	0,00E+00	0,00E+00	0,00E+00	4,93E+04	3,14E+04	0,00E+00
P57678, GEMI4	5	5,7	32,18	0,00E+00	0,00E+00	0,00E+00	5,24E+03	2,02E+03	4,06E+03
P57740, NU107	9	14,7	62,937	0,00E+00	0,00E+00	0,00E+00	3,31E+04	5,46E+03	1,25E+04
P58557, YBEY	2	14,4	12,919	0,00E+00	0,00E+00	0,00E+00	8,65E+04	0,00E+00	7,28E+04
P60228, EIF3E	2	5,6	12,043	0,00E+00	0,00E+00	0,00E+00	0,00E+00	1,75E+03	8,87E+02
P60468, SC61B	2	26	29,803	7,88E+03	0,00E+00	0,00E+00	0,00E+00	9,24E+04	2,09E+05
P60602, ROMO1	1	21,5	16,091	0,00E+00	0,00E+00	0,00E+00	0,00E+00	0,00E+00	0,00E+00
P60604, UB2G2	1	14,5	57,043	0,00E+00	0,00E+00	0,00E+00	8,55E+04	0,00E+00	1,16E+05
P60709, ACTB	18	65,9	40,885	0,00E+00	0,00E+00	0,00E+00	0,00E+00	0,00E+00	0,00E+00
P60842, IF4A1	7	24,6	262,35	8,02E+03	1,85E+04	2,06E+04	6,68E+04	6,27E+04	8,86E+04
P60866, RS20	1	9,2	7,6416	0,00E+00	1,70E+04	1,99E+04	7,29E+03	0,00E+00	1,14E+04
P61019, RAB2A	2	12,3	12,082	0,00E+00	0,00E+00	0,00E+00	5,55E+03	1,17E+04	0,00E+00
P61163, ACTZ	3	14,6	21,977	0,00E+00	1,70E+04	0,00E+00	7,27E+03	0,00E+00	5,59E+03
P61204, ARF3	5	40,9	15,805	0,00E+00	6,12E+03	0,00E+00	4,94E+04	4,53E+04	5,08E+04
P61221, ABCE1	6	13,7	38,082	0,00E+00	0,00E+00	0,00E+00	0,00E+00	6,44E+03	2,49E+04
P61225, RAP2B	3	20,2	18,502	0,00E+00	0,00E+00	0,00E+00	4,23E+04	0,00E+00	1,53E+04
P61247, RS3A	1	6,4	6,5322	0,00E+00	3,10E+03	7,01E+03	8,20E+03	0,00E+00	7,48E+03
P61353, RL27	1	5,9	6,3341	0,00E+00	3,87E+04	5,28E+04	3,52E+04	4,84E+04	0,00E+00
P61421, VA0D1	1	7,7	8,1808	0,00E+00	0,00E+00	0,00E+00	1,37E+04	0,00E+00	1,12E+04
P61513, RL37A	1	19,6	7,8588	0,00E+00	0,00E+00	0,00E+00	3,23E+04	0,00E+00	3,31E+04
P61619, S61A1	8	24,4	173,73	4,18E+03	0,00E+00	6,52E+03	4,81E+05	2,65E+05	5,22E+05
P61626, LYSC	1	8,1	7,5678	0,00E+00	0,00E+00	0,00E+00	0,00E+00	2,28E+04	0,00E+00
P61803, DAD1	3	28,3	23,785	0,00E+00	0,00E+00	0,00E+00	3,46E+05	3,29E+05	3,11E+05
P61978, HNRPK	15	42,5	260,14	4,41E+04	1,92E+05	2,63E+05	0,00E+00	5,45E+04	4,34E+04
P62241, RS8	3	18,8	19,559	0,00E+00	0,00E+00	0,00E+00	8,46E+03	2,10E+04	8,46E+04
P62244, RS15A	2	16,9	13,403	0,00E+00	0,00E+00	8,15E+03	1,07E+04	0,00E+00	0,00E+00
P62249, RS16	3	19,9	18,072	0,00E+00	1,35E+04	3,40E+04	1,04E+04	1,19E+04	5,63E+04
P62263, RS14	2	15,9	25,446	0,00E+00	7,46E+04	1,09E+05	3,87E+04	8,49E+04	2,24E+05
P62266, RS23	2	16,1	12,078	0,00E+00	0,00E+00	1,24E+04	0,00E+00	1,24E+04	6,65E+03

P62269, RS18	6	29,6	59,77	0,00E+00	4,09E+04	3,03E+04	0,00E+00	7,29E+04	2,99E+05
P62273, RS29	1	19,6	7,1628	0,00E+00	0,00E+00	0,00E+00	0,00E+00	0,00E+00	4,89E+04
P62277, RS13	4	29,1	25,823	0,00E+00	2,93E+04	2,91E+04	1,46E+04	5,51E+04	6,88E+04
P62304, RUXE	1	12	7,9148	0,00E+00	0,00E+00	0,00E+00	6,54E+04	0,00E+00	0,00E+00
P62314, SMD1	2	27,7	12,703	0,00E+00	5,03E+04	0,00E+00	0,00E+00	0,00E+00	0,00E+00
P62318, SMD3	1	7,9	6,5536	0,00E+00	0,00E+00	0,00E+00	2,11E+04	0,00E+00	2,85E+04
P62424, RL7A	1	5,3	6,5556	0,00E+00	0,00E+00	1,13E+04	0,00E+00	0,00E+00	0,00E+00
P62805, H4	5	41,7	35,141	9,63E+04	2,03E+05	3,21E+05	5,40E+05	6,10E+05	1,32E+06
P62826, RAN	3	18,1	18,488	0,00E+00	0,00E+00	0,00E+00	2,16E+04	0,00E+00	4,25E+04
P62829, RL23	1	14,3	10,118	0,00E+00	0,00E+00	0,00E+00	0,00E+00	0,00E+00	0,00E+00
P62847, RS24	1	9	6,4057	0,00E+00	0,00E+00	1,39E+04	0,00E+00	1,83E+04	1,52E+04
Q9HAV0, GBB4	2	6,2	12,771	0,00E+00	0,00E+00	0,00E+00	3,89E+04	2,51E+04	3,09E+04
P62888, RL30	2	24,3	21,182	0,00E+00	0,00E+00	0,00E+00	0,00E+00	0,00E+00	0,00E+00
P62899, RL31	1	11,2	7,2981	0,00E+00	1,19E+04	1,40E+04	6,28E+03	0,00E+00	1,08E+04
P62917, RL8	1	4,3	7,7843	0,00E+00	0,00E+00	2,64E+04	0,00E+00	1,43E+04	2,06E+04
P63092, GNAS2	7	25,1	43,338	0,00E+00	0,00E+00	0,00E+00	2,45E+04	7,66E+04	4,13E+04
P63096, GNAI1	5	20,1	13,921	0,00E+00	0,00E+00	0,00E+00	5,08E+03	8,21E+03	0,00E+00
P63104, 1433Z	4	24,9	27,353	0,00E+00	7,10E+04	0,00E+00	0,00E+00	0,00E+00	7,84E+03
P63173, RL38	2	32,9	21,625	0,00E+00	0,00E+00	0,00E+00	9,96E+04	0,00E+00	5,64E+04
P63244, RACK1	4	13,2	31,347	0,00E+00	3,09E+03	0,00E+00	4,83E+04	3,56E+04	2,51E+04
P63261, ACTG	18	65,9	323,31	9,94E+03	3,21E+06	9,96E+05	7,62E+05	1,12E+06	1,36E+06
P67809, YBOX1	4	24,4	28,965	0,00E+00	0,00E+00	8,48E+03	5,05E+03	1,70E+04	3,69E+04
P67812, SC11A	4	19,6	33,061	0,00E+00	7,83E+03	1,49E+04	3,27E+05	1,89E+05	3,18E+05
P68133, ACTS	10	26,8	25,08	0,00E+00	4,03E+05	1,23E+05	0,00E+00	1,55E+04	3,78E+04
P68104, EF1A1	6	17,7	107,96	2,06E+04	1,60E+04	2,52E+04	3,32E+05	1,53E+05	1,98E+05
P68363, TBA1B	13	45,9	162,66	1,61E+04	3,80E+04	2,51E+04	3,92E+05	3,47E+05	4,66E+05
P78527, PRKDC	67	19,3	323,31	0,00E+00	0,00E+00	0,00E+00	1,00E+05	2,56E+04	2,73E+04
P78540, ARGI2	2	9,3	14,731	0,00E+00	0,00E+00	0,00E+00	2,98E+04	6,13E+03	4,88E+03
P82650, RT22	9	32,2	69,761	8,39E+03	3,39E+04	2,40E+04	1,45E+05	8,15E+04	7,11E+04
P82664, RT10	3	21,9	20,209	0,00E+00	9,23E+03	5,38E+03	3,74E+04	1,78E+04	4,65E+04
P82673, RT35	3	13,9	24,073	0,00E+00	0,00E+00	9,92E+03	1,22E+04	6,99E+03	7,19E+03
P82675, RT05	4	12,8	26,119	0,00E+00	0,00E+00	0,00E+00	2,87E+03	1,30E+03	9,67E+02
P82912, RT11	3	16,5	20,03	0,00E+00	0,00E+00	0,00E+00	4,07E+04	0,00E+00	2,15E+04
P82921, RT21	1	16,1	17,576	0,00E+00	0,00E+00	0,00E+00	1,23E+05	0,00E+00	1,69E+04
P82930, RT34	6	34,4	44,759	0,00E+00	0,00E+00	0,00E+00	7,63E+04	3,57E+04	2,15E+04
P82933, RT09	5	15,9	48,498	0,00E+00	9,85E+03	1,48E+04	5,02E+04	3,44E+04	6,78E+04
P83111, LACTB	12	28,3	107,34	0,00E+00	0,00E+00	0,00E+00	2,65E+03	1,46E+05	1,13E+05
P84090, ERH	1	10,6	12,017	0,00E+00	2,81E+04	3,07E+04	0,00E+00	0,00E+00	7,46E+04
P84095, RHOG	5	38,2	49,535	0,00E+00	0,00E+00	0,00E+00	9,12E+04	4,77E+04	8,58E+04
P84098, RL19	2	13,3	15,583	0,00E+00	0,00E+00	0,00E+00	6,13E+04	3,50E+04	1,44E+05
P98164, LRP2	9	2,4	53,123	0,00E+00	0,00E+00	0,00E+00	0,00E+00	1,52E+03	0,00E+00
P98175, RBM10	6	12,9	44,258	3,09E+03	2,17E+04	5,12E+03	0,00E+00	6,15E+03	9,96E+03
P98194, AT2C1	3	5,5	22,158	0,00E+00	0,00E+00	0,00E+00	1,07E+04	3,34E+03	2,52E+03
Q00325, MPCP	9	30,7	323,31	0,00E+00	2,72E+04	5,32E+04	3,88E+05	5,89E+04	1,37E+05
Q00341, VIGLN	2	2,6	14,334	0,00E+00	0,00E+00	2,01E+03	0,00E+00	1,17E+03	0,00E+00
Q00587, BORG5	1	5,1	7,3674	0,00E+00	0,00E+00	0,00E+00	1,05E+04	0,00E+00	0,00E+00

Q00610, CLH1	21	17,4	148,16	0,00E+00	1,26E+03	5,06E+02	7,27E+03	1,91E+04	3,33E+04
Q00839, HNRPU	7	10,5	48,995	0,00E+00	1,21E+03	5,43E+03	3,00E+04	1,83E+04	5,92E+04
Q01082, SPTB2	29	15	204,31	1,02E+03	1,82E+04	1,95E+04	2,17E+03	2,03E+03	4,13E+03
Q01469, FABP5	2	13,3	13,888	1,23E+04	1,74E+05	0,00E+00	0,00E+00	0,00E+00	0,00E+00
Q01650, LAT1	4	10,8	54,633	0,00E+00	0,00E+00	2,09E+03	1,68E+05	8,49E+04	7,73E+04
Q02218, ODO1	7	9,4	45,062	0,00E+00	0,00E+00	0,00E+00	6,98E+03	1,18E+04	0,00E+00
Q02383, SEMG2	3	7,9	11,978	0,00E+00	5,01E+03	0,00E+00	0,00E+00	0,00E+00	0,00E+00
Q02413, DSG1	2	2,9	15,364	0,00E+00	3,55E+03	0,00E+00	0,00E+00	0,00E+00	0,00E+00
Q02487, DSC2	4	7,5	18,736	0,00E+00	0,00E+00	0,00E+00	6,56E+03	2,23E+03	2,24E+03
Q02809, PLOD1	12	25	75,955	0,00E+00	0,00E+00	0,00E+00	1,94E+04	2,77E+04	5,29E+03
Q02878, RL6	4	17,7	33,322	3,93E+03	6,29E+03	1,80E+04	9,08E+04	5,26E+04	6,12E+04
Q02978, M2OM	13	53,5	323,31	8,81E+03	1,36E+05	1,80E+05	9,23E+05	2,48E+05	6,87E+05
Q04721, NOTC2	2	1	15,713	0,00E+00	0,00E+00	0,00E+00	2,52E+03	3,41E+03	2,45E+03
Q04837, SSBP	5	38,5	71,649	4,93E+04	2,24E+05	1,05E+05	9,65E+04	1,09E+04	1,23E+05
Q07021, C1QBP	6	31,6	194,13	4,92E+03	2,27E+04	8,39E+03	4,70E+05	1,29E+05	3,22E+05
Q07065, CKAP4	9	20,6	65,409	0,00E+00	0,00E+00	0,00E+00	1,08E+04	2,81E+04	1,69E+04
Q07157, ZO1	5	4,3	30,795	0,00E+00	0,00E+00	0,00E+00	3,58E+03	0,00E+00	0,00E+00
Q07820, MCL1	4	19,7	23,904	0,00E+00	0,00E+00	0,00E+00	9,43E+03	0,00E+00	6,25E+03
Q07954, LRP1	9	3	56,262	0,00E+00	0,00E+00	0,00E+00	1,76E+02	1,23E+03	0,00E+00
Q08188, TGM3	6	12,3	58,952	0,00E+00	2,24E+04	0,00E+00	0,00E+00	0,00E+00	0,00E+00
Q08211, DHX9	8	8,2	50,776	0,00E+00	6,94E+02	4,52E+03	4,89E+03	7,84E+02	3,60E+03
Q08379, GOGA2	3	3,4	21,781	0,00E+00	0,00E+00	6,37E+02	1,65E+04	1,54E+03	1,28E+04
Q08945, SSRP1	3	5,2	19,035	0,00E+00	0,00E+00	0,00E+00	0,00E+00	7,87E+03	7,27E+03
Q10471, GALT2	2	5,3	10,984	0,00E+00	0,00E+00	0,00E+00	0,00E+00	4,33E+03	0,00E+00
Q12769, NU160	8	6,8	61,603	0,00E+00	0,00E+00	0,00E+00	2,71E+04	3,48E+03	8,71E+03
Q12797, ASPH	3	6,2	20,646	0,00E+00	0,00E+00	0,00E+00	1,08E+04	3,30E+03	2,57E+03
Q12849, GRSF1	4	11	24,917	0,00E+00	0,00E+00	2,71E+03	1,47E+04	1,81E+04	0,00E+00
Q14839, CHD4	2	1,6	12,197	0,00E+00	0,00E+00	0,00E+00	8,96E+02	0,00E+00	7,18E+02
Q12887, COX10	1	4,3	8,8745	0,00E+00	0,00E+00	0,00E+00	1,30E+04	0,00E+00	0,00E+00
Q12893, TM115	1	5,1	9,1582	0,00E+00	0,00E+00	0,00E+00	4,43E+04	1,86E+04	0,00E+00
Q12905, ILF2	3	10,5	17,885	0,00E+00	0,00E+00	0,00E+00	1,26E+04	4,41E+03	1,52E+04
Q12906, ILF3	1	2	6,6594	0,00E+00	0,00E+00	0,00E+00	0,00E+00	0,00E+00	3,20E+03
Q12907, LMAN2	2	9,6	14,61	0,00E+00	0,00E+00	0,00E+00	0,00E+00	1,35E+04	0,00E+00
Q12923, PTN13	3	1,4	17,471	0,00E+00	1,07E+03	0,00E+00	6,84E+02	0,00E+00	9,05E+02
Q12931, TRAP1	16	31,5	153,5	0,00E+00	9,05E+03	9,83E+03	3,05E+05	1,60E+05	9,22E+04
Q13011, ECH1	1	4,9	8,1258	0,00E+00	0,00E+00	0,00E+00	7,90E+03	0,00E+00	3,35E+03
Q13084, RM28	1	6,6	16,941	0,00E+00	9,85E+03	0,00E+00	0,00E+00	0,00E+00	0,00E+00
Q13155, AIMP2	2	9,1	11,678	0,00E+00	0,00E+00	0,00E+00	6,71E+03	0,00E+00	7,10E+03
Q13162, PRDX4	2	7,7	12,308	0,00E+00	8,16E+03	0,00E+00	0,00E+00	0,00E+00	9,02E+03
Q13190, STX5	2	8,5	14,216	0,00E+00	0,00E+00	0,00E+00	1,15E+04	0,00E+00	0,00E+00
Q13232, NDK3	2	16	15,08	0,00E+00	3,46E+03	0,00E+00	3,19E+04	1,61E+04	2,85E+04
Q13283, G3BP1	1	3,6	6,2949	0,00E+00	0,00E+00	0,00E+00	0,00E+00	0,00E+00	9,69E+03
Q13286, CLN3	1	3,4	7,1755	0,00E+00	0,00E+00	0,00E+00	1,35E+04	9,09E+03	7,62E+03
Q13395, TARB1	1	0,9	6,3105	0,00E+00	0,00E+00	0,00E+00	1,51E+03	0,00E+00	0,00E+00
Q13405, RM49	3	23,5	22,286	0,00E+00	4,60E+04	1,92E+04	2,95E+04	1,50E+04	5,89E+04
Q13409, DC1I2	2	5,5	11,107	0,00E+00	0,00E+00	0,00E+00	8,69E+03	0,00E+00	0,00E+00

Q13423, NNTM	16	19,2	179,38	0,00E+00	0,00E+00	0,00E+00	4,87E+04	8,93E+04	5,18E+04
Q13438, OS9	4	8,1	27,979	0,00E+00	0,00E+00	0,00E+00	1,03E+04	1,83E+04	0,00E+00
Q13444, ADA15	3	4,6	17,345	0,00E+00	0,00E+00	0,00E+00	4,25E+03	0,00E+00	1,51E+03
Q13445, TMED1	2	11,5	12,9	0,00E+00	0,00E+00	0,00E+00	2,16E+04	1,21E+04	1,65E+04
Q13472, TOP3A	1	1,2	6,3807	0,00E+00	0,00E+00	0,00E+00	1,23E+03	0,00E+00	0,00E+00
Q13505, MTX1	6	20,4	43,792	0,00E+00	0,00E+00	0,00E+00	6,41E+04	2,75E+04	4,48E+04
Q13586, STIM1	2	3,5	11,289	0,00E+00	0,00E+00	0,00E+00	2,39E+03	0,00E+00	1,17E+03
Q13637, RAB32	4	20,4	24,861	0,00E+00	0,00E+00	0,00E+00	2,55E+04	0,00E+00	6,85E+03
Q13724, MOGS	5	8,2	32,911	0,00E+00	0,00E+00	0,00E+00	4,70E+03	3,05E+03	4,82E+03
Q13813, SPTN1	32	16,5	213,72	1,07E+03	1,96E+04	1,80E+04	9,27E+02	3,60E+03	2,19E+03
Q13948, CASP	2	3,7	13,872	0,00E+00	0,00E+00	0,00E+00	5,96E+03	1,64E+03	3,74E+03
Q14103, HNRPD	1	3,9	6,6277	0,00E+00	1,18E+04	1,06E+04	0,00E+00	0,00E+00	0,00E+00
Q14126, DSG2	12	16,3	90,211	0,00E+00	0,00E+00	0,00E+00	7,94E+04	1,17E+04	4,11E+03
Q14152, EIF3A	4	3,5	24,418	0,00E+00	0,00E+00	1,65E+03	2,35E+03	5,76E+03	9,40E+03
Q14156, EFR3A	8	15	67,343	0,00E+00	0,00E+00	0,00E+00	2,14E+04	1,03E+04	9,00E+03
Q14160, SCRIB	12	11,2	91,936	0,00E+00	0,00E+00	0,00E+00	1,93E+04	3,03E+03	6,17E+03
Q14168, MPP2	5	11,1	31,343	0,00E+00	0,00E+00	0,00E+00	0,00E+00	1,43E+04	7,27E+03
Q14203, DCTN1	4	5,6	26,184	0,00E+00	0,00E+00	0,00E+00	4,46E+03	0,00E+00	3,68E+03
Q14204, DYHC1	83	22,4	323,31	0,00E+00	0,00E+00	4,33E+02	6,87E+04	1,33E+04	1,89E+04
Q14254, FLOT2	10	30,1	107,05	0,00E+00	0,00E+00	0,00E+00	7,38E+04	5,89E+04	3,05E+04
Q14257, RCN2	11	45,4	323,31	4,36E+03	8,77E+03	1,28E+04	1,10E+06	3,02E+05	5,33E+05
Q14318, FKBP8	5	17,7	76,332	0,00E+00	0,00E+00	0,00E+00	8,86E+04	7,83E+04	1,59E+05
Q14344, GNA13	3	10,3	18,071	0,00E+00	0,00E+00	0,00E+00	0,00E+00	1,42E+04	0,00E+00
Q14517, FAT1	6	1,8	38,264	0,00E+00	0,00E+00	0,00E+00	1,50E+03	3,17E+02	0,00E+00
Q14571, ITPR2	7	3,3	46,453	0,00E+00	0,00E+00	0,00E+00	3,97E+03	7,15E+02	3,01E+03
Q14573, ITPR3	4	1,6	23,046	0,00E+00	0,00E+00	0,00E+00	4,66E+02	0,00E+00	2,56E+03
Q14574, DSC3	5	9,7	32,121	0,00E+00	0,00E+00	7,93E+02	1,25E+04	0,00E+00	4,87E+03
Q14643, ITPR1	2	0,8	11,927	0,00E+00	0,00E+00	0,00E+00	2,46E+02	0,00E+00	9,52E+02
Q14677, EPN4	3	6,7	17,483	0,00E+00	0,00E+00	0,00E+00	8,94E+03	0,00E+00	0,00E+00
Q14681, KCTD2	6	41,1	262,36	1,91E+05	1,88E+05	2,80E+05	0,00E+00	0,00E+00	2,00E+04
Q14683, SMC1A	2	1,7	11,346	0,00E+00	0,00E+00	0,00E+00	3,81E+03	0,00E+00	0,00E+00
Q14697, GANAB	17	19,9	117,58	0,00E+00	0,00E+00	0,00E+00	2,48E+04	1,47E+04	1,64E+04
Q14728, MFS10	1	2,9	7,6837	0,00E+00	0,00E+00	0,00E+00	5,33E+03	0,00E+00	6,33E+03
Q14739, LBR	4	8,1	50,8	0,00E+00	0,00E+00	0,00E+00	1,60E+05	3,36E+04	2,29E+05
Q14766, LTBP1	10	9,4	78,102	6,86E+03	7,07E+03	7,76E+03	2,68E+03	1,48E+04	2,99E+03
Q14789, GOGB1	6	2	37,305	0,00E+00	0,00E+00	0,00E+00	3,70E+03	6,15E+02	0,00E+00
Q14974, IMB1	4	7	28,978	0,00E+00	7,20E+02	0,00E+00	1,55E+04	7,40E+03	1,81E+04
Q14BN4, SLMAP	2	3,1	11,776	0,00E+00	0,00E+00	0,00E+00	2,64E+03	8,64E+02	0,00E+00
Q14CZ7, FAKD3	3	4,8	17,576	0,00E+00	0,00E+00	0,00E+00	0,00E+00	3,05E+03	1,13E+04
Q15006, EMC2	6	26,3	46,525	0,00E+00	0,00E+00	0,00E+00	1,50E+04	5,53E+04	5,92E+04
Q15021, CND1	6	5,2	37,431	0,00E+00	0,00E+00	0,00E+00	1,01E+04	0,00E+00	2,34E+03
Q15031, SYLM	7	11	45,97	0,00E+00	0,00E+00	0,00E+00	3,56E+04	8,28E+03	1,69E+04
Q15043, S39AE	1	2,4	6,8955	0,00E+00	0,00E+00	0,00E+00	6,81E+03	7,25E+03	1,14E+04
Q15046, SYK	4	8,9	28,726	0,00E+00	0,00E+00	1,08E+03	2,03E+04	1,41E+04	2,00E+04
Q15070, OXA1L	5	11,7	32,267	0,00E+00	0,00E+00	0,00E+00	1,85E+04	1,03E+04	6,04E+04
Q15084, PDIA6	4	14,5	30,591	3,14E+03	0,00E+00	1,06E+04	3,86E+04	1,92E+04	5,12E+04

Q15111, PLCL1	1	1,2	8,0384	0,00E+00	0,00E+00	0,00E+00	0,00E+00	0,00E+00	0,00E+00
Q15118, PDK1	2	5	12,009	0,00E+00	0,00E+00	0,00E+00	7,02E+03	4,06E+03	1,87E+03
Q15120, PDK3;REV__SP	5	17	33,235	0,00E+00	2,31E+03	0,00E+00	2,47E+04	9,92E+03	3,72E+03
Q15149, PLEC	7	2,1	45,104	0,00E+00	0,00E+00	0,00E+00	1,92E+03	8,35E+02	8,24E+02
Q15155, NOMO1	15	18,5	103,37	0,00E+00	0,00E+00	0,00E+00	3,44E+04	2,05E+04	2,15E+04
Q15165, PON2	1	4,8	9,8143	0,00E+00	0,00E+00	0,00E+00	1,46E+04	2,59E+03	5,09E+03
Q15208, STK38	5	16,8	36,427	0,00E+00	1,83E+04	1,31E+03	0,00E+00	0,00E+00	0,00E+00
Q15233, NONO	2	6,6	12,76	0,00E+00	2,72E+04	0,00E+00	0,00E+00	8,21E+03	5,17E+03
Q15293, RCN1	7	24,8	63,074	0,00E+00	0,00E+00	0,00E+00	2,18E+05	1,73E+04	1,08E+05
Q15365, PCBP1	3	9,8	12,021	0,00E+00	0,00E+00	6,28E+03	0,00E+00	7,73E+03	1,96E+04
Q15366, PCBP2	4	13,4	27,736	0,00E+00	1,66E+04	2,05E+04	4,67E+03	1,65E+04	2,79E+04
Q15388, TOM20	3	27,6	19,8	0,00E+00	0,00E+00	3,12E+04	9,35E+03	6,97E+03	2,52E+05
Q15392, DHC24	4	10,5	28,618	0,00E+00	0,00E+00	0,00E+00	1,01E+04	5,91E+03	2,54E+04
Q15393, SF3B3	4	3,9	26,816	0,00E+00	7,64E+02	1,96E+03	3,99E+03	3,56E+03	5,30E+03
Q15629, TRAM1	2	5,6	13,408	2,79E+03	0,00E+00	0,00E+00	5,51E+04	5,47E+04	6,51E+04
Q15717, ELAV1	1	3,4	6,4476	0,00E+00	0,00E+00	0,00E+00	4,04E+03	5,37E+03	6,16E+03
Q15738, NSDHL	6	27,3	75,042	0,00E+00	0,00E+00	0,00E+00	5,68E+04	7,06E+04	5,91E+04
Q15750, TAB1	1	2,2	6,6619	0,00E+00	0,00E+00	1,81E+03	0,00E+00	0,00E+00	0,00E+00
Q15758, AAAT	12	32,3	323,01	3,16E+03	2,94E+04	2,59E+04	4,91E+05	1,28E+06	1,41E+06
Q15773, MLF2	1	4,8	6,9083	0,00E+00	0,00E+00	0,00E+00	2,10E+04	9,48E+03	1,30E+04
Q16540, RM23	4	29,4	34,696	1,13E+04	5,04E+04	1,59E+04	9,59E+04	4,41E+04	4,47E+04
Q16563, SYPL1	1	4,2	7,0814	0,00E+00	0,00E+00	0,00E+00	0,00E+00	2,88E+04	0,00E+00
Q16643, DREB	3	6,9	20,534	0,00E+00	1,15E+04	0,00E+00	0,00E+00	0,00E+00	0,00E+00
Q16698, DECR	3	13,7	18,255	0,00E+00	0,00E+00	0,00E+00	1,23E+04	0,00E+00	0,00E+00
Q16706, MA2A1	1	1	6,3684	0,00E+00	0,00E+00	0,00E+00	1,61E+03	0,00E+00	0,00E+00
Q16718, NDUA5	2	31	15,795	0,00E+00	0,00E+00	0,00E+00	9,63E+04	0,00E+00	1,56E+05
Q16739, CEGT	2	7,9	12,617	0,00E+00	0,00E+00	0,00E+00	1,03E+04	2,05E+03	0,00E+00
Q16762, THTR	2	10,4	15,465	0,00E+00	0,00E+00	0,00E+00	1,69E+04	1,68E+04	0,00E+00
Q16769, QPCT	6	22,2	45,941	1,22E+04	5,77E+04	3,46E+04	1,65E+04	5,05E+04	2,41E+04
Q16795, NDUA9	13	45,6	172,86	0,00E+00	0,00E+00	0,00E+00	2,16E+05	7,22E+04	1,03E+05
Q16822, PCKGM	8	14,8	50,658	0,00E+00	0,00E+00	0,00E+00	1,35E+04	2,44E+04	2,35E+04
Q16836, HCDH	5	27,4	56,21	0,00E+00	0,00E+00	0,00E+00	6,85E+04	7,28E+04	2,46E+04
Q16850, CP51A	1	2,8	6,9699	0,00E+00	0,00E+00	0,00E+00	0,00E+00	0,00E+00	1,66E+03
Q16891, MIC60	28	47,2	323,31	1,40E+03	2,68E+03	2,79E+03	1,37E+06	3,88E+05	5,89E+05
Q1W6H9, F110C	1	4	6,294	0,00E+00	0,00E+00	0,00E+00	0,00E+00	0,00E+00	1,12E+05
Q29RF7, PDS5A	2	1,8	11,469	0,00E+00	0,00E+00	0,00E+00	7,38E+03	0,00E+00	0,00E+00
Q32P28, P3H1	4	6,8	25,938	0,00E+00	0,00E+00	0,00E+00	1,37E+04	2,20E+04	1,12E+04
Q3KQZ1, S2535	1	3,7	6,9033	0,00E+00	0,00E+00	0,00E+00	1,89E+03	0,00E+00	3,47E+03
Q3SXM5, HSDL1	7	23	53,739	0,00E+00	2,66E+03	0,00E+00	2,08E+05	7,83E+04	7,96E+04
Q3SXY8, AR13B	1	3	6,623	0,00E+00	0,00E+00	0,00E+00	4,16E+03	1,80E+03	3,49E+03
Q3SY69, AL1L2	15	25,5	159,3	0,00E+00	7,96E+02	1,47E+03	4,48E+04	3,93E+04	2,59E+04
Q3V6T2, GRDN	3	2,1	21,153	0,00E+00	3,96E+03	1,72E+03	0,00E+00	0,00E+00	0,00E+00
Q3ZCQ8, TIM50	7	28,6	133,1	2,25E+04	2,91E+04	6,37E+04	1,15E+06	5,37E+05	6,00E+05
Q49A26, GLYR1	3	8	26,781	2,74E+03	1,78E+04	1,19E+04	0,00E+00	0,00E+00	0,00E+00
Q4G0N4, NAKD2	1	3,2	7,2182	0,00E+00	0,00E+00	0,00E+00	5,70E+03	0,00E+00	0,00E+00
Q53EU6, GPAT3	1	2,8	6,9355	0,00E+00	0,00E+00	0,00E+00	0,00E+00	4,14E+03	0,00E+00

Q53GQ0, DHB12	3	12,5	33,845	0,00E+00	1,35E+04	3,92E+03	1,46E+04	0,00E+00	9,11E+04
Q53H12, AGK	12	48,6	323,31	0,00E+00	0,00E+00	2,41E+03	8,46E+05	1,79E+05	4,21E+05
Q53R41, FAKD1	7	11	48,398	0,00E+00	0,00E+00	0,00E+00	2,24E+04	1,24E+04	1,30E+04
Q562R1, ACTBL	4	11,2	7,0623	0,00E+00	9,29E+03	4,77E+03	0,00E+00	0,00E+00	0,00E+00
Q567V2, M17L2	2	10,7	13,42	0,00E+00	0,00E+00	0,00E+00	3,10E+04	6,21E+03	2,47E+04
Q5BJF2, SGMR2	2	13,1	11,715	0,00E+00	0,00E+00	0,00E+00	5,87E+04	4,67E+04	6,78E+04
Q5BJH7, YIF1B	1	4,1	6,4539	0,00E+00	0,00E+00	0,00E+00	2,25E+04	1,51E+04	3,19E+04
Q5BKT4, AG10A	3	8,2	17,725	0,00E+00	0,00E+00	0,00E+00	0,00E+00	2,10E+03	1,34E+04
Q5HY98, ZN766	1	3,4	6,3567	0,00E+00	0,00E+00	0,00E+00	0,00E+00	2,15E+04	2,49E+04
Q5HYI7, MTX3	2	10,6	12,916	0,00E+00	0,00E+00	0,00E+00	1,91E+04	0,00E+00	3,56E+03
Q5HYI8, RABL3	1	8,5	7,0805	0,00E+00	0,00E+00	0,00E+00	7,09E+03	0,00E+00	0,00E+00
Q5HYK3, COQ5	8	34,9	74,534	0,00E+00	0,00E+00	0,00E+00	5,60E+04	4,55E+03	3,17E+03
Q5J8M3, EMC4	2	12	14,08	0,00E+00	0,00E+00	0,00E+00	1,32E+04	6,14E+03	4,90E+04
Q5JRA6, TGO1	6	3,6	36,205	0,00E+00	0,00E+00	0,00E+00	8,72E+03	0,00E+00	0,00E+00
Q5JRX3, PREP	4	4,7	25,314	0,00E+00	0,00E+00	0,00E+00	9,57E+03	0,00E+00	0,00E+00
Q5JTZ9, SYAM	18	27,3	153,14	0,00E+00	0,00E+00	0,00E+00	1,43E+05	5,58E+04	2,79E+04
Q5JU69, TOR2A	2	9,3	11,79	0,00E+00	0,00E+00	0,00E+00	1,08E+04	1,29E+03	6,45E+03
Q5RI15, COX20	2	22	14,463	0,00E+00	0,00E+00	0,00E+00	2,04E+04	1,49E+04	3,15E+04
Q5SQN1, SNP47	6	19	43,182	0,00E+00	0,00E+00	0,00E+00	3,02E+04	0,00E+00	5,14E+03
Q5SRE5, NU188	8	6,2	52,466	0,00E+00	0,00E+00	0,00E+00	7,73E+03	4,73E+02	2,97E+03
Q5ST30, SYVM	1	0,8	6,6355	0,00E+00	0,00E+00	0,00E+00	3,73E+03	1,84E+03	1,43E+03
Q5SWX8, ODR4	2	5,3	12,594	2,04E+03	0,00E+00	2,30E+03	4,79E+03	6,14E+03	0,00E+00
Q5T160, SYRM	12	26	83,707	0,00E+00	0,00E+00	0,00E+00	0,00E+00	5,62E+04	6,26E+04
Q9Y6H1, CHCH2	1	15,9	12,726	0,00E+00	0,00E+00	0,00E+00	1,10E+05	0,00E+00	7,70E+04
Q5T3U5, MRP7	1	1,1	7,2302	0,00E+00	0,00E+00	0,00E+00	0,00E+00	1,10E+03	2,00E+03
Q5T440, CAF17	2	7	13,239	0,00E+00	5,75E+03	8,85E+03	1,31E+04	0,00E+00	0,00E+00
Q5T653, RM02	2	12,1	13,803	0,00E+00	0,00E+00	3,98E+03	1,23E+04	0,00E+00	1,50E+04
Q5T9A4, ATD3B	20	38,6	71,585	3,68E+03	0,00E+00	7,03E+03	6,40E+04	7,60E+04	6,91E+04
Q5VT06, CE350	3	1,3	18,115	0,00E+00	0,00E+00	8,91E+02	0,00E+00	0,00E+00	0,00E+00
Q5VT66, MARC1	3	17,5	24,1	0,00E+00	0,00E+00	0,00E+00	2,46E+04	7,59E+03	7,22E+03
Q5VUD6, DIK1B	1	2,8	7,4392	0,00E+00	0,00E+00	0,00E+00	9,64E+03	0,00E+00	0,00E+00
Q5VV42, CDKAL	2	4,3	12,584	0,00E+00	0,00E+00	0,00E+00	0,00E+00	8,20E+03	5,77E+03
Q5VXT5, SYPL2	1	5,1	6,5263	0,00E+00	0,00E+00	0,00E+00	5,72E+03	7,30E+03	0,00E+00
Q5VYK3, ECM29	2	1,5	12,477	0,00E+00	0,00E+00	0,00E+00	1,96E+03	0,00E+00	8,49E+02
Q5XKP0, MIC13	2	35,6	105,04	0,00E+00	0,00E+00	0,00E+00	2,71E+05	7,36E+04	2,09E+05
Q68CQ7, GL8D1	4	16,7	29,747	0,00E+00	0,00E+00	0,00E+00	1,36E+05	2,09E+04	3,94E+04
Q6DKK2, TTC19	4	11,1	25,7	0,00E+00	0,00E+00	0,00E+00	3,50E+04	2,49E+04	2,66E+04
Q6IAN0, DRS7B	3	14,2	22,519	0,00E+00	0,00E+00	0,00E+00	3,17E+04	2,74E+03	2,04E+04
Q6IQ22, RAB12	2	12,3	11,808	0,00E+00	0,00E+00	0,00E+00	7,22E+03	0,00E+00	3,93E+03
Q6JQN1, ACD10	3	4,1	18,157	0,00E+00	0,00E+00	0,00E+00	0,00E+00	1,06E+03	2,52E+03
Q6KCM7, SCMC2	3	10,9	20,308	0,00E+00	0,00E+00	0,00E+00	2,33E+04	5,84E+03	9,03E+03
Q6L8Q7, PDE12	3	8,4	22,226	0,00E+00	0,00E+00	0,00E+00	1,08E+04	6,60E+03	2,75E+03
Q6NTF9, RHBD2	2	8,8	13,942	0,00E+00	0,00E+00	0,00E+00	7,00E+04	1,32E+04	3,85E+04
Q6NUK1, SCMC1	16	42,1	310,9	0,00E+00	3,53E+03	4,24E+03	6,62E+05	2,31E+05	6,06E+05
Q6NUQ1, RINT1	3	6,1	17,908	0,00E+00	0,00E+00	0,00E+00	7,16E+03	3,39E+03	2,63E+03
Q6NVY1, HIBCH	1	2,8	6,631	0,00E+00	0,00E+00	0,00E+00	2,82E+03	0,00E+00	1,35E+03

Q6P087, RUSD3	1	4,6	7,0827	0,00E+00	0,00E+00	1,65E+03	1,10E+04	0,00E+00	3,11E+03
Q6P161, RM54	1	7,2	6,7547	1,60E+04	0,00E+00	2,39E+04	5,82E+04	3,76E+04	5,03E+04
Q6P1L8, RM14	1	9,7	8,0321	0,00E+00	0,00E+00	0,00E+00	1,18E+04	8,00E+03	1,67E+04
Q6P1M0, S27A4	6	10,6	37,383	0,00E+00	0,00E+00	0,00E+00	0,00E+00	1,69E+04	4,08E+04
Q6P3W7, SCYL2	3	4,4	20,798	2,16E+03	0,00E+00	2,27E+03	8,29E+03	0,00E+00	0,00E+00
Q6P444, MTFR2	4	13,2	24,477	0,00E+00	0,00E+00	0,00E+00	2,84E+04	0,00E+00	0,00E+00
Q6P4A7, SFXN4	10	49,3	133,46	3,85E+03	0,00E+00	7,84E+03	4,34E+05	1,33E+05	1,54E+05
Q6PI48, SYDM	10	20,6	76,663	0,00E+00	0,00E+00	0,00E+00	5,60E+03	4,35E+04	0,00E+00
Q6PI78, TMM65	3	14,2	18,33	0,00E+00	0,00E+00	0,00E+00	1,97E+04	5,63E+03	5,96E+04
Q6PML9, ZNT9	4	8,8	34,259	0,00E+00	0,00E+00	0,00E+00	3,46E+04	2,57E+04	3,53E+04
Q6SZW1, SARM1	7	15,9	72,952	0,00E+00	0,00E+00	0,00E+00	3,62E+04	8,87E+03	2,40E+04
Q6UB35, C1TM	16	21,1	114,71	1,06E+04	2,81E+04	2,78E+04	9,68E+04	1,03E+05	1,65E+04
Q6UVY6, MOXD1	5	10	33,262	0,00E+00	0,00E+00	0,00E+00	5,18E+04	6,21E+03	6,02E+03
Q6UW68, TM205	2	15,9	26,198	0,00E+00	0,00E+00	0,00E+00	3,96E+04	6,00E+03	1,09E+05
Q6UW78, UQCC3	1	23,7	8,6756	0,00E+00	0,00E+00	0,00E+00	4,62E+04	3,61E+04	3,53E+04
Q6UWP7, LCLT1	4	9,7	25,35	0,00E+00	0,00E+00	0,00E+00	3,68E+04	4,23E+04	4,25E+04
Q6YN16, HSDL2	4	15,6	27,23	0,00E+00	0,00E+00	0,00E+00	2,78E+04	1,73E+04	1,17E+04
Q6ZMG9, CERS6	1	2,9	8,582	0,00E+00	0,00E+00	0,00E+00	2,37E+04	1,27E+04	1,20E+04
Q6ZNB6, NFXL1	2	4,6	12,499	0,00E+00	0,00E+00	0,00E+00	0,00E+00	0,00E+00	4,13E+03
Q6ZT21, TMPPE	2	4	12,313	0,00E+00	0,00E+00	0,00E+00	0,00E+00	0,00E+00	6,64E+03
Q6ZXV5, TMTC3	4	5,1	25,661	0,00E+00	0,00E+00	0,00E+00	1,92E+04	1,97E+03	1,64E+04
Q709C8, VP13C	10	3,1	60,725	0,00E+00	0,00E+00	0,00E+00	4,07E+03	9,69E+01	0,00E+00
Q70HW3, SAMC	2	9,5	14,291	0,00E+00	0,00E+00	0,00E+00	4,57E+03	0,00E+00	0,00E+00
Q71U36, TBA1A	13	45,9	6,3357	0,00E+00	0,00E+00	0,00E+00	0,00E+00	2,09E+03	2,57E+03
Q7KZF4, SND1	6	10,3	36,528	0,00E+00	0,00E+00	0,00E+00	2,95E+03	1,50E+04	0,00E+00
Q7KZN9, COX15	5	16,6	37,07	0,00E+00	0,00E+00	2,56E+03	8,35E+04	1,19E+04	2,07E+04
Q7L0J3, SV2A	2	4,4	13,04	0,00E+00	0,00E+00	0,00E+00	3,57E+03	0,00E+00	0,00E+00
Q7L0Y3, TM10C	6	20,6	66,114	0,00E+00	0,00E+00	0,00E+00	3,30E+04	9,53E+03	6,67E+03
Q7L2E3, DHX30	24	24,3	196,3	8,85E+03	1,56E+04	3,42E+04	1,02E+05	3,14E+04	3,73E+04
Q7L3T8, SYPM	5	15,2	46,963	0,00E+00	0,00E+00	0,00E+00	2,79E+04	0,00E+00	6,29E+03
Q7L592, NDUF7	6	18,8	43,28	0,00E+00	0,00E+00	2,04E+03	1,22E+04	1,43E+04	6,86E+03
Q7L8L6, FAKD5	14	27,5	171,46	0,00E+00	0,00E+00	0,00E+00	1,01E+05	3,68E+04	5,30E+04
Q7LGA3, HS2ST	2	7,3	12,588	0,00E+00	0,00E+00	0,00E+00	8,89E+03	1,36E+04	0,00E+00
Q7Z2W4, ZCCHV	1	1,6	6,7189	0,00E+00	0,00E+00	0,00E+00	1,85E+03	0,00E+00	6,83E+02
Q7Z2W9, RM21	2	15,1	14,375	0,00E+00	9,33E+03	5,39E+03	4,94E+04	1,82E+04	9,66E+03
Q7Z3C6, ATG9A	10	14,3	64,458	0,00E+00	0,00E+00	0,00E+00	3,21E+04	3,06E+03	1,42E+04
Q7Z4H8, PLGT3	1	3,4	8,7889	2,71E+03	2,94E+03	3,01E+03	0,00E+00	0,00E+00	3,78E+03
Q7Z591, AKNA	1	1	6,5557	1,88E+02	0,00E+00	0,00E+00	0,00E+00	0,00E+00	0,00E+00
Q7Z5G4, GOGA7	3	24,1	18,523	0,00E+00	0,00E+00	0,00E+00	0,00E+00	0,00E+00	3,14E+04
Q7Z5H3, RHG22	4	4,4	24,984	5,06E+03	9,17E+03	1,76E+03	0,00E+00	0,00E+00	0,00E+00
Q7Z7G8, VP13B	1	0,3	6,523	0,00E+00	0,00E+00	0,00E+00	3,74E+02	0,00E+00	0,00E+00
Q86TV6, TTC7B	3	4,6	35,479	0,00E+00	0,00E+00	0,00E+00	6,05E+03	1,15E+03	3,95E+03
Q86UL3, GPAT4	2	5,7	11,694	0,00E+00	0,00E+00	0,00E+00	0,00E+00	0,00E+00	2,30E+04
Q86UP2, KTN1	2	2,2	11,694	0,00E+00	0,00E+00	0,00E+00	8,48E+02	0,00E+00	5,04E+02
Q86UT6, NLRX1	3	3,9	18,419	0,00E+00	0,00E+00	0,00E+00	7,24E+03	2,30E+03	2,54E+03
Q86V85, GP180	3	11,6	19,142	0,00E+00	0,00E+00	0,00E+00	1,58E+04	1,57E+04	9,87E+03

Q86VD7, S2542	1	6,9	6,3356	0,00E+00	0,00E+00	0,00E+00	6,85E+03	0,00E+00	0,00E+00
Q86VI3, IQGA3	2	1,6	12,147	0,00E+00	0,00E+00	0,00E+00	8,85E+02	0,00E+00	6,16E+02
Q86VP6, CAND1	6	6	35,37	4,31E+03	2,70E+03	0,00E+00	3,44E+03	7,41E+02	4,02E+03
Q86VR2, RETR3	1	3,2	7,0088	0,00E+00	0,00E+00	0,00E+00	4,40E+03	0,00E+00	5,37E+03
Q86VU5, CMTD1	2	12,2	13,169	0,00E+00	0,00E+00	0,00E+00	2,80E+03	1,12E+04	0,00E+00
Q86Y39, NDUAB	3	24,8	72,05	0,00E+00	0,00E+00	0,00E+00	3,73E+05	9,85E+04	3,52E+05
Q86YW9, MD12L	1	0,4	6,4405	0,00E+00	0,00E+00	0,00E+00	0,00E+00	0,00E+00	0,00E+00
Q8IUH5, ZDH17	2	3	11,403	0,00E+00	0,00E+00	0,00E+00	0,00E+00	0,00E+00	8,06E+03
Q8IV08, PLD3	2	4,1	12,016	0,00E+00	0,00E+00	0,00E+00	0,00E+00	4,81E+03	0,00E+00
Q8IVL6, P3H3	4	9,1	24,429	0,00E+00	0,00E+00	0,00E+00	3,05E+03	7,08E+02	2,43E+03
Q8IVS2, FABD	2	9,2	12,935	0,00E+00	0,00E+00	0,00E+00	3,59E+03	0,00E+00	2,14E+03
Q8IWA4, MFN1	4	6,5	25,883	0,00E+00	0,00E+00	0,00E+00	1,98E+04	3,13E+03	6,07E+03
Q8IWF2, FXRD2	1	2,5	7,1134	0,00E+00	0,00E+00	0,00E+00	1,58E+03	1,90E+03	1,48E+03
Q8IXB1, DJC10	3	5,2	20,868	0,00E+00	0,00E+00	2,09E+03	1,68E+04	0,00E+00	5,92E+03
Q8IXI1, MIRO2	15	37,1	195,78	0,00E+00	0,00E+00	2,19E+03	2,71E+05	1,34E+05	1,06E+05
Q8IXI2, MIRO1	9	19,1	52,398	0,00E+00	0,00E+00	0,00E+00	6,64E+04	5,20E+04	2,44E+04
Q8IXM3, RM41	2	12,4	12,423	0,00E+00	0,00E+00	0,00E+00	0,00E+00	0,00E+00	7,57E+04
Q8IY17, PLPL6	3	3,8	21,661	0,00E+00	0,00E+00	0,00E+00	5,11E+03	1,78E+03	3,83E+03
Q8IY26, PLPP6	1	8,8	8,7976	0,00E+00	0,00E+00	0,00E+00	6,23E+03	0,00E+00	0,00E+00
Q8IYB8, SUV3	2	3,9	12,682	0,00E+00	0,00E+00	0,00E+00	2,06E+03	4,01E+03	0,00E+00
Q8IYS2, K2013	2	4,3	11,171	0,00E+00	0,00E+00	0,00E+00	7,23E+03	0,00E+00	0,00E+00
Q8IYU8, MICU2	2	6,9	13,313	0,00E+00	0,00E+00	0,00E+00	5,63E+03	0,00E+00	6,55E+03
Q8IZ52, CHSS2	3	5,5	19,035	0,00E+00	0,00E+00	0,00E+00	1,05E+04	0,00E+00	0,00E+00
Q8IZV5, RDH10	2	6,7	11,385	0,00E+00	0,00E+00	0,00E+00	0,00E+00	0,00E+00	7,62E+03
Q8N0V3, RBFA	1	5,8	8,9623	0,00E+00	0,00E+00	0,00E+00	5,54E+03	3,38E+03	2,98E+03
Q8N0X7, SPART	2	3,6	12,515	0,00E+00	0,00E+00	0,00E+00	1,60E+04	0,00E+00	0,00E+00
Q8N122, RPTOR	1	1	6,623	0,00E+00	0,00E+00	0,00E+00	0,00E+00	0,00E+00	1,42E+03
Q8N1F7, NUP93	8	13,6	53,441	0,00E+00	0,00E+00	0,00E+00	4,90E+04	1,20E+04	2,33E+04
Q8N1F8, S11IP	12	13,1	79,137	0,00E+00	0,00E+00	0,00E+00	4,84E+04	1,72E+03	1,27E+04
Q8N2F6, ARM10	1	4,7	7,6295	0,00E+00	0,00E+00	0,00E+00	5,03E+03	0,00E+00	2,69E+03
Q8N2K0, ABD12	3	8,3	18,572	0,00E+00	0,00E+00	0,00E+00	6,56E+03	3,40E+03	3,60E+03
Q8N442, GUF1	10	22,1	62,56	0,00E+00	0,00E+00	0,00E+00	4,49E+04	2,63E+03	4,21E+03
Q8N490, PNKD	2	6	13,592	7,78E+03	0,00E+00	7,21E+03	3,74E+04	1,40E+04	8,78E+04
Q8N4Q0, PTGR3	1	4	7,708	0,00E+00	0,00E+00	0,00E+00	1,65E+04	8,99E+03	6,44E+03
Q8N4Q1, MIA40	4	29,6	49,012	0,00E+00	0,00E+00	0,00E+00	5,01E+04	2,76E+04	1,57E+05
Q8N4V1, MMGT1	1	18,3	9,2773	0,00E+00	0,00E+00	0,00E+00	3,72E+04	0,00E+00	1,14E+05
Q8N5M9, JAGN1	1	6,6	8,4794	0,00E+00	0,00E+00	0,00E+00	5,03E+03	0,00E+00	6,71E+04
Q8N5N7, RM50	2	19	12,031	0,00E+00	0,00E+00	0,00E+00	8,71E+03	0,00E+00	1,42E+04
Q8N5Z5, KCD17	5	25,9	52,733	1,94E+04	5,21E+04	8,09E+04	3,09E+04	1,04E+04	4,16E+04
Q8N6L1, KTAP2	1	12,5	9,9393	0,00E+00	0,00E+00	0,00E+00	1,41E+05	9,47E+04	2,52E+05
Q8N766, EMC1	16	25	120,62	0,00E+00	0,00E+00	0,00E+00	1,69E+04	3,56E+04	2,51E+04
Q8N8L6, ARL10	3	16	18,472	0,00E+00	0,00E+00	0,00E+00	4,18E+03	0,00E+00	8,14E+03
Q8N983, RM43	5	21,9	37,172	0,00E+00	2,39E+04	7,68E+03	2,51E+04	3,60E+04	9,66E+04
Q8NAN2, MIGA1	2	5,4	13,785	0,00E+00	0,00E+00	0,00E+00	2,29E+03	0,00E+00	3,20E+03
Q8NB49, AT11C	5	6	31,991	0,00E+00	0,00E+00	0,00E+00	1,27E+03	3,50E+03	3,63E+03
Q8NBI6, XXLT1	1	4,8	7,7595	0,00E+00	0,00E+00	0,00E+00	1,87E+03	3,35E+03	0,00E+00

Q8NBJ5, GT251	7	12,4	44,075	0,00E+00	0,00E+00	0,00E+00	1,64E+03	2,53E+04	5,49E+03
Q8NBM4, UBAC2	4	18,9	26,458	0,00E+00	0,00E+00	0,00E+00	6,84E+04	9,18E+03	1,36E+04
Q8NBN3, TM87A	2	4,9	14,372	0,00E+00	0,00E+00	0,00E+00	1,40E+04	0,00E+00	0,00E+00
Q8NBN7, RDH13	5	21,8	33,307	0,00E+00	0,00E+00	0,00E+00	2,33E+04	9,52E+03	3,56E+04
Q8NBP0, TTC13	2	2,9	15,222	0,00E+00	0,00E+00	0,00E+00	8,29E+03	2,98E+03	3,17E+03
Q8NBS9, TXND5	2	6,7	12,873	0,00E+00	0,00E+00	0,00E+00	4,60E+03	0,00E+00	0,00E+00
Q8NBU5, ATAD1	9	34,9	63,984	0,00E+00	0,00E+00	0,00E+00	1,99E+05	5,23E+04	7,05E+04
Q8NBX0, SCPDL	3	10,3	21,928	0,00E+00	0,00E+00	0,00E+00	0,00E+00	2,26E+04	4,52E+03
Q8NC60, NOA1	2	4,3	13,882	0,00E+00	0,00E+00	0,00E+00	5,50E+03	0,00E+00	0,00E+00
Q8NCG7, DGLB	3	6,4	18,744	0,00E+00	0,00E+00	0,00E+00	0,00E+00	4,04E+03	5,31E+03
Q8NCH0, CHSTE	2	5,9	11,903	0,00E+00	0,00E+00	0,00E+00	0,00E+00	6,43E+03	0,00E+00
Q8NCM8, DYHC2	2	0,6	11,901	0,00E+00	0,00E+00	0,00E+00	2,04E+02	0,00E+00	0,00E+00
Q8NDZ4, DIK2A	2	6	14,982	0,00E+00	0,00E+00	0,00E+00	8,36E+03	4,66E+03	6,00E+03
Q8NE01, CNNM3	5	12,7	32,386	0,00E+00	0,00E+00	0,00E+00	1,14E+04	1,64E+03	1,80E+03
Q8NE86, MCU	4	13,4	25,943	0,00E+00	0,00E+00	0,00E+00	3,86E+04	4,03E+03	1,38E+04
Q8NEW0, ZNT7	4	13,8	32,657	0,00E+00	0,00E+00	0,00E+00	3,87E+04	2,12E+04	3,25E+04
Q8NFC6, BD1L1	1	0,5	6,6152	0,00E+00	7,25E+03	4,64E+03	1,33E+04	8,68E+03	7,03E+03
Q8NFF5, FAD1	4	12,4	35,09	0,00E+00	0,00E+00	0,00E+00	1,54E+04	3,11E+03	4,60E+03
Q8NFH4, NUP37	1	4,9	6,8159	0,00E+00	0,00E+00	0,00E+00	4,18E+03	0,00E+00	0,00E+00
Q8NFQ8, TOIP2	3	9,1	20,827	0,00E+00	0,00E+00	0,00E+00	0,00E+00	1,14E+04	2,26E+03
Q8NHH9, ATLA2	2	4,3	12,673	0,00E+00	0,00E+00	0,00E+00	0,00E+00	3,01E+03	9,11E+03
Q8NI60, COQ8A	5	11,3	36,639	0,00E+00	3,06E+03	6,32E+03	6,02E+04	2,45E+04	4,42E+04
Q8TB37, NUBPL	2	10,7	12,54	0,00E+00	0,00E+00	0,00E+00	0,00E+00	0,00E+00	6,18E+03
Q8TB61, S35B2	4	10,2	25,681	0,00E+00	0,00E+00	0,00E+00	3,28E+04	6,43E+03	1,29E+04
Q8TBP6, S2540	3	11,2	19,121	0,00E+00	0,00E+00	0,00E+00	9,78E+03	1,49E+04	7,67E+03
Q8TC12, RDH11	3	12,3	18,656	0,00E+00	7,58E+03	0,00E+00	0,00E+00	0,00E+00	8,96E+03
Q8TCJ2, STT3B	4	4,8	20,132	0,00E+00	0,00E+00	0,00E+00	1,28E+04	1,20E+04	1,10E+04
Q8TCS8, PNPT1	5	7,4	32,701	0,00E+00	0,00E+00	0,00E+00	2,58E+04	5,05E+03	4,90E+03
Q8TCT9, HM13	2	5	11,435	0,00E+00	0,00E+00	0,00E+00	8,10E+03	8,92E+03	8,98E+03
Q8TDB4, HUMMR	2	30	12,365	0,00E+00	0,00E+00	0,00E+00	3,60E+04	0,00E+00	0,00E+00
Q8TEM1, PO210	14	9,4	92,864	0,00E+00	0,00E+00	0,00E+00	2,02E+04	1,55E+04	5,68E+03
Q8TEQ6, GEMI5	4	3,6	23,365	0,00E+00	0,00E+00	0,00E+00	3,17E+03	0,00E+00	1,49E+03
Q8TF71, MOT10	1	2,1	8,1945	0,00E+00	0,00E+00	0,00E+00	0,00E+00	0,00E+00	1,48E+04
Q8WU76, SCFD2	2	4,4	14,655	0,00E+00	0,00E+00	5,59E+03	2,33E+03	1,30E+03	2,72E+03
Q8WUK0, PTPM1	3	18,9	29,184	0,00E+00	0,00E+00	0,00E+00	3,97E+04	0,00E+00	2,33E+04
Q8WUM0, NU133	7	7,4	46,878	0,00E+00	0,00E+00	0,00E+00	1,20E+04	0,00E+00	6,87E+03
Q8WUM4, PDC6I	4	6,3	27,871	0,00E+00	0,00E+00	0,00E+00	1,70E+03	5,56E+03	0,00E+00
Q8WUM9, S20A1	3	6	20,71	0,00E+00	0,00E+00	0,00E+00	2,79E+04	3,92E+03	0,00E+00
Q8WVI0, SMIM4	1	15,7	9,5508	0,00E+00	3,79E+04	5,28E+04	3,20E+05	1,84E+05	2,58E+05
Q8WVM0, TFB1M	2	6,9	12,071	0,00E+00	0,00E+00	0,00E+00	5,38E+03	3,45E+03	3,39E+03
Q8WVM8, SCFD1	3	7,6	23,865	0,00E+00	0,00E+00	0,00E+00	5,75E+03	2,67E+03	6,77E+03
Q8WVX9, FACR1	5	11,7	32,71	0,00E+00	0,00E+00	0,00E+00	2,92E+04	1,43E+04	4,40E+04
Q8WWY3, PRP31	2	7,6	12,604	0,00E+00	3,13E+03	3,00E+03	0,00E+00	0,00E+00	0,00E+00
Q8WY22, BRI3B	1	6,8	7,0616	0,00E+00	0,00E+00	0,00E+00	0,00E+00	0,00E+00	1,34E+04
Q92499, DDX1	2	4,3	13,248	0,00E+00	0,00E+00	0,00E+00	3,18E+03	0,00E+00	0,00E+00
Q92504, S39A7	1	5,5	13,463	0,00E+00	0,00E+00	0,00E+00	4,80E+04	2,77E+04	3,23E+04

Q92542, NICA	6	10,4	37,699	0,00E+00	0,00E+00	0,00E+00	4,95E+04	1,71E+04	3,23E+03
Q92544, TM9S4	3	5,8	20,024	0,00E+00	0,00E+00	0,00E+00	1,04E+04	8,17E+03	2,37E+03
Q92545, TM131	1	0,7	6,5822	0,00E+00	0,00E+00	0,00E+00	8,73E+02	0,00E+00	5,74E+02
Q92552, RT27	13	33,8	107,62	0,00E+00	3,16E+04	2,10E+04	2,41E+05	1,37E+05	2,20E+05
Q92581, SL9A6	1	1,8	6,7136	0,00E+00	0,00E+00	0,00E+00	5,03E+03	0,00E+00	0,00E+00
Q92604, LGAT1	4	14,3	29,171	0,00E+00	0,00E+00	0,00E+00	2,74E+04	1,18E+04	1,86E+04
Q92615, LAR4B	1	2,3	7,1134	0,00E+00	0,00E+00	0,00E+00	0,00E+00	0,00E+00	1,95E+03
Q92616, GCN1	26	13,8	206,54	0,00E+00	0,00E+00	1,58E+02	1,89E+04	1,12E+04	2,44E+04
Q92621, NU205	25	16,5	244,31	0,00E+00	0,00E+00	0,00E+00	6,98E+04	2,09E+04	4,07E+04
Q92643, GPI8	2	5,8	11,814	0,00E+00	0,00E+00	0,00E+00	0,00E+00	1,89E+04	9,04E+03
Q92665, RT31	6	22,3	47,924	4,80E+03	0,00E+00	0,00E+00	1,02E+05	2,68E+04	6,84E+04
Q92667, AKAP1	7	12,1	46,793	0,00E+00	0,00E+00	0,00E+00	3,09E+04	1,38E+03	9,05E+03
Q92841, DDX17	2	3,6	6,3633	0,00E+00	0,00E+00	0,00E+00	2,84E+03	0,00E+00	0,00E+00
Q92878, RAD50	1	1,4	6,8435	0,00E+00	0,00E+00	0,00E+00	5,58E+02	0,00E+00	0,00E+00
Q92896, GSLG1	3	2,9	23,373	0,00E+00	0,00E+00	0,00E+00	4,48E+03	0,00E+00	9,73E+02
Q92900, RENT1	4	5,2	24,913	0,00E+00	0,00E+00	0,00E+00	1,60E+03	8,08E+02	2,48E+03
Q92947, GCDH	8	27,9	323,31	0,00E+00	0,00E+00	0,00E+00	3,13E+05	1,21E+05	6,49E+04
Q93008, USP9X	2	0,9	11,62	0,00E+00	0,00E+00	0,00E+00	1,55E+03	4,00E+02	0,00E+00
Q93063, EXT2	2	3,2	12,516	0,00E+00	0,00E+00	0,00E+00	5,85E+03	0,00E+00	2,06E+03
Q969N2, PIGT	4	11,8	42,033	0,00E+00	0,00E+00	0,00E+00	0,00E+00	1,70E+04	1,76E+04
Q969S9, RRF2M	3	4,7	16,833	0,00E+00	0,00E+00	0,00E+00	3,88E+03	1,29E+03	0,00E+00
Q969V5, MUL1	3	17,3	20,888	0,00E+00	0,00E+00	0,00E+00	1,64E+04	5,51E+03	8,09E+03
Q969Y2, GTPB3	5	18,7	39,657	0,00E+00	0,00E+00	0,00E+00	5,13E+04	1,25E+04	1,64E+04
Q969Z0, FAKD4	11	26,1	93,12	0,00E+00	2,31E+03	1,85E+03	1,70E+03	6,53E+04	7,82E+04
Q96A33, CCD47	7	17,8	88,555	0,00E+00	2,84E+03	2,68E+03	0,00E+00	8,88E+04	8,56E+04
Q96A35, RM24	3	14,8	18,891	0,00E+00	3,22E+03	0,00E+00	5,75E+04	3,43E+04	3,12E+04
Q96A46, MFRN2	3	11	20,723	0,00E+00	0,00E+00	0,00E+00	4,81E+04	0,00E+00	0,00E+00
Q96A65, EXOC4	3	5,2	19,626	0,00E+00	0,00E+00	0,00E+00	5,76E+03	0,00E+00	0,00E+00
Q96AA3, RFT1	2	4,8	14,157	0,00E+00	0,00E+00	0,00E+00	1,14E+04	8,52E+03	4,52E+03
Q96AE7, TTC17	2	2,4	11,961	0,00E+00	0,00E+00	0,00E+00	3,34E+03	0,00E+00	1,04E+03
Q96AG3, S2546	5	23,4	36,922	0,00E+00	0,00E+00	0,00E+00	4,52E+04	7,25E+03	1,40E+04
Q96AG4, LRC59	5	16,3	34,566	5,04E+03	0,00E+00	5,51E+03	6,67E+04	5,17E+04	1,06E+04
Q96AQ6, PBIP1	2	2,9	11,85	0,00E+00	0,00E+00	0,00E+00	3,80E+03	5,49E+03	2,03E+03
Q96BI3, APH1A	2	5,3	12,554	0,00E+00	0,00E+00	0,00E+00	7,77E+04	0,00E+00	0,00E+00
Q96BW9, TAM41	6	16,4	78,75	0,00E+00	0,00E+00	0,00E+00	1,37E+05	1,40E+04	5,25E+04
Q96C03, MID49	2	8,6	14,272	0,00E+00	0,00E+00	0,00E+00	1,18E+04	0,00E+00	4,13E+03
Q96C36, P5CR2	8	28,8	173,84	0,00E+00	0,00E+00	0,00E+00	2,98E+05	1,61E+04	9,79E+04
Q96CM8, ACSF2	2	7,3	14,173	0,00E+00	0,00E+00	0,00E+00	0,00E+00	3,86E+03	0,00E+00
Q96CQ1, S2536	2	10,6	10,04	0,00E+00	0,00E+00	0,00E+00	1,49E+04	6,17E+03	0,00E+00
Q96CS3, FAF2	8	29,4	98,07	0,00E+00	0,00E+00	0,00E+00	4,69E+04	2,43E+04	4,88E+04
Q96DA6, TIM14	2	28,4	49,183	0,00E+00	0,00E+00	0,00E+00	3,46E+04	0,00E+00	2,55E+04
Q96DV4, RM38	6	14,5	43,691	0,00E+00	2,50E+04	1,16E+04	3,47E+04	2,57E+04	3,48E+04
Q96E29, MTEF3	3	8,6	17,374	0,00E+00	0,00E+00	0,00E+00	1,36E+04	3,33E+03	0,00E+00
Q96E52, OMA1	3	5,5	19,585	0,00E+00	0,00E+00	0,00E+00	9,08E+03	2,11E+03	2,43E+03
Q96EL3, RM53	1	8,9	6,4235	0,00E+00	0,00E+00	0,00E+00	2,13E+04	0,00E+00	2,56E+04
Q96ER9, MITOK	7	21,4	115,32	0,00E+00	0,00E+00	0,00E+00	1,00E+05	2,71E+04	7,43E+04

Q96ES6, MFSD3	1	3,4	6,3633	0,00E+00	0,00E+00	0,00E+00	2,63E+04	0,00E+00	1,28E+04
Q96EY1, DNJA3	11	30,8	170,42	2,15E+03	5,14E+03	6,94E+03	4,55E+05	1,79E+05	1,19E+05
Q96EY7, PTCD3	12	20,2	130,38	1,09E+04	2,61E+04	1,87E+04	1,36E+05	6,24E+04	7,64E+04
Q96G23, CERS2	3	11,8	20,512	0,00E+00	0,00E+00	0,00E+00	2,81E+04	2,13E+04	2,45E+04
Q96GD4, AURKB	1	3,8	6,336	0,00E+00	0,00E+00	0,00E+00	0,00E+00	2,00E+03	2,22E+03
Q96GJ1, TRM2	1	3	7,708	0,00E+00	0,00E+00	0,00E+00	2,37E+03	0,00E+00	0,00E+00
Q96GQ5, RUS1	3	7,9	20,439	0,00E+00	0,00E+00	0,00E+00	3,17E+04	0,00E+00	7,99E+03
Q96GW9, SYMM	2	5,4	11,594	0,00E+00	0,00E+00	0,00E+00	0,00E+00	2,83E+03	0,00E+00
Q96H55, MYO19	6	9,2	38,746	0,00E+00	0,00E+00	0,00E+00	1,22E+04	2,35E+03	5,69E+03
Q96HS1, PGAM5	13	38,1	312,27	4,27E+04	1,16E+05	1,51E+05	1,03E+06	7,87E+05	6,74E+05
Q96HY6, DDRGK	3	15,3	20,582	0,00E+00	0,00E+00	0,00E+00	2,59E+04	0,00E+00	0,00E+00
Q96HY7, DHTK1	1	2,4	7,1253	0,00E+00	0,00E+00	0,00E+00	0,00E+00	1,48E+03	0,00E+00
Q96I51, RCC1L	2	5,8	16,205	0,00E+00	0,00E+00	0,00E+00	1,08E+04	0,00E+00	3,30E+03
Q96I99, SUCB2	3	10,4	18,035	0,00E+00	0,00E+00	0,00E+00	2,54E+04	0,00E+00	6,84E+03
Q96IX5, ATPMD	3	44,8	119,24	0,00E+00	0,00E+00	0,00E+00	3,87E+05	3,50E+05	8,28E+05
Q96IY1, NSL1	2	11,7	12,168	0,00E+00	0,00E+00	0,00E+00	1,13E+04	0,00E+00	0,00E+00
Q96JB2, COG3	2	3,5	19,329	0,00E+00	0,00E+00	0,00E+00	0,00E+00	0,00E+00	5,76E+03
Q96JB5, CK5P3	5	16,4	43,502	0,00E+00	0,00E+00	0,00E+00	0,00E+00	2,72E+04	5,71E+04
Q96JX3, SRAC1	3	5,5	18,125	0,00E+00	0,00E+00	0,00E+00	6,78E+03	2,00E+03	0,00E+00
Q96K37, S35E1	4	17,6	36,392	0,00E+00	0,00E+00	0,00E+00	1,23E+05	0,00E+00	5,11E+04
Q96KA5, CLP1L	1	3	7,4439	0,00E+00	0,00E+00	0,00E+00	0,00E+00	0,00E+00	5,37E+03
Q96KP1, EXOC2	2	2,2	11,416	0,00E+00	0,00E+00	0,00E+00	1,15E+03	0,00E+00	1,21E+03
Q96L58, B3GT6	2	7	12,649	0,00E+00	0,00E+00	0,00E+00	1,10E+04	0,00E+00	0,00E+00
Q96LW7, CAR19	2	8,8	11,548	0,00E+00	0,00E+00	0,00E+00	9,74E+03	0,00E+00	0,00E+00
Q96N66, MBOA7	2	5,9	13,567	0,00E+00	0,00E+00	0,00E+00	1,87E+04	1,32E+04	1,94E+04
Q96N67, DOCK7	1	0,7	6,3357	0,00E+00	0,00E+00	0,00E+00	8,75E+02	0,00E+00	0,00E+00
Q96NB2, SFXN2	5	15,2	50,118	0,00E+00	0,00E+00	4,15E+03	2,63E+05	9,50E+04	8,73E+04
Q96PG2, M4A10	1	3,4	6,4367	2,68E+04	0,00E+00	1,39E+04	2,35E+04	3,35E+03	0,00E+00
Q96QD8, S38A2	2	7,3	16,05	0,00E+00	0,00E+00	0,00E+00	0,00E+00	1,20E+04	1,50E+04
Q96RL7, VP13A	3	1,1	17,234	0,00E+00	0,00E+00	0,00E+00	5,02E+02	5,26E+02	0,00E+00
Q96RP9, EFGM	11	19	72,651	0,00E+00	0,00E+00	0,00E+00	7,09E+04	4,57E+04	6,53E+03
Q96RQ1, ERGI2	1	3,4	7,0128	0,00E+00	0,00E+00	0,00E+00	1,40E+04	0,00E+00	0,00E+00
Q96RQ3, MCCA	5	9,8	47,507	0,00E+00	0,00E+00	0,00E+00	2,09E+04	1,87E+04	0,00E+00
Q96RR1, PEO1	5	9,1	32,05	0,00E+00	0,00E+00	0,00E+00	1,82E+04	0,00E+00	6,93E+03
Q96RT1, ERBIN	2	1,6	11,636	0,00E+00	4,77E+02	0,00E+00	0,00E+00	0,00E+00	5,12E+02
Q96S52, PIGS	6	14,2	35,472	0,00E+00	0,00E+00	0,00E+00	0,00E+00	1,90E+04	4,78E+03
Q96S66, CLCC1	3	7,6	22,304	0,00E+00	0,00E+00	0,00E+00	0,00E+00	6,65E+03	2,18E+03
Q96SZ6, CK5P1	2	3,8	12,647	0,00E+00	0,00E+00	0,00E+00	0,00E+00	4,82E+03	0,00E+00
Q96TA2, YMEL1	12	21,7	124,22	1,07E+03	2,43E+03	1,25E+04	1,80E+03	7,94E+04	9,97E+04
Q99523, SORT	1	1,8	7,6491	0,00E+00	0,00E+00	0,00E+00	8,44E+03	0,00E+00	0,00E+00
Q99536, VAT1	2	8,1	12,504	0,00E+00	0,00E+00	0,00E+00	3,02E+03	1,04E+04	8,60E+03
Q99595, TI17A	2	32,2	44,086	0,00E+00	0,00E+00	0,00E+00	5,43E+04	0,00E+00	0,00E+00
Q99623, PHB2	14	56,2	323,31	2,72E+04	2,10E+04	3,70E+04	1,91E+06	7,35E+05	1,04E+06
Q99714, HCD2	5	35,6	64,003	0,00E+00	7,36E+03	7,64E+03	1,16E+05	9,70E+03	0,00E+00
Q99729, ROAA	1	3,9	6,8733	0,00E+00	0,00E+00	8,31E+03	0,00E+00	0,00E+00	0,00E+00
Q99758, ABCA3	4	3,2	25,175	0,00E+00	0,00E+00	0,00E+00	2,85E+03	1,40E+03	1,04E+03

Q99798, ACON	3	5,9	20,683	0,00E+00	0,00E+00	0,00E+00	1,24E+03	2,34E+03	0,00E+00
Q99805, TM9S2	7	11,6	193,37	0,00E+00	2,58E+03	0,00E+00	6,69E+04	3,75E+04	5,64E+04
Q99808, S29A1	2	4,4	11,292	0,00E+00	0,00E+00	0,00E+00	1,23E+04	2,39E+04	1,01E+04
Q99829, CPNE1	1	3,7	9,1283	0,00E+00	0,00E+00	0,00E+00	0,00E+00	1,13E+04	0,00E+00
Q99832, TCPH	1	2,6	6,8573	0,00E+00	0,00E+00	1,45E+03	0,00E+00	4,05E+03	0,00E+00
Q99942, RNF5	2	12,2	29,749	0,00E+00	0,00E+00	0,00E+00	1,79E+05	1,72E+05	2,76E+05
Q9BPW8, NIPS1	8	32	64,517	0,00E+00	6,18E+03	0,00E+00	2,93E+05	6,16E+04	1,78E+05
Q9BPX3, CND3	5	6,7	37,383	0,00E+00	0,00E+00	0,00E+00	1,16E+04	2,08E+03	2,97E+03
Q9BPX6, MICU1	1	3,2	7,9993	0,00E+00	0,00E+00	0,00E+00	1,13E+04	0,00E+00	5,17E+03
Q9BQ52, RNZ2	3	4,7	20,135	0,00E+00	0,00E+00	0,00E+00	1,33E+04	0,00E+00	0,00E+00
Q9BQ95, ECSIT	9	35	75,265	0,00E+00	0,00E+00	0,00E+00	8,66E+04	4,71E+04	4,18E+04
Q9BQA1, MEP50	10	53,2	222,25	1,15E+05	1,44E+06	2,61E+05	1,79E+04	3,19E+05	8,83E+04
Q9BQG0, MBB1A	3	3,5	18,166	0,00E+00	0,00E+00	0,00E+00	0,00E+00	1,75E+03	3,39E+02
Q9BQP7, MGME1	5	14,5	30,083	0,00E+00	0,00E+00	0,00E+00	3,44E+04	0,00E+00	7,50E+03
Q9BRJ2, RM45	3	11,4	20,643	0,00E+00	0,00E+00	0,00E+00	3,20E+04	0,00E+00	4,22E+03
Q9BRK5, CAB45	6	22,4	53,445	0,00E+00	0,00E+00	0,00E+00	1,37E+05	3,12E+04	3,10E+04
Q9BRQ6, MIC25	3	14,5	17,909	0,00E+00	0,00E+00	0,00E+00	1,96E+04	3,34E+03	1,52E+04
Q9BSF4, TIM29	5	30	37,761	0,00E+00	0,00E+00	0,00E+00	4,29E+04	2,48E+04	5,67E+04
Q9BSH4, TACO1	1	3,4	8,3253	0,00E+00	0,00E+00	0,00E+00	1,04E+04	0,00E+00	0,00E+00
Q9BSJ2, GCP2	4	5,5	25,204	0,00E+00	0,00E+00	0,00E+00	6,68E+03	0,00E+00	0,00E+00
Q9BSJ8, ESYT1	18	25,8	158,76	0,00E+00	7,17E+02	7,83E+02	8,00E+04	4,64E+04	4,72E+04
Q9BSK2, S2533	3	9,7	19,882	0,00E+00	0,00E+00	0,00E+00	9,43E+04	3,10E+04	2,00E+04
Q9BT22, ALG1	7	21,8	92,188	0,00E+00	0,00E+00	1,48E+03	6,01E+04	3,45E+04	3,42E+04
Q9BT67, NFIP1	1	7,7	31,395	0,00E+00	0,00E+00	0,00E+00	0,00E+00	0,00E+00	0,00E+00
Q9BTV4, TMM43	2	8,5	12,431	0,00E+00	0,00E+00	0,00E+00	0,00E+00	0,00E+00	1,93E+03
Q9BTZ2, DHRS4	2	9,4	13,406	0,00E+00	0,00E+00	0,00E+00	1,38E+04	6,77E+03	0,00E+00
Q9BU23, LMF2	4	9,1	28,994	0,00E+00	0,00E+00	0,00E+00	2,21E+03	4,65E+03	2,23E+04
Q9BU61, NDUF3	1	6	7,1021	0,00E+00	0,00E+00	0,00E+00	1,31E+04	0,00E+00	0,00E+00
Q9BUA3, SPNDC	1	4,7	6,9079	0,00E+00	4,46E+03	0,00E+00	0,00E+00	0,00E+00	0,00E+00
Q9BUB7, TMM70	5	23,8	38,62	0,00E+00	3,64E+03	3,53E+03	1,90E+05	3,23E+04	1,95E+05
Q9BV35, SCMC3	2	6,4	12,908	0,00E+00	0,00E+00	0,00E+00	3,00E+03	0,00E+00	1,76E+03
Q9BVC6, TM109	1	4,9	7,04	0,00E+00	0,00E+00	0,00E+00	0,00E+00	1,42E+04	2,65E+04
Q9BVG9, PTSS2	4	13,6	31,818	0,00E+00	0,00E+00	0,00E+00	5,15E+04	1,38E+04	3,52E+04
Q9BVK8, TM147	1	7,6	32,127	0,00E+00	0,00E+00	0,00E+00	0,00E+00	2,16E+04	1,93E+04
Q9BVP2, GNL3	1	2,7	6,9993	0,00E+00	0,00E+00	0,00E+00	0,00E+00	0,00E+00	7,05E+03
Q9BVV7, TIM21	5	21,8	30,663	0,00E+00	3,20E+03	0,00E+00	7,23E+04	4,38E+04	7,79E+04
Q9BVX2, T106C	1	6,8	7,1917	0,00E+00	0,00E+00	0,00E+00	1,85E+04	0,00E+00	0,00E+00
Q9BW27, NUP85	5	9,3	29,068	0,00E+00	0,00E+00	0,00E+00	1,07E+04	3,59E+03	3,83E+03
Q9BW92, SYTM	22	39,4	170,6	0,00E+00	1,54E+03	3,11E+03	2,97E+05	8,47E+04	5,23E+04
Q9BWM7, SFXN3	5	22,1	30,033	4,10E+03	6,40E+03	0,00E+00	2,56E+05	1,02E+05	1,18E+05
Q9BXK5, B2L13	4	13	26,216	0,00E+00	0,00E+00	0,00E+00	3,37E+04	2,60E+03	2,79E+04
Q9BXW7, HDHD5	10	35,7	136,22	0,00E+00	4,26E+03	3,36E+03	3,14E+05	1,44E+05	1,45E+05
Q9BY50, SC11C	1	5,2	6,7228	0,00E+00	0,00E+00	0,00E+00	1,01E+04	0,00E+00	1,03E+04
Q9BYD1, RM13	6	41	40,542	0,00E+00	7,26E+03	0,00E+00	2,62E+04	6,15E+03	2,69E+04
Q9BYD3, RM04	4	18	30,416	0,00E+00	1,74E+04	7,83E+03	3,18E+04	3,73E+04	4,00E+04
Q9BYD6, RM01	5	22,5	38,276	0,00E+00	9,91E+03	2,71E+03	2,06E+04	2,83E+04	3,99E+04

Q9BZE1, RM37	11	29,8	77,332	2,53E+03	8,90E+03	1,21E+04	1,22E+05	7,27E+04	4,35E+04
Q9BZF1, OSBL8	3	4,7	17,853	0,00E+00	0,00E+00	0,00E+00	9,92E+03	4,41E+03	5,09E+03
Q9BZG1, RAB34	1	6,2	6,3686	0,00E+00	0,00E+00	0,00E+00	3,28E+03	0,00E+00	0,00E+00
Q9BZQ6, EDEM3	8	11,3	59,561	0,00E+00	0,00E+00	0,00E+00	1,94E+04	1,52E+04	1,87E+04
Q9C0D2, CE295	2	0,9	11,363	0,00E+00	0,00E+00	3,88E+02	1,55E+03	1,51E+03	0,00E+00
Q9C0D9, EPT1	1	4	8,673	0,00E+00	0,00E+00	0,00E+00	0,00E+00	0,00E+00	6,42E+04
Q9C0E8, LNP	2	6,1	12,417	0,00E+00	0,00E+00	0,00E+00	0,00E+00	4,73E+03	1,35E+04
Q9GZT3, SLIRP	7	66,1	68,947	5,19E+04	8,71E+04	9,40E+04	1,14E+05	3,05E+05	5,94E+05
Q9GZY8, MFF	1	3,2	6,8124	0,00E+00	0,00E+00	0,00E+00	5,02E+03	0,00E+00	0,00E+00
Q9H019, MFR1L	3	14	18,585	0,00E+00	0,00E+00	0,00E+00	1,36E+04	0,00E+00	4,32E+03
Q9H061, T126A	4	28,7	27,622	0,00E+00	0,00E+00	0,00E+00	6,98E+04	0,00E+00	5,83E+04
Q9H078, CLPB	17	34,1	152,57	0,00E+00	1,82E+03	0,00E+00	2,92E+03	1,72E+05	1,27E+05
Q9H0P0, 5NT3A	2	9,2	12,939	0,00E+00	0,00E+00	0,00E+00	1,50E+04	0,00E+00	7,44E+03
Q9H0U3, MAGT1	2	6,9	13,035	0,00E+00	0,00E+00	0,00E+00	6,25E+03	0,00E+00	3,42E+04
Q9H0U6, RM18	2	12,2	14,38	0,00E+00	0,00E+00	0,00E+00	6,51E+04	1,79E+04	2,45E+04
Q9H2D1, MFTC	6	29,2	78,842	0,00E+00	0,00E+00	3,25E+03	9,28E+04	2,99E+04	5,76E+04
Q9H2H9, S38A1	1	2,3	6,3474	0,00E+00	0,00E+00	0,00E+00	0,00E+00	1,00E+04	5,91E+03
Q9H2J7, S6A15	3	5,9	18,572	0,00E+00	0,00E+00	0,00E+00	6,10E+03	5,80E+03	0,00E+00
Q9H2M9, RBGPR	6	5	42,607	0,00E+00	0,00E+00	0,00E+00	8,14E+03	2,39E+03	6,00E+03
Q9H2U2, IPYR2	4	16,5	27,253	0,00E+00	0,00E+00	4,36E+03	1,43E+04	2,09E+04	1,16E+04
Q9H2V7, SPNS1	5	19,9	55,543	0,00E+00	0,00E+00	0,00E+00	1,28E+05	4,77E+04	5,92E+04
Q9H2W6, RM46	1	5	7,3058	0,00E+00	3,72E+03	0,00E+00	1,17E+04	0,00E+00	0,00E+00
Q9H3U1, UN45A	2	2,4	11,697	0,00E+00	0,00E+00	0,00E+00	0,00E+00	1,15E+03	0,00E+00
Q9H3U5, MFSD1	1	2,6	7,4129	0,00E+00	0,00E+00	0,00E+00	2,25E+04	1,90E+04	1,50E+04
Q9H490, PIGU	1	3,9	7,6628	0,00E+00	0,00E+00	0,00E+00	0,00E+00	0,00E+00	1,10E+04
Q9H497, TOR3A	3	9,6	20,972	0,00E+00	0,00E+00	0,00E+00	1,29E+04	3,50E+03	0,00E+00
Q9H4I3, TRABD	5	13,8	37,069	0,00E+00	3,77E+03	2,89E+03	8,37E+04	2,55E+04	2,70E+04
Q9H4K7, MTG2	2	7,1	11,746	0,00E+00	0,00E+00	0,00E+00	7,23E+03	4,25E+03	4,08E+03
Q9H553, ALG2	1	4,1	6,4104	0,00E+00	0,00E+00	0,00E+00	4,33E+03	0,00E+00	4,83E+03
Q9H583, HEAT1	8	5,2	49,499	0,00E+00	0,00E+00	2,14E+02	6,93E+03	1,51E+03	3,46E+03
Q9H5Q4, TFB2M	6	15,9	38,961	0,00E+00	0,00E+00	0,00E+00	1,54E+05	4,01E+04	2,56E+04
Q9H6R6, ZDHC6	1	2,9	6,8939	0,00E+00	0,00E+00	0,00E+00	5,75E+03	0,00E+00	0,00E+00
Q9H7Z7, PGES2	2	8,8	11,577	0,00E+00	0,00E+00	0,00E+00	3,75E+03	0,00E+00	3,15E+03
Q9H845, ACAD9	12	24,3	101,37	0,00E+00	3,99E+03	1,34E+03	9,67E+02	6,89E+04	2,84E+04
Q9H857, NT5D2	3	6,3	17,353	0,00E+00	0,00E+00	0,00E+00	3,82E+03	0,00E+00	6,07E+03
Q9H920, RN121	1	5,2	29	0,00E+00	0,00E+00	0,00E+00	1,47E+04	0,00E+00	0,00E+00
Q9H936, GHC1	9	36,8	227,9	0,00E+00	5,47E+03	6,82E+03	3,90E+05	1,83E+05	2,16E+05
Q9H9B4, SFXN1	12	53,1	323,31	1,98E+04	7,93E+04	7,21E+04	1,88E+06	8,23E+05	1,06E+06
Q9H9J2, RM44	3	14,2	22,915	3,67E+03	2,00E+04	9,75E+03	6,26E+04	3,38E+04	3,48E+04
Q9H9P8, L2HDH	5	15,3	47,178	0,00E+00	0,00E+00	0,00E+00	5,12E+04	2,75E+04	2,74E+04
Q9H9S3, S61A2	5	15,5	13,551	0,00E+00	0,00E+00	0,00E+00	2,18E+04	1,01E+04	1,44E+04
Q9HA92, RSAD1	4	12	28,952	0,00E+00	0,00E+00	0,00E+00	3,30E+04	1,39E+04	2,66E+04
Q9HBH5, RDH14	4	18,8	24,004	0,00E+00	0,00E+00	0,00E+00	2,74E+03	9,14E+03	8,55E+03
Q9HBR0, S38AA	4	5,5	23,326	0,00E+00	0,00E+00	0,00E+00	7,31E+03	1,82E+03	0,00E+00
Q9HC07, TM165	4	22,5	36,831	0,00E+00	0,00E+00	0,00E+00	1,01E+05	0,00E+00	2,20E+04
Q9HC21, TPC	4	10,6	24,136	0,00E+00	0,00E+00	0,00E+00	3,20E+03	1,01E+04	4,80E+03

Q9HC36, MRM3	3	7,9	19,265	3,21E+04	0,00E+00	1,59E+04	3,59E+04	4,12E+03	0,00E+00
Q9HCC0, MCCB	5	16	47,824	3,97E+03	0,00E+00	0,00E+00	0,00E+00	1,98E+04	4,81E+03
Q9HCU4, CELR2	6	2,5	37,371	0,00E+00	0,00E+00	0,00E+00	2,39E+03	1,32E+03	7,12E+02
Q9HCU5, PREB	5	20,9	36,184	0,00E+00	0,00E+00	0,00E+00	4,00E+04	1,75E+04	1,96E+04
Q9HD20, AT131	6	5,6	37,802	0,00E+00	0,00E+00	0,00E+00	8,15E+03	5,92E+03	3,33E+03
Q9HD23, MRS2	6	21	46,144	0,00E+00	0,00E+00	0,00E+00	2,95E+04	1,54E+04	1,45E+04
Q9HD45, TM9S3	6	11,5	53,03	0,00E+00	0,00E+00	3,46E+03	2,35E+04	2,16E+04	1,76E+04
Q9HDC9, APMAP	2	3,8	11,859	0,00E+00	0,00E+00	0,00E+00	1,38E+04	0,00E+00	0,00E+00
Q9NNW5, WDR6	13	18,7	105,48	0,00E+00	1,41E+03	3,01E+03	7,05E+04	3,45E+04	1,77E+04
Q9NP58, ABCB6	3	6,3	22,83	0,00E+00	0,00E+00	0,00E+00	6,93E+03	4,45E+03	9,79E+03
Q9NP92, RT30	3	10	21,854	0,00E+00	0,00E+00	0,00E+00	2,65E+04	7,13E+03	2,40E+04
Q9NPL8, TIDC1	10	44,2	97,879	0,00E+00	0,00E+00	0,00E+00	1,53E+05	3,80E+04	1,41E+05
Q9NR30, DDX21	2	3,4	13,188	0,00E+00	0,00E+00	0,00E+00	0,00E+00	5,61E+03	2,25E+03
Q9NR56, MBNL1	1	2,1	6,504	0,00E+00	0,00E+00	7,19E+05	0,00E+00	0,00E+00	5,96E+05
Q9NR77, PXMP2	3	17,9	18,4	0,00E+00	0,00E+00	0,00E+00	2,05E+04	7,77E+03	2,43E+04
Q9NRA2, S17A5	1	1,8	6,8891	0,00E+00	0,00E+00	0,00E+00	9,47E+03	0,00E+00	0,00E+00
Q9NRK6, ABCBA	12	21,7	142,48	0,00E+00	0,00E+00	0,00E+00	2,71E+03	3,09E+04	1,08E+05
Q9NRP0, OSTC	1	8,1	12,642	0,00E+00	0,00E+00	0,00E+00	0,00E+00	0,00E+00	0,00E+00
Q9NRX2, RM17	3	13,7	19,126	0,00E+00	0,00E+00	0,00E+00	1,74E+04	1,07E+04	1,37E+04
Q9NRX5, SERC1	1	3,8	6,4794	0,00E+00	0,00E+00	0,00E+00	1,18E+04	0,00E+00	0,00E+00
Q9NS69, TOM22	7	77,5	323,31	0,00E+00	6,96E+04	3,76E+04	1,87E+06	9,31E+05	2,57E+06
Q9NSE4, SYIM	14	19,8	132,31	0,00E+00	8,54E+02	9,37E+02	1,07E+05	1,79E+04	1,02E+04
Q9NTJ3, SMC4	3	2,9	19,212	0,00E+00	0,00E+00	0,00E+00	2,59E+03	0,00E+00	1,62E+03
Q9NTJ5, SAC1	5	10,7	31,451	0,00E+00	0,00E+00	0,00E+00	0,00E+00	5,88E+03	2,05E+04
Q9NTX5, ECHD1	4	16	25,106	0,00E+00	0,00E+00	0,00E+00	2,25E+04	5,12E+03	2,84E+04
Q9NU22, MDN1	14	3,4	86,869	0,00E+00	0,00E+00	0,00E+00	5,38E+02	1,76E+03	5,03E+03
Q9NUQ2, PLCE	2	6	12,242	0,00E+00	0,00E+00	0,00E+00	7,00E+03	0,00E+00	8,78E+03
Q9NUT2, MITOS	5	8,4	28,433	0,00E+00	0,00E+00	0,00E+00	0,00E+00	9,78E+03	1,73E+04
Q9NVC3, S38A7	2	4,5	13,894	0,00E+00	0,00E+00	0,00E+00	1,74E+04	0,00E+00	5,61E+03
Q9NVH0, EXD2	5	10,8	32,879	0,00E+00	0,00E+00	0,00E+00	1,28E+04	0,00E+00	2,22E+03
Q9NVH1, DJC11	10	26,5	134,31	0,00E+00	0,00E+00	0,00E+00	2,16E+04	4,32E+04	1,13E+05
Q9NVH6, TMLH	4	10,5	25,486	0,00E+00	1,76E+03	0,00E+00	1,11E+04	2,77E+03	2,35E+03
Q9NVI7, ATD3A	24	42,3	323,31	3,70E+04	5,30E+04	8,13E+04	3,44E+05	1,30E+06	8,31E+05
Q9NVJ2, ARL8B	1	7,5	6,4187	0,00E+00	0,00E+00	0,00E+00	9,94E+03	0,00E+00	0,00E+00
Q9NVV0, TM38B	3	13,1	37,048	0,00E+00	0,00E+00	0,00E+00	4,48E+04	2,51E+04	9,02E+04
Q9NVV4, PAPD1	1	3,1	6,6191	0,00E+00	0,00E+00	0,00E+00	1,43E+03	0,00E+00	0,00E+00
Q9NW15, ANO10	1	2,7	7,1325	0,00E+00	0,00E+00	0,00E+00	0,00E+00	0,00E+00	3,58E+03
Q9NWS8, RMND1	8	21,6	55,751	0,00E+00	0,00E+00	0,00E+00	1,13E+05	3,93E+04	7,51E+03
Q9NWU5, RM22	2	12,1	11,655	0,00E+00	0,00E+00	0,00E+00	1,61E+04	0,00E+00	0,00E+00
Q9NWW5, CLN6	2	10,9	15,482	0,00E+00	0,00E+00	0,00E+00	4,71E+04	1,97E+04	2,43E+04
Q9NX47, MARH5	1	5,8	6,369	0,00E+00	0,00E+00	0,00E+00	5,15E+03	0,00E+00	0,00E+00
Q9NX61, T161A	4	18	27,128	0,00E+00	0,00E+00	0,00E+00	1,29E+04	9,41E+03	6,44E+03
Q9NX63, MIC19	7	22,9	61,695	0,00E+00	0,00E+00	0,00E+00	2,40E+05	8,43E+04	3,64E+05
Q9NXE4, NSMA3	1	1,7	6,7039	0,00E+00	0,00E+00	0,00E+00	2,24E+03	0,00E+00	0,00E+00
Q9NXS2, QPCTL	11	37,2	89,126	1,02E+04	9,02E+04	9,06E+04	2,83E+05	1,37E+05	2,00E+05
Q9NXV2, KCTD5	6	37,2	156,99	1,48E+05	1,36E+05	2,57E+05	1,92E+05	1,92E+05	2,50E+05

Q9NXW2, DJB12	4	16	31,498	0,00E+00	0,00E+00	0,00E+00	7,71E+04	3,53E+04	4,05E+04
Q9NYK5, RM39	5	13,6	49,995	5,39E+03	1,29E+04	1,45E+04	6,85E+04	1,15E+04	3,14E+04
Q9NYL9, TMOD3	2	11,4	15,373	0,00E+00	2,69E+04	1,72E+03	0,00E+00	2,58E+03	2,35E+03
Q9NYP7, ELOV5	1	4,3	8,1379	0,00E+00	0,00E+00	0,00E+00	5,15E+04	0,00E+00	0,00E+00
Q9NYQ6, CELR1	3	1,1	18,547	0,00E+00	0,00E+00	0,00E+00	7,63E+02	2,06E+03	1,53E+03
Q9NYU1, UGGG2	4	3,1	24,205	0,00E+00	0,00E+00	0,00E+00	3,89E+03	1,15E+03	1,13E+03
Q9NYU2, UGGG1	3	2,8	18,213	0,00E+00	0,00E+00	0,00E+00	2,86E+03	8,73E+02	0,00E+00
Q9NYY8, FAKD2	12	23,8	93,973	9,79E+02	0,00E+00	1,70E+03	0,00E+00	5,48E+04	5,88E+04
Q9NZ01, TECR	6	19,2	84,987	0,00E+00	2,00E+04	1,55E+04	4,66E+05	2,81E+05	4,29E+05
Q9NZ45, CISD1	1	13,9	6,6549	0,00E+00	0,00E+00	0,00E+00	0,00E+00	0,00E+00	1,83E+04
Q9NZI8, IF2B1	9	20,6	131,04	4,79E+03	1,90E+04	6,75E+04	2,68E+03	4,89E+04	3,33E+04
Q9NZJ7, MTCH1	7	18,8	57,353	0,00E+00	0,00E+00	2,85E+03	3,87E+05	8,27E+04	2,53E+05
Q9NZT1, CALL5	3	34,2	20,914	1,55E+04	2,93E+04	0,00E+00	0,00E+00	6,53E+03	1,23E+04
Q9NZW5, MPP6	3	7	11,803	0,00E+00	0,00E+00	0,00E+00	0,00E+00	0,00E+00	6,43E+03
Q9P015, RM15	3	13,2	20,484	0,00E+00	0,00E+00	0,00E+00	5,48E+04	1,48E+04	2,50E+04
Q9P035, HACD3	8	24	84,844	5,80E+03	1,02E+04	1,69E+04	3,74E+05	2,77E+05	2,84E+05
Q9P0I2, EMC3	4	19,5	26,948	0,00E+00	0,00E+00	0,00E+00	5,75E+03	2,15E+04	3,46E+04
Q9P0J0, NDUAD	7	50,7	65,857	0,00E+00	1,91E+04	3,05E+04	7,14E+05	5,00E+04	2,03E+05
Q9P0M9, RM27	2	14,2	11,618	0,00E+00	0,00E+00	0,00E+00	1,89E+04	1,20E+04	2,16E+04
Q9P0S9, TM14C	1	25,9	7,8394	0,00E+00	0,00E+00	0,00E+00	0,00E+00	1,79E+04	0,00E+00
Q9P0U1, TOM7	1	30,9	11,166	0,00E+00	0,00E+00	0,00E+00	1,03E+05	0,00E+00	1,87E+05
Q9P219, DAPLE	4	2,6	26,538	0,00E+00	0,00E+00	2,44E+03	0,00E+00	0,00E+00	0,00E+00
Q9P2E5, CHPF2	2	2,8	12,145	0,00E+00	0,00E+00	0,00E+00	2,66E+03	0,00E+00	2,05E+03
Q9P2R3, ANFY1	2	2	11,769	0,00E+00	0,00E+00	2,27E+03	0,00E+00	0,00E+00	0,00E+00
Q9P2R7, SUCB1	10	25,9	97,316	0,00E+00	0,00E+00	0,00E+00	2,77E+05	4,25E+04	1,82E+04
Q9P2W9, STX18	3	11,6	17,321	0,00E+00	0,00E+00	0,00E+00	2,19E+04	4,47E+03	5,41E+03
Q9UBG3, CRNN	5	20,8	40,595	0,00E+00	7,28E+03	0,00E+00	0,00E+00	0,00E+00	0,00E+00
Q9UBM7, DHCR7	5	13,3	47,939	0,00E+00	0,00E+00	0,00E+00	4,65E+05	3,01E+05	5,35E+05
Q9UBS4, DJB11	5	16,5	40,97	0,00E+00	0,00E+00	5,28E+03	1,22E+05	5,05E+04	6,70E+04
Q9UBV2, SE1L1	7	16,1	72,768	0,00E+00	0,00E+00	1,60E+03	2,37E+04	1,81E+04	2,21E+04
Q9UBX3, DIC	10	42,9	323,31	0,00E+00	2,36E+04	1,95E+04	8,55E+05	4,15E+05	3,81E+05
Q9UDR5, AASS	6	9,2	90,281	0,00E+00	7,02E+02	1,19E+03	6,90E+04	3,36E+04	3,59E+04
Q9UDW1, QCR9	2	38,1	14,871	0,00E+00	0,00E+00	0,00E+00	0,00E+00	5,85E+04	1,16E+05
Q9UDX5, MTFP1	5	45,2	36,24	0,00E+00	0,00E+00	0,00E+00	1,85E+05	8,81E+04	1,16E+05
Q9UG56, PISD	1	3,2	6,623	0,00E+00	0,00E+00	0,00E+00	6,32E+03	0,00E+00	3,45E+03
Q9UG63, ABCF2	2	4	13,375	0,00E+00	0,00E+00	0,00E+00	7,63E+03	1,09E+03	2,56E+03
Q9UGM6, SYWM	1	4,4	8,1763	0,00E+00	0,00E+00	0,00E+00	1,20E+04	6,81E+03	0,00E+00
Q9UGP8, SEC63	4	5,7	23,879	0,00E+00	0,00E+00	0,00E+00	3,88E+03	1,02E+03	0,00E+00
Q9UH62, ARMX3	4	15	33,078	0,00E+00	0,00E+00	0,00E+00	4,85E+04	2,68E+04	2,86E+04
Q9UH99, SUN2	4	8,8	26,005	0,00E+00	9,19E+03	0,00E+00	0,00E+00	3,24E+03	0,00E+00
Q9UHB9, SRP68	2	5,9	11,685	0,00E+00	0,00E+00	0,00E+00	0,00E+00	4,88E+03	0,00E+00
Q9UHI6, DDX20	2	3,5	12,889	0,00E+00	0,00E+00	0,00E+00	2,48E+03	0,00E+00	0,00E+00
Q9UI09, NDUAC	2	20	13,111	0,00E+00	0,00E+00	0,00E+00	1,96E+04	1,53E+04	3,18E+04
Q9UI30, TR112	2	20,8	11,199	0,00E+00	0,00E+00	0,00E+00	2,09E+04	0,00E+00	0,00E+00
Q9UIQ6, LCAP	4	4,8	24,745	0,00E+00	0,00E+00	0,00E+00	7,12E+03	3,16E+03	1,88E+03
Q9UIW2, PLXA1	1	0,5	6,5536	0,00E+00	0,00E+00	0,00E+00	1,59E+03	0,00E+00	1,37E+03

Q9UJ14, GGT7	3	4,8	17,567	0,00E+00	0,00E+00	0,00E+00	1,15E+04	0,00E+00	6,88E+03
Q9UJS0, CMC2	33	64,3	323,31	3,58E+04	6,82E+04	9,28E+04	3,45E+06	1,37E+06	1,66E+06
Q9UJZ1, STML2	7	33,7	70,952	1,98E+03	2,60E+04	1,20E+04	3,14E+05	2,62E+05	2,28E+05
Q9UK39, NOCT	1	3,5	7,9213	0,00E+00	0,00E+00	0,00E+00	8,60E+03	0,00E+00	0,00E+00
Q9UK73, FEM1B	1	1,8	7,3349	0,00E+00	0,00E+00	0,00E+00	0,00E+00	9,62E+02	1,58E+03
Q9UKM7, MA1B1	5	12,2	50,96	0,00E+00	0,00E+00	0,00E+00	5,52E+03	0,00E+00	7,38E+03
Q9UKU7, ACAD8	3	11,8	22,872	0,00E+00	0,00E+00	0,00E+00	1,43E+04	3,00E+03	3,89E+03
Q9UKV5, AMFR	6	11,2	36,928	0,00E+00	0,00E+00	0,00E+00	1,67E+04	1,26E+04	1,45E+04
Q9UKY4, POMT2	3	6,3	17,762	0,00E+00	0,00E+00	0,00E+00	2,60E+03	0,00E+00	2,18E+03
Q9ULH0, KDIS	13	9,5	108,65	0,00E+00	0,00E+00	0,00E+00	1,23E+04	2,42E+03	1,81E+04
Q9UM00, TMCO1	3	15,5	40,218	0,00E+00	0,00E+00	0,00E+00	1,19E+05	8,94E+03	2,20E+05
Q9UM54, MYO6	4	4,9	28,593	0,00E+00	1,57E+03	0,00E+00	5,01E+03	8,81E+03	2,49E+03
Q9UN86, G3BP2	1	3,5	8,4192	0,00E+00	0,00E+00	0,00E+00	0,00E+00	0,00E+00	1,34E+04
Q9UNL2, SSRG	1	7,6	15,624	0,00E+00	0,00E+00	0,00E+00	4,91E+05	1,98E+05	3,98E+05
Q9UPQ8, DOLK	2	4,1	14,553	0,00E+00	0,00E+00	0,00E+00	8,51E+03	4,09E+03	0,00E+00
Q9UQ90, SPG7	5	10,7	40,83	0,00E+00	0,00E+00	0,00E+00	6,79E+03	3,38E+03	2,68E+03
Q9UQE7, SMC3	5	4,8	31,759	0,00E+00	0,00E+00	0,00E+00	1,17E+04	4,44E+03	3,97E+03
Q9Y241, HIG1A	4	75,3	323,31	0,00E+00	4,59E+04	8,33E+04	2,37E+06	1,26E+06	1,79E+06
Q9Y256, FACE2	1	4,3	6,7189	0,00E+00	0,00E+00	0,00E+00	9,55E+03	0,00E+00	0,00E+00
Q9Y262, EIF3L	3	7,1	19,097	0,00E+00	0,00E+00	0,00E+00	0,00E+00	7,60E+03	0,00E+00
Q9Y276, BCS1	2	7,6	12,483	0,00E+00	0,00E+00	0,00E+00	4,28E+03	2,23E+03	0,00E+00
Q9Y277, VDAC3	7	30,4	87,18	0,00E+00	5,97E+03	0,00E+00	6,86E+04	1,18E+04	1,40E+05
Q9Y282, ERGI3	1	3,9	7,6511	0,00E+00	0,00E+00	0,00E+00	2,51E+04	9,09E+03	9,79E+03
Q9Y285, SYFA	4	8,9	31,314	0,00E+00	0,00E+00	0,00E+00	0,00E+00	8,59E+03	3,95E+04
Q9Y289, SC5A6	4	8	37,806	0,00E+00	0,00E+00	0,00E+00	4,38E+04	3,66E+03	1,06E+04
Q9Y2C4, EXOG	3	12,2	20,46	0,00E+00	0,00E+00	0,00E+00	2,19E+04	0,00E+00	0,00E+00
Q9Y2G0, EFR3B	2	3,2	6,3833	0,00E+00	0,00E+00	0,00E+00	0,00E+00	0,00E+00	2,45E+03
Q9Y2H1, ST38L	2	6,7	16,718	3,97E+03	1,06E+04	5,91E+03	0,00E+00	0,00E+00	0,00E+00
Q9Y2H6, FND3A	1	1,3	8,2776	0,00E+00	0,00E+00	0,00E+00	8,00E+03	3,84E+03	3,42E+03
Q9Y2I1, NISCH	1	0,8	6,8106	0,00E+00	0,00E+00	0,00E+00	2,37E+03	0,00E+00	1,52E+03
Q9Y2Q9, RT28	3	26,2	19,654	0,00E+00	0,00E+00	0,00E+00	3,02E+04	1,79E+04	3,27E+04
Q9Y2R0, COA3	1	9,4	6,5006	0,00E+00	0,00E+00	0,00E+00	4,01E+04	0,00E+00	4,40E+04
Q9Y2S7, PDIP2	11	35,9	86,582	9,33E+03	1,29E+04	2,14E+04	1,33E+05	6,40E+04	5,83E+04
Q9Y2V7, COG6	2	4,3	12,132	0,00E+00	0,00E+00	0,00E+00	0,00E+00	0,00E+00	3,65E+03
Q9Y2W6, TDRKH	3	8,9	19,255	0,00E+00	0,00E+00	0,00E+00	0,00E+00	6,27E+03	9,86E+03
Q9Y2Z2, MTO1	2	5	12,456	0,00E+00	0,00E+00	0,00E+00	0,00E+00	1,46E+03	1,96E+03
Q9Y2Z4, SYYM	8	22,6	77,231	0,00E+00	1,43E+03	1,86E+03	3,76E+04	1,60E+04	7,98E+03
Q9Y2Z9, COQ6	3	8,8	19,81	0,00E+00	0,00E+00	0,00E+00	1,07E+04	8,84E+03	5,39E+03
Q9Y305, ACOT9	4	11,8	23,848	0,00E+00	0,00E+00	0,00E+00	6,08E+04	7,46E+03	3,79E+04
Q9Y320, TMX2	1	5,1	7,5579	0,00E+00	0,00E+00	0,00E+00	3,12E+03	0,00E+00	2,16E+03
Q9Y375, CIA30	2	10,4	12,466	0,00E+00	0,00E+00	0,00E+00	8,60E+03	0,00E+00	0,00E+00
Q9Y383, LC7L2	1	3,8	6,6573	0,00E+00	0,00E+00	0,00E+00	6,61E+03	3,73E+03	0,00E+00
Q9Y399, RT02	6	14,5	34,806	0,00E+00	5,96E+03	0,00E+00	1,40E+04	2,82E+04	6,82E+04
Q9Y3B3, TMED7	2	13,4	12,351	0,00E+00	0,00E+00	0,00E+00	5,86E+03	0,00E+00	1,19E+04
Q9Y3D9, RT23	1	5,3	6,313	0,00E+00	1,67E+04	0,00E+00	2,10E+03	0,00E+00	1,87E+03
Q9Y3E5, PTH2	2	16,2	14,101	0,00E+00	0,00E+00	0,00E+00	5,09E+03	1,12E+04	1,22E+04

Q9Y3L5, RAP2C	2	10,4	6,8891	0,00E+00	0,00E+00	0,00E+00	7,95E+04	0,00E+00	7,94E+04
Q9Y4L1, HYOU1	14	20,5	95,677	0,00E+00	0,00E+00	0,00E+00	1,33E+04	7,22E+04	6,30E+03
Q9Y4P3, TBL2	6	19,2	44,822	0,00E+00	0,00E+00	0,00E+00	1,04E+04	1,80E+04	5,68E+03
Q9Y4W6, AFG32	21	30,7	225,51	0,00E+00	1,10E+03	4,59E+03	4,87E+05	7,43E+04	9,70E+04
Q9Y512, SAM50	3	7,5	19,95	0,00E+00	0,00E+00	0,00E+00	8,23E+03	1,47E+03	6,27E+03
Q9Y584, TIM22	1	7,7	7,7077	0,00E+00	0,00E+00	0,00E+00	2,58E+04	0,00E+00	3,39E+04
Q9Y5J9, TIM8B	2	28,9	16,617	0,00E+00	0,00E+00	0,00E+00	2,50E+05	3,74E+04	1,45E+05
Q9Y5L4, TIM13	4	53,7	39,248	0,00E+00	0,00E+00	0,00E+00	6,44E+05	2,40E+05	3,04E+05
Q9Y5M8, SRPRB	9	47,2	110,51	4,74E+03	4,38E+03	7,13E+03	2,32E+05	1,47E+05	1,67E+05
Q9Y5V3, MAGD1	2	3,5	11,804	0,00E+00	0,00E+00	0,00E+00	3,82E+03	4,79E+03	0,00E+00
Q9Y5Y0, FLVC1	2	4,7	11,71	0,00E+00	0,00E+00	0,00E+00	7,09E+03	3,55E+03	0,00E+00
Q9Y5Y5, PEX16	2	6,2	11,538	0,00E+00	0,00E+00	0,00E+00	1,34E+03	0,00E+00	4,77E+03
Q9Y619, ORNT1	1	5,3	8,1306	0,00E+00	0,00E+00	0,00E+00	9,01E+03	0,00E+00	0,00E+00
Q9Y672, ALG6	1	2,6	7,1127	0,00E+00	0,00E+00	0,00E+00	9,14E+03	8,97E+03	3,77E+03
Q9Y673, ALG5	2	9,3	12,924	0,00E+00	0,00E+00	0,00E+00	0,00E+00	2,98E+04	0,00E+00
Q9Y676, RT18B	4	19	29,259	0,00E+00	4,66E+04	4,15E+04	1,38E+04	6,38E+03	2,73E+03
Q9Y678, COPG1	3	4,1	17,01	0,00E+00	0,00E+00	5,43E+02	0,00E+00	0,00E+00	3,80E+03
Q9Y679, AUP1	4	15,6	33,936	0,00E+00	0,00E+00	0,00E+00	3,05E+04	2,16E+04	4,30E+04
Q9Y697, NFS1	2	7,2	14,738	0,00E+00	0,00E+00	0,00E+00	1,37E+04	0,00E+00	0,00E+00
Q9Y6C9, MTCH2	10	45,9	323,31	0,00E+00	0,00E+00	1,17E+04	5,66E+05	8,84E+04	3,18E+05
Q9Y6K0, CEPT1	1	2,6	7,1519	0,00E+00	0,00E+00	0,00E+00	0,00E+00	5,71E+03	2,52E+04

Table 8-2: Detailed list of proteins and their peptides used in the sPRM analysis

Protein	Peptide Sequence	Precursor Charge	Precursor Mz	Best Retention Time
Smim26	NSDEDTTIVEK	2	625.790972	21.79+/-0.42
(ENSDARG00000096346.2)	TTAFTETTVIQR	2	684.361898	41.16+/-0.94
	AGTVEYHTR	2	517.256705	11.46+/-0.25
	NDSPPENK	2	450.706514	6.7+/-0.07
Apolipoprotein A-Ib	SALQVYADHLK	3	415.559305	40.51+/-0.95
(A0A0R4IKF0)	SLTHLDDTEFK	2	653.319699	38.14+/-0.76
	LEPVVLSLK	2	499.318243	57.36+/-0.76
	IPPNWEETK	2	557.282388	31.84+/-0.78
	VAENVQELR	2	529.285462	26.57+/-0.59
Keratin 4	ASVENEFVLLK	2	624.845353	60.56+/-0.77
(F1QK60)	AVYEAELR	2	475.750724	30.62+/-0.68
	AEAESWYK	2	492.227082	28.8+/-0.8
	AEIAELNR	2	458.248349	27.94+/-0.69
	LQNEIDAVK	2	515.282388	28.7+/-0.69
	ANLEAQIAEAEER	2	722.357344	46.09+/-0.67
	ELEEALQR	2	494.258913	28.52+/-0.62
	LLEGEESR	2	466.737814	18.49+/-0.46
Creatine kinase	ELFDPVISDR	2	595.806228	56.16+/-0.59
(Q7T306)	HLTDLNWENLK	2	691.856783	51.56+/-0.77
	GGDDLDPNYVLSSR	2	754.354802	49.55+/-0.57
	FEEILTR	2	454.247817	39.04+/-0.74
	LGSSEVQQVQLVVDGVK	2	892.991265	61.15+/-0.68
Small ribosomal subunit	LNNLVLFDK	2	538.310949	56.55+/-0.81
protein eS25	LITPAVVSER	2	542.821681	42.61+/-0.85
(Q6PBI5)	AALQELLGK	2	471.784567	51.47+/-0.85
	AQVIYTR	2	425.742702	21.32+/-0.65

8.2 List of Figures

8.3 List of Tables

8.4 List of Abbreviations

°C	Degree celcius
µg	Microgramm
µl	Microliter
µm	Micrometer
µM	Micromolar
2D	Two dimensional
Å	Angstrom
aa	Amino acid
ACN	Acetonitrile
ADP	Adenosine diphosphate
AEBSF	4-(2-Aminoethyl)benzolsulfonylfluorid
AGC	Automatic gain control
AIF	Apoptosis inducing factor
ALN	Another-regulin
alt-LAMA3	Alternative lamin subunit alpha-3
alt-ORF	Alternative ORFs
altProts	Alternative proteins
AML	Acute myeloid leukemia
Amp	Ampicillin
AMPK	AMP-activated protein kinase
APAF1	Apoptotic peptidase activating factor 1
Apoa1b	Apolipoprotein A-Ib
APPLE	A peptide located in ER
APS	Ammonium persulfate
ASDURF	ASNSD1 upstream open reading frame protein
ASRPS	A small regulatory peptide of STAT3
ATF4	Activating transcription factor 4
ATP	Adenosine trisphosphate
AUG	Adenin-Uracil-Guanine
BAK	Bcl-2 homologous antagonist killer
BAX	Bcl-2 associated X protein
BLAST	Basic local alignment search tool
bp	Basepair
BR	Brawnin
BRCA	Breast cancer
BS3	Bis(sulfosuccinimidyl) suberate
BSA	Bovine Serum Albumin
CASIMO1	Cancer-associated small integral membrane open reading frame 1
cDNA	complementary DNA
CDS	Protein-coding sequence
CHOL	Cholangiocarcinoma
CID	Collision-induced dissociation

C I	Respiratory chain complex I
C II	Respiratory chain complex II
C III	Respiratory chain complex III
CIP2A-BP	CIP2A binding peptide
circCUX1	Circular RNA CUT-like homeobox 1
circRNAs	Circular RNAs
C IV	Respiratory chain complex IV
CK2	Casein kinase 2
Ckmb	Creatine kinase
CLCC1	Chloride channel CLIC like 1
cm	Centimeter
CRC	Colorectal cancer
CoA	Coenzyme A
COAD	Colon adenocarcinoma
CoQ	Coenzyme Q
CRISPR	Clustered Regularly Interspaced Short Palindromic Repeats
CRNDEP	Colorectal neoplasia differentially expressed protein
CSCC	Cutaneous squamous cell carcinoma
CYREN	Cell cycle regulator of non-homologous end joining
Cyt c	Cytochrome c
D. melanogaster	*Drosophila melanogaster*
d49	Deletion mutant SMIM26 knockout zebrafish
Da	Dalton
DAPI	4′,6-diamidino-2-phenylindole
DDA	Data dependent analysis
DEDD2	Death effector domain containing 2
DMEM	Dulbecco's modified Eagle's medium
dN/dS	Nonsynonymous versus synonymous substitution ratios
DNA	Deoxyribonucleic acid
doORFs	Downstream overlapping ORFs
dORFs	Downstream ORFs
dpf	days post fertilization
DRP1	Dynamin-related protein 1
DSS	Disuccinimidyl suberate
DTAB	Dodecyltrimethylammonium bromide
DTT	Dithiothreitol
DWORF	Dwarf open reading frame
E. coli	*Escherichia coli*
ECAR	Extracellular acidification rate
EDTA	Ethylenediaminetetraacetic acid
EGFR	Epidermal growth factor
ELN	Endoregulin
E_{max}	Maximum effect
EMT	Epithelial-mesenchymal transition

ENO1	Enhancing enolase 1
ER	Endoplasmatic reticulum
EREG	Epiregulin
ERLIC	Electrostatic repulsion-hydrophilic interaction chromatography
ESCA	Esophageal carcinoma
ETC	Electron transport chain
EtOH	Ethanol
F/H	FLAG-HA-tag
FA	Formic acid
FAD	Flavin adenine dinucleotide
FBS	Fetal bovine serum
FCCP	Carbonyl cyanide-p-trifluoromethoxyphenylhydrazone
FDA	Food and Drug Administration
fmol	Femtomol
FUNDC1	FUN14 domain-containing protein 1
GAPDH	Glyceraldehyde 3-phosphate dehydrogenase
Gau	Gene antisense ubiquitous in mtDNAs
GBM	Glioblastoma
GCN4	General control transcription factor
gDNA	Genomic DNA
GO	Gene ontology
gRNAs	Guide RNAs
GSEA	Gene set enrichment analysis
h	Hour
HCC	Hepatocellular carcinoma
HET	Heterozygous
HGP	Human Genome Project
HIGD1A	HIG1 domain family member 1A
Hi-RIEF	High-resolution isoelectric focusing
HN	Humanin
HNSCC	Head and neck squamous cell carcinoma
HOM	Homozygous
HR	Hazard ratio
HT	Halo-tag
Hz	Hertz
iBAQ	Intensity-based absolute quantification
IF	Immunofluorescence
IGF2BP1	Insulin-like growth factor 2 mRNA-binding protein 1
IL-12	Interleukin-12
IMM	Inner mitochondrial membrane
IMS	Intermembrane space
insdel	Insertion and deletion mutant SMIM26 knockout zebrafish
iORFs	Internal ORFs
IP	immunoprecipitation

IRAK1	Interleukin-1 receptor associated kinase 1
IRES	Internal ribosome entry sites
JAK2	Janus kinase 2
kDa	Kilodalton
KO	Knockout
KRASIM	KRAS-interacting microprotein
Krt4	Keratin-4
kV	Kilovolt
LC-MS/MS	Liquid chromatography coupled with tandem MS
LDS	lithium dodecyl sulfate
LIHC	Liver hepatocellular carcinoma
LINC00493	Long intergenic non-protein coding RNA 493
LINE-1	Long interspersed nuclear element-1
lncRNAs	Long non-coding RNAs
M	Molar
m^6A	N^6-Methyladenosine
m^7G	7-methylguanosine
MALAT1	Metastasis associated lung adenocarcinoma transcript 1
MAPK	Mitogen-activated kinase
MAVI1	Microprotein in antiviral immunity 1
MAVS	Mitochondrial antiviral-signaling protein
MCU	Mitochondrial calcium uniporter
MEM	Minimum Essential Medium
MeOH	Methanol
MFN2	Mitofusin-2
MHC-I	Major histocompatibility complex class I
MIAC	Micropeptide inhibiting actin cytoskeleton
MICOS	Mitochondrial contact site and cristae organizing system
MID51	Mitochondrial dynamic protein of 51 kDa
MIEF1	Mitochondrial elongation factor 1
MIEF1-MP	MIEF1 microprotein
min	Minute
MINAS-60	Microprotein that negatively regulates assembly of the pre-60S ribosomal subunit
miPEPs	MicroRNA-encoded peptides
MIPS	Monoisotopic precursor selection
miRNA	Micro RNA
ml	Milliliter
mLDH	Mitochondrial lactate dehydrogenase
MLN	Myoregulin
mM	Millimolar
mm	Millimeter
mM	Millimolar
mm	Millimeter

Mm47	Mitochondrial micropeptide-47
MMP	Mitochondrial membrane potential
MOCCI	Modulator of cytochrome C oxidase during inflammation
MOTS-c	Mitochondrial ORF of the 12S rRNA type-c
MOXI	Micropeptide regulator of ß-oxidation
MP31	Microprotein-31
MPM	Micropeptide in mitochondria
MS	Mass spectrometry
MSA	Multiple sequence alignment
MSD	Mean squared displacement
MTALTND4	Mitochondrial alternative ND4 protein
MT-ATP8	Mitochondrially encoded ATP synthase membrane subunit 8
mtDNA	Mitochondrial genome
MTLBN	Mitolamban
MTLN	Mitoregulin
MT-ND4L	Mitochondrially encoded NADH:ubiquinone oxidoreductase core subunit 4L
mTORC1	Mechanistic target of rapamycin complex 1
mt-rRNAs	Mitochondrial ribosomal RNAs
mt-tRNAs	Mitochondrial transfer RNAs
Mustn1	Musculoskeletal embryonic nuclear protein 1
Mut	Mutant
mV	Millivolt
MWCO	Molecular weight cutoff
N	Normal tissue
N1DARP	Notch1 degradation-associated regulatory polypeptide
NAD(H)	Nicotinamide adenine dinucleotide
ncRNAs	Non-coding RNAs
NCX	Na^+/Ca^{2+} exchanger
NEHJ	Non-homologous end joining
NEMEP	Nodal enhanced mesendoderm peptide
ng	Nanogramm
NGS	Next-generation sequencing
NJ	Neighbor-Joining
NKA	Na^+/K^+ ATPase
nl	Nanoliter
NLRP3	NLR family pyrin domain containing 3
nm	Nanometer
nM	Nanomolar
NMD	Nonsense-mediated decay
NoBody	Non-annotated P-body dissociating polypeptide
NONO	Non-POU domain-containing octamer-binding protein
NPC	Nasopharyngeal carcinoma
nt	Nucleotide

nuORFs	Novel or unannotated ORFs
O_2	Oxygen
OCR	Oxygen consumption rate
OE	Overexpression
OMM	Outer mitochondrial membrane
ORFs	Open reading frames
OSCC	Oral squamous cell carcinoma
OXPHOS	oxidative phosphorylation
p./n.p.	Ratio of phosphorylated to non-phosphorylated peptide
PAAD	Pancreatic adenocarcinoma
PACMP	PAR-amplifying and CtIP-maintaining micropeptide
PAF1	Polymerase associated factor 1
PAGE	Polyacrylamide gel electrophoresis
PAM	Protospacer adjacent motif
P-bodies	Processing bodies
PBS	Phosphate-buffered saline
PCR	Polymerase chain reaction
PFA	Paraformaldehyde
PI3K	Phosphoinositide 3-kinases
PIGBOS	PIGB opposite strand
PINK1	PTEN-induced putative kinase protein 1
PKM	Pyruvate kinase M
pLDDT	predicted Local Distance Difference Test
PLM	Phospholemman
PLN	Phospholamban
pmol	Picomol
PNK	Polynucleotide kinase
PPIA	Peptidylprolyl isomerase A
ppm	Parts per million
pri	Polished rice
pri-miRNAs	Primary microRNAs
PTFE	Polytetrafluoroethylene
pTINCR	Peptide encoded by terminal differentiation-induced lncRNA
qPCR	quantitative PCR
RBRP	RNA-binding regulatory peptide
RCC	Renal cell carcinoma
READ	Rectum adenocarcinoma
RHOT2	Mitochondrial Rho GTPase 2
Ribo-seq	Ribosome profiling
RNA	Ribonucleic acid
RNA-seq	RNA sequencing
RNP	Ribonucleoprotein
ROS	Reactive oxygen species
RPL32	Ribosomal protein L32

RPL36	Ribosomal protein L36
Rps25	Ribosomal protein S25
RT	Room temperature
S	Serine
s	Second
SAM	S-adenosylmethionine
SCX	Strong cation exchange chromatography
SD	Standard deviation
SDS	Sodium dodecyl sulfate
SDS-PAGE	SDS-polyacryl gel electrophoresis
SEHB	Short ORF-encoded histone binding protein
SEPs	sORF-encoded polypeptides
SERCA	Sarcoplasmic/endoplasmic reticulum calcium ATPase
SFXN1	Sideroflexin 1
sgRNA	Single guide RNA
SHLPs	Small humanin-like peptides
SHMOOSE	Small human mitochondrial ORF over serine tRNA
siNC	Negative control knockdown
siPGAM5	PGAM5 knockdown
siSLC25A6	SLC25A6 knockdown
siSMIM26	SMIM26 knockdown
siVDAC1	VDAC1 knockdown
SLC25	Solute carrier family 25
SLC25A11	Solute carrier family 25 member 11
SLC25A5	Solute carrier family 25 member 5
SLC25A6	Solute carrier family 25 member 6
SLC35A4	Solute carrier family 35 member A4
SLC35A4-MP	SLC35A4 microprotein
SLIC	Sequence- and ligation independent cloning
SLN	Sarcolipin
SMAC	Second mitochondria-derived activator of caspase
SMIM26	Small integral membrane protein 26
SMIM26ΔC	C-terminally truncated SMIM26 variant
SMIM30	Small integral membrane protein 30
SMIM4	Small integral membrane protein 4
smORFs	Small ORFs
sORF	Short ORF
SPAR	Small regulatory polypeptide of amino acid response
sPRM	scheduled Parallel Reaction Monitoring
SRM	Selected reaction monitoring
ST	SnapTag
STAD	Stomach adenocarcinoma
STAT3	Signal transducer and activator of transcription 3
STAT5	Signal transducer and activator of transcription 5

Svb	Shavenbaby
T	Threonine
T	Tumor tissue
TBS	Tris Buffered Saline
TCA	Trichloroacetic acid
TCGA	The cancer genome atlas
TEMED	Tetramethylethylenediamine
TFA	Trifluoroacetic acid
TH	Trehalose
TIMM44	Mitochondrial import inner membrane translocase subunit TIM44
TI-seq	Translation initiation sequencing
TMD	Transmembrane domain
TMEM24	Transmembrane protein 24
TMT	Tandem mass tag
TOMM20	Mitochondrial import receptor subunit TOM20 homolog
TRPC5OS	Transient receptor potential channel 5 opposite strand
U	Unit
uoORFs	Upstream overlapping ORFs
uORFs	Upstream ORFs
UPR	Unfolded protein response
UQCC3	Ubiquinol-cytochrome c reductase complex assembly factor 3
UQCC4	Ubiquinol-cytochrome c reductase complex assembly factor 4
UTR	Untranslated region
VDAC1	Voltage-dependent anion channel 1
VDAC2	Voltage-dependent anion channel 2
VDAC3	Voltage-dependent anion channel 3
WCE	whole cell extract
WT	Wild-type
Y	Tyrosine
YYB1M	Yin Yang 1-binding micropeptide
ΔΨm	Membrane potential

9 References

Abramson, J., Adler, J., Dunger, J., Evans, R., Green, T., Pritzel, A., Ronneberger, O., Willmore, L., Ballard, A.J., and Bambrick, J., et al. (2024). Accurate structure prediction of biomolecular interactions with AlphaFold 3. Nature *630*, 493-500. https://doi.org/10.1038/s41586-024-07487-w.

Ahlers, B.A., Zhang, X.-Q., Moorman, J.R., Rothblum, L.I., Carl, L.L., Song, J., Wang, J., Geddis, L.M., Tucker, A.L., and Mounsey, J.P., et al. (2005). Identification of an endogenous inhibitor of the cardiac Na+/Ca2+ exchanger, phospholemman. The Journal of biological chemistry *280*, 19875-19882. https://doi.org/10.1074/jbc.M414703200.

Anderson, D.M., Anderson, K.M., Chang, C.-L., Makarewich, C.A., Nelson, B.R., McAnally, J.R., Kasaragod, P., Shelton, J.M., Liou, J., and Bassel-Duby, R., et al. (2015). A micropeptide encoded by a putative long noncoding RNA regulates muscle performance. Cell *160*, 595-606. https://doi.org/10.1016/j.cell.2015.01.009.

Anderson, D.M., Makarewich, C.A., Anderson, K.M., Shelton, J.M., Bezprozvannaya, S., Bassel-Duby, R., and Olson, E.N. (2016). Widespread control of calcium signaling by a family of SERCA-inhibiting micropeptides. Science signaling *9*, ra119. https://doi.org/10.1126/scisignal.aaj1460.

Arnoult, N., Correia, A., Ma, J., Merlo, A., Garcia-Gomez, S., Maric, M., Tognetti, M., Benner, C.W., Boulton, S.J., and Saghatelian, A., et al. (2017). Regulation of DNA repair pathway choice in S and G2 phases by the NHEJ inhibitor CYREN. Nature *549*, 548-552. https://doi.org/10.1038/nature24023.

Aspden, J.L., Eyre-Walker, Y.C., Phillips, R.J., Amin, U., Mumtaz, M.A.S., Brocard, M., and Couso, J.-P. (2014). Extensive translation of small Open Reading Frames revealed by Poly-Ribo-Seq. eLife *3*, e03528. https://doi.org/10.7554/eLife.03528.

Barzegar Behrooz, A., Talaie, Z., Jusheghani, F., Łos, M.J., Klonisch, T., and Ghavami, S. (2022). Wnt and PI3K/Akt/mTOR Survival Pathways as Therapeutic Targets in Glioblastoma. International journal of molecular sciences *23*, 1353. https://doi.org/10.3390/ijms23031353.

Basrai, M.A., Hieter, P., and Boeke, J.D. (1997). Small open reading frames: beautiful needles in the haystack. Genome research *7*, 768-771. https://doi.org/10.1101/gr.7.8.768.

Bastide, A., Karaa, Z., Bornes, S., Hieblot, C., Lacazette, E., Prats, H., and Touriol, C. (2008). An upstream open reading frame within an IRES controls expression of a specific VEGF-A isoform. Nucleic Acids Res *36*, 2434-2445. https://doi.org/10.1093/nar/gkn093.

Bazzini, A.A., Johnstone, T.G., Christiano, R., Mackowiak, S.D., Obermayer, B., Fleming, E.S., Vejnar, C.E., Lee, M.T., Rajewsky, N., and Walther, T.C., et al. (2014). Identification of small ORFs in vertebrates using ribosome footprinting and evolutionary conservation. The EMBO journal *33*, 981-993. https://doi.org/10.1002/embj.201488411.

Bertholet, A.M., Natale, A.M., Bisignano, P., Suzuki, J., Fedorenko, A., Hamilton, J., Brustovetsky, T., Kazak, L., Garrity, R., and Chouchani, E.T., et al. (2022). Mitochondrial uncouplers induce proton leak by activating AAC and UCP1. Nature *606*, 180-187. https://doi.org/10.1038/s41586-022-04747-5.

Bhagawati, M., Arroum, T., Webeling, N., Montoro, A.G., Mootz, H.D., and Busch, K.B. (2021). The receptor subunit Tom20 is dynamically associated with the TOM complex in mitochondria of human cells. Molecular biology of the cell *32*, br1. https://doi.org/10.1091/mbc.E21-01-0042.

Bhatta, A., Atianand, M., Jiang, Z., Crabtree, J., Blin, J., and Fitzgerald, K.A. (2020). A Mitochondrial Micropeptide Is Required for Activation of the Nlrp3 Inflammasome. Journal of immunology (Baltimore, Md. : 1950) *204*, 428-437. https://doi.org/10.4049/jimmunol.1900791.

Boix, O., Martinez, M., Vidal, S., Giménez-Alejandre, M., Palenzuela, L., Lorenzo-Sanz, L., Quevedo, L., Moscoso, O., Ruiz-Orera, J., and Ximénez-Embún, P., et al. (2022). pTINCR microprotein promotes epithelial differentiation and suppresses tumor growth through CDC42 SUMOylation and activation. Nature Communications. https://doi.org/10.1038/s41467-022-34529-6.

Branca, R.M.M., Orre, L.M., Johansson, H.J., Granholm, V., Huss, M., Pérez-Bercoff, Å., Forshed, J., Käll, L., and Lehtiö, J. (2014). HiRIEF LC-MS enables deep proteome coverage and unbiased proteogenomics. Nature methods *11*, 59-62. https://doi.org/10.1038/nmeth.2732.

Brunet, M.A., Jacques, J.-F., Nassari, S., Tyzack, G.E., McGoldrick, P., Zinman, L., Jean, S., Robertson, J., Patani, R., and Roucou, X. (2021). The FUS gene is dual-coding with both proteins contributing to FUS-mediated toxicity. EMBO reports *22*, e50640. https://doi.org/10.15252/embr.202050640.

Brunet, M.A., Leblanc, S., and Roucou, X. (2020). Reconsidering proteomic diversity with functional investigation of small ORFs and alternative ORFs. Experimental cell research *393*, 112057. https://doi.org/10.1016/j.yexcr.2020.112057.

Brunet, M.A., Levesque, S.A., Hunting, D.J., Cohen, A.A., and Roucou, X. (2018). Recognition of the polycistronic nature of human genes is critical to understanding the genotype-phenotype relationship. Genome research *28*, 609-624. https://doi.org/10.1101/gr.230938.117.

Busch, J.D., Fielden, L.F., Pfanner, N., and Wiedemann, N. (2023). Mitochondrial protein transport: Versatility of translocases and mechanisms. Molecular cell *83*, 890-910. https://doi.org/10.1016/j.molcel.2023.02.020.

Cai, Y., Li, D., Lv, D., Yu, J., Ma, Y., Jiang, T., Ding, N., Liu, Z., Li, Y., and Xu, J. (2024). MHC-I-presented non-canonical antigens expand the cancer immunotherapy targets in acute myeloid leukemia. Scientific data *11*, 831. https://doi.org/10.1038/s41597-024-03660-y.

Camarena, M.E., Theunissen, P., Ruiz, M., Ruiz-Orera, J., Calvo-Serra, B., Castelo, R., Castro, C., Sarobe, P., Fortes, P., and Perera-Bel, J., et al. (2024). Microproteins encoded by noncanonical ORFs are a major source of tumor-specific antigens in a liver cancer patient meta-cohort. Science advances *10*, eadn3628. https://doi.org/10.1126/sciadv.adn3628.

Camargo, A.P., Sourkov, V., Pereira, G.A.G., and Carazzolle, M.F. (2020). RNAsamba: neural network-based assessment of the protein-coding potential of RNA sequences. NAR genomics and bioinformatics *2*, lqz024. https://doi.org/10.1093/nargab/lqz024.

Campeau, E., Ruhl, V.E., Rodier, F., Smith, C.L., Rahmberg, B.L., Fuss, J.O., Campisi, J., Yaswen, P., Cooper, P.K., and Kaufman, P.D. (2009). A versatile viral system for expression and depletion of proteins in mammalian cells. PloS one *4*, e6529. https://doi.org/10.1371/journal.pone.0006529.

Cao, K., Hajy Heydary, Y., Tong, G., and Martinez, T.F. (2023). Integrated workflow for discovery of microprotein-coding small open reading frames. STAR protocols *4*, 102649. https://doi.org/10.1016/j.xpro.2023.102649.

Cao, X., Khitun, A., Harold, C.M., Bryant, C.J., Zheng, S.-J., Baserga, S.J., and Slavoff, S.A. (2022). Nascent alt-protein chemoproteomics reveals a pre-60S assembly checkpoint inhibitor. Nature chemical biology *18*, 643-651. https://doi.org/10.1038/s41589-022-01003-9.

Cao, X., Khitun, A., Luo, Y., Na, Z., Phoodokmai, T., Sappakhaw, K., Olatunji, E., Uttamapinant, C., and Slavoff, S.A. (2021). Alt-RPL36 downregulates the PI3K-AKT-mTOR signaling pathway by interacting with TMEM24. Nat Commun *12*, 1-15. https://doi.org/10.1038/s41467-020-20841-6.

Chaudhuri, D., Sancak, Y., Mootha, V.K., and Clapham, D.E. (2013). MCU encodes the pore conducting mitochondrial calcium currents. eLife *2*, e00704. https://doi.org/10.7554/eLife.00704.

Chen, G., Han, Z., Du Feng, Chen, Y., Chen, L., Wu, H., Huang, L., Zhou, C., Cai, X., and Fu, C., et al. (2014). A Regulatory Signaling Loop Comprising the PGAM5 Phosphatase and CK2 Controls Receptor-Mediated Mitophagy. Molecular cell *54*, 362-377. https://doi.org/10.1016/j.molcel.2014.02.034.

Chen, J., Brunner, A.-D., Cogan, J., Nuñez, J.K., Fields, A.P., Adamson, B., Itzhak, D.N., Li, J.Y., Mann, M., and Leonetti, M., et al. (2020). Pervasive functional translation of noncanonical human open reading frames. Science. https://doi.org/10.1126/science.aay0262.

Cheung, J.Y., Zhang, X.-Q., Song, J., Gao, E., Chan, T.O., Rabinowitz, J.E., Koch, W.J., Feldman, A.M., and Wang, J. (2013). Coordinated regulation of cardiac Na(+)/Ca (2+) exchanger and Na (+)-K (+)-ATPase by phospholemman (FXYD1). Advances in experimental medicine and biology *961*, 175-190. https://doi.org/10.1007/978-1-4614-4756-6_15.

Chu, Q., Martinez, T.F., Novak, S.W., Donaldson, C.J., Tan, D., Vaughan, J.M., Chang, T., Diedrich, J.K., Andrade, L., and Kim, A., et al. (2019). Regulation of the ER stress response by a mitochondrial microprotein. Nature Communications *10*, 4883. https://doi.org/10.1038/s41467-019-12816-z.

Chugunova, A., Loseva, E., Mazin, P., Mitina, A., Navalayeu, T., Bilan, D., Vishnyakova, P., Marey, M., Golovina, A., and Serebryakova, M., et al. (2019). LINC00116 codes for a mitochondrial peptide linking respiration and lipid metabolism. Proceedings of the National Academy of Sciences *116*, 4940-4945. https://doi.org/10.1073/pnas.1809105116.

Cloutier, P., Poitras, C., Faubert, D., Bouchard, A., Blanchette, M., Gauthier, M.-S., and Coulombe, B. (2020). Upstream ORF-Encoded ASDURF Is a Novel Prefoldin-like Subunit of the PAQosome. Journal of proteome research *19*, 18-27. https://doi.org/10.1021/acs.jproteome.9b00599.

Cobb, L.J., Lee, C., Xiao, J., Yen, K., Wong, R.G., Nakamura, H.K., Mehta, H.H., Gao, Q., Ashur, C., and Huffman, D.M., et al. (2016). Naturally occurring mitochondrial-derived peptides are age-dependent regulators of apoptosis, insulin sensitivity, and inflammatory markers. Aging *8*, 796-809. https://doi.org/10.18632/aging.100943.

Combe, C.W., Graham, M., Kolbowski, L., Fischer, L., and Rappsilber, J. (2024). xiVIEW: Visualisation of Crosslinking Mass Spectrometry Data. Journal of Molecular Biology *436*, 168656. https://doi.org/10.1016/j.jmb.2024.168656.

Couzigou, J.-M., André, O., Guillotin, B., Alexandre, M., and Combier, J.-P. (2016). Use of microRNA-encoded peptide miPEP172c to stimulate nodulation in soybean. The New phytologist *211*, 379-381. https://doi.org/10.1111/nph.13991.

Crambert, G., and Geering, K. (2003). FXYD proteins: new tissue-specific regulators of the ubiquitous Na,K-ATPase. Science's STKE : signal transduction knowledge environment *2003*, RE1. https://doi.org/10.1126/stke.2003.166.re1.

Cui, Y., Peng, J., Zheng, M., Ge, H., Wu, X., Xia, Y., Huang, Y., Wang, S., Yin, Y., and Fu, Z., et al. (2022). TRPC5OS induces tumorigenesis by increasing ENO1-mediated glucose uptake in breast cancer. Translational oncology *22*, 101447. https://doi.org/10.1016/j.tranon.2022.101447.

Cunningham, C.N., and Rutter, J. (2020). 20,000 picometers under the OMM: diving into the vastness of mitochondrial metabolite transport. EMBO reports *21*, e50071. https://doi.org/10.15252/embr.202050071.

D'Lima, N.G., Ma, J., Winkler, L., Chu, Q., Loh, K.H., Corpuz, E.O., Budnik, B., Lykke-Andersen, J., Saghatelian, A., and Slavoff, S.A. (2017). A human microprotein that interacts with the mRNA decapping complex. Nature chemical biology. https://doi.org/10.1038/nchembio.2249.

Denli, A.M., Narvaiza, I., Kerman, B.E., Pena, M., Benner, C., Marchetto, M.C.N., Diedrich, J.K., Aslanian, A., Ma, J., and Moresco, J.J., et al. (2015). Primate-specific ORF0 contributes to retrotransposon-mediated diversity. Cell *163*, 583-593. https://doi.org/10.1016/j.cell.2015.09.025.

Dennerlein, S., Poerschke, S., Oeljeklaus, S., Wang, C., Richter-Dennerlein, R., Sattmann, J., Bauermeister, D., Hanitsch, E., Stoldt, S., and Langer, T., et al. (2021). Defining the interactome of the human mitochondrial ribosome identifies SMIM4 and TMEM223 as respiratory chain assembly factors. eLife *10*. https://doi.org/10.7554/eLife.68213.

Desmurs, M., Foti, M., Raemy, E., Vaz, F.M., Martinou, J.-C., Bairoch, A., and Lane, L. (2015). C11orf83, a mitochondrial cardiolipin-binding protein involved in bc1 complex assembly and supercomplex stabilization. Molecular and cellular biology *35*, 1139-1156. https://doi.org/10.1128/MCB.01047-14.

Dever, T.E., Ivanov, I.P., and Hinnebusch, A.G. (2023). Translational regulation by uORFs and start codon selection stringency. Genes & development *37*, 474-489. https://doi.org/10.1101/gad.350752.123.

Du, H., Xu, T., Yu, S., Wu, S., and Zhang, J. (2025). Mitochondrial metabolism and cancer therapeutic innovation. Signal transduction and targeted therapy *10*, 245. https://doi.org/10.1038/s41392-025-02311-x.

Ducommun, S., Jannig, P.R., Cervenka, I., Murgia, M., Mittenbühler, M.J., Chernogubova, E., Dias, J.M., Jude, B., Correia, J.C., and van Vranken, J.G., et al. (2024). Mustn1 is a smooth muscle cell-secreted microprotein that modulates skeletal muscle extracellular matrix composition. Molecular metabolism *82*, 101912. https://doi.org/10.1016/j.molmet.2024.101912.

Duffy, E.E., Assad, E.G., Kalish, B.T., and Greenberg, M.E. (2024). Small but mighty: the rise of microprotein biology in neuroscience. Front. Mol. Neurosci. *17*, 1386219. https://doi.org/10.3389/fnmol.2024.1386219.

Erhard, F., Halenius, A., Zimmermann, C., L'Hernault, A., Kowalewski, D.J., Weekes, M.P., Stevanovic, S., Zimmer, R., and Dölken, L. (2018). Improved Ribo-seq enables identification of cryptic translation events. Nature methods *15*, 363-366. https://doi.org/10.1038/nmeth.4631.

Faure, E., Delaye, L., Tribolo, S., Levasseur, A., Seligmann, H., and Barthélémy, R.-M. (2011). Probable presence of an ubiquitous cryptic mitochondrial gene on the antisense strand of the cytochrome oxidase I gene. Biology direct *6*, 56. https://doi.org/10.1186/1745-6150-6-56.

Fernandez, J., Yaman, I., Huang, C., Liu, H., Lopez, A.B., Komar, A.A., Caprara, M.G., Merrick, W.C., Snider, M.D., and Kaufman, R.J., et al. (2005). Ribosome stalling regulates IRES-mediated translation in eukaryotes, a parallel to prokaryotic attenuation. Molecular cell *17*, 405-416. https://doi.org/10.1016/j.molcel.2004.12.024.

Flores-Romero, H., Dadsena, S., and García-Sáez, A.J. (2023). Mitochondrial pores at the crossroad between cell death and inflammatory signaling. Molecular cell *83*, 843-856. https://doi.org/10.1016/j.molcel.2023.02.021.

Floyd, B.J., Wilkerson, E.M., Veling, M.T., Minogue, C.E., Xia, C., Beebe, E.T., Wrobel, R.L., Cho, H., Kremer, L.S., and Alston, C.L., et al. (2016). Mitochondrial Protein Interaction Mapping Identifies Regulators of Respiratory Chain Function. Molecular cell *63*, 621-632. https://doi.org/10.1016/j.molcel.2016.06.033.

Friesen, M., Warren, C.R., Yu, H., Toyohara, T., Ding, Q., Florido, M.H.C., Sayre, C., Pope, B.D., Goff, L.A., and Rinn, J.L., et al. (2020). Mitoregulin Controls β-Oxidation in Human and Mouse Adipocytes. Stem cell reports *14*, 590-602. https://doi.org/10.1016/j.stemcr.2020.03.002.

Fritsch, C., Herrmann, A., Nothnagel, M., Szafranski, K., Huse, K., Schumann, F., Schreiber, S., Platzer, M., Krawczak, M., and Hampe, J., et al. (2012). Genome-wide search for novel human uORFs and N-terminal protein extensions using ribosomal footprinting. Genome research *22*, 2208-2218. https://doi.org/10.1101/gr.139568.112.

Fu, G., Li, S.-T., Jiang, Z., Mao, Q., Xiong, N., Li, X., Hao, Y., and Zhang, H. (2023). PGAM5 deacetylation mediated by SIRT2 facilitates lipid metabolism and liver cancer proliferation. ABBS *55*, 1370-1379. https://doi.org/10.3724/abbs.2023155.

Fu, H., Wang, T., Kong, X., Yan, K., Yang, Y., Cao, J., Yuan, Y., Wang, N., Kee, K., and Lu, Z.J., et al. (2022). A Nodal enhanced micropeptide NEMEP regulates glucose uptake during mesendoderm differentiation of embryonic stem cells. Nature Communications *13*, 3984. https://doi.org/10.1038/s41467-022-31762-x.

Gao, X., Wan, J., Liu, B., Ma, M., Shen, B., and Qian, S.-B. (2015). Quantitative profiling of initiating ribosomes in vivo. Nature methods *12*, 147-153. https://doi.org/10.1038/nmeth.3208.

Ge, Q., Jia, D., Cen, D., Qi, Y., Shi, C., Li, J., Sang, L., Yang, L.-J., He, J., and Lin, A., et al. (2021). Micropeptide ASAP encoded by LINC00467 promotes colorectal cancer progression by directly modulating ATP synthase activity. The Journal of clinical investigation *131*. https://doi.org/10.1172/JCI152911.

Ghosh, S., Fan, F., Powell, R., Park, Y.S., Stephan, C., Kopetz, E.S., Ellis, L.M., and Bhattacharya, R. (2024). Enhancing efficacy of the MEK inhibitor trametinib with paclitaxel in KRAS-mutated colorectal cancer. Therapeutic advances in medical oncology *16*, 17588359241303302. https://doi.org/10.1177/17588359241303302.

Giacomello, M., Pyakurel, A., Glytsou, C., and Scorrano, L. (2020). The cell biology of mitochondrial membrane dynamics. Nat Rev Mol Cell Biol *21*, 204-224. https://doi.org/10.1038/s41580-020-0210-7.

Giampazolias, E., and Tait, S.W.G. (2016). Mitochondria and the hallmarks of cancer. The FEBS Journal *283*, 803-814. https://doi.org/10.1111/febs.13603.

Götze, M., Pettelkau, J., Fritzsche, R., Ihling, C.H., Schäfer, M., and Sinz, A. (2015). Automated assignment of MS/MS cleavable cross-links in protein 3D-structure analysis. Journal of the American Society for Mass Spectrometry *26*, 83-97. https://doi.org/10.1007/s13361-014-1001-1.

Guo, B., Wu, S., Zhu, X., Zhang, L., Deng, J., Li, F., Wang, Y., Zhang, S., Wu, R., and Lu, J., et al. (2020). Micropeptide CIP2A-BP encoded by LINC00665 inhibits triple-negative breast cancer progression. The EMBO journal *39*, e102190. https://doi.org/10.15252/embj.2019102190.

Guo, Z.-W., Meng, Y., Zhai, X.-M., Xie, C., Zhao, N., Li, M., Zhou, C.-L., Li, K., Liu, T.-C., and Yang, X.-X., et al. (2019). Translated Long Non-Coding Ribonucleic Acid ZFAS1 Promotes Cancer Cell Migration by Elevating Reactive Oxygen Species Production in Hepatocellular Carcinoma. Frontiers in genetics *10*, 1111. https://doi.org/10.3389/fgene.2019.01111.

Guttman, M., Russell, P., Ingolia, N.T., Weissman, J.S., and Lander, E.S. (2013). Ribosome profiling provides evidence that large noncoding RNAs do not encode proteins. Cell *154*, 240-251. https://doi.org/10.1016/j.cell.2013.06.009.

Hanada, K., Zhang, X., Borevitz, J.O., Li, W.-H., and Shiu, S.-H. (2007). A large number of novel coding small open reading frames in the intergenic regions of the Arabidopsis thaliana genome are transcribed and/or under purifying selection. Genome research *17*, 632-640. https://doi.org/10.1101/gr.5836207.

Hanahan, D., and Weinberg, R.A. (2011). Hallmarks of cancer: the next generation. Cell *144*, 646-674. https://doi.org/10.1016/j.cell.2011.02.013.

Handler, A.A., Lim, J.E., and Losick, R. (2008). Peptide inhibitor of cytokinesis during sporulation in Bacillus subtilis. Molecular microbiology *68*, 588-599. https://doi.org/10.1111/j.1365-2958.2008.06173.x.

Hao, Y., Zhang, L., Niu, Y., Cai, T., Luo, J., He, S., Zhang, B., Zhang, D., Qin, Y., and Yang, F., et al. (2018). SmProt: a database of small proteins encoded by annotated coding and non-coding RNA loci. Briefings in bioinformatics *19*, 636-643. https://doi.org/10.1093/bib/bbx005.

Hashimoto, Y., Ito, Y., Niikura, T., Shao, Z., Hata, M., Oyama, F., and Nishimoto, I. (2001a). Mechanisms of neuroprotection by a novel rescue factor humanin from Swedish mutant amyloid precursor protein. Biochemical and biophysical research communications *283*, 460-468. https://doi.org/10.1006/bbrc.2001.4765.

Hashimoto, Y., Kurita, M., Aiso, S., Nishimoto, I., and Matsuoka, M. (2009). Humanin inhibits neuronal cell death by interacting with a cytokine receptor complex or complexes involving CNTF receptor alpha/WSX-1/gp130. Molecular biology of the cell *20*, 2864-2873. https://doi.org/10.1091/mbc.e09-02-0168.

Hashimoto, Y., Niikura, T., Ito, Y., Sudo, H., Hata, M., Arakawa, E., Abe, Y., Kita, Y., and Nishimoto, I. (2001b). Detailed characterization of neuroprotection by a rescue factor humanin against various Alzheimer's disease-relevant insults. The Journal of neuroscience : the official journal of the Society for Neuroscience *21*, 9235-9245. https://doi.org/10.1523/JNEUROSCI.21-23-09235.2001.

Hashimoto, Y., Niikura, T., Tajima, H., Yasukawa, T., Sudo, H., Ito, Y., Kita, Y., Kawasumi, M., Kouyama, K., and Doyu, M., et al. (2001c). A rescue factor abolishing neuronal cell death by a wide spectrum of familial Alzheimer's disease genes and Abeta. Proceedings of the National Academy of Sciences of the United States of America *98*, 6336-6341. https://doi.org/10.1073/pnas.101133498.

He, C., Jia, C., Zhang, Y., and Xu, P. (2018). Enrichment-Based Proteogenomics Identifies Microproteins, Missing Proteins, and Novel smORFs in Saccharomyces cerevisiae. Journal of proteome research *17*, 2335-2344. https://doi.org/10.1021/acs.jproteome.8b00032.

He, W., He, W., Sun, Z., and He, P. (2025). Physiological and pathological roles of PGAM5: An update and future trend. iScience *28*, 111539. https://doi.org/10.1016/j.isci.2024.111539.

Hemm, M.R., Paul, B.J., Schneider, T.D., Storz, G., and Rudd, K.E. (2008). Small membrane proteins found by comparative genomics and ribosome binding site models. Molecular microbiology *70*, 1487-1501. https://doi.org/10.1111/j.1365-2958.2008.06495.x.

Heslop, K.A., Milesi, V., and Maldonado, E.N. (2021). VDAC Modulation of Cancer Metabolism: Advances and Therapeutic Challenges. Frontiers in physiology *12*, 742839. https://doi.org/10.3389/fphys.2021.742839.

Hinnebusch, A.G. (2005). Translational regulation of GCN4 and the general amino acid control of yeast. Annual review of microbiology *59*, 407-450. https://doi.org/10.1146/annurev.micro.59.031805.133833.

Ho, L., Tan, S.Y.X., Wee, S., Wu, Y., Tan, S.J.C., Ramakrishna, N.B., Chng, S.C., Nama, S., Szczerbinska, I., and Chan, Y.-S., et al. (2015). ELABELA Is an Endogenous Growth Factor that Sustains hESC Self-Renewal via the PI3K/AKT Pathway. Cell stem cell *17*, 435-447. https://doi.org/10.1016/j.stem.2015.08.010.

Hofman, D.A., Ruiz-Orera, J., Yannuzzi, I., Murugesan, R., Brown, A., Clauser, K.R., Condurat, A.L., van Dinter, J.T., Engels, S.A.G., and Goodale, A., et al. (2024). Translation of non-canonical open reading frames as a cancer cell survival mechanism in childhood medulloblastoma. Molecular cell *84*, 261-276.e18. https://doi.org/10.1016/j.molcel.2023.12.003.

Hong, S.-Y., Sun, B., Straub, D., Blaakmeer, A., Mineri, L., Koch, J., Brinch-Pedersen, H., Holme, I.B., Burow, M., and Lyngs Jørgensen, H.J., et al. (2020). Heterologous microProtein expression identifies LITTLE NINJA, a dominant regulator of jasmonic acid signaling. Proceedings of the National Academy of Sciences *117*, 26197-26205. https://doi.org/10.1073/pnas.2005198117.

Ho-Xuan, H., Lehmann, G., Glazar, P., Gypas, F., Eichner, N., Heizler, K., Schlitt, H.J., Zavolan, M., Rajewsky, N., and Meister, G., et al. (2020). Gene Expression Signatures of a Preclinical Mouse Model during Colorectal Cancer Progression under Low-Dose Metronomic Chemotherapy. Cancers *13*. https://doi.org/10.3390/cancers13010049.

Huang, H., Chen, M., Feng, S., Lin, Z., and Liu, Y. (2025). The dual role of VDAC in cancer: Molecular mechanisms and advances in targeted therapy. Biomedicine & pharmacotherapy = Biomedecine & pharmacotherapie *191*, 118530. https://doi.org/10.1016/j.biopha.2025.118530.

Huang, J.-Z., Chen, M., de Chen, Gao, X.-C., Zhu, S., Huang, H., Hu, M., Zhu, H., and Yan, G.-R. (2017). A Peptide Encoded by a Putative lncRNA HOXB-AS3 Suppresses Colon Cancer Growth. Molecular cell *68*, 171-184.e6. https://doi.org/10.1016/j.molcel.2017.09.015.

Huang, N., Li, F., Zhang, M., Zhou, H., Chen, Z., Ma, X., Yang, L., Wu, X., Zhong, J., and Xiao, F., et al. (2021). An Upstream Open Reading Frame in Phosphatase and Tensin Homolog Encodes a Circuit Breaker of Lactate Metabolism. Cell metabolism *33*, 128-144.e9. https://doi.org/10.1016/j.cmet.2020.12.008.

Hurt, J.A., Robertson, A.D., and Burge, C.B. (2013). Global analyses of UPF1 binding and function reveal expanded scope of nonsense-mediated mRNA decay. Genome research *23*, 1636-1650. https://doi.org/10.1101/gr.157354.113.

Hüttemann, M., Helling, S., Sanderson, T.H., Sinkler, C., Samavati, L., Mahapatra, G., Varughese, A., Lu, G., Liu, J., and Ramzan, R., et al. (2012). Regulation of mitochondrial respiration and apoptosis through cell signaling: cytochrome c oxidase and cytochrome c in ischemia/reperfusion injury and inflammation. Biochimica et biophysica acta *1817*, 598-609. https://doi.org/10.1016/j.bbabio.2011.07.001.

Igor Dolgalev (2025). msigdbr: MSigDB Gene Sets for Multiple Organisms in a Tidy Data Format.

Ikonen, M., Liu, B., Hashimoto, Y., Ma, L., Lee, K.-W., Niikura, T., Nishimoto, I., and Cohen, P. (2003). Interaction between the Alzheimer's survival peptide humanin and insulin-like growth factor-binding protein 3 regulates cell survival and apoptosis. Proceedings of the National Academy of Sciences of the United States of America *100*, 13042-13047. https://doi.org/10.1073/pnas.2135111100.

Immarigeon, C., Frei, Y., Delbare, S.Y.N., Gligorov, D., Machado Almeida, P., Grey, J., Fabbro, L., Nagoshi, E., Billeter, J.-C., and Wolfner, M.F., et al. (2021). Identification of a micropeptide and multiple secondary cell genes that modulate Drosophila male reproductive success.

Proceedings of the National Academy of Sciences *118*. https://doi.org/10.1073/pnas.2001897118.

Ingolia, N.T., Brar, G.A., Rouskin, S., McGeachy, A.M., and Weissman, J.S. (2012). The ribosome profiling strategy for monitoring translation in vivo by deep sequencing of ribosome-protected mRNA fragments. Nature protocols *7*, 1534-1550. https://doi.org/10.1038/nprot.2012.086.

Ingolia, N.T., Ghaemmaghami, S., Newman, J.R.S., and Weissman, J.S. (2009). Genome-wide analysis in vivo of translation with nucleotide resolution using ribosome profiling. Science (New York, N.Y.) *324*, 218-223. https://doi.org/10.1126/science.1168978.

Ingolia, N.T., Lareau, L.F., and Weissman, J.S. (2011). Ribosome profiling of mouse embryonic stem cells reveals the complexity and dynamics of mammalian proteomes. Cell *147*, 789-802. https://doi.org/10.1016/j.cell.2011.10.002.

International Human Genome Sequencing Consortium (2004). Finishing the euchromatic sequence of the human genome. Nature *431*, 931-945. https://doi.org/10.1038/nature03001.

Jackson, R., Kroehling, L., Khitun, A., Bailis, W., Jarret, A., York, A.G., Khan, O.M., Brewer, J.R., Skadow, M.H., and Duizer, C., et al. (2018). The translation of non-canonical open reading frames controls mucosal immunity. Nature *564*, 434-438. https://doi.org/10.1038/s41586-018-0794-7.

Jeong, J.-Y., Yim, H.-S., Ryu, J.-Y., Lee, H.S., Lee, J.-H., Seen, D.-S., and Kang, S.G. (2012). One-step sequence- and ligation-independent cloning as a rapid and versatile cloning method for functional genomics studies. Applied and environmental microbiology *78*, 5440-5443. https://doi.org/10.1128/AEM.00844-12.

Ji, Z., Song, R., Regev, A., and Struhl, K. (2015). Many lncRNAs, 5'UTRs, and pseudogenes are translated and some are likely to express functional proteins. eLife *4*, e08890. https://doi.org/10.7554/eLife.08890.

Jiang, Y.-X., Shi, W.-J., Ma, D.-D., Zhang, J.-N., Ying, G.-G., Zhang, H., and Ong, C.-N. (2019). Male-biased zebrafish sex differentiation and metabolomics profile changes caused by dydrogesterone. Aquatic Toxicology *214*, 105242. https://doi.org/10.1016/j.aquatox.2019.105242.

John, G.B., Shang, Y., Li, L., Renken, C., Mannella, C.A., Selker, J.M.L., Rangell, L., Bennett, M.J., and Zha, J. (2005). The mitochondrial inner membrane protein mitofilin controls cristae morphology. Molecular biology of the cell *16*, 1543-1554. https://doi.org/10.1091/mbc.e04-08-0697.

Johnstone, T.G., Bazzini, A.A., and Giraldez, A.J. (2016). Upstream ORFs are prevalent translational repressors in vertebrates. The EMBO journal *35*, 706-723. https://doi.org/10.15252/embj.201592759.

Käll, L., Canterbury, J.D., Weston, J., Noble, W.S., and MacCoss, M.J. (2007). Semi-supervised learning for peptide identification from shotgun proteomics datasets. Nature methods *4*, 923-925. https://doi.org/10.1038/nmeth1113.

Kang, M., Tang, B., Li, J., Zhou, Z., Liu, K., Wang, R., Jiang, Z., Bi, F., Patrick, D., and Kim, D., et al. (2020). Identification of miPEP133 as a novel tumor-suppressor microprotein encoded by miR-34a pri-miRNA. Molecular cancer *19*, 143. https://doi.org/10.1186/s12943-020-01248-9.

Kassambara, A., Kosinski, M., and Biecek, P. (2016). CRAN: Contributed Packages.

Kastenmayer, J.P., Ni, L., Chu, A., Kitchen, L.E., Au, W.-C., Yang, H., Carter, C.D., Wheeler, D., Davis, R.W., and Boeke, J.D., et al. (2006). Functional genomics of genes with small open

reading frames (sORFs) in S. cerevisiae. Genome research *16*, 365-373. https://doi.org/10.1101/gr.4355406.

Keppler, A., Gendreizig, S., Gronemeyer, T., Pick, H., Vogel, H., and Johnsson, K. (2003). A general method for the covalent labeling of fusion proteins with small molecules in vivo. Nature Biotechnology *21*, 86-89. https://doi.org/10.1038/nbt765.

Khitun, A., and Slavoff, S.A. (2019). Proteomic Detection and Validation of Translated Small Open Reading Frames. Current protocols in chemical biology *11*, e77. https://doi.org/10.1002/cpch.77.

Khosravi, S., and Harner, M.E. (2020). The MICOS complex, a structural element of mitochondria with versatile functions. Biological chemistry *401*, 765-778. https://doi.org/10.1515/hsz-2020-0103.

Kienzle, L., Bettinazzi, S., Choquette, T., Brunet, M., Khorami, H.H., Jacques, J.-F., Moreau, M., Roucou, X., Landry, C.R., and Angers, A., et al. (2023). A small protein coded within the mitochondrial canonical gene nd4 regulates mitochondrial bioenergetics. BMC biology *21*, 111. https://doi.org/10.1186/s12915-023-01609-y.

Kim, S.-J., Guerrero, N., Wassef, G., Xiao, J., Mehta, H.H., Cohen, P., and Yen, K. (2016). The mitochondrial-derived peptide humanin activates the ERK1/2, AKT, and STAT3 signaling pathways and has age-dependent signaling differences in the hippocampus. Oncotarget *7*, 46899-46912. https://doi.org/10.18632/oncotarget.10380.

Koh, M., Ahmad, I., Ko, Y., Zhang, Y., Martinez, T.F., Diedrich, J.K., Chu, Q., Moresco, J.J., Erb, M.A., and Saghatelian, A., et al. (2021). A short ORF-encoded transcriptional regulator. Proceedings of the National Academy of Sciences *118*. https://doi.org/10.1073/pnas.2021943118.

Konina, D., Sparber, P., Viakhireva, I., Filatova, A., and Skoblov, M. (2021). Investigation of LINC00493/SMIM26 Gene Suggests Its Dual Functioning at mRNA and Protein Level. International journal of molecular sciences *22*. https://doi.org/10.3390/ijms22168477.

Kozak, M. (1987). An analysis of 5'-noncoding sequences from 699 vertebrate messenger RNAs. Nucleic acids research *15*, 8125-8148. https://doi.org/10.1093/nar/15.20.8125.

Kranias, E.G., and Hajjar, R.J. (2012). Modulation of cardiac contractility by the phospholamban/SERCA2a regulatome. Circulation research *110*, 1646-1660. https://doi.org/10.1161/CIRCRESAHA.111.259754.

Kuhn, T., Hettich, J., Davtyan, R., and Gebhardt, J.C.M. (2021). Single molecule tracking and analysis framework including theory-predicted parameter settings. Scientific reports *11*, 9465. https://doi.org/10.1038/s41598-021-88802-7.

Kumagai, H., Kim, S.-J., Miller, B., Zempo, H., Tanisawa, K., Natsume, T., Lee, S.H., Wan, J., Leelaprachakul, N., and Kumagai, M.E., et al. (2024). MOTS-c modulates skeletal muscle function by directly binding and activating CK2. iScience *27*, 111212. https://doi.org/10.1016/j.isci.2024.111212.

Kumagai, H., Miller, B., Kim, S.-J., Leelaprachakul, N., Kikuchi, N., Yen, K., and Cohen, P. (2023). Novel Insights into Mitochondrial DNA: Mitochondrial Microproteins and mtDNA Variants Modulate Athletic Performance and Age-Related Diseases. Genes *14*. https://doi.org/10.3390/genes14020286.

Kunji, E.R.S., King, M.S., Ruprecht, J.J., and Thangaratnarajah, C. (2020). The SLC25 Carrier Family: Important Transport Proteins in Mitochondrial Physiology and Pathology. Physiology (Bethesda, Md.) *35*, 302-327. https://doi.org/10.1152/physiol.00009.2020.

Lamb, Y.N. (2022). Pacritinib: First Approval. Drugs *82*, 831-838. https://doi.org/10.1007/s40265-022-01718-y.

Lambert, C.J., Freshner, B.C., Chung, A., Stevenson, T.J., Bowles, D.M., Samuel, R., Gale, B.K., and Bonkowsky, J.L. (2018). An automated system for rapid cellular extraction from live zebrafish embryos and larvae: Development and application to genotyping. PloS one *13*, e0193180. https://doi.org/10.1371/journal.pone.0193180.

Lander, E.S., Linton, L.M., Birren, B., Nusbaum, C., Zody, M.C., Baldwin, J., Devon, K., Dewar, K., Doyle, M., and FitzHugh, W., et al. (2001). Initial sequencing and analysis of the human genome. Nature *409*, 860-921. https://doi.org/10.1038/35057062.

Lauressergues, D., Couzigou, J.-M., Clemente, H.S., Martinez, Y., Dunand, C., Bécard, G., and Combier, J.-P. (2015). Primary transcripts of microRNAs encode regulatory peptides. Nature *520*, 90-93. https://doi.org/10.1038/nature14346.

Lauressergues, D., Ormancey, M., Guillotin, B., San Clemente, H., Camborde, L., Duboé, C., Tourneur, S., Charpentier, P., Barozet, A., and Jauneau, A., et al. (2022). Characterization of plant microRNA-encoded peptides (miPEPs) reveals molecular mechanisms from the translation to activity and specificity. Cell reports *38*, 110339. https://doi.org/10.1016/j.celrep.2022.110339.

Lazarou, M., Thorburn, D.R., Ryan, M.T., and McKenzie, M. (2009). Assembly of mitochondrial complex I and defects in disease. Biochimica et biophysica acta *1793*, 78-88. https://doi.org/10.1016/j.bbamcr.2008.04.015.

Lee, C., Zeng, J., Drew, B.G., Sallam, T., Martin-Montalvo, A., Wan, J., Kim, S.-J., Mehta, H., Hevener, A.L., and Cabo, R. de, et al. (2015). The mitochondrial-derived peptide MOTS-c promotes metabolic homeostasis and reduces obesity and insulin resistance. Cell metabolism *21*, 443-454. https://doi.org/10.1016/j.cmet.2015.02.009.

Lee, C.Q.E., Kerouanton, B., Chothani, S., Zhang, S., Chen, Y., Mantri, C.K., Hock, D.H., Lim, R., Nadkarni, R., and Huynh, V.T., et al. (2021). Coding and non-coding roles of MOCCI (C15ORF48) coordinate to regulate host inflammation and immunity. Nat Commun *12*, 2130. https://doi.org/10.1038/s41467-021-22397-5.

Lee, S., Liu, B., Lee, S., Huang, S.-X., Shen, B., and Qian, S.-B. (2012). Global mapping of translation initiation sites in mammalian cells at single-nucleotide resolution. Proceedings of the National Academy of Sciences of the United States of America *109*, E2424-32. https://doi.org/10.1073/pnas.1207846109.

Lees, J.A., Messa, M., Sun, E.W., Wheeler, H., Torta, F., Wenk, M.R., Camilli, P. de, and Reinisch, K.M. (2017). Lipid transport by TMEM24 at ER-plasma membrane contacts regulates pulsatile insulin secretion. Science (New York, N.Y.) *355*. https://doi.org/10.1126/science.aah6171.

Leng, F., Miu, Y.-Y., Zhang, Y., Luo, H., Lu, X.-L., Cheng, H., and Zheng, Z.-G. (2021). A micro-peptide encoded by HOXB-AS3 promotes the proliferation and viability of oral squamous cell carcinoma cell lines by directly binding with IGF2BP2 to stabilize c-Myc. Oncology letters *22*, 697. https://doi.org/10.3892/ol.2021.12958.

Li, M., Li, X., Zhang, Y., Wu, H., Zhou, H., Ding, X., Zhang, X., Jin, X., Wang, Y., and Yin, X., et al. (2020). Micropeptide MIAC Inhibits HNSCC Progression by Interacting with Aquaporin 2. Journal of the American Chemical Society *142*, 6708-6716. https://doi.org/10.1021/jacs.0c00706.

Li, M., Liu, G., Jin, X., Guo, H., Setrerrahmane, S., Xu, X., Li, T., Lin, Y., and Xu, H. (2022). Micropeptide MIAC inhibits the tumor progression by interacting with AQP2 and inhibiting EREG/EGFR signaling in renal cell carcinoma. Molecular cancer *21*, 181. https://doi.org/10.1186/s12943-022-01654-1.

Li, X., Yang, L., and Chen, L.-L. (2018). The Biogenesis, Functions, and Challenges of Circular RNAs. Molecular cell *71*, 428-442. https://doi.org/10.1016/j.molcel.2018.06.034.

Liang, C., Zhang, S., Robinson, D., Ploeg, M.V., Wilson, R., Nah, J., Taylor, D., Beh, S., Lim, R., and Sun, L., et al. (2022). Mitochondrial microproteins link metabolic cues to respiratory chain biogenesis. Cell reports *40*, 111204. https://doi.org/10.1016/j.celrep.2022.111204.

Lin, M.F., Jungreis, I., and Kellis, M. (2011). PhyloCSF: a comparative genomics method to distinguish protein coding and non-coding regions. Bioinformatics (Oxford, England) *27*, i275-82. https://doi.org/10.1093/bioinformatics/btr209.

Linden, A., Deckers, M., Parfentev, I., Pflanz, R., Homberg, B., Neumann, P., Ficner, R., Rehling, P., and Urlaub, H. (2020). A Cross-linking Mass Spectrometry Approach Defines Protein Interactions in Yeast Mitochondria. Molecular & cellular proteomics : MCP *19*, 1161-1178. https://doi.org/10.1074/mcp.RA120.002028.

Lloyd, C.R., Park, S., Fei, J., and Vanderpool, C.K. (2017). The Small Protein SgrT Controls Transport Activity of the Glucose-Specific Phosphotransferase System. Journal of bacteriology *199*. https://doi.org/10.1128/JB.00869-16.

Los, G.V., Encell, L.P., McDougall, M.G., Hartzell, D.D., Karassina, N., Zimprich, C., Wood, M.G., Learish, R., Ohana, R.F., and Urh, M., et al. (2008). HaloTag: a novel protein labeling technology for cell imaging and protein analysis. ACS chemical biology *3*, 373-382. https://doi.org/10.1021/cb800025k.

Losko, M., Kotlinowski, J., and Jura, J. (2016). Long Noncoding RNAs in Metabolic Syndrome Related Disorders. Mediators of inflammation *2016*, 5365209. https://doi.org/10.1155/2016/5365209.

Love, M.I., Huber, W., and Anders, S. (2014). Moderated estimation of fold change and dispersion for RNA-seq data with DESeq2. Genome biology *15*, 550. https://doi.org/10.1186/s13059-014-0550-8.

Low, T.Y., van Heesch, S., van den Toorn, H., Giansanti, P., Cristobal, A., Toonen, P., Schafer, S., Hübner, N., van Breukelen, B., and Mohammed, S., et al. (2013). Quantitative and qualitative proteome characteristics extracted from in-depth integrated genomics and proteomics analysis. Cell reports *5*, 1469-1478. https://doi.org/10.1016/j.celrep.2013.10.041.

Lu, H., Wei, M., Zhai, Y., Li, Q., Ye, Z., Wang, L., Luo, W., Chen, J., and Lu, Z. (2019). MOTS-c peptide regulates adipose homeostasis to prevent ovariectomy-induced metabolic dysfunction. Journal of molecular medicine (Berlin, Germany) *97*, 473-485. https://doi.org/10.1007/s00109-018-01738-w.

Luengo, A., Li, Z., Gui, D.Y., Sullivan, L.B., Zagorulya, M., Do, B.T., Ferreira, R., Naamati, A., Ali, A., and Lewis, C.A., et al. (2021). Increased demand for NAD+ relative to ATP drives aerobic glycolysis. Molecular cell *81*, 691-707.e6. https://doi.org/10.1016/j.molcel.2020.12.012.

Ma, J., Diedrich, J.K., Jungreis, I., Donaldson, C., Vaughan, J., Kellis, M., Yates, J.R., and Saghatelian, A. (2016). Improved Identification and Analysis of Small Open Reading Frame Encoded Polypeptides. Analytical chemistry *88*, 3967-3975. https://doi.org/10.1021/acs.analchem.6b00191.

MacLean, B., Tomazela, D.M., Shulman, N., Chambers, M., Finney, G.L., Frewen, B., Kern, R., Tabb, D.L., Liebler, D.C., and MacCoss, M.J. (2010). Skyline: an open source document editor for creating and analyzing targeted proteomics experiments. Bioinformatics (Oxford, England) *26*, 966-968. https://doi.org/10.1093/bioinformatics/btq054.

MacLennan, D.H., and Kranias, E.G. (2003). Phospholamban: a crucial regulator of cardiac contractility. Nature reviews. Molecular cell biology *4*, 566-577. https://doi.org/10.1038/nrm1151.

Makarewich, C.A., Baskin, K.K., Munir, A.Z., Bezprozvannaya, S., Sharma, G., Khemtong, C., Shah, A.M., McAnally, J.R., Malloy, C.R., and Szweda, L.I., et al. (2018a). MOXI Is a

Mitochondrial Micropeptide That Enhances Fatty Acid β-Oxidation. Cell reports *23*, 3701-3709. https://doi.org/10.1016/j.celrep.2018.05.058.

Makarewich, C.A., Munir, A.Z., Bezprozvannaya, S., Gibson, A.M., Young Kim, S., Martin-Sandoval, M.S., Mathews, T.P., Szweda, L.I., Bassel-Duby, R., and Olson, E.N. (2022). The cardiac-enriched microprotein mitolamban regulates mitochondrial respiratory complex assembly and function in mice. Proceedings of the National Academy of Sciences *119*. https://doi.org/10.1073/pnas.2120476119.

Makarewich, C.A., Munir, A.Z., Schiattarella, G.G., Bezprozvannaya, S., Raguimova, O.N., Cho, E.E., Vidal, A.H., Robia, S.L., Bassel-Duby, R., and Olson, E.N. (2018b). The DWORF micropeptide enhances contractility and prevents heart failure in a mouse model of dilated cardiomyopathy. eLife *7*. https://doi.org/10.7554/eLife.38319.

Marc Carlson (2017). org.Hs.eg.db (Bioconductor).

Martinez, T.F., Chu, Q., Donaldson, C., Tan, D., Shokhirev, M.N., and Saghatelian, A. (2020). Accurate annotation of human protein-coding small open reading frames. Nature chemical biology *16*, 458-468. https://doi.org/10.1038/s41589-019-0425-0.

Martinez, T.F., Lyons-Abbott, S., Bookout, A.L., Souza, E.V. de, Donaldson, C., Vaughan, J.M., Lau, C., Abramov, A., Baquero, A.F., and Baquero, K., et al. (2023). Profiling mouse brown and white adipocytes to identify metabolically relevant small ORFs and functional microproteins. Cell metabolism *35*, 166-183.e11. https://doi.org/10.1016/j.cmet.2022.12.004.

Matsumoto, A., Clohessy, J.G., and Pandolfi, P.P. (2017). SPAR, a lncRNA encoded mTORC1 inhibitor. Cell cycle (Georgetown, Tex.) *16*, 815-816. https://doi.org/10.1080/15384101.2017.1304735.

Mavuduru, V.A., Vadupu, L., Ghosh, K.K., Chakrabortty, S., Gulyás, B., Padmanabhan, P., and Ball, W.B. (2024). Mitochondrial phospholipid transport: Role of contact sites and lipid transport proteins. Progress in lipid research *94*, 101268. https://doi.org/10.1016/j.plipres.2024.101268.

McCormack, A.L., Schieltz, D.M., Goode, B., Yang, S., Barnes, G., Drubin, D., and Yates, J.R. (1997). Direct analysis and identification of proteins in mixtures by LC/MS/MS and database searching at the low-femtomole level. Analytical chemistry *69*, 767-776. https://doi.org/10.1021/ac960799q.

McLysaght, A., and Hurst, L.D. (2016). Open questions in the study of de novo genes: what, how and why. Nature reviews. Genetics *17*, 567-578. https://doi.org/10.1038/nrg.2016.78.

Meister, G., Landthaler, M., Patkaniowska, A., Dorsett, Y., Teng, G., and Tuschl, T. (2004). Human Argonaute2 mediates RNA cleavage targeted by miRNAs and siRNAs. Molecular cell *15*, 185-197. https://doi.org/10.1016/j.molcel.2004.07.007.

Meng, K., Lu, S., Li, Y.-Y., Hu, L.-L., Zhang, J., Cao, Y., Wang, Y., Zhang, C.Z., and He, Q.-Y. (2023). LINC00493-encoded microprotein SMIM26 exerts anti-metastatic activity in renal cell carcinoma. EMBO reports *24*, e56282. https://doi.org/10.15252/embr.202256282.

Mercer, T.R., Neph, S., Dinger, M.E., Crawford, J., Smith, M.A., Shearwood, A.-M.J., Haugen, E., Bracken, C.P., Rackham, O., and Stamatoyannopoulos, J.A., et al. (2011). The human mitochondrial transcriptome. Cell *146*, 645-658. https://doi.org/10.1016/j.cell.2011.06.051.

Mick, D.U., Dennerlein, S., Wiese, H., Reinhold, R., Pacheu-Grau, D., Lorenzi, I., Sasarman, F., Weraarpachai, W., Shoubridge, E.A., and Warscheid, B., et al. (2012). MITRAC links mitochondrial protein translocation to respiratory-chain assembly and translational regulation. Cell *151*, 1528-1541. https://doi.org/10.1016/j.cell.2012.11.053.

Miller, B., Kim, S.-J., Mehta, H.H., Cao, K., Kumagai, H., Thumaty, N., Leelaprachakul, N., Braniff, R.G., Jiao, H., and Vaughan, J., et al. (2023). Mitochondrial DNA variation in Alzheimer's disease reveals a unique microprotein called SHMOOSE. Mol Psychiatry *28*, 1813-1826. https://doi.org/10.1038/s41380-022-01769-3.

Min, K.-W., Davila, S., Zealy, R.W., Lloyd, L.T., Lee, I.Y., Lee, R., Roh, K.H., Jung, A., Jemielity, J., and Choi, E.-J., et al. (2017). eIF4E phosphorylation by MST1 reduces translation of a subset of mRNAs, but increases lncRNA translation. Biochimica et biophysica acta. Gene regulatory mechanisms *1860*, 761-772. https://doi.org/10.1016/j.bbagrm.2017.05.002.

Mise, S., Matsumoto, A., Shimada, K., Hosaka, T., Takahashi, M., Ichihara, K., Shimizu, H., Shiraishi, C., Saito, D., and Suyama, M., et al. (2022). Kastor and Polluks polypeptides encoded by a single gene locus cooperatively regulate VDAC and spermatogenesis. Nat Commun *13*, 1071. https://doi.org/10.1038/s41467-022-28677-y.

Miura, K. (2020). Bleach correction ImageJ plugin for compensating the photobleaching of time-lapse sequences. F1000Research *9*, 1494. https://doi.org/10.12688/f1000research.27171.1.

Montigny, A., Tavormina, P., Duboe, C., San Clémente, H., Aguilar, M., Valenti, P., Lauressergues, D., Combier, J.-P., and Plaza, S. (2021). Drosophila primary microRNA-8 encodes a microRNA-encoded peptide acting in parallel of miR-8. Genome biology *22*, 118. https://doi.org/10.1186/s13059-021-02345-8.

Morales, E.D., Yue, Y., Watkins, T.B., Han, J., Pan, X., Gibson, A.M., Hu, B., Brito-Estrada, O., Yao, G., and Makarewich, C.A., et al. (2023). Dwarf Open Reading Frame (DWORF) Gene Therapy Ameliorated Duchenne Muscular Dystrophy Cardiomyopathy in Aged mdx Mice. JAHA *12*, e027480. https://doi.org/10.1161/JAHA.122.027480.

Mortensen, K.I., Churchman, L.S., Spudich, J.A., and Flyvbjerg, H. (2010). Optimized localization analysis for single-molecule tracking and super-resolution microscopy. Nature methods *7*, 377-381. https://doi.org/10.1038/nmeth.1447.

Moura, J.P., Oliveira, P.J., and Urbano, A.M. (2025). Mitochondria: An overview of their origin, genome, architecture, and dynamics. Biochimica et biophysica acta. Molecular basis of disease *1871*, 167803. https://doi.org/10.1016/j.bbadis.2025.167803.

Mudge, J.M., Ruiz-Orera, J., Prensner, J.R., Brunet, M.A., Calvet, F., Jungreis, I., Gonzalez, J.J., Magrane, M., Martinez, T.F., and Schulz, J., et al. (2022). Standardized annotation of translated open reading frames. Nature Biotechnology. https://doi.org/10.1038/s41587-022-01369-0.

Muzumdar, R.H., Huffman, D.M., Atzmon, G., Buettner, C., Cobb, L.J., Fishman, S., Budagov, T., Cui, L., Einstein, F.H., and Poduval, A., et al. (2009). Humanin: a novel central regulator of peripheral insulin action. PloS one *4*, e6334. https://doi.org/10.1371/journal.pone.0006334.

Na, Z., Dai, X., Zheng, S.-J., Bryant, C.J., Loh, K.H., Su, H., Luo, Y., Buhagiar, A.F., Cao, X., and Baserga, S.J., et al. (2022). Mapping subcellular localizations of unannotated microproteins and alternative proteins with MicroID. Molecular cell *82*, 2900-2911.e7. https://doi.org/10.1016/j.molcel.2022.06.035.

Na, Z., Luo, Y., Cui, D.S., Khitun, A., Smelyansky, S., Loria, J.P., and Slavoff, S.A. (2021). Phosphorylation of a Human Microprotein Promotes Dissociation of Biomolecular Condensates. Journal of the American Chemical Society *143*, 12675-12687. https://doi.org/10.1021/jacs.1c05386.

Na, Z., Luo, Y., Schofield, J.A., Smelyansky, S., Khitun, A., Muthukumar, S., Valkov, E., Simon, M.D., and Slavoff, S.A. (2020). The NBDY Microprotein Regulates Cellular RNA Decapping. Biochemistry *59*, 4131-4142. https://doi.org/10.1021/acs.biochem.0c00672.

Nah, J., Mahendran, S., Kerouanton, B., Cui, L., Hock, D.H., Cabrera-Orefice, A., Dunlap, K., Robinson, D., Tung, D.W.H., and Leong, S.H., et al. (2025). Microprotein SMIM26 drives oxidative metabolism via serine-responsive mitochondrial translation. Molecular cell *85*, 2759-2775.e12. https://doi.org/10.1016/j.molcel.2025.05.033.

Nelson, B.R., Makarewich, C.A., Anderson, D.M., Winders, B.R., Troupes, C.D., Wu, F., Reese, A.L., McAnally, J.R., Chen, X., and Kavalali, E.T., et al. (2016). A peptide encoded by a transcript annotated as long noncoding RNA enhances SERCA activity in muscle. Science (New York, N.Y.) *351*, 271-275. https://doi.org/10.1126/science.aad4076.

Neville, M.D.C., Kohze, R., Erady, C., Meena, N., Hayden, M., Cooper, D.N., Mort, M., and Prabakaran, S. (2021). A platform for curated products from novel open reading frames prompts reinterpretation of disease variants. Genome research *31*, 327-336. https://doi.org/10.1101/gr.263202.120.

Niu, L., Lou, F., Sun, Y., Sun, L., Cai, X., Liu, Z., Zhou, H., Wang, H., Wang, Z., and Bai, J., et al. (2020). A micropeptide encoded by lncRNA MIR155HG suppresses autoimmune inflammation via modulating antigen presentation. Science advances *6*, eaaz2059. https://doi.org/10.1126/sciadv.aaz2059.

Noskov, S.Y., Rostovtseva, T.K., and Bezrukov, S.M. (2013). ATP Transport through VDAC and the VDAC–Tubulin Complex Probed by Equilibrium and Nonequilibrium MD Simulations. Biochemistry *52*, 9246-9256. https://doi.org/10.1021/bi4011495.

Odermatt, A., Becker, S., Khanna, V.K., Kurzydlowski, K., Leisner, E., Pette, D., and MacLennan, D.H. (1998). Sarcolipin regulates the activity of SERCA1, the fast-twitch skeletal muscle sarcoplasmic reticulum Ca2+-ATPase. The Journal of biological chemistry *273*, 12360-12369. https://doi.org/10.1074/jbc.273.20.12360.

Okazaki, Y., Furuno, M., Kasukawa, T., Adachi, J., Bono, H., Kondo, S., Nikaido, I., Osato, N., Saito, R., and Suzuki, H., et al. (2002). Analysis of the mouse transcriptome based on functional annotation of 60,770 full-length cDNAs. Nature *420*, 563-573. https://doi.org/10.1038/nature01266.

Olexiouk, V., Crappé, J., Verbruggen, S., Verhegen, K., Martens, L., and Menschaert, G. (2016). sORFs.org: a repository of small ORFs identified by ribosome profiling. Nucleic acids research *44*, D324-9. https://doi.org/10.1093/nar/gkv1175.

Olexiouk, V., van Criekinge, W., and Menschaert, G. (2018). An update on sORFs.org: a repository of small ORFs identified by ribosome profiling. Nucleic acids research *46*, D497-D502. https://doi.org/10.1093/nar/gkx1130.

Osellame, L.D., Blacker, T.S., and Duchen, M.R. (2012). Cellular and molecular mechanisms of mitochondrial function. Best practice & research. Clinical endocrinology & metabolism *26*, 711-723. https://doi.org/10.1016/j.beem.2012.05.003.

Ouspenskaia, T., Law, T., Clauser, K.R., Klaeger, S., Sarkizova, S., Aguet, F., Li, B., Christian, E., Knisbacher, B.A., and Le, P.M., et al. (2022). Unannotated proteins expand the MHC-I-restricted immunopeptidome in cancer. Nature Biotechnology *40*, 209-217. https://doi.org/10.1038/s41587-021-01021-3.

Oyama, M., Itagaki, C., Hata, H., Suzuki, Y., Izumi, T., Natsume, T., Isobe, T., and Sugano, S. (2004). Analysis of small human proteins reveals the translation of upstream open reading frames of mRNAs. Genome research *14*, 2048-2052. https://doi.org/10.1101/gr.2384604.

Oyama, M., Kozuka-Hata, H., Suzuki, Y., Semba, K., Yamamoto, T., and Sugano, S. (2007). Diversity of translation start sites may define increased complexity of the human short ORFeome. Molecular & cellular proteomics : MCP *6*, 1000-1006. https://doi.org/10.1074/mcp.M600297-MCP200.

Palme, J., Hochreiter, S., and Bodenhofer, U. (2015). KeBABS: an R package for kernel-based analysis of biological sequences. Bioinformatics (Oxford, England) *31*, 2574-2576. https://doi.org/10.1093/bioinformatics/btv176.

Pang, Y., Liu, Z., Han, H., Wang, B., Li, W., Mao, C., and Liu, S. (2020). Peptide SMIM30 promotes HCC development by inducing SRC/YES1 membrane anchoring and MAPK pathway activation. Journal of hepatology *73*, 1155-1169. https://doi.org/10.1016/j.jhep.2020.05.028.

Peterson, A.C., Russell, J.D., Bailey, D.J., Westphall, M.S., and Coon, J.J. (2012). Parallel reaction monitoring for high resolution and high mass accuracy quantitative, targeted proteomics. Molecular & cellular proteomics : MCP *11*, 1475-1488. https://doi.org/10.1074/mcp.O112.020131.

Polycarpou-Schwarz, M., Groß, M., Mestdagh, P., Schott, J., Grund, S.E., Hildenbrand, C., Rom, J., Aulmann, S., Sinn, H.-P., and Vandesompele, J., et al. (2018). The cancer-associated microprotein CASIMO1 controls cell proliferation and interacts with squalene epoxidase modulating lipid droplet formation. Oncogene *37*, 4750-4768. https://doi.org/10.1038/s41388-018-0281-5.

Prel, A., Dozier, C., Combier, J.-P., Plaza, S., and Besson, A. (2021). Evidence That Regulation of Pri-miRNA/miRNA Expression Is Not a General Rule of miPEPs Function in Humans. International journal of molecular sciences *22*. https://doi.org/10.3390/ijms22073432.

Qi, Y., Rajbanshi, B., Hao, R., Dang, Y., Xu, C., Lu, W., Dai, L., Zhang, B., and Zhang, X. (2025). The dual role of PGAM5 in inflammation. Experimental & molecular medicine *57*, 298-311. https://doi.org/10.1038/s12276-025-01391-7.

Ran, F.A., Hsu, P.D., Wright, J., Agarwala, V., Scott, D.A., and Zhang, F. (2013). Genome engineering using the CRISPR-Cas9 system. Nature protocols *8*, 2281-2308. https://doi.org/10.1038/nprot.2013.143.

Rath, S., Sharma, R., Gupta, R., Ast, T., Chan, C., Durham, T.J., Goodman, R.P., Grabarek, Z., Haas, M.E., and Hung, W.H.W., et al. (2021). MitoCarta3.0: an updated mitochondrial proteome now with sub-organelle localization and pathway annotations. Nucleic Acids Res *49*, D1541-D1547. https://doi.org/10.1093/nar/gkaa1011.

Rathore, A., Chu, Q., Tan, D., Martinez, T.F., Donaldson, C.J., Diedrich, J.K., Yates, J.R., III, and Saghatelian, A. (2018). MIEF1 Microprotein Regulates Mitochondrial Translation. Biochemistry *57*, 5564-5575. https://doi.org/10.1021/acs.biochem.8b00726.

Reers, M., Smith, T.W., and Chen, L.B. (1991). J-aggregate formation of a carbocyanine as a quantitative fluorescent indicator of membrane potential. Biochemistry *30*, 4480-4486. https://doi.org/10.1021/bi00232a015.

Reisser, M., Palmer, A., Popp, A.P., Jahn, C., Weidinger, G., and Gebhardt, J.C.M. (2018). Single-molecule imaging correlates decreasing nuclear volume with increasing TF-chromatin associations during zebrafish development. Nat Commun *9*, 5218. https://doi.org/10.1038/s41467-018-07731-8.

Rocha, A.L., Pai, V., Perkins, G., Chang, T., Ma, J., Souza, E.V. de, Chu, Q., Vaughan, J.M., Diedrich, J.K., and Ellisman, M.H., et al. (2024). An Inner Mitochondrial Membrane Microprotein from the SLC35A4 Upstream ORF Regulates Cellular Metabolism. Journal of Molecular Biology *436*, 168559. https://doi.org/10.1016/j.jmb.2024.168559.

Rosenberger, F.A., Moore, D., Atanassov, I., Moedas, M.F., Clemente, P., Végvári, Á., Fissi, N.E., Filograna, R., Bucher, A.-L., and Hinze, Y., et al. (2021). The one-carbon pool controls mitochondrial energy metabolism via complex I and iron-sulfur clusters. Science advances *7*. https://doi.org/10.1126/sciadv.abf0717.

Ruiz-Orera, J., and Albà, M.M. (2019). Translation of Small Open Reading Frames: Roles in Regulation and Evolutionary Innovation. Trends in Genetics *35*, 186-198. https://doi.org/10.1016/j.tig.2018.12.003.

Ruiz-Orera, J., Verdaguer-Grau, P., Villanueva-Cañas, J.L., Messeguer, X., and Albà, M.M. (2018). Translation of neutrally evolving peptides provides a basis for de novo gene evolution. Nat Ecol Evol *2*, 890-896. https://doi.org/10.1038/s41559-018-0506-6.

Ruprecht, J.J., and Kunji, E.R. (2020). The SLC25 Mitochondrial Carrier Family: Structure and Mechanism. Trends in Biochemical Sciences *45*, 244-258. https://doi.org/10.1016/j.tibs.2019.11.001.

Samandi, S., Roy, A.V., Delcourt, V., Lucier, J.-F., Gagnon, J., Beaudoin, M.C., Vanderperre, B., Breton, M.-A., Motard, J., and Jacques, J.-F., et al. (2017). Deep transcriptome annotation enables the discovery and functional characterization of cryptic small proteins. eLife *6*. https://doi.org/10.7554/eLife.27860.

Schindelin, J., Arganda-Carreras, I., Frise, E., Kaynig, V., Longair, M., Pietzsch, T., Preibisch, S., Rueden, C., Saalfeld, S., and Schmid, B., et al. (2012). Fiji: an open-source platform for biological-image analysis. Nature methods *9*, 676-682. https://doi.org/10.1038/nmeth.2019.

Schliep, K.P. (2011). phangorn: phylogenetic analysis in R. Bioinformatics (Oxford, England) *27*, 592-593. https://doi.org/10.1093/bioinformatics/btq706.

Sekine, S., Yao, A., Hattori, K., Sugawara, S., Naguro, I., Koike, M., Uchiyama, Y., Takeda, K., and Ichijo, H. (2016). The Ablation of Mitochondrial Protein Phosphatase Pgam5 Confers Resistance Against Metabolic Stress. eBioMedicine *5*, 82-92. https://doi.org/10.1016/j.ebiom.2016.01.031.

Sharma, A., Badola, P.K., Bhatia, C., Sharma, D., and Trivedi, P.K. (2020). Primary transcript of miR858 encodes regulatory peptide and controls flavonoid biosynthesis and development in Arabidopsis. Nature plants *6*, 1262-1274. https://doi.org/10.1038/s41477-020-00769-x.

Sharma, L.K., Lu, J., and Bai, Y. (2009). Mitochondrial respiratory complex I: structure, function and implication in human diseases. Current medicinal chemistry *16*, 1266-1277. https://doi.org/10.2174/092986709787846578.

Shi, T.-T., Huang, Y., Li, Y., Dai, X.-L., He, Y.-H., Ding, J.-C., Ran, T., Shi, Y., Yuan, Q., and Li, W.-J., et al. (2023). MAVI1, an endoplasmic reticulum-localized microprotein, suppresses antiviral innate immune response by targeting MAVS on mitochondrion. Science advances *9*, eadg7053. https://doi.org/10.1126/sciadv.adg7053.

Shoshan-Barmatz, V., Shteinfer-Kuzmine, A., and Verma, A. (2020). VDAC1 at the Intersection of Cell Metabolism, Apoptosis, and Diseases. Biomolecules *10*. https://doi.org/10.3390/biom10111485.

Simon, F., Tinevez, J.-Y., and van Teeffelen, S. (2023). ExTrack characterizes transition kinetics and diffusion in noisy single-particle tracks. The Journal of cell biology *222*. https://doi.org/10.1083/jcb.202208059.

Slavoff, S.A., Heo, J., Budnik, B.A., Hanakahi, L.A., and Saghatelian, A. (2014). A human short open reading frame (sORF)-encoded polypeptide that stimulates DNA end joining. The Journal of biological chemistry *289*, 10950-10957. https://doi.org/10.1074/jbc.C113.533968.

Slavoff, S.A., Mitchell, A.J., Schwaid, A.G., Cabili, M.N., Ma, J., Levin, J.Z., Karger, A.D., Budnik, B.A., Rinn, J.L., and Saghatelian, A. (2013). Peptidomic discovery of short open reading frame-encoded peptides in human cells. Nature chemical biology *9*, 59-64. https://doi.org/10.1038/nchembio.1120.

Sousa, C., Johansson, C., Charon, C., Manyani, H., Sautter, C., Kondorosi, A., and Crespi, M. (2001). Translational and structural requirements of the early nodulin gene enod40, a short-open reading frame-containing RNA, for elicitation of a cell-specific growth response in the alfalfa root cortex. Molecular and cellular biology *21*, 354-366. https://doi.org/10.1128/MCB.21.1.354-366.2001.

Spinelli, J.B., and Haigis, M.C. (2018). The multifaceted contributions of mitochondria to cellular metabolism. Nature cell biology *20*, 745-754. https://doi.org/10.1038/s41556-018-0124-1.

Stadtfeld, M., Maherali, N., Breault, D.T., and Hochedlinger, K. (2008). Defining molecular cornerstones during fibroblast to iPS cell reprogramming in mouse. Cell stem cell *2*, 230-240. https://doi.org/10.1016/j.stem.2008.02.001.

Staudt, A.-C., and Wenkel, S. (2011). Regulation of protein function by 'microProteins'. EMBO reports *12*, 35-42. https://doi.org/10.1038/embor.2010.196.

Stefani, D. de, Patron, M., and Rizzuto, R. (2015). Structure and function of the mitochondrial calcium uniporter complex. Biochimica et biophysica acta *1853*, 2006-2011. https://doi.org/10.1016/j.bbamcr.2015.04.008.

Stein, C.S., Jadiya, P., Zhang, X., McLendon, J.M., Abouassaly, G.M., Witmer, N.H., Anderson, E.J., Elrod, J.W., and Boudreau, R.L. (2018). Mitoregulin: A lncRNA-Encoded Microprotein that Supports Mitochondrial Supercomplexes and Respiratory Efficiency. Cell reports *23*, 3710-3720.e8. https://doi.org/10.1016/j.celrep.2018.06.002.

Storz, G., Wolf, Y.I., and Ramamurthi, K.S. (2014). Small proteins can no longer be ignored. Annual review of biochemistry *83*, 753-777. https://doi.org/10.1146/annurev-biochem-070611-102400.

Su, H., Katz, S.G., and Slavoff, S.A. (2025). Nested small open reading frames are translated from alternative transcripts. bioRxiv : the preprint server for biology. https://doi.org/10.1101/2024.10.22.619581.

Sun, L., Wang, W., Han, C., Huang, W., Sun, Y., Fang, K., Zeng, Z., Yang, Q., Pan, Q., and Chen, T., et al. (2021). The oncomicropeptide APPLE promotes hematopoietic malignancy by enhancing translation initiation. Molecular cell *81*, 4493-4508.e9. https://doi.org/10.1016/j.molcel.2021.08.033.

Suomalainen, A., and Nunnari, J. (2024). Mitochondria at the crossroads of health and disease. Cell *187*, 2601-2627. https://doi.org/10.1016/j.cell.2024.04.037.

Szafron, L.M., Balcerak, A., Grzybowska, E.A., Pienkowska-Grela, B., Felisiak-Golabek, A., Podgorska, A., Kulesza, M., Nowak, N., Pomorski, P., and Wysocki, J., et al. (2015). The Novel Gene CRNDE Encodes a Nuclear Peptide (CRNDEP) Which Is Overexpressed in Highly Proliferating Tissues. PloS one *10*, e0127475. https://doi.org/10.1371/journal.pone.0127475.

Szczepanowska, K., Senft, K., Heidler, J., Herholz, M., Kukat, A., Höhne, M.N., Hofsetz, E., Becker, C., Kaspar, S., and Giese, H., et al. (2020). A salvage pathway maintains highly functional respiratory complex I. Nat Commun *11*, 1643. https://doi.org/10.1038/s41467-020-15467-7.

Tang, Z., Kang, B., Li, C., Chen, T., and Zhang, Z. (2019). GEPIA2: an enhanced web server for large-scale expression profiling and interactive analysis. Nucleic Acids Res *47*, W556-W560. https://doi.org/10.1093/nar/gkz430.

Taus, T., Köcher, T., Pichler, P., Paschke, C., Schmidt, A., Henrich, C., and Mechtler, K. (2011). Universal and confident phosphorylation site localization using phosphoRS. Journal of proteome research *10*, 5354-5362. https://doi.org/10.1021/pr200611n.

Temperley, R.J., Wydro, M., Lightowlers, R.N., and Chrzanowska-Lightowlers, Z.M. (2010). Human mitochondrial mRNAs--like members of all families, similar but different. Biochimica et biophysica acta *1797*, 1081-1085. https://doi.org/10.1016/j.bbabio.2010.02.036.

Terry M Therneau (2024). A Package for Survival Analysis in R.

Therneau, T.M. (2001). CRAN: Contributed Packages.

Thiele, C., and Hirschfeld, G. (2021). cutpointr : Improved Estimation and Validation of Optimal Cutpoints in R. J. Stat. Soft. *98*, 1-27. https://doi.org/10.18637/jss.v098.i11.

Tsiatsiani, L., and Heck, A.J.R. (2015). Proteomics beyond trypsin. The FEBS Journal *282*, 2612-2626. https://doi.org/10.1111/febs.13287.

Tupy, J.L., Bailey, A.M., Dailey, G., Evans-Holm, M., Siebel, C.W., Misra, S., Celniker, S.E., and Rubin, G.M. (2005). Identification of putative noncoding polyadenylated transcripts in Drosophila melanogaster. Proceedings of the National Academy of Sciences of the United States of America *102*, 5495-5500. https://doi.org/10.1073/pnas.0501422102.

Vallée, A., Lecarpentier, Y., and Vallée, J.-N. (2021). The Key Role of the WNT/β-Catenin Pathway in Metabolic Reprogramming in Cancers under Normoxic Conditions. Cancers *13*. https://doi.org/10.3390/cancers13215557.

van Heesch, S., Witte, F., Schneider-Lunitz, V., Schulz, J.F., Adami, E., Faber, A., Kirchner, M., Maatz, H., Blachut, S., and Sandmann, C.-L., et al. (2019). The Translational Landscape of the Human Heart. Cell. https://doi.org/10.1016/j.cell.2019.05.010.

van Vranken, J.G., Bricker, D.K., Dephoure, N., Gygi, S.P., Cox, J.E., Thummel, C.S., and Rutter, J. (2014). SDHAF4 promotes mitochondrial succinate dehydrogenase activity and prevents neurodegeneration. Cell metabolism *20*, 241-252. https://doi.org/10.1016/j.cmet.2014.05.012.

Vanderperre, B., Lucier, J.-F., Bissonnette, C., Motard, J., Tremblay, G., Vanderperre, S., Wisztorski, M., Salzet, M., Boisvert, F.-M., and Roucou, X. (2013). Direct detection of alternative open reading frames translation products in human significantly expands the proteome. PloS one *8*, e70698. https://doi.org/10.1371/journal.pone.0070698.

Vanderpool, C.K., and Gottesman, S. (2004). Involvement of a novel transcriptional activator and small RNA in post-transcriptional regulation of the glucose phosphoenolpyruvate phosphotransferase system. Molecular microbiology *54*, 1076-1089. https://doi.org/10.1111/j.1365-2958.2004.04348.x.

Vasan, K., Werner, M., and Chandel, N.S. (2020). Mitochondrial Metabolism as a Target for Cancer Therapy. Cell metabolism *32*, 341-352. https://doi.org/10.1016/j.cmet.2020.06.019.

Vattem, K.M., and Wek, R.C. (2004). Reinitiation involving upstream ORFs regulates ATF4 mRNA translation in mammalian cells. Proceedings of the National Academy of Sciences of the United States of America *101*, 11269-11274. https://doi.org/10.1073/pnas.0400541101.

Wadler, C.S., and Vanderpool, C.K. (2007). A dual function for a bacterial small RNA: SgrS performs base pairing-dependent regulation and encodes a functional polypeptide. Proceedings of the National Academy of Sciences of the United States of America *104*, 20454-20459. https://doi.org/10.1073/pnas.0708102104.

Wang, J., Zhang, X.-Q., Ahlers, B.A., Carl, L.L., Song, J., Rothblum, L.I., Stahl, R.C., Carey, D.J., and Cheung, J.Y. (2006). Cytoplasmic Tail of Phospholemman Interacts with the Intracellular Loop of the Cardiac Na+/Ca2+ Exchanger. Journal of Biological Chemistry *281*, 32004-32014. https://doi.org/10.1016/S0021-9258(19)84114-5.

Wang, S.-F., Tseng, L.-M., and Lee, H.-C. (2023). Role of mitochondrial alterations in human cancer progression and cancer immunity. Journal of biomedical science *30*, 61. https://doi.org/10.1186/s12929-023-00956-w.

Wang, Y., Wu, S., Zhu, X., Zhang, L., Deng, J., Li, F., Guo, B., Zhang, S., Wu, R., and Zhang, Z., et al. (2020). LncRNA-encoded polypeptide ASRPS inhibits triple-negative breast cancer angiogenesis. The Journal of experimental medicine *217*. https://doi.org/10.1084/jem.20190950.

Wang, Y., Zeng, Z., Zhao, S., Tang, L., Yan, J., Li, N., Zou, L., Fan, X., Xu, C., and Huang, J., et al. (2021). Humanin Alleviates Insulin Resistance in Polycystic Ovary Syndrome: A Human and Rat Model-Based Study. Endocrinology *162*. https://doi.org/10.1210/endocr/bqab056.

Weinstein, J.N., Collisson, E.A., Mills, G.B., Shaw, K.R.M., Ozenberger, B.A., Ellrott, K., Shmulevich, I., Sander, C., and Stuart, J.M. (2013). The Cancer Genome Atlas Pan-Cancer analysis project. Nature genetics *45*, 1113-1120. https://doi.org/10.1038/ng.2764.

Wiśniewski, J.R., Zougman, A., Nagaraj, N., and Mann, M. (2009). Universal sample preparation method for proteome analysis. Nature methods *6*, 359-362. https://doi.org/10.1038/nmeth.1322.

Wu, Q., Wright, M., Gogol, M.M., Bradford, W.D., Zhang, N., and Bazzini, A.A. (2020a). Translation of small downstream ORFs enhances translation of canonical main open reading frames. The EMBO journal *39*, e104763. https://doi.org/10.15252/embj.2020104763.

Wu, S., Zhang, L., Deng, J., Guo, B., Li, F., Wang, Y., Wu, R., Zhang, S., Lu, J., and Zhou, Y. (2020b). A Novel Micropeptide Encoded by Y-Linked LINC00278 Links Cigarette Smoking and AR Signaling in Male Esophageal Squamous Cell Carcinoma. Cancer research *80*, 2790-2803. https://doi.org/10.1158/0008-5472.CAN-19-3440.

Wu, T., Hu, E., Xu, S., Chen, M., Guo, P., Dai, Z., Feng, T., Zhou, L., Tang, W., and Zhan, L., et al. (2021). clusterProfiler 4.0: A universal enrichment tool for interpreting omics data. Innovation (Cambridge (Mass.)) *2*, 100141. https://doi.org/10.1016/j.xinn.2021.100141.

Xian, H., and Liou, Y.-C. (2021). Functions of outer mitochondrial membrane proteins: mediating the crosstalk between mitochondrial dynamics and mitophagy. Cell death and differentiation *28*, 827-842. https://doi.org/10.1038/s41418-020-00657-z.

Xiao, M.-H., Lin, Y.-F., Xie, P.-P., Chen, H.-X., Deng, J.-W., Zhang, W., Zhao, N., Xie, C., Meng, Y., and Liu, X., et al. (2022). Downregulation of a mitochondrial micropeptide, MPM, promotes hepatoma metastasis by enhancing mitochondrial complex I activity. Molecular therapy : the journal of the American Society of Gene Therapy *30*, 714-725. https://doi.org/10.1016/j.ymthe.2021.08.032.

Xiao, W., Halabi, R., Lin, C.-H., Nazim, M., Yeom, K.-H., and Black, D.L. (2024). The lncRNA Malat1 is trafficked to the cytoplasm as a localized mRNA encoding a small peptide in neurons. Genes & development *38*, 294-307. https://doi.org/10.1101/gad.351557.124.

Xie, C., Wang, F.-Y., Sang, Y., Chen, B., Huang, J.-H., He, F.-J., Li, H., Zhu, Y., Liu, X., and Zhuang, S.-M., et al. (2022). Mitochondrial Micropeptide STMP1 Enhances Mitochondrial Fission to Promote Tumor Metastasis. Cancer research *82*, 2431-2443. https://doi.org/10.1158/0008-5472.CAN-21-3910.

Xin, H., Zhao, Z., Guo, S., Tian, R., Ma, L., Yang, Y., Zhao, L., Wang, G., Li, B., and Hu, X., et al. (2025). Targeting the JAK2-STAT3-UCHL3-ENO1 axis suppresses glycolysis and enhances the sensitivity to 5-FU chemotherapy in TP53-mutant colorectal cancer. Acta pharmaceutica Sinica. B *15*, 2529-2544. https://doi.org/10.1016/j.apsb.2025.03.041.

Xu, W., Deng, B., Lin, P., Liu, C., Li, B., Huang, Q., Zhou, H., Yang, J., and Qu, L. (2020). Ribosome profiling analysis identified a KRAS-interacting microprotein that represses oncogenic

signaling in hepatocellular carcinoma cells. Science China. Life sciences *63*, 529-542. https://doi.org/10.1007/s11427-019-9580-5.

Yang, F., Hu, A., Guo, Y., Wang, J., Li, D., Wang, X., Jin, S., Yuan, B., Cai, S., and Zhou, Y., et al. (2021). p113 isoform encoded by CUX1 circular RNA drives tumor progression via facilitating ZRF1/BRD4 transactivation. Molecular cancer *20*, 123. https://doi.org/10.1186/s12943-021-01421-8.

Yang, H., Li, Q., Stroup, E.K., Wang, S., and Ji, Z. (2024). Widespread stable noncanonical peptides identified by integrated analyses of ribosome profiling and ORF features. Nature Communications *15*, 1932. https://doi.org/10.1038/s41467-024-46240-9.

Yang, J.-E., Zhong, W.-J., Li, J.-F., Lin, Y.-Y., Liu, F.-T., Tian, H., Chen, Y.-J., Luo, X.-Y., and Zhuang, S.-M. (2023). LINC00998-encoded micropeptide SMIM30 promotes the G1/S transition of cell cycle by regulating cytosolic calcium level. Molecular oncology *17*, 901-916. https://doi.org/10.1002/1878-0261.13358.

Yang, M., Xie, Y., Wang, L., Jungreis, I., Ou, T., Kellis, M., Wang, J., and Zhu, Y. (2025). Proteogenomics-enabled discovery of novel small open reading frame (sORF)-encoded polypeptides in human and mouse tissues. Nucleic Acids Res *53*. https://doi.org/10.1093/nar/gkaf687.

Yeasmin, F., Imamachi, N., Tanu, T., Taniue, K., Kawamura, T., Yada, T., and Akimitsu, N. (2021). Identification and analysis of short open reading frames (sORFs) in the initially annotated noncoding RNA LINC00493 from human cells. Journal of biochemistry *169*, 421-434. https://doi.org/10.1093/jb/mvaa143.

Zaid, H., Abu-Hamad, S., Israelson, A., Nathan, I., and Shoshan-Barmatz, V. (2005). The voltage-dependent anion channel-1 modulates apoptotic cell death. Cell death and differentiation *12*, 751-760. https://doi.org/10.1038/sj.cdd.4401599.

Zanet, J., Benrabah, E., Li, T., Pélissier-Monier, A., Chanut-Delalande, H., Ronsin, B., Bellen, H.J., Payre, F., and Plaza, S. (2015). Pri sORF peptides induce selective proteasome-mediated protein processing. Science (New York, N.Y.) *349*, 1356-1358. https://doi.org/10.1126/science.aac5677.

Zhai, S., Lin, J., Ji, Y., Zhang, R., Zhang, Z., Cao, Y., Liu, Y., Tang, X., Liu, J., and Liu, P., et al. (2023). A microprotein N1DARP encoded by LINC00261 promotes Notch1 intracellular domain (N1ICD) degradation via disrupting USP10-N1ICD interaction to inhibit chemoresistance in Notch1-hyperactivated pancreatic cancer. Cell discovery *9*, 95. https://doi.org/10.1038/s41421-023-00592-6.

Zhang, C., Zhou, B., Gu, F., Liu, H., Wu, H., Yao, F., Zheng, H., Fu, H., Chong, W., and Cai, S., et al. (2022). Micropeptide PACMP inhibition elicits synthetic lethal effects by decreasing CtIP and poly(ADP-ribosyl)ation. Molecular cell *82*, 1297-1312.e8. https://doi.org/10.1016/j.molcel.2022.01.020.

Zhang, M., Zhao, K., Xu, X., Yang, Y., Yan, S., Wei, P., Liu, H., Xu, J., Xiao, F., and Zhou, H., et al. (2018). A peptide encoded by circular form of LINC-PINT suppresses oncogenic transcriptional elongation in glioblastoma. Nature Communications *9*, 4475. https://doi.org/10.1038/s41467-018-06862-2.

Zhang, S., Guo, Y., Fidelito, G., Robinson, D.R.L., Liang, C., Lim, R., Bichler, Z., Guo, R., Wu, G., and Xu, H., et al. (2023). LINC00116-encoded microprotein mitoregulin regulates fatty acid metabolism at the mitochondrial outer membrane. iScience *26*, 107558. https://doi.org/10.1016/j.isci.2023.107558.

Zhang, S., Reljić, B., Liang, C., Kerouanton, B., Francisco, J.C., Peh, J.H., Mary, C., Jagannathan, N.S., Olexiouk, V., and Tang, C., et al. (2020). Mitochondrial peptide BRAWNIN is essential for

vertebrate respiratory complex III assembly. Nat Commun *11*, 1312. https://doi.org/10.1038/s41467-020-14999-2.

Zhang, Y., Jia, C., Fullwood, M.J., and Kwoh, C.K. (2021). DeepCPP: a deep neural network based on nucleotide bias information and minimum distribution similarity feature selection for RNA coding potential prediction. Briefings in bioinformatics *22*, 2073-2084. https://doi.org/10.1093/bib/bbaa039.

Zhao, L., Tang, M., Bode, A.M., Liao, W., and Cao, Y. (2021). ANTs and cancer: Emerging pathogenesis, mechanisms, and perspectives. Biochimica et biophysica acta. Reviews on cancer *1875*, 188485. https://doi.org/10.1016/j.bbcan.2020.188485.

Zhu, S., Wang, J.-Z., de Chen, He, Y.-T., Meng, N., Chen, M., Lu, R.-X., Chen, X.-H., Zhang, X.-L., and Yan, G.-R. (2020a). An oncopeptide regulates m6A recognition by the m6A reader IGF2BP1 and tumorigenesis. Nat Commun *11*, 1685. https://doi.org/10.1038/s41467-020-15403-9.

Zhu, Y., Gu, L., Lin, X., Liu, C., Lu, B., Cui, K., Zhou, F., Zhao, Q., Prochownik, E.V., and Fan, C., et al. (2020b). Dynamic Regulation of ME1 Phosphorylation and Acetylation Affects Lipid Metabolism and Colorectal Tumorigenesis. Molecular cell *77*, 138-149.e5. https://doi.org/10.1016/j.molcel.2019.10.015.

Zong, Y., Li, H., Liao, P., Chen, L., Pan, Y., Zheng, Y., Zhang, C., Liu, D., Zheng, M., and Gao, J. (2024). Mitochondrial dysfunction: mechanisms and advances in therapy. Signal transduction and targeted therapy *9*, 124. https://doi.org/10.1038/s41392-024-01839-8.

Zorova, L.D., Popkov, V.A., Plotnikov, E.Y., Silachev, D.N., Pevzner, I.B., Jankauskas, S.S., Babenko, V.A., Zorov, S.D., Balakireva, A.V., and Juhaszova, M., et al. (2018). Mitochondrial membrane potential. Analytical biochemistry *552*, 50-59. https://doi.org/10.1016/j.ab.2017.07.009.

10 Acknowledgments

First and foremost, I want to thank Gunter Meister not only for giving me the opportunity to do my PhD in his lab, but also for giving me the freedom to grow both as a scientist and person in my time in this lab. Thank you for your support and ideas in our many discussions that helped me develop my scientific thinking and move my challenging but always exciting project forward. You gave me the room to new things and always had an open door for me. Moreover, I am truly grateful that you entrusted me with responsibilities that went beyond those of a normal PhD student. I enjoyed my time in your lab and am very happy to forever be part of the Meister family.

Secondly, I want to thank Gernot Längst, Markus Kretz, Joachim Griesenbeck and Klaus Grasser for being part of my thesis examination committee.

Furthermore, I want to thank my mentor and collaboration partner Sven Diederichs for the support and inspiring discussion. Additionally, a big thank you goes to my other collaboration partners Anastasia Chugunova, Andrea Pauli, Mara Hofmann, Christof Gebhardt, Lukas Wöhrl, Christian Werno, Stefanie Bader, Tatjana Jahner, Christian Wetzel, Vladimir Milenkovic, Jan Procházka, Michaela Prochazkova, Radislav Sedlacek and Marisa Riester for all the help moving my project forward and allowing me to be involved in a broad spectrum of different methods and topics.

I also want to thank Hung Ho for being a great supervisor during my master thesis and the early phase of my PhD. I certainly wouldn't be the scientist I am now without your mentorship, always open ear and all the suggestions you gave not just me but everyone else in the lab while making every day we spent in the lab fun.

A special thank you goes to all former and current members of Biochemistry I. I am grateful that I got to spend the time in my PhD with so many wonderful colleagues and friends. First, Birgit– our good soul and lab mum that is always there for everyone in the lab and solves so many problems before anyone even realizes they exist. I will never forget all the events we organized together and the spontaneous wine escalations we had. Thank you to Sigi, Corinna, Gerhard, Norbert and Robert. You keep the lab running with all your hard work and without you we would definitely all be lost. A very big thank you goes to all my PhD colleagues. Working with the Biochemistry Lovers & Partybeasts was a blast. I am thankful for the close bonds we

built during our time together and all the support we shared with each other. Thank you for all the help and discussions and even more so for all the fun events, beer hours and parties together! A am also thankful for the “young generation” for accepting the PhD grandpa in the group, the gossip sessions and fun together in the lab.

A big thank you goes to all my friends. First of all, my biochemiker and friends Michi, Georg, Simon, Tommy, Domi and Julia for going through all the highs and lows together, the support, fun boardgame or movie nights and amazing trips together! Secondly, the Naxler and Krisenrat Jojo, Bina, Michi, Rich and Dr. Franzbert for fun holiday trips (where we definitely never took the scenic route by accident), gossiping, pöbel-days and just all the fun we had all these years. I also want to thank Anja for the many gourmet cooking evenings we had as well as all the scientific and mental support you gave me.

Moreover, I am very happy to have my Jahn-family Marcel, Lukas, Daniele, Freibi, Simona, Jo, Philipp, Bruno and Luka. You helped me get my head clear in stressful times in the lab and I am grateful for all the hard-earned wins, tragic losses and all the fun and friendship we have along the way.

Lastly, thank you to those friends that rarely meet me but always make me feel like home whenever we are together. Stephan, Chris, Vanessa, Josef, Madelaine, Co, Eva, Markus and Flo for the weekend trips, supporting local heroes at the Wiesn and all the memories we created together (and for accepting who really is the better Wattn-Team), Dennis and Julian for the deep friendship we built from just a Blue Waters holiday almost 20 years ago and the MST group for all the fun events, dart nights and accepting me as if I was with you every single day. A very special thank goes to the person living the farthest apart from me. Maris, I am so grateful to have you by my side and for us to support each other through all the highs and lows all these years.

Most of all, I want to thank my family. I can’t imagine where I would be without my grandma, mum, dad and my siblings Dennis, Vivienne and Jasmin. You helped me become the person I am now and develop the drive we all share to always achieve the highest possible goal we can while being there for the people around us along the way. I know whatever happens in life I can always rely on you, and for that I am forever grateful. Love you all!